

5-13-91
E6068

NASA Conference Publication 10064

Structural Integrity and Durability of Reusable Space Propulsion Systems

LIMITED DISTRIBUTION DOCUMENT

Because of its significant technological potential, this information which has been developed under a U.S. Government program is being given a limited distribution whereby advanced access is provided for use by domestic interests. This legend shall be marked on any reproduction of this information in whole or in part.

Date for general release May 1993.

*Proceedings of a conference held at
NASA Lewis Research Center
Cleveland, Ohio
May 14 and 15, 1991*

NASA

Structural Integrity and Durability of Reusable Space Propulsion Systems

*Proceedings of a conference
held at NASA Lewis Research Center
Cleveland, Ohio
May 14 and 15, 1991*

NASA

National Aeronautics and
Space Administration

Office of Management

**Scientific and Technical
Information Division**

1991

Page intentionally left blank

PREFACE

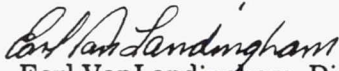
A major part of the NASA space technology program is focused on advanced propulsion systems that are targeted towards providing exceptional operational and cost benefits to current, next generation, and future Earth-to-orbit (ETO) space transportation systems. The Space Shuttle Main Engine (SSME) development program has provided technologists with a unique opportunity to identify and assess deficiencies that existed in our past design and analysis activities. As a consequence we have been able to initiate solutions to those deficiencies for use in future propulsion systems design and development. Where appropriate and beneficial, selected technology advancements stemming from this effort have been incorporated directly into the SSME itself.

Specific propulsion system goals for the future include enhanced safety and reliability; improved hardware quality and producibility; greater durability; enhanced system operability; and reduced life-cycle-costs. Past experience clearly tells us that if these goals are to be achieved, our ability to accurately establish hardware design margins, and to define system performance and operational characteristics, must be greatly enhanced; methods for producing higher-quality, lower-cost hardware must be developed; and unacceptably high operations costs must be sharply reduced. Accurate predictions of propulsion design margins and performance and operational characteristics can only be accomplished through greatly improved and validated design and analysis tools. In order to produce higher-quality, lower-cost hardware, advanced manufacturing processes must be developed, verified, and documented. Lower operations costs can only be achieved through the development and demonstration of automated inspection, servicing, and checkout systems and on-board integrated health management and control systems. Having these capabilities in hand for design purposes *prior* to the initiation of complex and expensive flight hardware development programs will have an enormous positive impact on program risk, cost, and potential schedule delays. The NASA Office of Aeronautics, Exploration and Technology (OAET) ETO Propulsion Technology Program is focused on providing the technology base that will allow achievement of these critical propulsion system goals and thus is a major key to the nation's ability to develop competitive space transportation systems in the future.

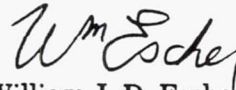
The Structural Integrity and Durability Program funded by the NASA Office of Space Flight (OSF) is an integral part of the ETO effort. It is aimed primarily at 1) enhancing analytical simulations of internal engine environments using Computational Fluid Dynamics (CFD) techniques; 2) defining steady and unsteady thermal and mechanical loads imposed on engine components by those environments; 3) predicting resulting component material behavior and thermo-structural response, and 4) accurately defining design margins and fatigue life. These advanced analytical tools will also provide the capability to achieve component designs that create less hostile internal environments, as well as designs that offer greater durability. The program is currently focused on the hot gas sections of typical rocket engines, particularly the hot gas flow through turbine stages. It includes not only the development of improved analytical models and computer codes, but also the use of special test rigs to generate meaningful experimental data bases needed for code validation. A special version of the SSME is also being used as a Technology Test Bed (TTB) to verify and validate selected analytical models and advanced component designs derived from the ETO program, in true internal engine environments. The SSME test bed testing activity is also managed and funded by OSF. In parallel with TTB validation, subsystem level validation will also be accomplished in large scale combustor and turbomachinery test beds that are planned activities in the ETO propulsion technology program.

The status of specific areas of effort that will be reviewed during this conference include hot

gas flow characterization (CFD), aerothermodynamic loads definition, probabilistic structural analysis, fracture mechanics, high cycle/low cycle interactions, fatigue life prediction, and research instrumentation. Working together, our ultimate purpose is to "improve the breed."



Earl VanLandingham, Director
Propulsion, Power, and Energy Division
NASA Headquarters
Washington, D.C.



William J. D. Escher, Manager
ETO Propulsion Technology Program
NASA Headquarters
Washington, D.C.

FOREWORD

This fourth biannual conference provided a summary of eight years of NASA's effort to improve the structural integrity and durability of reusable space propulsion systems. Although the program is now being redirected, it is time to reflect on where we have been and how the program has contributed to the overall space shuttle main engine (SSME) program.

The program was initiated in late 1983 by the NASA Office of Space Flight (OSF) when a deficiency in the SSME technology base was recognized. It was decided to augment the Earth-to-Orbit Propulsion Technology Program sponsored by the Office of Aeronautics and Exploration Technology (OAET). That deficiency was the inability to predict the life of structural components in high-performance reusable rocket engines. It was manifested by the SSME component replacement and repair requirements. Development of the analytical models for aerothermodynamic loads, structural response, and fatigue/fracture effects was, therefore, undertaken to produce more accurate life prediction design tools.

As the models and analytical methods were being developed, they were used to assess immediate SSME needs, such as problems related to thermal cracking. In the past two years, several technology items have reached sufficient maturity levels to be disseminated to the propulsion community. Probabilistic structural analysis and life prediction codes have been released through workshops and are being used by engine manufacturers; advanced instrumentation techniques have been developed for final validation. In addition, the fatigue/life prediction methods developed under this program are being used to examine the high cycle/low cycle fatigue interaction effects on the potential materials in the Pratt & Whitney Alternate Turbopump.

In the past year, the program has been extensively reviewed by the Office of Space Flight and the SSME engine office at the Marshall Space Flight Center. This structural durability program is viewed as being technology-oriented as well as SSME specific. Upon review of the various elements of the program, it is being integrated into the technology development program of the SSME engine office in part. In 1992, the portion of the program related to material modeling, structural response prediction and aerothermal load modeling will be a part of the SSME engine program and remain SSME specific. The remaining portion will be integrated into the Earth-to-Orbit Propulsion program and redirected to meet OAET objectives. The intention is to continue the development of structural durability models and codes.

This conference provided a forum for representatives from government, industry, and academia to learn about and discuss the latest findings and progress of the Structural Durability program. Extended abstracts and the figures used for each of the presentations at the two-day conference are included in these proceedings.


Anita D. Liang
Conference Chairman

Page intentionally left blank

CONTENTS

SESSION I - STRUCTURAL INTEGRITY AND DURABILITY

Chair, William C. Nieberding

| | |
|---|----|
| <i>Overview of the Instrumentation Program</i> William C. Nieberding, NASA Lewis Research Center | 1 |
| <i>Progress in the Measurement of SSME Turbine Heat Flux with Plug-Type Sensors</i> Curt H. Liebert, NASA Lewis Research Center | 3 |
| <i>Thin Film Heat Flux Sensor for Space Shuttle Main Engine Turbine Environment</i> Herbert Will, NASA Lewis Research Center | 9 |
| <i>Thin Film Thermocouples for High Temperature Turbine Application</i> Lisa C. Martin, NASA Lewis Research Center | 15 |
| <i>Rayleigh-Brillouin Scattering for High-Pressure Gas Temperature Measurements</i> Richard G. Seasholtz, NASA Lewis Research Center | 21 |
| <i>Neural Nets for Aligning Optical Components in Harsh Environments - Beam Smoothing Spatial Filter as an Example</i> Arthur J. Decker and Michael J. Krasowski, NASA Lewis Research Center | 29 |
| <i>Progress in Speckle-Shift Strain Measurement</i> Christian T. Lant, Sverdrup Technology, Inc., and John P. Barranger, Lawrence G. Oberle, and Lawrence C. Greer III, NASA Lewis Research Center | 39 |
| <i>OPAD 1991 - A Status Report</i> W.T. Powers and A.E. Cooper, NASA George C. Marshall Space Flight Center | 45 |
| <i>An Integrated Eddy Current Detection and Imaging System on a Silicon Chip</i> H. Thurman Henderson, K.P. Kartalia, and Joseph D. Dury, University of Cincinnati | 51 |
| <i>Four Dimensional Reconstruction and Analysis of Plume Images</i> Atam P. Dhawan, Charles Peck III, and Peter Disimile, University of Cincinnati | 63 |

SESSION II - STRUCTURAL INTEGRITY AND DURABILITY

Chair, Christos C. Chamis

| | |
|---|----|
| <i>Structural Dynamics: Probabilistic Structural Analysis Methods Program Overview</i> Christos C. Chamis and Dale A. Hopkins, NASA Lewis Research Center | 65 |
|---|----|

| | |
|--|-----|
| <i>Structural Reliability Methods - Code Development Status</i> H. Millwater, B. Thacker, and Y.-T. Wu, Southwest Research Institute, and T. Cruse, Vanderbilt University | 71 |
| <i>Probabilistic Load Simulation - Code Development Status</i> J.F. Newell and H. Ho, Rockwell International Corp. | 77 |
| <i>Probabilistic Evaluation of SSME Structural Components</i> K.R. Rajagopal, J.F. Newell, and H. Ho, Rockwell International Corp. | 85 |
| <i>Rocketdyne PSAM - In House Enhancement/Application</i> J.F. Newell, K.R. Rajagopal, and K. O'Hara, Rockwell International Corp. | 97 |
| <i>Commercialization of Nessus - Status</i> Ben H. Thacker and Harry R. Millwater, Southwest Research Institute | 105 |
| <i>System Reliability and Risk Assessment Task Goals & Status</i> T.A. Cruse and S. Mahadevan, Vanderbilt University | 111 |
| <i>Probabilistic Structural Analysis Algorithm Development for Computational Efficiency</i> Y.-T. Wu, Southwest Research Institute | 121 |
| <i>Expert System Development for Probabilistic Load Simulation</i> H. Ho and J.F. Newell, Rockwell International Corp. | 131 |
| <i>Probabilistic Fracture Finite Elements</i> W.K. Liu, T. Belytschko, and Y.J. Lua, Northwestern University | 137 |
| <i>Mapping Methods for Computationally Efficient and Accurate Structural Reliability</i> Michael C. Shiao, Sverdrup Technology, Inc., and Christos C. Chamis, NASA Lewis Research Center | 145 |
| <i>Probabilistic Simulation of the Human Factor in Structural Reliability</i> Ashwin R. Shah, Sverdrup Technology, Inc., and Christos C. Chamis, NASA Lewis Research Center | 159 |

SESSION III - STRUCTURAL INTEGRITY AND DURABILITY
Chair, Michael A. McGaw

| | |
|--|-----|
| <i>Overview of the Fatigue/Fracture/Life Prediction Working Group Program at the Lewis Research Center</i> Michael A. McGaw, NASA Lewis Research Center | 169 |
| <i>Cumulative Fatigue Damage Behavior of MAR M-247</i> Michael A. McGaw and Gary R. Halford, NASA Lewis Research Center, and Sreeramesh Kalluri, Sverdrup Technology, Inc. | 173 |

| | |
|--|-----|
| <i>The Effect of Porosity and γ-γ' Eutectic Content on the Low Cycle Fatigue Behavior of Hydrogen-Charged PWA 1480</i> John Gayda, Robert L. Dreshfield, and Timothy P. Gabb, NASA Lewis Research Center | 179 |
| <i>Constitutive and Damage Material Modeling in a High Pressure Hydrogen Environment</i> D.A. Russell and L.G. Fritzemeier, Rockwell International Corp. | 187 |
| <i>Secondary Orientation Effects in a Single Crystal Superalloy Under Mechanical and Thermal Loads</i> Sreeramesh Kalluri and Ali Abdul-Aziz, Sverdrup Technology, Inc., and Michael A. McGaw, NASA Lewis Research Center | 197 |
| <i>A Model for Predicting High-Temperature Fatigue Failure of a W/Cu Composite</i> M.J. Verrilli, Y.-S. Kim and T.P. Gabb, NASA Lewis Research Center | 207 |
| <i>Examination of the Effect of Propulsion System Performance Variables on the Life Prediction for the SSME LOX Post</i> D.A. Russell, K.R. Rajagopal, G. Orient, and J. Keremes, Rockwell International Corp. | 219 |
| <i>Life Extending Control - An Interdisciplinary Engineering Thrust</i> Carl F. Lorenzo and Walter C. Merrill, NASA Lewis Research Center | 229 |
| <i>Axial and Torsional Fatigue Behavior Of A Cobalt-Base Alloy</i> Peter J. Bonacuse, U.S. Army Aviation Systems Command, NASA Lewis Research Center, and Sreeramesh Kalluri, Sverdrup Technology, Inc. | 239 |

SESSION IV - STRUCTURAL INTEGRITY AND DURABILITY

Chair, Raymond E. Gaugler

| | |
|---|-----|
| <i>Overview of Aerothermodynamic Loads Definition Study</i> Raymond E. Gaugler, NASA Lewis Research Center | 247 |
| <i>Three-Dimensional Analysis of the Pratt & Whitney Alternate Design SSME Fuel Turbine</i> K.R. Kirtley and T.A. Beach, Sverdrup Technology, Inc., and J. J. Adamczyk, NASA Lewis Research Center | 255 |
| <i>Three-Dimensional Flow Calculations Inside SSME GGGT First Stage Blade Rows</i> Chunill Hah, NASA Lewis Research Center, Steven Nash, Sverdrup Technology, Inc., and Gregory Swartwout, NASA Lewis Research Center | 263 |
| <i>Localization of Aeroelastic Modes in Mistuned High-Energy Turbines</i> Todd E. Smith, Sverdrup Technology, Inc., Christophe Pierre, The University of Michigan and Durbha V. Murthy, The University of Toledo | 273 |

Heat Transfer and Pressure Measurements for the SSME Fuel Turbine
Michael G. Dunn and Jungho Kim, Calspan - UB Research Center 281

Penn State Axial Flow Turbine Facility: Performance and Nozzle Flow Field
B. Lakshminarayana and M. Zaccaria, The Pennsylvania State University,
and S. Itoh, National Defense Academy 283

OVERVIEW OF THE INSTRUMENTATION PROGRAM

William C. Nieberding
NASA Lewis Research Center
Cleveland, Ohio 44135

One of the major goals of the durability program is to develop computational models of the structural behavior, the fatigue life, and the environmental conditions pertinent to advanced reusable space propulsion systems. In many cases, however, there is very little experimental data available to either verify these models or to use as input conditions to the models.

The instrumentation portion of this durability program is thus aimed primarily at developing sensors and measurement systems capable of obtaining the data necessary to verify computational models. Indeed, some of these sensor systems, such as the plug type heat flux sensor, are finding their way into the test bed engine. Some may eventually reach advanced flight engines. This is increasingly likely because of the recent rise in importance of instrumentation for health monitoring purposes. The major effort, though, is still to develop what is needed for bench mark experiments in research rigs to more fully define the actual conditions experienced in a rocket engine. In some cases, the only research rig available will be the test bed engine simply because conditions cannot be adequately simulated in less extensive facilities.

One of the characteristics of measurement systems needed to verify codes is that the sensors must be nonintrusive or at least minimally intrusive so that the conditions being measured are not significantly perturbed. This is because the computer codes do not take into account the perturbations that would be caused by an intrusive sensor or probe. This leads to a heavy emphasis on laser optical techniques and on thin film sensors.

Another characteristic of such instruments is that they must be highly accurate and produce very high spatial and temporal resolution of the parameter being measured. Verifying codes demands this because the codes usually calculate highly resolved maps of such things as velocity, strain, temperature, species concentration, etc.

The needed measurement systems generally fall into a number of broad categories. First there are the measurements needed on the surfaces of components such as turbine blades and vanes. Some of the desired parameters are temperature, strain, and heat flux. In this session I will discuss the significant progress being made in these measurement areas.

Another broad category encompasses those measurements needed in the flow environment around these components. Here, the desired results are high resolution maps of such parameters as flow velocity, temperature, density, pressure, and species concentration.

The remaining category deals with measurements necessary for monitoring the health of engines. This category has loomed ever more important for the SSME since the Challenger disaster and takes on even greater significance when

one considers the long duration propulsion missions being considered for future engines. One paper deals with an optical method for determining the characteristics of the exhaust plume. Another deals with the problem of crack detection.

In summary, the instrumentation program is aimed at high accuracy, high resolution, minimally intrusive measurements on space propulsion system components and of the environment that surrounds these components. The primary goal is code verification but some of the results may apply to later flight instruments. Health monitoring is becoming ever more important particularly when one considers the future propulsion system missions.

PROGRESS IN THE MEASUREMENT OF SSME TURBINE HEAT FLUX WITH PLUG-TYPE SENSORS

Curt H. Liebert
NASA Lewis Research Center
Cleveland, Ohio 44135

Data reduction has been completed for tests of plug-type heat flux sensors (gauges) in a turbine blade thermal cycling tester (TBT). This TBT is located at NASA/Marshall Space Flight Center. A typical gauge is illustrated in figure 1. These tests were discussed last year at the 1990 Advanced Earth-to-Orbit Propulsion Technology Conference. This is the first time heat flux has been measured in a space shuttle main engine (SSME) turbopump turbine environment. The tests were highly successful.

The development of the concept for the gauge was done in a heat flux measurement facility located at Lewis. This facility was described at the 1987 Structural Integrity and Durability of Reusable Space Propulsion Systems Conference. In this facility, transient and steady state absorbed surface heat flux information was obtained from transient temperature measurements taken at points within the gauge. Figure 2 shows a gauge that has been placed at the external focus of an elliptical reflector in a lamp head attached to the side of a service module in the lamp system. A 100-kW Vortek arc lamp is used as a source of transient and steady state thermal radiant energy which impinges onto the active surfaces of heat flux gauges.

A schematic of the TBT is presented in figure 3. Three test blades with gauges built into their airfoils were located in position B of figure 3. On the upper blade, the active surface of the gauge is positioned on the airfoil pressure surface at midspan and midchord. Another gauge is mounted on the suction surface of the middle blade at the throat between the airfoil root and midspan. The gauge on the lower airfoil is positioned on the suction surface at midspan and midchord. The TBT was operated for 2½ cycles for a total test time of 48 seconds. A ruptured seal on a TBT component caused shutdown prior to the usual 5 cycle test series.

Plots of the absorbed surface heat flux measured on the three blades tested in the TBT are shown in figure 4. The uncertainty in the measurements is believed to be 7 to 30 percent (ref. 1). In general, the heat fluxes measured on all three blades followed nearly the same transient and quasi-steady state energy pattern. During startup, the transient heat flux varied irregularly as TBT gas pressure and temperature fluctuated through rapidly varying transients. After startup, the TBT operated at quasi-steady combustion conditions resulting in a smooth decrease in heat flux as the gauges and blades reached thermal equilibrium with their quasi-steady hot gas surroundings. The sign of the heat flux measured during this startup and quasi-steady portion of the cycle was positive which signifies that heat is being gained (absorbed) by the blades. Maximum temperatures achieved by the gauges were about 1460 K (2180 °F) as the blades approached equilibrium conditions with their hot surroundings. At this maximum temperature, measured heat flux was about 0.17 MW/m². This is about the lowest absolute value of heat flux that can be meaningfully measured with these gauges in the TBT. Negative values of tran-

sient heat flux (fig. 4) were generally obtained during the cooling part of the cycle when combustion is stopped and then very cold gas is admitted to the TBT. These negative values indicate that heat is being lost from the active surface of the gauge. The lowest temperatures measured with the gauges was about 93 K (-293 °F).

The solid line in figure 4 passes through the center blade heat flux data and is the most representative of the SSME turbopump turbine conditions. Center blade peak heat fluxes were measured as 14 and -14.7 MW/m² at maximum heating and cooling conditions. These values are in reasonable agreement with SSME design calculations. High quality heat flux values were measured on all three blades. The experiments demonstrated that reliable and durable gauges can be repeatedly fabricated into the airfoils. The experimental heat flux data are being used for verification of SSME analytical stress, boundary layer, and heat transfer design models. The measured heat flux of 14 MW/m² is 50 to 100 times those encountered in aircraft engines.

Future efforts include plans for using these gauges for absorbed surface heat flux measurement in SSME testbed engine turbopump nozzles at Marshall. Figure 5 shows a rear view of a plug gauge mounted into an SSME vane airfoil for heat flux measurement on the pressure surface. Figure 5 also shows a nozzle segment from which a vane was cut for mounting and testing in the heat flux measurement facility at Lewis. The heat flux tests demonstrated that the gauge was of high quality.

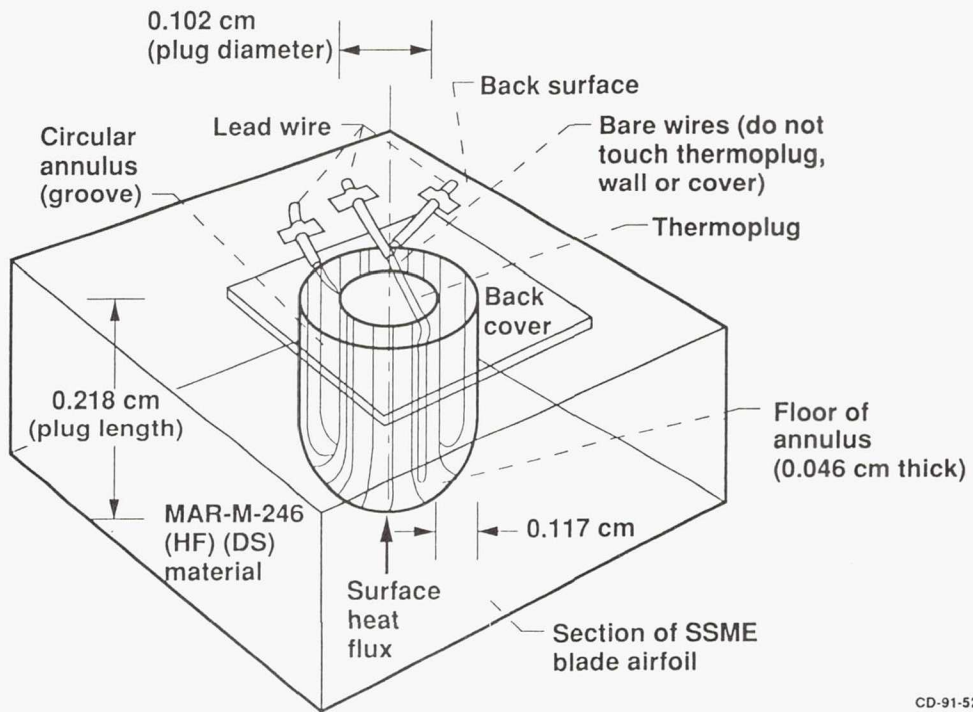
Research is continuing on the development of a rational basis for steady state and transient calibration of heat flux sensors. This research involves round robin tests with Pratt & Whitney and Case Western Reserve University. For this round robin, four gauges are being fabricated at Lewis. Each gauge is first being tested in the Lewis facility. Figure 6 shows some representative data obtained at low arc lamp input currents. Agreement of this data with the data taken with commercial Hi-Cal gauges is satisfactory. These measurements were obtained at the lower limit of arc lamp energy output thus demonstrating that heat fluxes can be satisfactorily measured for several seconds at lower levels of quasi-steady heating (and cooling) conditions such as occurred in the TBT.

Finally, these gauges are being considered for radial turbine rotor, advanced short takeoff and vertical landing aircraft research and for thin film heat flux gauge and thin film thermocouple experiments at Lewis.

REFERENCES:

1. Liebert, C. H.: Heat Flux Measurement in SSME Turbine Blade Tester. NASA TM-103274, 1990.

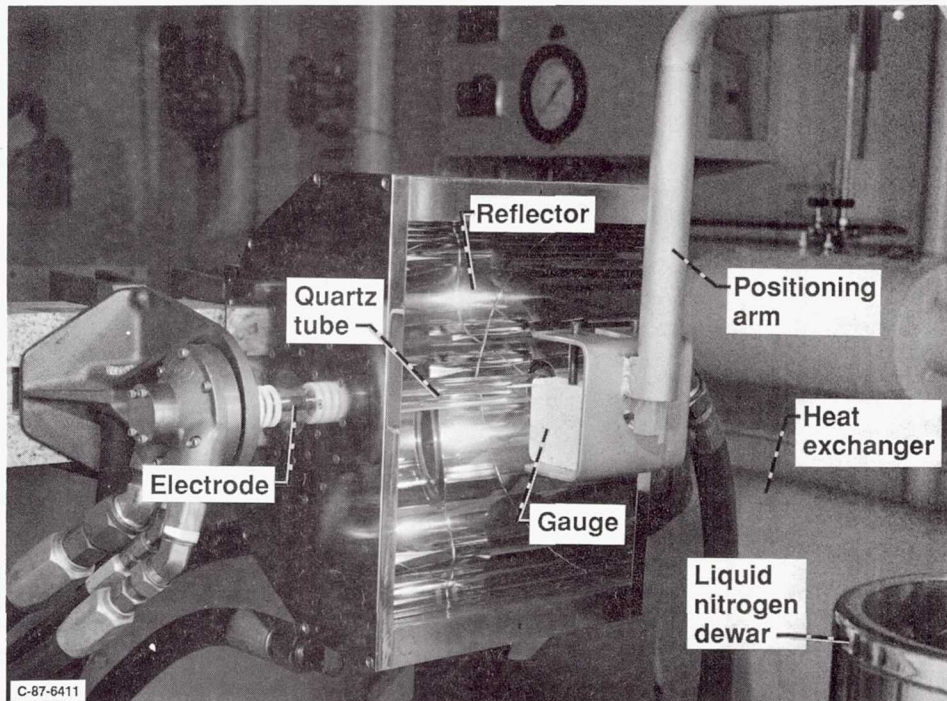
Plug Heat Flux Gage



CD-91-52049

Figure 1

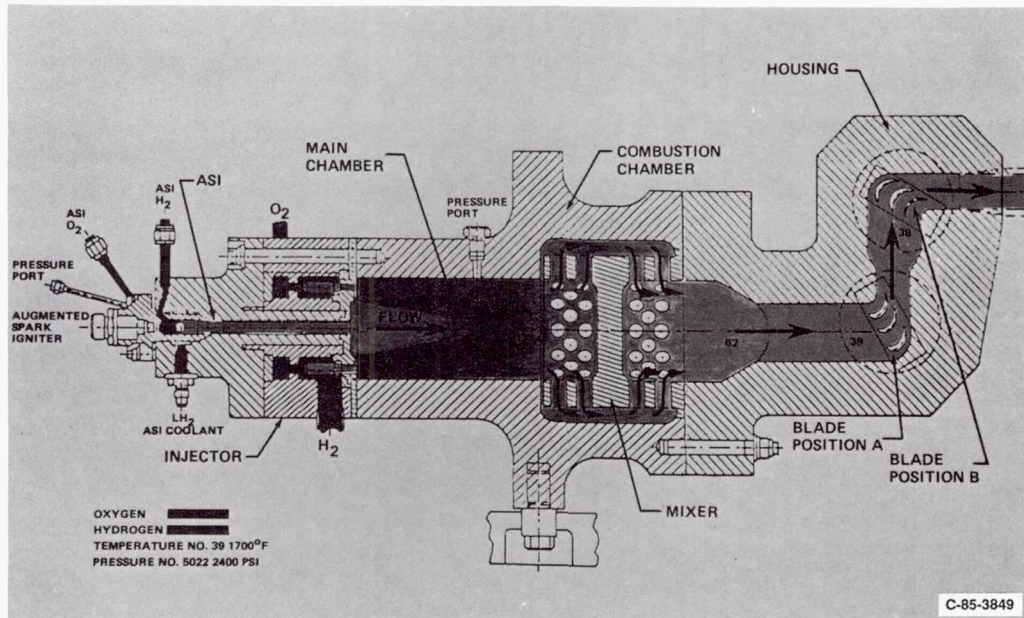
Lamphead and Positioning Arm



CD-91-52050

Figure 2

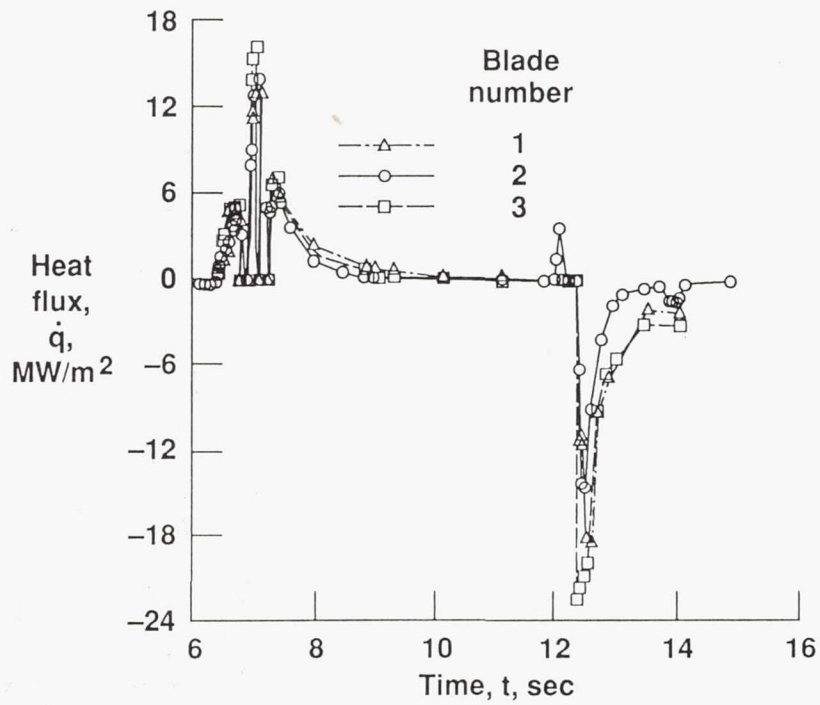
Turbine Blade Thermal Cycling Tester



CD-91-52051

Figure 3

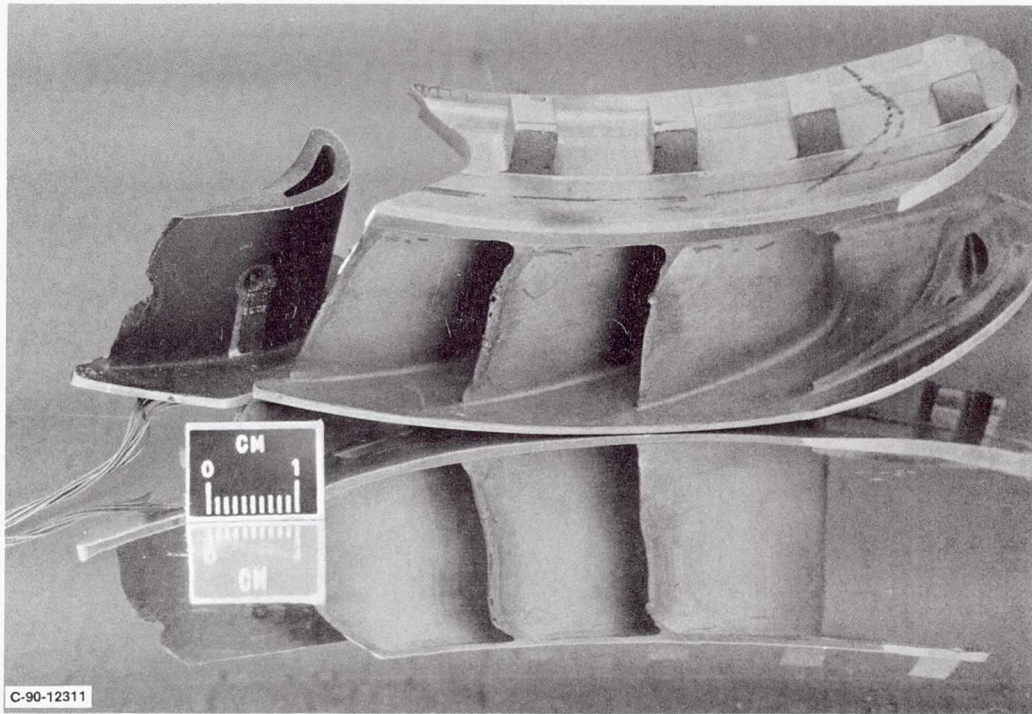
Heat Flux Measurements on Three Blades



CD-91-52052

Figure 4

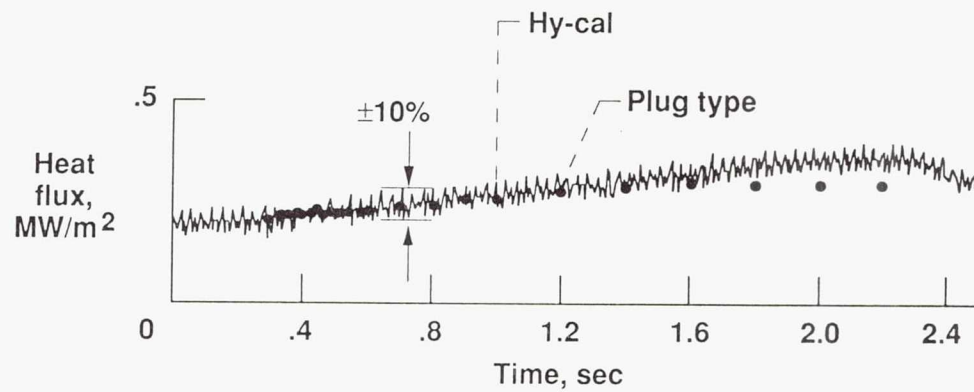
Plug Gauge in SSME Nozzle Vane



CD-91-52053

Figure 5

Heat Flux Measurements on Three Blades



CD-91-52054

Figure 6

Page intentionally left blank

THIN FILM HEAT FLUX SENSOR FOR SPACE SHUTTLE MAIN ENGINE TURBINE ENVIRONMENT

Herbert Will
NASA Lewis Research Center
Cleveland, Ohio 44135

The space shuttle main engine (SSME) turbine environment stresses engine components to their design limits and beyond. The extremely high temperatures and rapid temperature cycling can easily cause parts to fail if they are not properly designed. Thin film heat flux sensors can provide heat loading information with almost no disturbance of gas flows or of the blade. These sensors can provide steady-state and transient heat flux information.

Most heat flux sensors determine the heat flux by measuring the temperature on the top and bottom of a slab of insulating material. The heat flow per unit area through the insulating material is expressed as

$$\frac{H}{A} = \frac{K(T_1 - T_2)}{t}$$

where K is the coefficient of thermal conductivity, A is the area, t is the thickness, T_1 is the temperature of one face, and T_2 is the temperature of the other face.

In order to measure heat flux using the above equation, it is necessary to measure the temperature across an insulating layer. This is accomplished by putting a thermocouple on the top and bottom surfaces of the insulating layer. The two thermocouples are connected electrically so the voltages subtract. The subtracted output voltage is the difference between the two thermocouples. This difference voltage is then proportional to $(T_1 - T_2)$, which is the temperature difference across the insulating layer.

The above equation tells us that the thicker the insulating layer, the easier it is to measure the temperature difference across the layer. The heat flux encountered in an SSME environment can be several megawatts per square meter. For a $1\text{-}\mu$ -thick aluminum oxide layer, it can be shown that a temperature difference of 0.17 K will be obtained for a heat flux of 1 MW/m^2 . This small temperature difference is difficult to measure with high-temperature thermocouples such as Pt-Pt13%Rh.

The thin film heat flux sensor described herein makes it easier to measure small temperature differences across very thin insulating layers. This is done by patterning 100 thermocouple sensors on the top surface and 100 sensors on the bottom surface of the insulating layer (refs. 1 and 2). A top and bottom thermocouple pair is connected through the insulating layer so the outputs subtract. The thermocouple pairs are connected in a thermopile arrangement so their difference voltages add. The resultant output voltage is proportional to the temperature difference across the insulating layer and is 100 times that of a single thermocouple pair.

A three-dimensional drawing of a 10-thermocouple-pair heat flux sensor is shown in figure 1. The heat flux sensor consists of an insulating layer with 10 pairs of thermocouples on the top and bottom surfaces of the layer. The thermocouple pairs are sputter deposited onto the insulator surface in a circle. This configuration was chosen so that the sensor measures only the heat flux normal to the surface. The connecting wires are sputter deposited through holes in the insulator on the circumference of a larger diameter circle. This is done so the connecting wires do not disturb the heat flow in the vicinity of the thermocouple junctions.

The thin film heat flux sensor can be applied directly to the surface of engine parts. If the surface that the sensor is to be put on is electrically conducting, then an insulating layer must be applied first. All the layers are applied using RF diode sputtering. The thermocouples are patterned using photoresist lift-off and wet chemical etching techniques.

A previous presentation (refs. 1 and 2) on this subject indicated a problem with holes in the insulating layer between the sensor and the substrate. This problem has been solved by heating the substrate to 600 °C during the sputtering of an aluminum oxide insulating layer.

A thin film heat flux sensor fabricated on a silicon substrate is shown in figure 2. Although the sensor is not without problems, it did work when tested. The resistance of the sensor was 171 ohms across the terminals. The resistance between sensor and substrate was greater than 10 megohms, indicating no shorting through the insulator. The expected output of the gage as a function of heat flux is shown in figure 3. The measured output using a heat gun as a source of heat was 0.2 to 0.4 mV. This heat flux sensor failed after repeated temperature cycling. The failure was an open circuit in at least one of the thermocouple legs. Figure 4 shows a voltage contrast scanning electron micrograph of a failed thermocouple leg. It appears that the failure is at the plated through holes of the thermal barrier layer (see arrow in photograph).

So far all of the work on thin film heat flux gages has concentrated on flat substrates. SSME turbine blades are not flat. It is a problem to put a thin film pattern on the blade. The standard process of applying the thin film pattern is by sputter depositing a metal through a photoresist mask. When the photoresist mask is removed, the thin film pattern is left behind.

We are considering three methods for putting patterns on curved surfaces. In the first method, the pattern is produced on a flexible mask. Photoresist is applied to the curved surface. The mask is then held against the photoresist and the photoresist is exposed through the mask with ultraviolet light. The advantages of this method are that it is cheap and simple to implement. The disadvantage is that the mask cannot be accurately placed, which makes multilayered structures very difficult to fabricate. A variation of this method would be to use a flexible metal mask, and sputter deposit through the metal mask, eliminating the photoresist.

A second method under consideration makes use of a flat mask to put patterns on parts of the blade that are not highly curved, thus employing the same precision mask alignment equipment used for the flat samples. The advantage of this method is that it makes multilayered structures easier to

fabricate because of the precision alignment equipment. The disadvantages are that the pattern can only be applied to surfaces with a large radius of curvature, the light source must be highly collimated, and the alignment equipment is moderately expensive (\$5000 to \$50 000).

A third method makes use of a computer-controlled laser write pattern generator. A computer controls the writing of a small spot on the photoresist surface and also controls the X,Y,Z and tilt of the blade. The contour of the blade would have to be programmed into the computer ahead of time. By moving and tilting the blade, the pattern is written onto the blade. No mask is needed. An advantage of this method is that it is potentially very accurate and could be used to write patterns on highly curved surfaces. The disadvantages are that it would be very slow (it may take several hours to produce one pattern) and that this equipment can be very expensive (maybe \$1/2 to \$1 million).

REFERENCES

1. Will, H.: Thin Film Heat Flux Sensor: Electrochemical Society Proceedings, May 1990.
2. Will, H.: Thin Film Heat Flux Sensor: Advanced Earth-to-Orbit Propulsion Technology, Marshall Space Flight Center, May 1990.

Thin Film Heat Flux Sensor With 10 Thermocouple Pairs

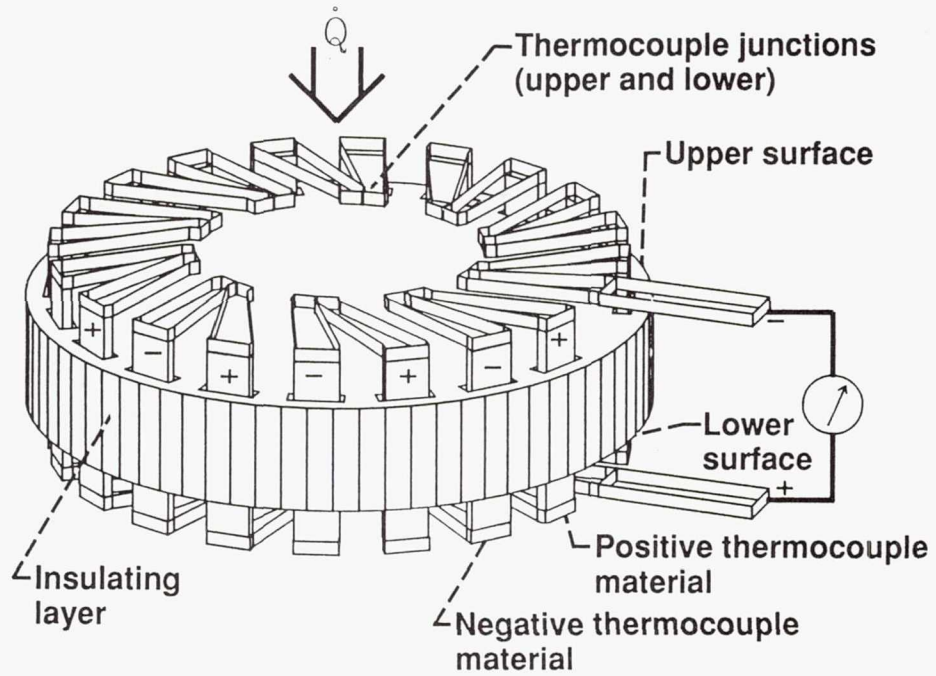


Figure 1

CD-91-52024

Complete Thin Film Heat Flux Sensor

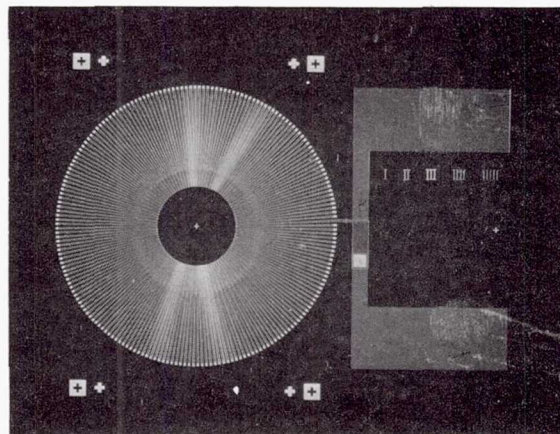


Figure 2

CD-91-52025

Expected Output of Thin Film Heat Flux Gage as a Function of Heat Flux

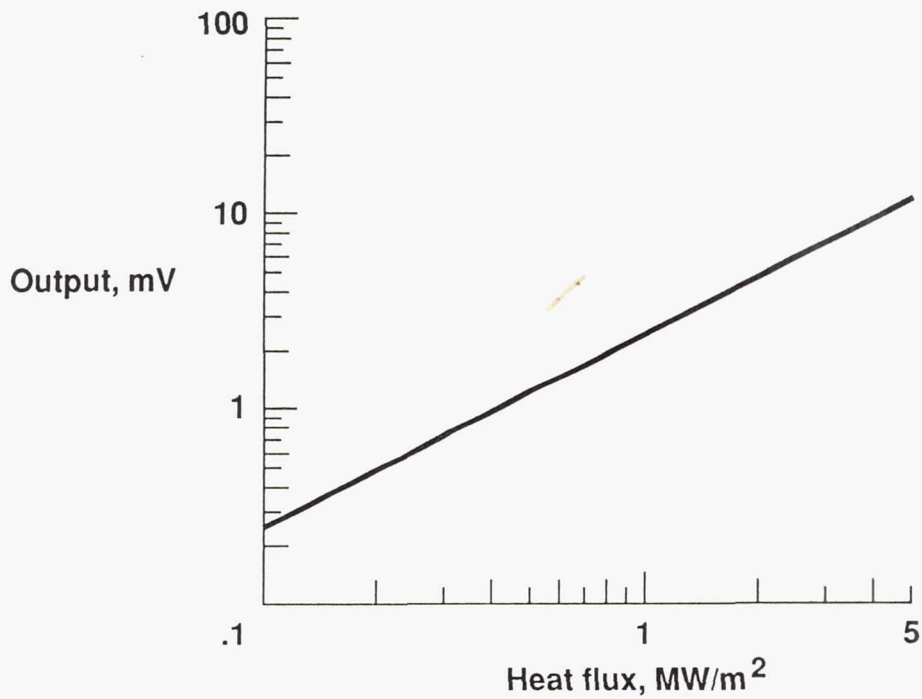


Figure 3

CD-91-52026

Scanning Electron Micrograph of Failed Thermocouple Leg

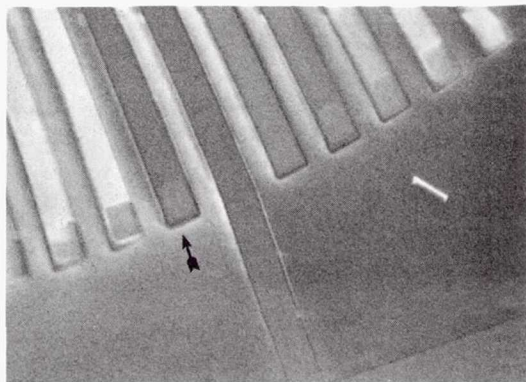


Figure 4

CD-91-052027

Page intentionally left blank

THIN FILM THERMOCOUPLES FOR HIGH TEMPERATURE TURBINE APPLICATION

Lisa C. Martin
NASA Lewis Research Center
Cleveland, Ohio 44135

The objective of this in-house program is to develop thin film thermocouples (TFTC) for space shuttle main engine (SSME) components such as high-pressure fuel turbopump (HPFTP) blades and to test TFTC survivability and durability in the SSME environment. The purpose for developing TFTC's for SSME components is to obtain blade temperatures for computational models developed for fluid mechanics and structures. The TFTC must be able to withstand the presence of high-temperature, high-pressure hydrogen as well as a severe thermal transient due to a cryogenic-to-combustion temperature change. TFTC's will eventually be installed and tested on SSME propulsion system components in the SSME test bed engine.

TFTC's were successfully fabricated on flat coupons of MAR-M 246 (+Hf), which is the superalloy material used for HPFTP turbine blades. The multi-layer sensor, as adapted from technology developed for aircraft gas turbine engines, is shown in figure 1 (refs. 1 to 4). The platinum and platinum-13% rhodium thermocouple legs are sputter deposited on an electrically insulating aluminum oxide layer. Aluminum oxide is initially thermally grown on a NiCoCrAlY coating and then an additional aluminum oxide layer is sputter deposited to insure an electrically insulating coating. The NiCoCrAlY coating is a thermal barrier coating with a composition of 23% Co, 18% Cr, 12% Al, 0.3% Y, and the balance Ni. TFTC's fabricated on flat coupons (fig. 2) survived thermal shock cycling as well as testing in a heat flux measurement facility which provided a rapid thermal transient (ref. 5).

The same fabrication procedure was used to deposit TFTC's on HPFTP first-stage rotor blades (fig. 3). Three blades, each with three TFTC's, were mounted in a wired blade holder (fig. 4) and subsequently tested in the Turbine Blade Tester (TBT) facility located at the NASA Marshall Space Flight Center (fig. 5). The TBT simulates the SSME HPFTP turbine environment with the combustion of oxygen and hydrogen at approximately 930 °C (1700 °F) and 16 MPa (2400 psi). The test cycled between cryogenic temperatures and 930 °C for two and one-half cycles. As shown in figure 6, the TFTC's were unable to withstand the SSME simulated environment and consequently were completely removed from the blade surfaces during testing.

Analysis by energy dispersive spectroscopy (EDS) revealed trace amounts of silicon originating from the masking technique that was used in fabricating the platinum and platinum-13% rhodium films on the turbine blades. The masking technique consisted of a thin strip of mylar tape that was used to delineate the thermocouple leg. A thin coating of adhesive was sprayed over the remaining surface area, the tape was removed, platinum was sputtered onto the exposed surface, and the adhesive was removed. The mylar tape is the source of silicon and may have contributed to poor film adherence. However, additional study has demonstrated that the combination of treatments used to fabricate the insulating aluminum oxide film as well as the platinum films is also critical in producing a high degree of adherence between the two layers in both the as-deposited and thermally cycled conditions (ref. 6). These

treatments include variables such as substrate temperature, oxygen content, and power levels used during sputter deposition of aluminum oxide, platinum and platinum-13% rhodium. It is critical to the platinum adherence that a pure, defect-free, insulating oxide be formed. Because of the temperature limits of the adhesive used in the masking procedure, changes in some of these variables from that used previously have dictated that a different masking procedure be used in fabricating the TFTC's. Alternate masking procedures are also being investigated.

TFTC's are being fabricated on coupons in preparation for testing in a hydrogen-oxygen rocket engine facility located at the NASA Lewis Research Center (figs. 7 and 8). Hydrogen-oxygen combustion gases ranging in temperature from about 1000 °C (1800 °F) to about 2700 °C (5000 °F) are obtainable at combustion chamber pressures up to 4 MPa (600 psi) and are discharged to the atmosphere. The sample can be mounted in the combustion chamber or downstream of the exhaust nozzle (ref. 7). This facility will be used to test samples prepared with different fabrication procedures to determine which procedure provides the greatest degree of film adherence when the film is subjected to a hot gas flow environment. TFTC's will then be fabricated on SSME turbine blades and tested in the TBT.

REFERENCES

1. Grant, H.P.; Przybyszewski, J.S.; and Claing, R.G.: Thin-Film Temperature Sensor. (PWA-5526-31, Pratt & Whitney Aircraft Group; NASA Contract NAS3-20768), NASA CR-159782, 1980.
2. Grant, H.P.; Przybyszewski, J.S.; and Claing, R.G.: Turbine Blade Temperature Measurements Using Thin-Film Temperature Sensors. (PWA-5604-31, Pratt & Whitney Aircraft Group; NASA Contract NAS3-20831), NASA CR-165201, 1981.
3. Grant, H.P., et al.: Thin Film Temperature Sensors, Phase III. (PWA-5708-26, Pratt & Whitney Aircraft Group; NASA Contract NAS3-22002), NASA CR-165476, 1982.
4. Kreider, K.G.; Semancik, S.; and Olson, C.: Advanced Thin Film Thermocouples. (NBSIR-84-2949 National Bureau of Standards; Interagency Agreement C-54715-D), NASA CR-175541, 1984.
5. Liebert, C.H.; and Weikle, D.H.: Heat Flux Measurements. NASA TM-101428, 1989.
6. Prakash, S.: Thin-Film Temperature Sensors for Gas Turbines. Ph.D. Thesis, UCLA, 1987.
7. Melis, M.E.; and Gladden, H.J.: A Unique High Heat Flux Facility for Testing Hypersonic Engine Components. AIAA Paper 90-5228, Oct. 1990.

Basic Thin-Film Thermocouple Technology

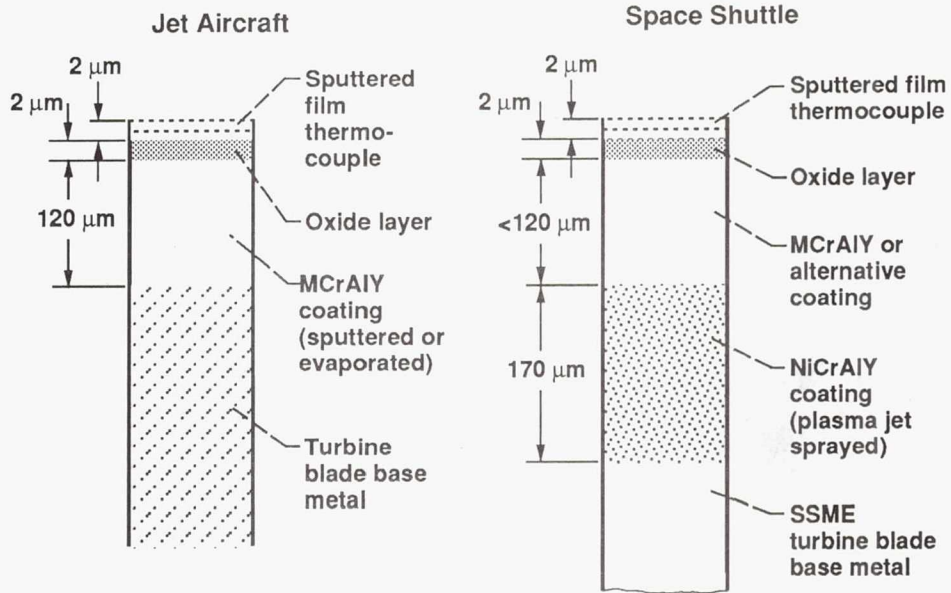


Figure 1

CD-91-52057

TFTC on SC PWA 1480 Coupon

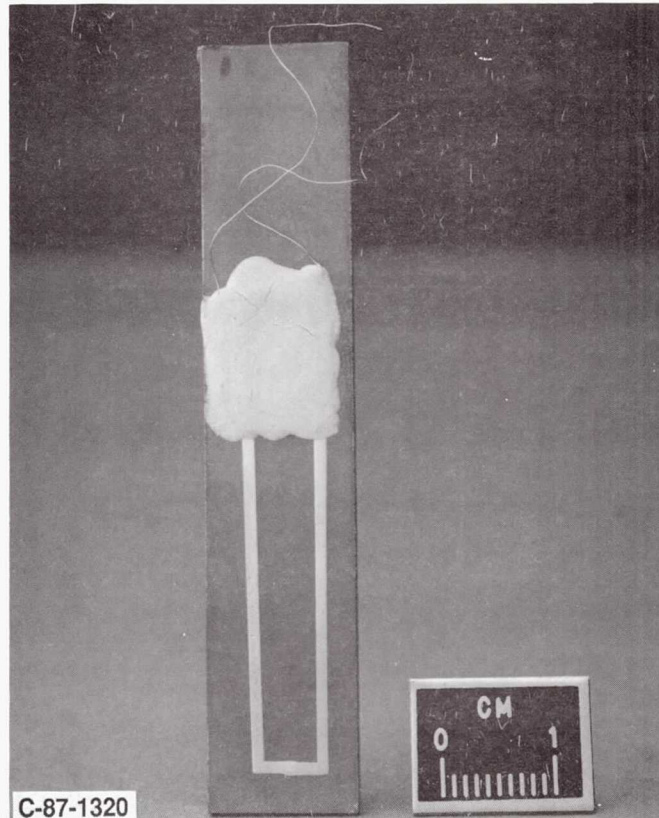


Figure 2

CD-91-52058

TFTC's on SSME Blade Chromel/Alumel Wire Thermocouple on Shank

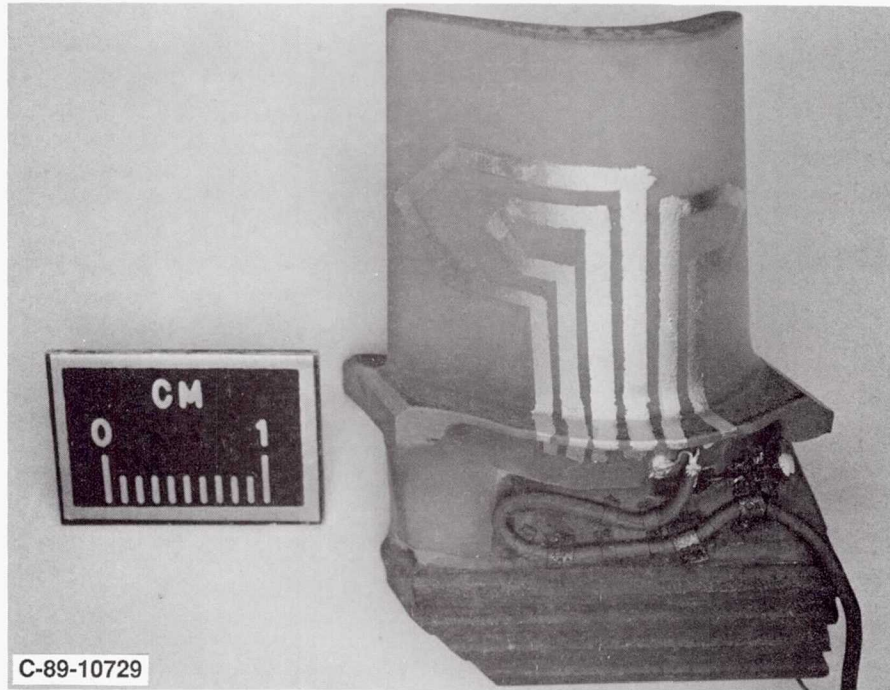


Figure 3

CD-91-52059

Blade Holder Assembly

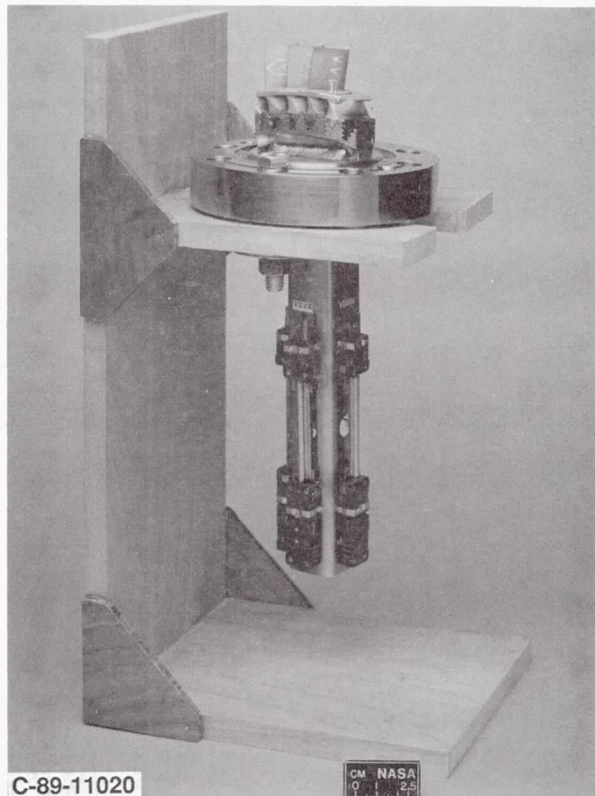


Figure 4

CD-91-52060

Schematic of MSFC Turbine Blade Tester

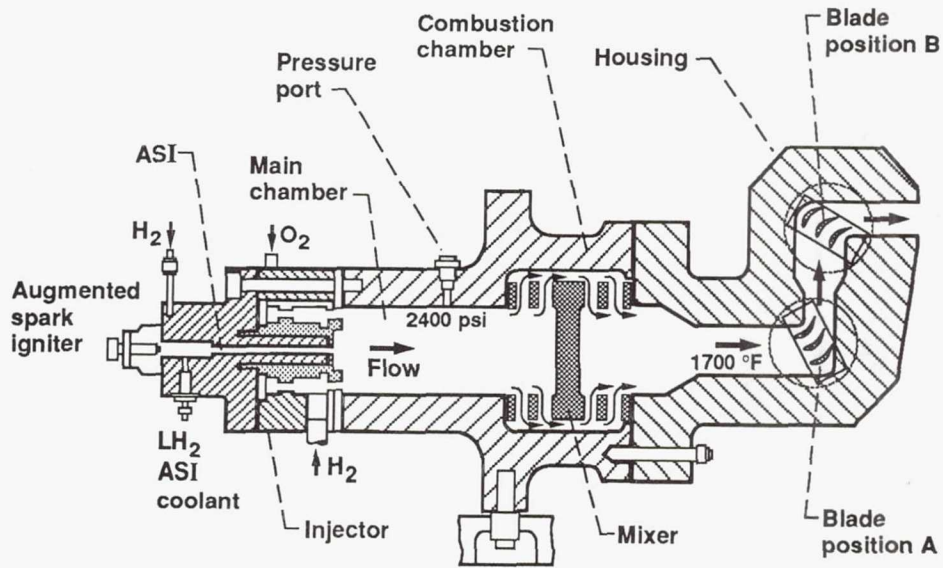


Figure 5

CD-91-52061

SSME Blade Tested in TBT



Figure 6

CD-91-52062

Hydrogen-Oxygen Rocket Engine Facility During Operation

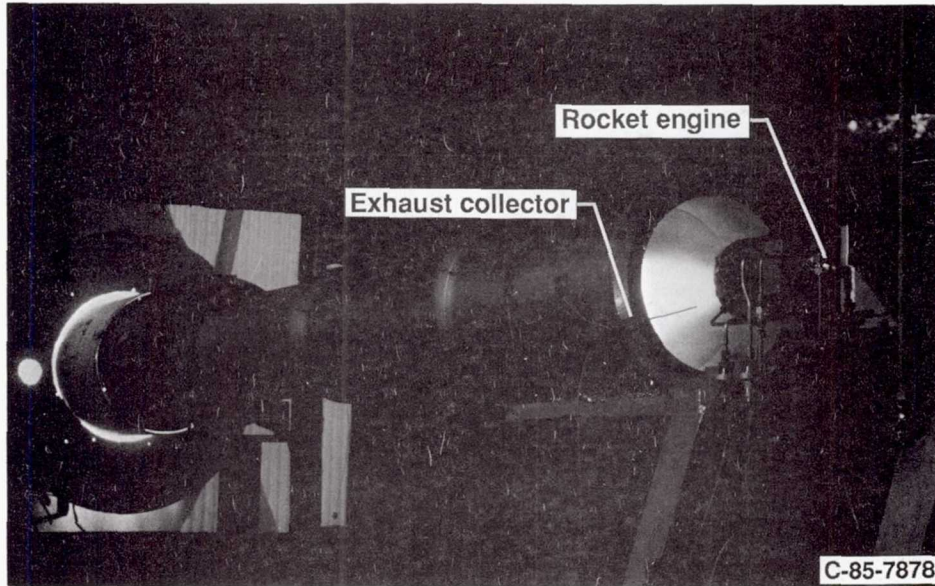


Figure 7

CD-91-52063

Test Specimen Mounted in Exhaust Flow During Operation

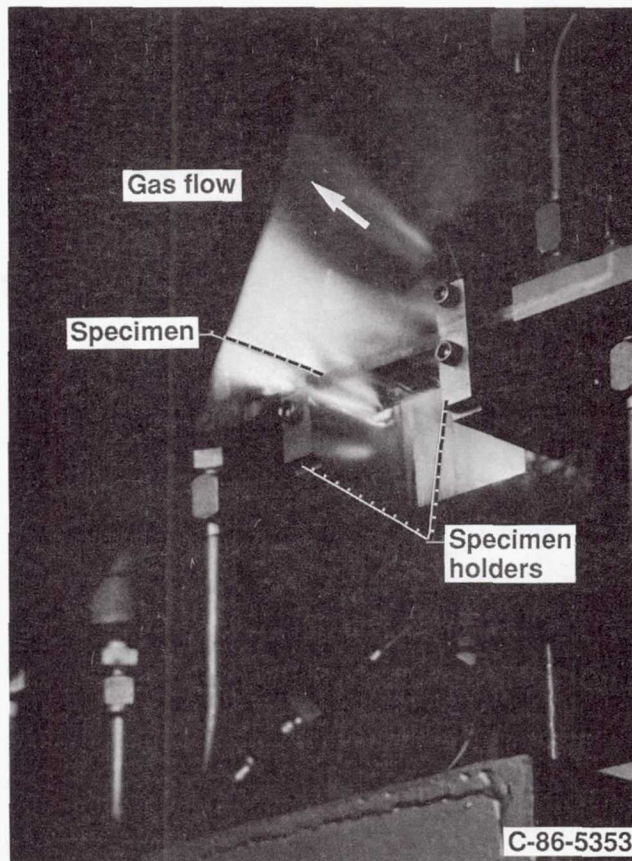


Figure 8

CD-91-52064

RAYLEIGH-BRILLOUIN SCATTERING FOR HIGH-PRESSURE GAS TEMPERATURE MEASUREMENTS

Richard G. Seasholtz
NASA Lewis Research Center
Cleveland, Ohio 44135

The spectrum of laser light scattered by density fluctuations in a gas is a function of the molecular velocity distribution function. The distribution function is characterized by the macroscopic gas parameters, including temperature. For low density gases, where the molecular mean-free-path l_{mfp} is much longer than the wavelength λ_s involved in the scattering, the molecular motions are uncorrelated, and the spectrum of the scattered light is Gaussian for a gas with a Maxwellian velocity distribution. (The ratio λ_s/l_{mfp} is usually given the symbol y ; so, by low density, we mean $y \ll 1$). The width of the spectrum for low density gases is thus proportional to the square root of the ratio of the gas temperature to the molecular weight. If we know the molecular weight of the gas, we can use the width of the spectrum as a measure of gas temperature. An example of the application of Rayleigh scattering in this regime is given in reference 1.

On the other hand, for high density gases ($y \gg 1$), the molecular motions are correlated and the spectrum of the scattered light consists of 3 parts - a central peak at the laser wavelength and 2 side peaks. The side peaks can be thought of as arising from scattering of laser light from random thermally excited acoustic waves in the gas. This is usually referred to as Brillouin or Rayleigh-Brillouin scattering². For this high density situation, the frequency shift of the Brillouin peaks relative to the laser frequency is proportional to the speed of sound in the gas. Because the speed of sound is proportional to the square root of the gas temperature, the position of the Brillouin peaks provides a measure of gas temperature.

The spectrum of Brillouin scattering in high density gases ($y \gg 1$) can be calculated using a relatively simple continuum (hydrodynamic) theory³. In this theory, the spectrum is a function of two non-dimensional parameters. The first parameter is a non-dimensional frequency, $x = 2\pi f/aK$ where f is the frequency shift from the laser frequency, $a = (2\kappa T/m)^{1/2}$ is the "most probable" molecular velocity, and $K = (2\pi/\lambda_s) = (4\pi/\lambda)\sin(\theta_s/2)$, with θ_s being the scattering angle. The other parameter is y (same parameter as discussed above), which can be written as a function of the pressure and shear viscosity of the gas as $y = p/\mu Ka$. The frequency shift corresponding to the Brillouin peaks is only a weak function of y for high pressure gases; for nitrogen it occurs at $x = x_p = (\gamma/2)^{1/2} = 0.837$. Measurement of the frequency shift of this peak from the laser frequency allows us to determine the gas temperature.

An experiment has been set up to evaluate the feasibility of using Rayleigh-Brillouin scattering as a diagnostic technique for measuring gas temperature in high pressure environments, such as the SSME preburner. A high-pressure furnace (rated for 3000 psia at 1300 K) is used as the scattering chamber. Either nitrogen or hydrogen may be used. An argon-ion laser beam ($\lambda = 514.5$ nm, 1W) is focused into the furnace. Light backscattered from the gas in the furnace is collected

and analyzed with a 5-pass scanning Fabry-Perot interferometer⁴ and photon counting electronics. The multi-pass configuration provides the high frequency selectivity needed to measure the Brillouin peaks in the presence of large amounts of spuriously scattered light at the laser frequency.

Preliminary measurements have been made at room temperature in nitrogen at pressures up to 2000 psia. The free spectral range of the interferometer and frequency separation of the Brillouin peaks are determined from measured spectra. Temperature measurements are then obtained using the simple continuum theory with low frequency values of specific heat ratio and shear viscosity. The measured temperatures are within 10% of the true value. It is anticipated that the accuracy will be significantly better if a more refined theory^{5,6} is used.

At high temperatures, large thermal gradient occurs in the transition region between the high temperature at the center of the furnace and the cooler parts near the windows. The gradients cause severe beam distortion and prevent focusing of the beam. To eliminate this problem, sapphire cylinders (110 mm long x 12 mm dia.) will be placed in the furnace adjacent to the windows. This will provide an optical path to the hot zone with much less distortion. Tests are planned for both nitrogen and hydrogen.

REFERENCES

1. Seasholtz, R.G., F.J. Zupanc, and S.J. Schneider, "Spectrally resolved Rayleigh scattering diagnostic for hydrogen-oxygen rocket plume studies", 29th Aerospace Sciences Meeting, Reno, AIAA-91-0462, 1991.
2. Sandoval, R.P., and R.L. Armstrong, "Rayleigh-Brillouin spectra in molecular nitrogen", *Phys. Rev. A* **13**, 1976, pp. 752-757.
3. Mountain, R.D., "Spectral distribution of scattered light in a simple fluid", *Rev. Mod. Phys.* **38**, 1966, pp. 205-214.
4. Sandercock, J.R., "Some recent developments in Brillouin scattering", *RCA Review* **36**, 1975, pp. 89-107.
5. Boley, C.D., Desai, R.C., and G. Tenti, "Kinetic models and Brillouin scattering in a molecular gas", *Can. J. Phys.* **50**, 1972, pp. 2158-2173.
6. Lao, Q.H., Schoen, P.E., and B. Chu, "Rayleigh-Brillouin scattering of gases with internal relaxation", *J. Chem. Phys.* **64**, 1976, pp. 3547-3555.

RAYLEIGH-BRILLOUIN SCATTERING

$$P_s(f) df d\Omega = I_o n V_{sc} \left(\frac{d\sigma}{d\Omega} \right) \sin^2\chi S(f) df d\Omega$$

I_o = irradiance of incident beam

n = molecular number density

V_{sc} = scattering volume

χ = polarization direction

$\left(\frac{d\sigma}{d\Omega} \right)$ = Rayleigh scattering cross section

$S(f)$ = normalized spectrum of scattered light

RAYLEIGH SCATTERING NOMENCLATURE

$$\mathbf{K} = \mathbf{k}_s - \mathbf{k}_o$$

$$K = |\mathbf{K}| = \frac{4\pi}{\lambda} \sin \frac{\theta_s}{2}$$

$$a = \sqrt{\frac{2\kappa T}{m}}$$

NONDIMENSIONAL PARAMETERS

$$x = \frac{2\pi f}{aK}$$

$$y = \frac{\rho}{\mu Ka}$$

μ = shear viscosity

EXAMPLE OF NITROGEN AT 1000 psia

Mirror spacing $d = 21.8$ mm

Free Spectral Range FSR = 6.88 GHz

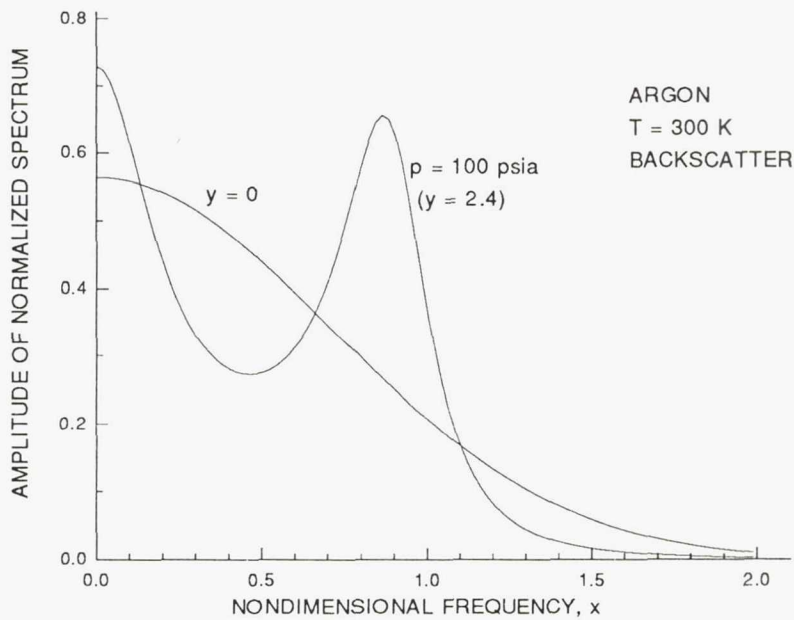
$$x_p = (\gamma/2)^{1/2} = 0.837$$

$$K = 2.44 \times 10^7 \text{ m}^{-1}$$

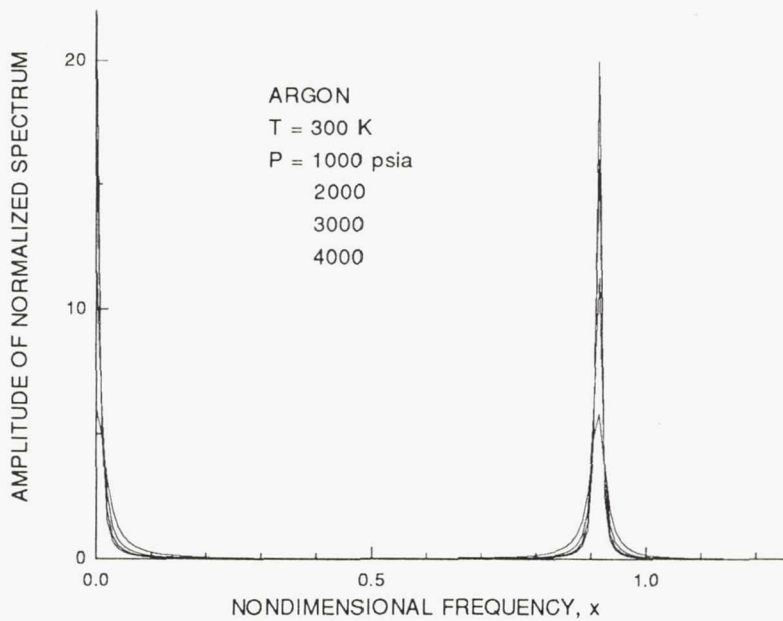
$$a = 399 \text{ m/sec}$$

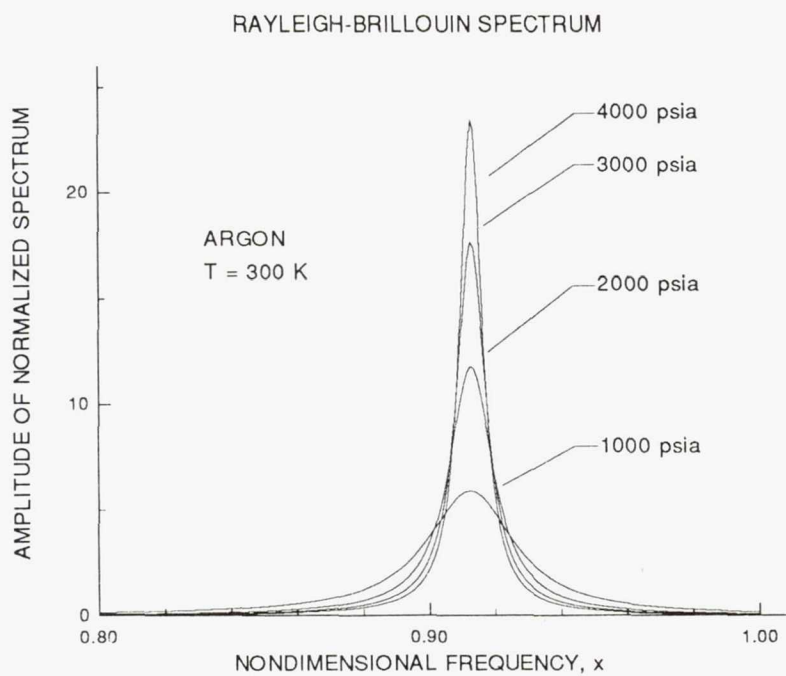
$$T = 317 \text{ K}$$

RAYLEIGH-BRILLOUIN SPECTRUM

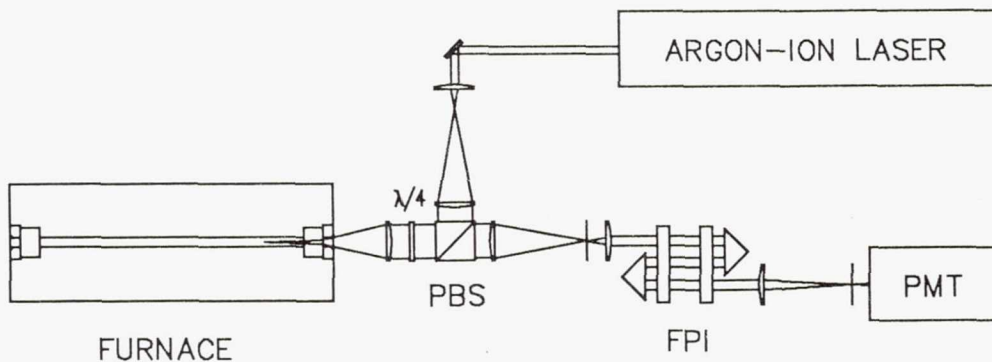


RAYLEIGH-BRILLOUIN SPECTRUM

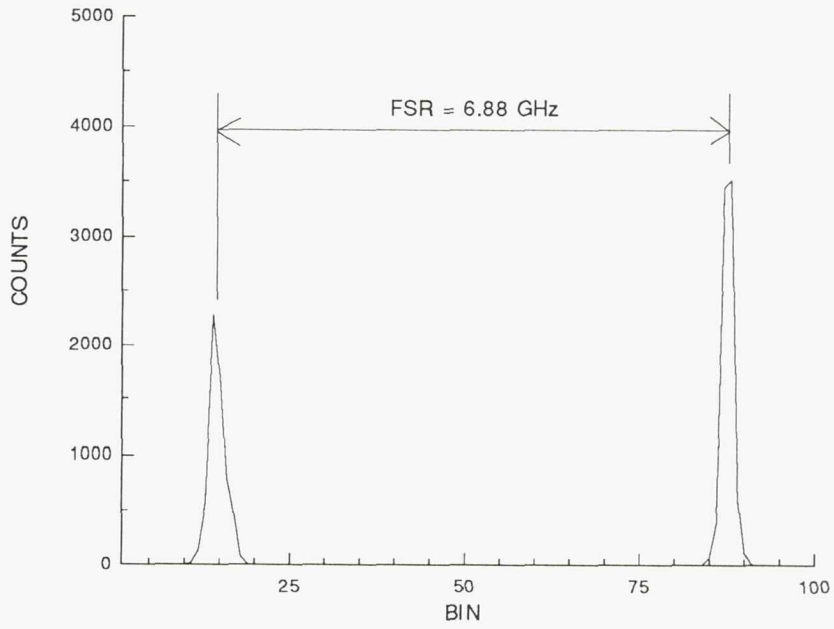




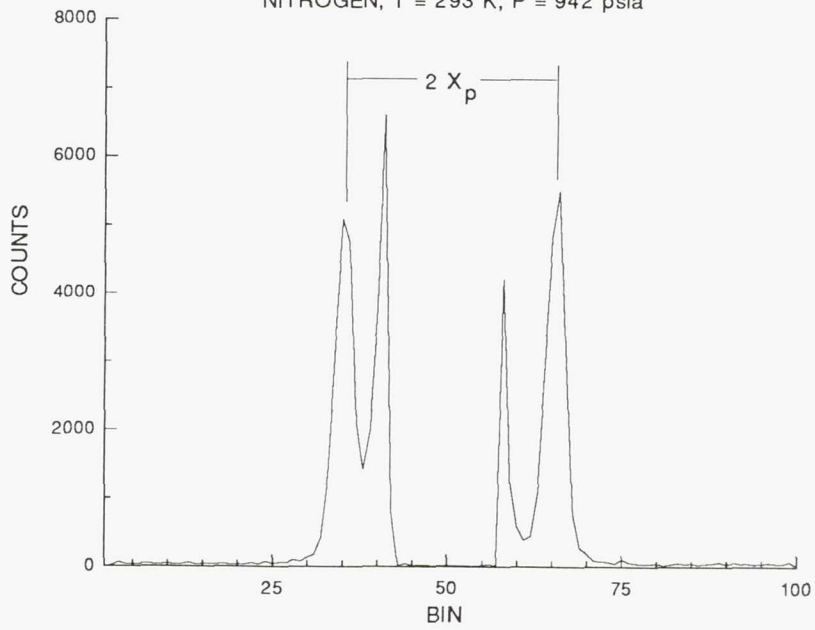
RAYLEIGH-BRILLOUIN SCATTERING DIAGNOSTIC FOR HIGH PRESSURE FURNACE



FREE SPECTRAL RANGE MEASUREMENT



MEASURED RAYLEIGH-BRILLOUIN SPECTRUM
NITROGEN, T = 293 K, P = 942 psia



Page intentionally left blank

NEURAL NETS FOR ALIGNING OPTICAL COMPONENTS IN HARSH ENVIRONMENTS – BEAM SMOOTHING SPATIAL FILTER AS AN EXAMPLE

Arthur J. Decker and Michael J. Krasowski
NASA Lewis Research Center
Cleveland, Ohio 44135

The goal of this project is to develop an approach to automating the alignment and adjustment of optical measurement, visualization, inspection, and control systems.

Developments in the last decade in inexpensive computing, fiber optics, sensitive and selective detectors, and motorized mounting hardware have made optical spectroscopy, interferometry, deflectometry, and imaging valuable for non-intrusive measurements and inspections of aerospace flows and structures. Nevertheless, optical techniques still require skilled people for setup, alignment, adjustment, and operation. The simplest dual-beam holography setup for example requires that a technician perform 50 to 100 separate translations and rotations of optical components before a single hologram is recorded. A spectroscopy setup might require 1000 or more actions before data is collected. The human specialist must adjust the optical system for changes in the scene and must realign to compensate for environmental disturbances. These activities are a nuisance in the laboratory and are difficult, impractical, or impossible in harsh and dangerous test and launch environments.

Classical controls, expert systems, and neural networks are three approaches to automating the alignment of an optical system. We in the Instrumentation and Control Technology Division at Lewis Research Center have decided to pursue neural networks based on two judgements.

First, neural networks classify automatically and learn by example. Therefore, they require the least specialized knowledge of controls and optical phenomena. What is more important, the neural networks require the least self-knowledge from a human operator. The human operator need only execute a representative set (training set) of alignments, and no explanations are necessary. Hence, the alignment of a component is reduced to a series of steps, where each step consists of a mapping between input and output observations and actions.

For optical alignment, the input to the human operator and to the neural network can include beam position, beam pattern, and beam brightness as well as a memory or flag of the action taken previously. The output of the human-operator or neural-network controlled component consists of an action (linear or rotational motion) which terminates at a new condition of position, pattern, or brightness. There is no need to know the theoretical details of beam positioning, beam pattern, or beam brightness or to know or measure the positions of the mechanical actuators. In fact, as is the case with a human operator, there is no need to achieve exactly the same result each time a step is executed. This feature is useful in handling the non-linearities and errors present in the very sensitive mechanical actuators. If the training set is representative, then the neural network will eventually achieve and recognize an aligned condition.

The second reason for selecting neural networks is that neural-network hardware and software are available and being developed and improved. Some of the packages are small enough that one envisions a separate network for each adjustable optical component. The separate nets would receive inputs from one or more visualization systems and would be linked eventually with one another or with a master network. Hence, optical components can be automated and tested one at a time. Full automation can be brought on line gradually.

We are testing our judgments by using neural networks to automate the alignment of the ubiquitous laser-beam-smoothing spatial filter. The spatial filter is challenging and complex enough to be non-trivial, yet is simple enough to be modeled exactly. The most common version of a spatial filter assembly is a pinhole 10 micrometers in diameter and a 20X microscope objective. The pinhole is mounted in an XY stage, and the microscope objective is mounted in a linear stage for focus (Z-axis) control. In alignment, the laser beam is focused through the pinhole. Scattered light, from dust particles for example, is not focused and does not pass through the pinhole. Hence, a smoothed beam exits the filter. Alignment is a 3-degree-of-freedom process: the pinhole is translated perpendicular to the laser-beam axis in the XY plane, and the microscope objective is translated along the axis in Z. There are 2 diffraction regions. Most of the alignment steps are in the first region where the out-of-focus beam fills the pinhole, and a symmetrical pattern of diffraction rings is observed. Several serial adjustments of X, Y, and Z covering total distances of several hundred micrometers each may be required in this region. The second diffraction region occurs within about 10 micrometers of focus, where an asymmetrical, knife-edge pattern may be observed. One or two very slight adjustments are required here to create a symmetrical beam. The brightness of the beam reflected from a backstop may vary by 6 orders of magnitude during an alignment.

A technician created a training set for our initial efforts with neural networks. The training set contained 37 alignments beginning from random positions and a total of 337 alignment steps. The input vector of an alignment step consisted of a flag of the control (X, Y, Z, or none) operated in the previous step, the position of the beam bright spot (x, y) on a backstop, a flag indicating the diffraction pattern (symmetrical rings or knife edge), and the logarithm of the intensity. The output vector of the alignment step consisted of a flag of the control to be operated, the new incremental beam position, and the logarithm of the predicted output intensity. A training set was also created using a model of the spatial filter.

Several commercial neural network packages were procured which involve both hardware and software. The work reported herein was accomplished with a Hecht-Nielsen neurocomputer which consists of a co-processor for a PC and a substantial package of software. The software includes C language subroutines which will instruct the co-processor to execute a number of published neural network algorithms and a compiler for creating custom designed neural networks. A system of neural networks was created to learn the training set and to control the alignment of the spatial filter. The training set was pre-classified into 13 classes using an unsupervised network (Adaptive Resonance Theory 2). Unsupervised networks classify vectors according to some criterion such as Euclidean distance. Each of the classes was then used to train a back propagation network. Back propagation networks learn the mapping between input and output vectors which minimizes the mean squared error between actual responses and the correct responses of the training set. Learning is encoded in weighted connections between processing elements or neurons.¹ The

system of networks can respond to inputs not in the original training set and, hence, has a certain generalization ability.

There are many networks; their effectiveness must be judged by performance. The network system described above was used to direct the alignment of an actual spatial filter. A technician was the eyes and hands for this test. The technician aligned the filter and then backed off the XYZ controls for arbitrary mis-alignment. The input vectors were passed to the network. The technician performed the actions directed by the output vectors of the network. The network was able to direct a satisfactory alignment; it also knew when to stop the alignment process.

The neural network was also tested with inputs generated by a physical model of the spatial filter. The physical model included random errors to simulate the non-linearities and errors in the mechanical drives. The neural network was able to execute sets of alignment steps beginning at arbitrary starting points and terminating at aligned states.

Future work will be directed toward the gradual achievement of the following goals. An electrical-mechanical interface will be created between the neural network and the spatial filter assembly. A machine vision system consisting of a camera, frame grabber, and software will supply the input vectors to the neural network. The neural network will be transferred to miniature, commercially available hardware. A hands-off, self-aligning spatial filter will be demonstrated.

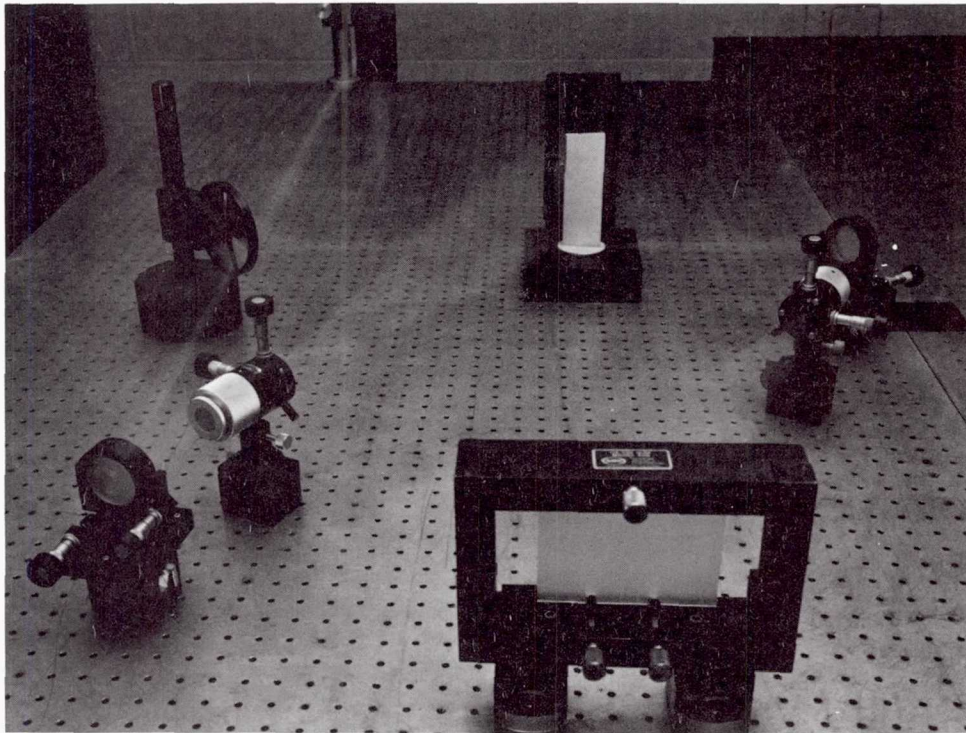
-
1. D. E. Rumelhart, G. E. Hinton, and R. J. Williams, "Learning Internal Representations by Error Propagation," in **Parallel Distributed Processing, Volume I: Foundations**, D. E. Rumelhart, J. L. McClelland, and the PDP Research Group, MIT Press, 1986, pp. 318-362.

OBJECTIVE

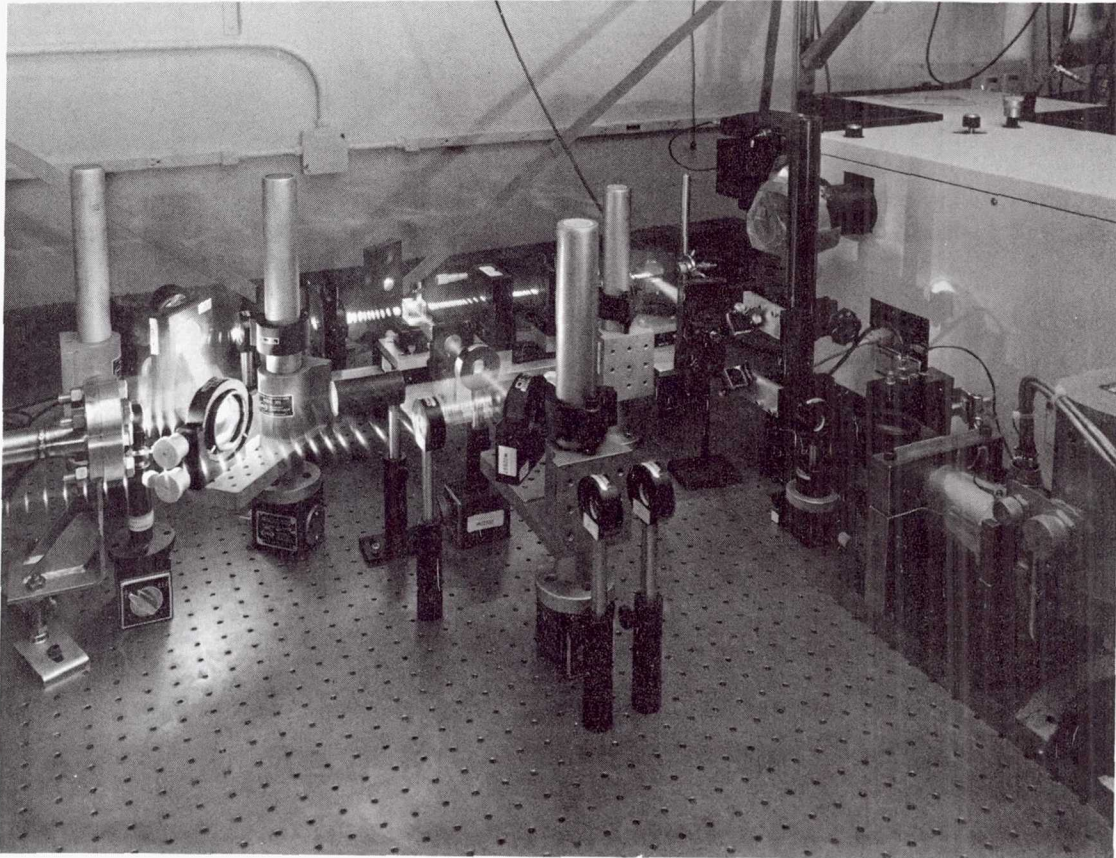
- AUTOMATE OPTICAL MEASUREMENT SYSTEM

Alignment
Adjustment
Operation
Realignment

SIMPLE HOLOGRAPHY SETUP



CD-86 21431



›

APPROACHES TO AUTOMATION OF ALIGNMENT

- DISCIPLINES
 - Classical Controls
 - Expert Systems
 - Neural Networks
- CHOICE == NEURAL NETWORKS

REASONS FOR CHOICE

- NEURAL NETWORKS REQUIRE

LEAST SPECIALIZED KNOWLEDGE,
LEAST SELF-KNOWLEDGE OF OPERATOR,
A REPRESENTATIVE TRAINING SET.
- NEURAL NETWORKS CLASSIFY.
- NEURAL NETWORKS GENERALIZE.
- NEURAL NETWORKS ARE AVAILABLE

in Software,
in Hardware.

NEURAL NETWORK



- PROCESSING ELEMENTS WITH LOCAL MEMORY AND
NON-LINEAR ACTIVATION FUNCTION
- WEIGHTED CONNECTIONS

OPTICAL ALIGNMENT

- INPUTS TO HUMAN OPERATOR AND NET

Light Beam Position
Light Beam Pattern
Memory of Last Action
Light Beam Brightness

- OUTPUTS

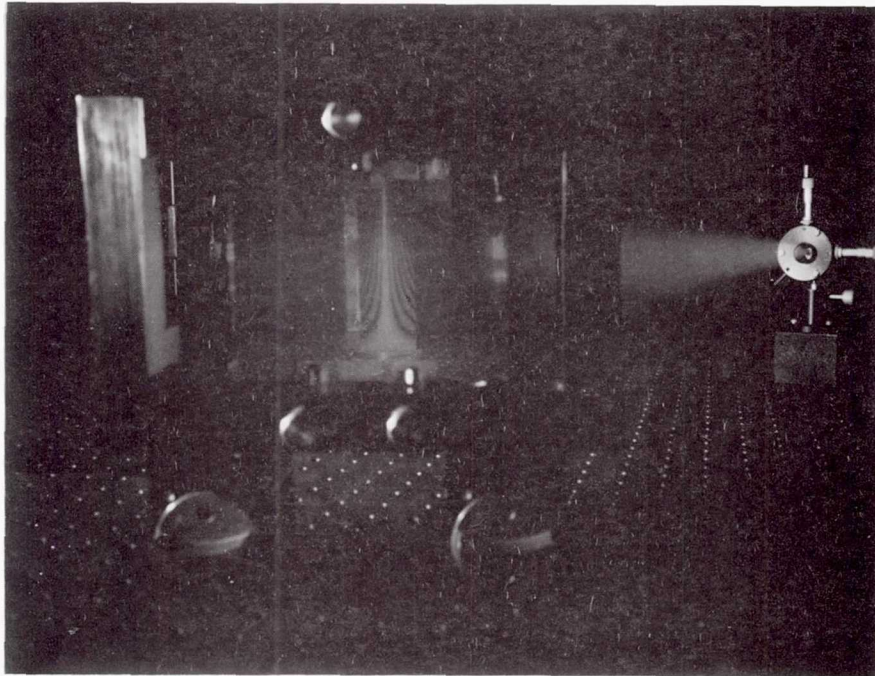
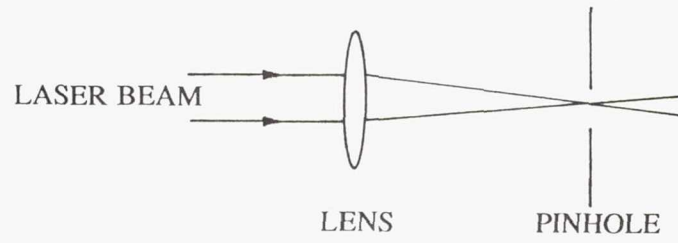
Action (Linear or Rotational Motion)
New Position, Pattern, or Brightness

- GOAL—STRING INPUT—OUTPUT STEPS TO ACHIEVE
ACCEPTABLE ALIGNMENT



TEST

- LASER-BEAM-SMOOTHING SPATIAL FILTER

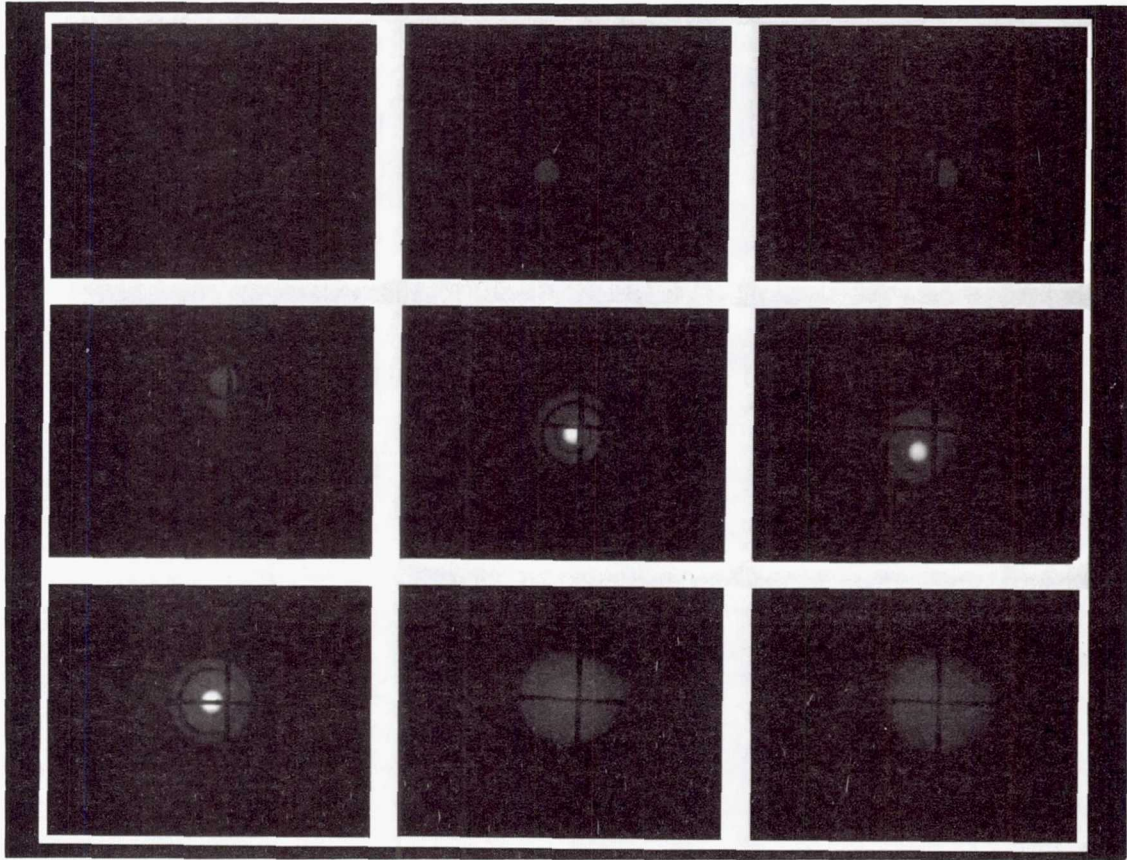


TYPICAL LABORATORY ALIGNMENT

- FILTER == 10 μm PINHOLE IN XY STAGE;
20X MICROSCOPE OBJECTIVE IN
Z STAGE.
- TWO GENERIC BEAM PATTERNS
- ALIGNMENT IN 5 TO 10 STEPS
- TOTAL MOTION IN X OR Y OR Z ==
SEVERAL HUNDRED MICROMETERS.
- BRIGHTNESS VARIATION == 6 ORDERS OF
MAGNITUDE.

TRAINING SETS

- TECHNICIAN: 37 ALIGNMENTS, 337 TOTAL STEPS
- PHYSICAL MODEL OF SPATIAL FILTER



FUTURE EFFORT

- HANDS AND EYES FOR SPATIAL FILTER
 - Actuators
 - Frame Grabber and Camera
- TEST FULL SELF-ALIGNMENT OF SPATIAL FILTER.
- MINIATURIZATION AND SELF-CONTAINMENT
- ENVIRONMENTAL TESTS

PROGRESS IN SPECKLE-SHIFT STRAIN MEASUREMENT

Christian T. Lant
Sverdrup Technology, Inc.
Brook Park, Ohio 44135

and

John P. Barranger, Lawrence G. Oberle, and Lawrence C. Greer III
NASA Lewis Research Center
Cleveland, Ohio 44135

INTRODUCTION

The Instrumentation and Control Technology Division of the Lewis Research Center has been developing an in-house capability to make one-dimensional and two-dimensional optical strain measurements on high temperature test specimens. The measurements are based on the two-beam speckle-shift technique of I. Yamaguchi.¹ Past work has demonstrated 1-D and 2-D strain measurements at temperatures beyond 750° Celsius, with a resolution of 15-45 $\mu\epsilon$, respectively.²⁻³

The development of composite materials for use in high temperature applications is generating interest in using the speckle-shift technique to measure strains on small diameter fibers and wires of various compositions. This paper will cover the results of preliminary speckle correlation tests on wire and fiber specimens, and describe the Advanced System currently under development. Some of these results have been presented before, and are described in more detail in the reference.⁴

Past implementations of the speckle-shift technique used a linear photodiode array to detect objective speckle reflected from a point on a diffuse test surface. Shifts of this speckle pattern are proportional to surface strain along the incident plane of the optical system. A feature of the speckle shift technique is its ability to automatically cancel many problematic terms of rigid body motion. However, excessive rigid body

motions can move the reference speckle pattern off the one-dimensional detector, terminating the measurement. The advanced system now under development addresses two practical limitations encountered in previous testing. The first limitation was excessive decorrelation, due to off-axis rigid body motion shifts, restricting the magnitude of specimen movements. The speckle-shift technique could be applied to more diverse test situations, such as component testing, if the specimen mounting and loading requirements were not rigorous. The second limitation was the low sampling rate of the strain measurements, on the order of 0.1 Hz, limiting the response time of the system. Higher sampling rates would allow continuous loading at higher strain rates.

The use of a two-dimensional charge-coupled device (CCD) for the detector will reduce decorrelation errors due to rigid body motions. In addition, either a high speed image processing system, or a real-time data storage system is intended to greatly decrease the time between strain measurements. Two systems, each using one of these processing techniques, are currently being built.

THEORY

The laser speckle patterns, generated by the spatially coherent illumination of a rough specimen surface, shift when the surface is strained or when the specimen undergoes

rigid body motion. The speckle patterns are recorded on a sensor array, and cross-correlations of the patterns before and after movement are calculated to determine the amount of shift between them. A dual beam measurement allows automatic cancellation of most terms of rigid body motion. By taking the difference in shifts of speckle patterns generated by two laser beams incident on the specimen from equal but opposite angles, error terms due to rigid body motion can be cancelled.

The geometry of the optical setup and careful alignment of the specimen limit the speckle shifts to an axis parallel to the sensitive axis of the measurement system, namely, the incident plane of the laser beams; the speckle patterns remain correlated as long as they do not shift along the transverse direction, off the linear photodiode array.

The current system will allow one-dimensional strain to be measured at a rate near the data acquisition rate, by providing a two-dimensional digital signal processor (DSP) based speckle tracking processor. Rigid body motion constraints and decorrelation events will be reduced by using a two-dimensional CCD array to record an extended speckle pattern. A two-dimensional speckle pattern will allow off-axis speckle shifts to be tracked dynamically.

Figure 1 shows the simplified geometry of the coordinate system. The specimen is in the lowercase x,y plane, and the sensor is defined to lie in the uppercase X,Y plane. The x,y and X,Y planes are separated by a distance L_0 along the z axis. Two-dimensional deformation of object points on the specimen are described by vector $a(x,y)$, and the resulting shifts of the speckle pattern are given by vector $A(x,y)$. The shaded rectangle in the figure indicates a one-dimensional reference slice of the speckle pattern (one line of the 2-D CCD array) shifted from the origin by $A(x,y)$. The x,z plane is the plane of the incident laser beam, which comes from source point L_S .

After rigid body motion terms are cancelled out of the simplified speckle-shift equations, the surface strain ϵ_{xx} in the x direction can be calculated by the relation

$$\epsilon_{xx} = \frac{-\Delta A_x}{2L_0 \cdot \sin(\theta)} \quad (1)$$

where $\theta = |\theta_S|$, and ΔA_x is the difference between speckle shifts from beam 1 and beam 2

$$\Delta A_x = A_x(\theta_S) - A_x(-\theta_S). \quad (2)$$

An analysis of the optical system gave a measure of the minimum sampling frequency required by the CCD array to accurately represent the speckle patterns. By applying the Nyquist sampling theorem to the spatial frequency distribution of the speckle pattern, the minimum sampling frequency was calculated to be $8/\pi$, or 2.55 pixels/speckle.⁴

The optical system uses a switched single beam design, for compactness, following the schematic in Figure 2. The argon ion laser beam can be diverted into the beam stop by the acousto-optic modulator (AOM) between tests and exposures. The Pockels cell and polarizing beamsplitter form an optical switch, in order to provide the two beam paths for error cancellation. The Pockels cell can rotate the polarization of the beam by $\pi/2$ radians in accordance with a control signal. This allows the beam to either pass through the polarizing beamsplitter (beam leg 1) or be reflected to beam leg 2. A waist positioning achromatic lens is used to provide a planar wavefront at the specimen surface.

ROOM TEMPERATURE TESTS

When using a specimen of small thermal mass it is important not to induce local heating by the laser beam. This kind of heating causes thermal strain at the gage location, which contributes to speckle shifts. Since the shifts are due to real strain, they cannot be cancelled; they will consequently degrade any stress-strain relationship being measured.

When the room temperature tests were initially performed on wires, thermal strain was a problem at high laser power density levels. Once the laser output power was reduced from 2 W to $1/2$ W, however, the stability of the speckle patterns over succes-

sive exposures increased. For an incident power of 0.5 W and a 30 ms exposure time, the speckle patterns varied between a shift of zero and one pixel over a series of twenty exposures (about 20 minutes duration). Thermal strains were, therefore, negligible. The correlation function was sharply peaked over the duration of the test. Tungsten and stainless steel wires with diameters of 76 and 813 μm (3 and 32 mils), respectively, were used for these tests.

Correlations were also performed on speckle patterns from a variety of unloaded ceramic fiber specimens. The lower reflectivity of the ceramic fibers reduced the signal-to-noise level compared to the metallic specimens.

HIGH TEMPERATURE TESTS

One of the critical questions associated with high temperature optical measurements is whether thermal density gradients during a test are severe enough to prohibit accurate readings. Past testing has indicated problems of this sort at temperatures as low as 450°C. Free convection set up by air temperature and density variations around a hot specimen can result in an unstable phase propagation medium for the speckle-forming laser light. Since a stable speckle pattern depends explicitly on stable phase relationships, dynamic density variations can severely degrade the measurements.

If the density variations occur within a spatial extent smaller than a cross-section of the solid angle subtended between the laser spot on the specimen and the speckle pattern on the sensor, the speckle pattern will exhibit a boiling action. If, on the other hand, the phase medium varies on a scale larger than the cross-section of this solid angle the speckle pattern will jitter or vibrate as a field at the sensor. The latter case was observed during early testing.² In later testing³ the specimen was enclosed in a thermally insulating box. Subsequently, the jitter effect was not observed at test temperatures beyond 750°C.

Thermal effects of the first kind (boiling) cannot be compensated for if they exceed some minimum criterion necessary to maintain correlation between exposures.

However, the situation is different for speckle shifts due to thermal variations of the second kind, ie. those on a scale larger than the aforementioned solid angle. These shifts can be cancelled as rigid body motions if the shifted speckle pattern pair (one exposure from each beam) can be acquired fast enough to stop the relative movement of the thermal zone between exposures.

Further experiments were necessary to determine if the problem would recur at the much higher temperatures desired for future materials testing. An ac light bulb was used to provide a very hot wire specimen. The bulb provided a means of testing a tungsten alloy in an inert atmosphere using standard hardware. The glass envelope sealed the wire filament in dry nitrogen gas to prevent oxidation of the tungsten. The operating pressure in the envelope was estimated to be ≈ 1.5 atm. The envelope was transparent and cylindrical in shape (measuring 9 cm long by 3 cm in diameter), allowing the necessary optical access for the laser beams and speckle patterns. A variac was used to adjust the voltage across the filament without clipping the ac signal, effectively varying the filament temperature. A calibration of temperature versus line voltage was obtained from the bulb manufacturer.

The filament was made from a 37 μm (1.5 mil) diameter wire of W-Re alloy. The wire was tightly wound into a 122 μm (4.8 mil) diameter filament. The speckle statistics accurately obeyed those of a 122 μm diameter solid wire. A series of speckle patterns were recorded and correlated with a single pair of reference patterns at a specimen temperature of 2480°C. Excellent stability was observed in the high temperature tests, indicating that the isolation provided by the glass envelope was sufficient to avoid thermally induced jitter. The correlation peak occurred at shift values of 0 and 1 pixels over time, which is within the resolution of the correlation algorithm. Figures 3.a and 3.b show a set of reference and shifted speckle patterns, and their correlation over a shift range of ± 60 pixels. The patterns were recorded using a linear photodiode array camera. Since the wire was subjected to neither load nor rigid body motion, there should be no offset between the patterns. Indeed, the correlation in

Figure 3.b is sharply peaked at an offset of zero, as expected. The speckle pattern stability was also very good at room temperature and 1825°C. A radiometric analysis of a typical test system shows that optical signals can be measured at temperatures around 3000°C.⁴ These results alone do not guarantee accurate measurements at high temperatures using a straight wire specimen. Acquisition of the speckle pattern pairs must always occur fast enough to stop the action of any translations of the specimen or changes in the strain state at the gage position introduced by the test apparatus.

ADVANCED SYSTEM REQUIREMENTS

The Advanced System effort concentrates on developing a one-dimensional strain measurement system capable of calculating strains from speckle pattern shifts using a high speed digital signal processor (DSP). The system will provide the abilities to continuously track on-axis and off-axis speckle movements from a stressed wire specimen, and measure the induced strain. The ability to track the reference speckle patterns when off-axis speckle movements occur diminishes decorrelation effects and increases the measurement range of the instrument. In addition, the alignment criteria for the test specimen will not be as stringent, and less specialized load apparatus can be used for the tests.

Two versions of a speckle tracking system are under development. One technique uses a high speed personal computer with a digital signal processor (DSP) to process strain data as it is acquired (concurrent processing). The concurrent processing system development emphasizes minimizing the amount of data transferred to the PC, and then calculating the strain quickly before acquiring new data. The second technique stores the speckle data for processing after the test run (post-processing), allowing potentially higher strain rates. The post-processing approach stores all of the incoming speckle data, in real time, for the duration of the test run. The strains are then calculated once the run is completed.

In both systems, full field speckle patterns

will be recorded electronically as the specimen undergoes strain and rigid body motions. When the speckle pattern shifts off the primary viewing axis during a run, the reference slice (the center video line of the unshifted speckle pattern) will still be somewhere on the two-dimensional sensor array and correlation can be maintained. It will be necessary to perform a number of correlations per strain point to track the speckle shifts. The reference speckle patterns must be correlated with video lines on the array both above and below the reference axis coordinate. This is essentially a limited two-dimensional correlation. The speckle tracking algorithm will search for a correlation peak in each video frame until some minimum confidence criterion is met. The coordinates of this correlation peak give the shift components along the sensitive strain axis as well as the transverse axis. In addition to finding the coordinates of the correlation peak, the DSP-based image processor will automatically update the reference patterns before decorrelation occurs, allowing a virtually unlimited range of strain and rigid body motion shifts.

CONCLUSIONS

An analysis of the optical considerations involved in speckle-shift strain measurements on high temperature wire or fiber specimens is reported. The speckle patterns generated by a highly asymmetric laser spot are suitable for a one-dimensional strain measurement. The minimum sampling interval of the CCD detector is 2.55 pixels/speckle. A radiometric analysis indicates that a speckle pattern should be visible using extended specimens at temperatures below about 3000°C.

Preliminary high temperature testing showed that stable objective speckle patterns can be recorded from a tungsten filament at 2480°C. The gas immediately surrounding the filament was enclosed by a thin glass envelope. Good speckle patterns are obtainable at room temperature from small diameter (~100 μ m) ceramic fibers, without the laser inducing noticeable local heating of the test section.

A high speed optical strain measurement

effort is in progress, which will be able to track moving speckle patterns in two dimensions. This high speed tracking ability will allow the speckle-shift technique to be used in more diverse test environments.

REFERENCES

1. Yamaguchi, I.: A Laser-Speckle Strain Gauge. J. Phys. E. Sci. Instrum., vol. 14, no. 11, Nov. 1981, pp. 1270-1273.
2. Lant, C.T., Qaqish, W.: Optical Strain Measurement System Development - Phase I. Sverdrup Technology, Inc., NASA Contract NAS3-24105, NASA CR-179619, 1987.
3. Lant, C.T.: Two-dimensional High Temperature Optical Strain Measurement System - Phase II. Sverdrup Technology, Inc., NASA Contract NAS3-25266, NASA CR-185116, 1989.
4. Lant, C.T.: Feasibility Study for the Advanced One-Dimensional High Temperature Optical Strain Measurement System - Phase III. Sverdrup Technology, Inc., NASA Contract NAS3-25266, NASA CR-185254, 1990.

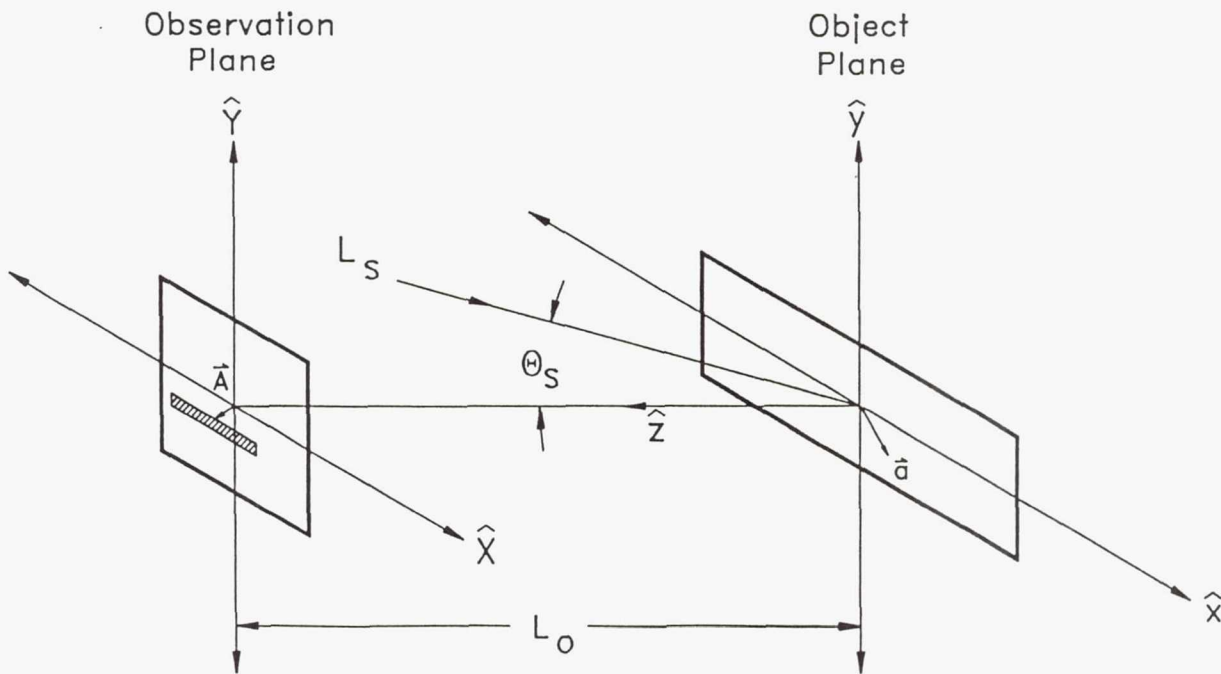


Figure 1. - Simplified coordinate system.

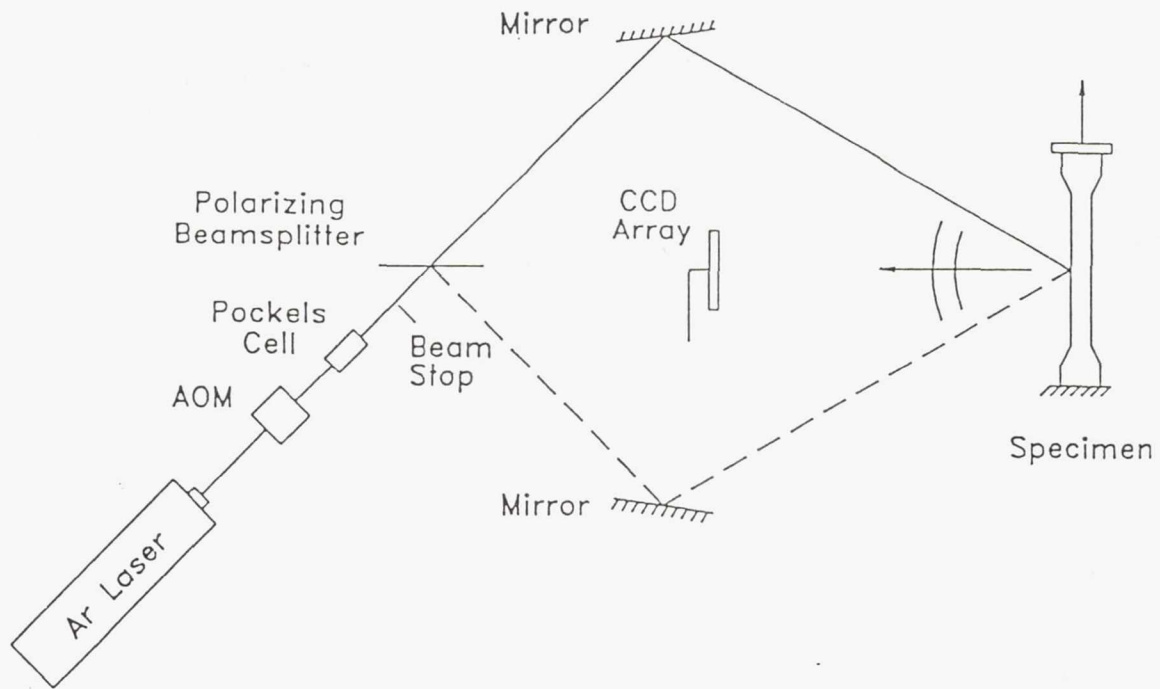
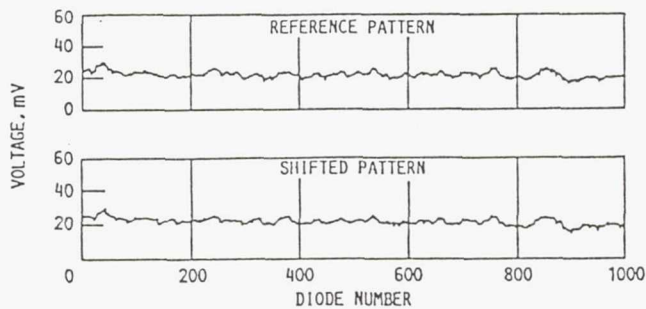
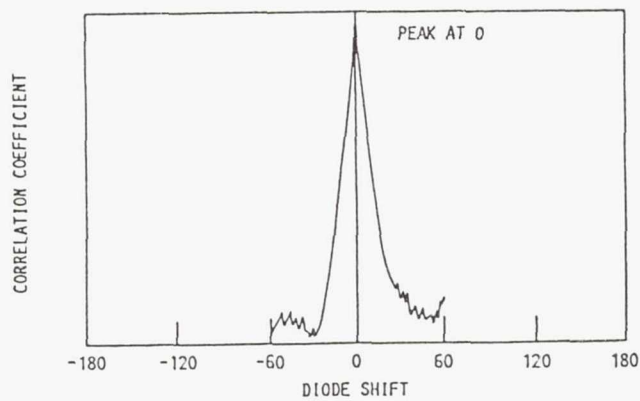


Figure 2. - Optical schematic.



(a) REFERENCE AND SHIFTED SPECKLE PATTERNS.



(b) CORRELATION.

Figure 3. - Typical speckle pattern pair and their correlation, for a tungsten wire at 2,480 °C.

OPAD 1991 - A STATUS REPORT

W.T. Powers and A.E. Cooper
NASA George C. Marshall Space Flight Center
Marshall Space Flight Center, Alabama 35812

The Optical Plume Anomaly Detection program, an experimental study in the attempt to create a rocket engine health monitor based on detection - and possible quantification - of anomalous atomic and molecular species in the exhaust plume, has been in existence for several years. The first year was used to acquire data allowing characterization of rocket plumes, specifically O_2/H_2 , since no information was available in the literature for these engines. Equipment used was that available from the repertoire, available at the AEDC - a matter of economics and convenience. As many as 17 instruments were used during this time. We learned what an average plume appeared to spectroscopic analysis and we learned about the equipment needed to really do the job. Basically, instruments allowing both a wide spectral range and high spectral resolution were needed, and since such units were not available commercially, custom designs were required. Several stages were passed through to bring us to the current configuration, which is described below.

Two optical instruments are employed - the polychromator and the spectrometer. The polychromator is a 16 channel spectroradiometer having independent channels individually adjustable for center wavelength and pass bandwidth. Those values may be mechanically reset, with the aid of certain lab equipment. The spectrometer is a multichannel spectral analyser having two 2048 element linear photodiode arrays at the exit plane of the dispersing instrument, which - like the 16 channel device - is a 1/2 meter grating spectrograph. These instruments are equipped with UV grade multifiber optical input cables, allowing the instruments to be placed in a benign environment. Telescopes mounted on the test stand observe the plume keeping the shock structure (mach disc) in view.

The data acquisition and control system consists of four (4) 80386-33 MHz computers - two at the test stand for instrument control and data preconditioning, and two in the test support building providing data archiving and display and system control. A fiber optic data link connects the two sets. A real time display utilizing multiple high resolution CRT's is provided. A meter (bar chart) style display is provided for the polychromator and two CRT's provide the full spectrum in a "waterfall" plot. The bar chart is filtered such that the readout movement is slow enough for a human observer to follow it. The "waterfall" plot yields a 3-dimensional display - wavelength, amplitude, and time; thus, many spectral samples are visible at any given time with the most recent sample always at the front. These displays also make later examination of the data easy. Since the data is available at the support building, processing may be initiated as soon as the engine firing is completed (it may be as much as 30 minutes before stand access is available). Quick-look data is also immediately available via oscillographic type printouts. That quick data permits selecting the most desirable areas to examine prior to complete processing of the data - which will require anywhere from several days to a few weeks, depending upon the nature of the test. That processing is discussed below.

DATA ANALYSIS

Currently, following each test, the data is studied for correlation to known engine activity, including instances of engine component erosion. This analysis is included as part of the post-test review. For example, in TTB016, we were asked to examine OPAD data to aid in identifying the time at which a pilot lip crack in the HPFTP occurred. Examination showed significant increases in Cr at approximately 5.838 sec. (Fig.1) TTB020 experienced significant faceplate erosion of the preburners. OPAD data, based on comparisons with previous SSME tests, indicated significant amounts of metallic elements, primarily Ni, Cr, Mn, and Fe throughout the test which was aborted at approximately 8 sec. (Fig.2).

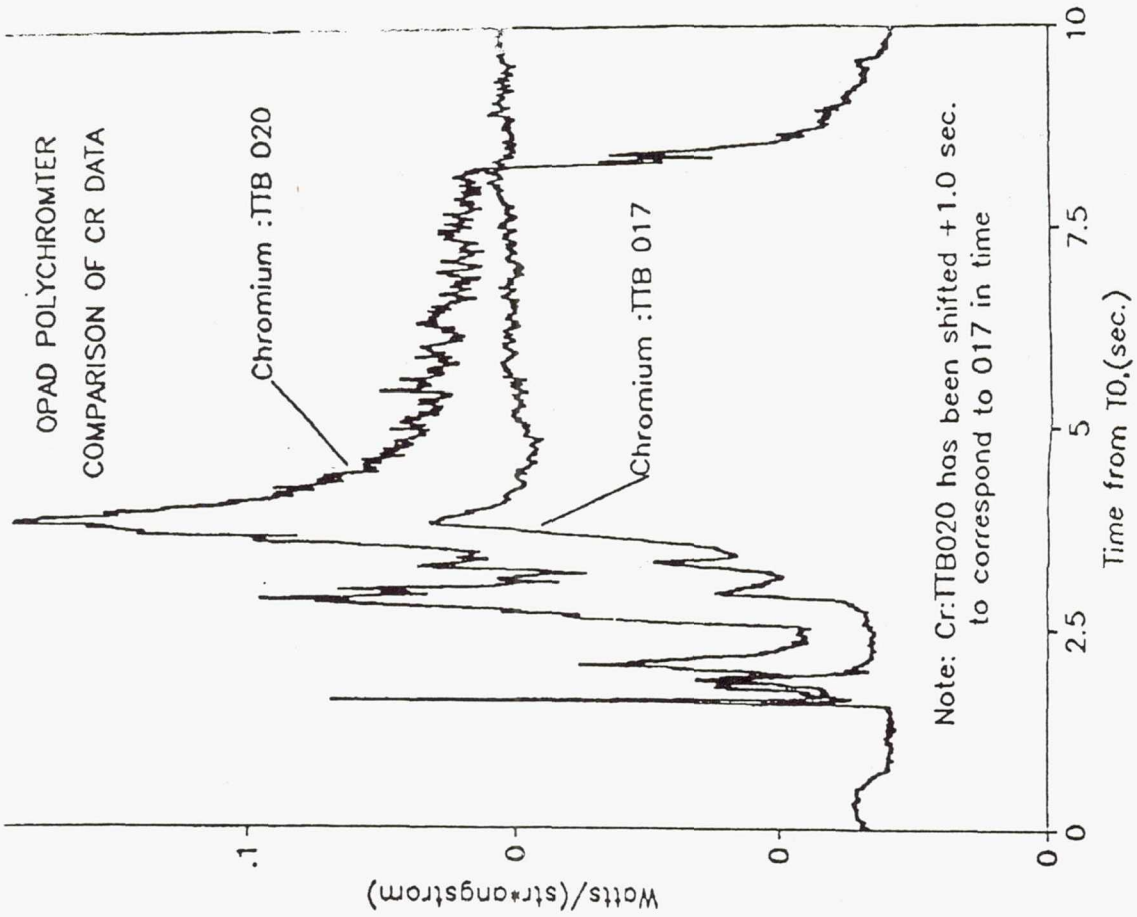
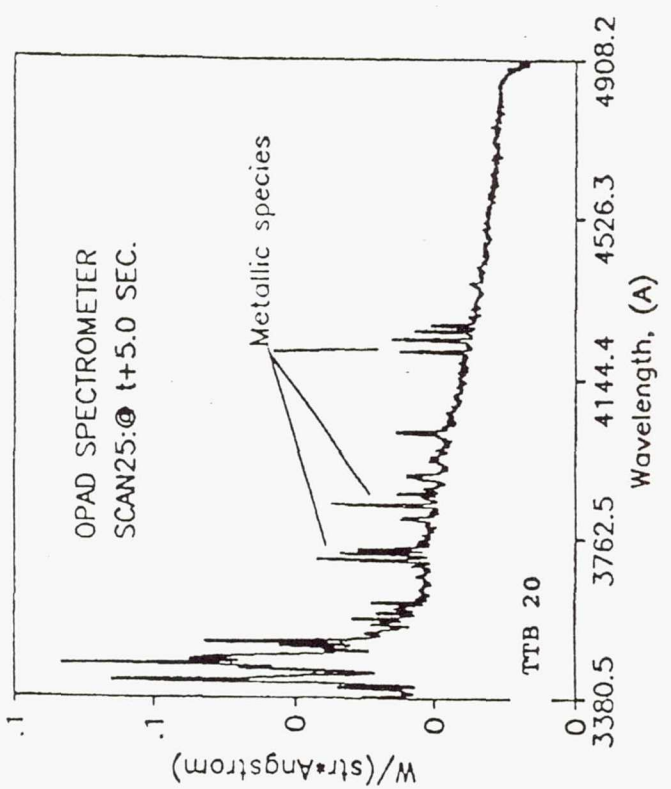
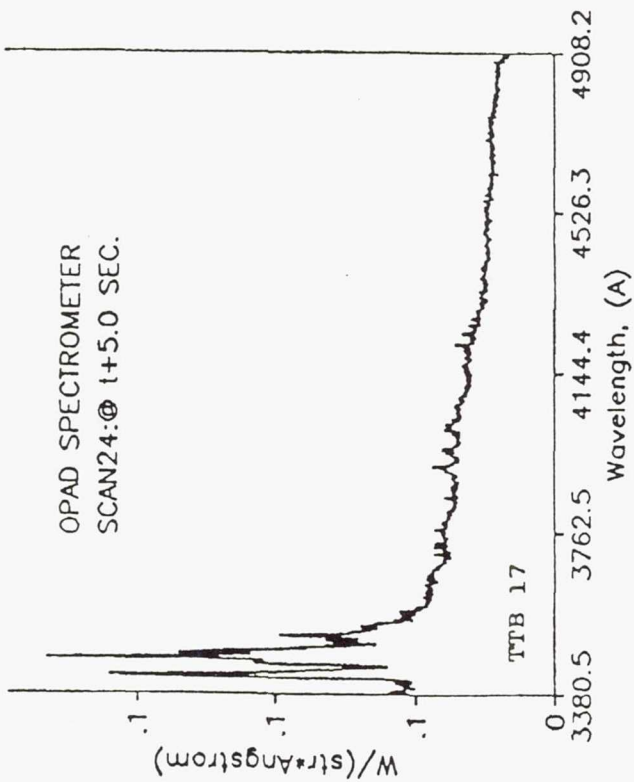
On a much broader basis, in the past year, an in-depth analysis of OPAD data collected on 21 tests of the SSME engine at the technology test bed stand at Marshall has begun. Some of the initial efforts include an investigation of spectral emissions at engine start-up, variations in baseline plume emissions due to changes in rated-power-level (RPL), variations of OH and continuum as a function of RPL, variations of Na as a function of RPL and an analysis of plume emissions at startup using a theoretical radiation model.

Correlation of spectral observations to engine operation at start-up is difficult because of the complexity of the SSME and the dynamic manner in which the exhaust plume evolves. However, in the polychromator data and to lesser degree in the spectrometer data, several events are clearly evident. Among these are the MCC prime time (the time at which initial combustion occurs), formation of the mach disk, and main stage operation.

An effort to understand and quantify the effects of changes in RPL on baseline plume emissions, on OH and continuum, and on atomic emission of Na is also underway. With increase in RPL the Mach disk moves away from the nozzle exit at a rate which is not linear with RPL (theoretically it is proportional to square-root of RPL). Total mass flow and chamber pressure are varied to achieve desired RPL, but the O/F ratio is held at constant value of 6.0. Hence, the chemistry should be somewhat independent of RPL. Findings also indicate that the movement of the Mach disk into the FOV of the OPAD instrument along with the change in pressure at the Mach disk is primarily responsible for the variations in the baseline OH and continuum. Surprisingly Na emission does not follow the movement in the Mach disk as does the OH and continuum. This will require further investigation.

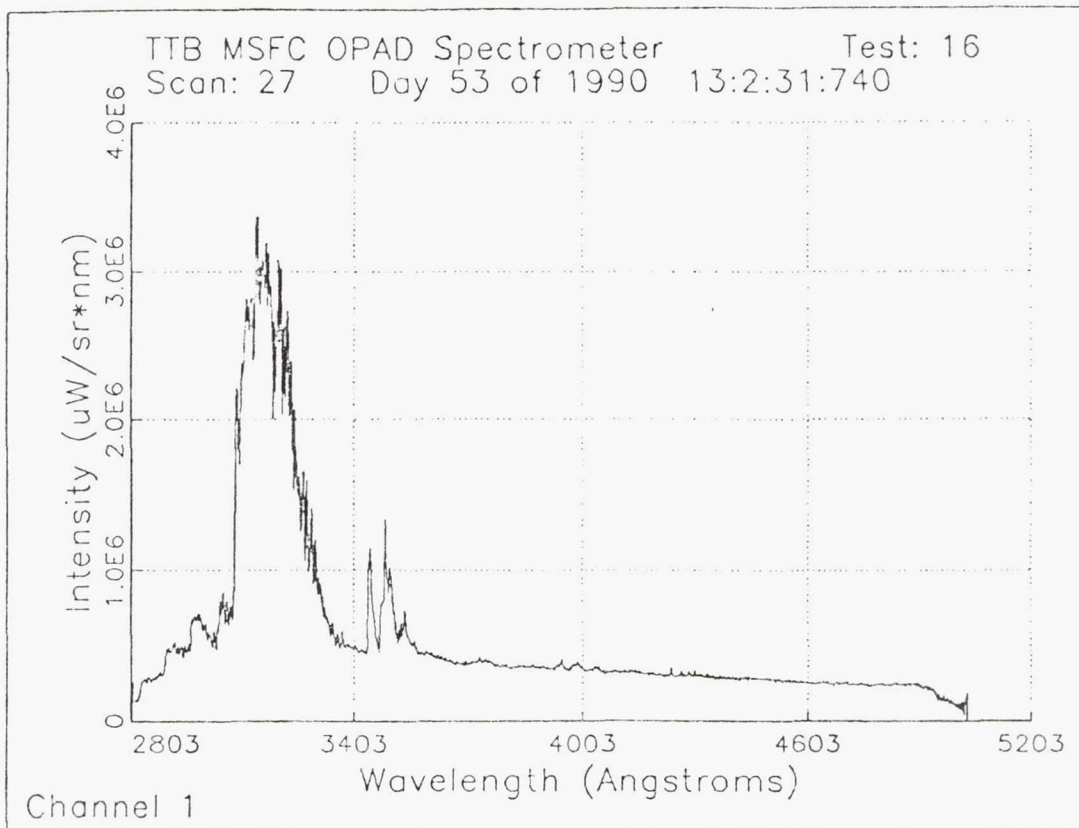
In a first attempt to determine element composition from spectral observations, an optically thin radiative model was developed by Tim Wallace of AEDC to predict absolute emission line intensities from a number of atomic species. While it assumes thermodynamic equilibrium and considers only collisional excitation of atoms, it will be a valuable tool in determining the spectral characterization of the plume.

Immediate plans for future data analysis include the development of radioactive transfer models which will enable us to determine material composition and erosion rates. It is believed that these models in combination with other experience gained from the OPAD project will provide us with a methodology to look at the data from an intelligent standpoint, permitting on-line judgments.

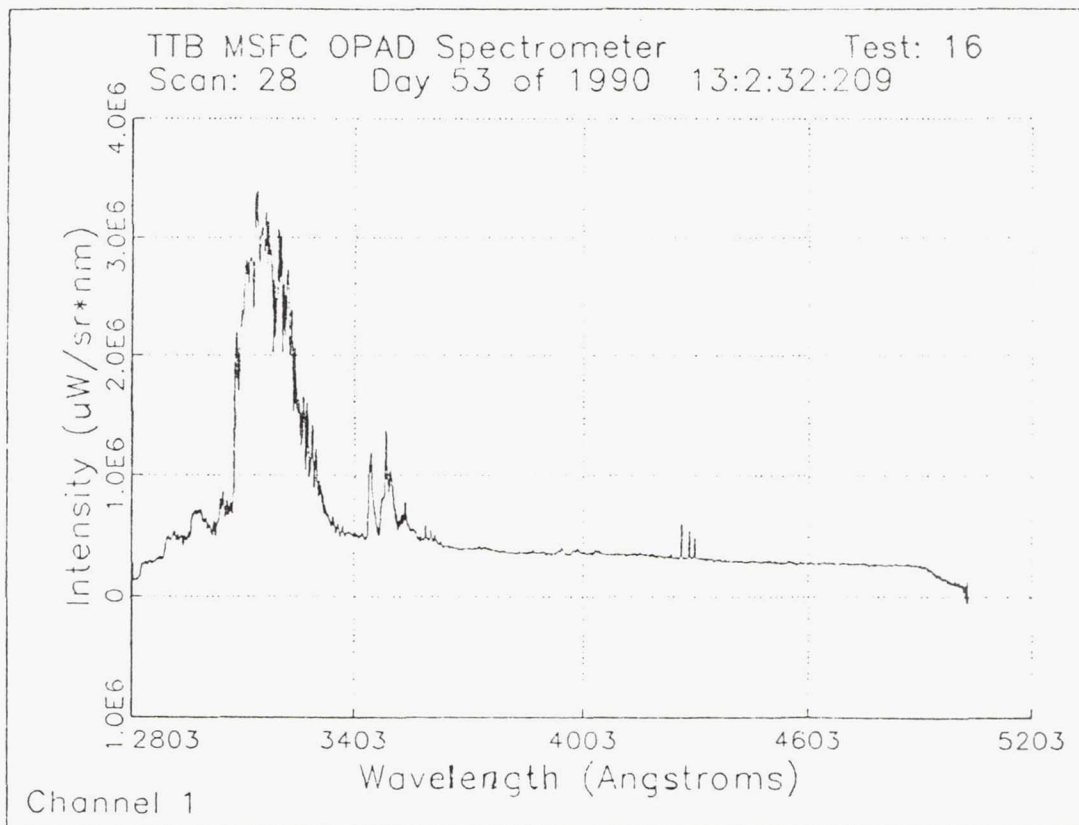


COMPARISON OF MATERIAL EROSION IN TTB20
TO NOMINAL CASE:TTB17

TYPICAL



HPFTP PILOT LIP CRACK



Page intentionally left blank

AN INTEGRATED EDDY CURRENT DETECTION AND IMAGING SYSTEM ON A SILICON CHIP

H. Thurman Henderson, K.P. Kartalia, and Joseph D. Dury
University of Cincinnati
Cincinnati, Ohio 45221

I. INTRODUCTION

Eddy Current probes have been used for many years for numerous sensing applications including crack detection in metals. However, these applications have traditionally used the eddy current effect in the form of a physically wound single or differential probe pairs which of necessity must be made quite large (order of a tenth of an inch) compared to microelectronics dimensions. Also, the traditional wound probe can only take a point reading, although that point might include tens of individual cracks or crack arrays, thus conventional eddy current probes are beset with two major problems: (1) no detailed information can be obtained about the crack or crack array -- simply that local inhomogeneties exist in the region (which just as well could be other surface defects) and (2) for applications such as quality assurance, a vast amount of time must be taken to scan a complete surface, even if robotic applications are used for a physical scan of the surface.

Laboratory efforts have been made to fabricate linear arrays of single turn probes in a thick film format on a ceramic substrate (hybrid technology) as well as in a flexible cable format, however such efforts inherently suffer from relatively large size requirements as well as sensitivity issues.

This paper describes PRELIMINARY efforts to extend eddy current probing from a point or single dimensional level, fully to a two-dimensional micro-eddycurrent format on a silicon chip which might overcome all of the above problems. Moreover, using a serial readout of rows and columns one might be able to achieve eddy current imaging. Thus the scanning (within the area of the chip) would be electronic rather than physical, resulting in an essentially instantaneous scan when compared to the physical scan method. Moreover, although the demonstration vehicle herein described is only a 10 x 10 array on a silicon chip of the order of .25 to .5 inch square, the ultimate chip could consist of an array covering a complete wafer of pizza size (four to eight inches in diameter). Also, in sufficiently thin silicon materials, the surface can conform to non-planar topographies. Also, in sufficiently thin silicon materials, the surface can conform to non-planar topographies.

If successful, the pixel size (based upon integrated eddy current coil size) might range of the order of a thousandth of an inch or smaller, although in our test the coil the spacing is of the order of 5 to 15 thousandths of an inch. This opens up the possibility of a resolution within the typical width of a crack, thus allowing identification of much smaller cracks, early onset of material fatigue from microcracks, classification of cracks and even imaging. Furthermore, with sufficient sensitivity it potentially becomes possible to resolve such things as surface smoothness, grain boundaries and material homogeneity, as fine structure or super fine structure on the signal response. Such a device might also be placed permanently for ongoing health monitoring at critical fatigue points in the vehicle.

There is no other technology but the integrated circuit lithographic technique which allows such miniaturization, resolution and replication uniformity. For example, the masks used for fabricating the geometries were generated by electron beam with a submicron resolution and line uniformity of the order of 0.1 micrometers.

II. PRESENT STATUS

A variety of chip sizes have been made, each consisting of a 10 x 10 array as shown in Fig. 1. Each of the 100 pixels or coil combinations shown in Fig. 2 consists of two flat coils in a "Manhattan" geometry (rectangular) for maximum area utilization, a primary and a secondary. Figure 3 is a scanning electron micrograph of a similar coil, showing a better perspective of the topography. The flat coils are aluminum, separated by insulating silicon dioxide. Figure 4 is an expanded view of the center region of one coil pair.

The aluminum thin film (about a micron thick and typically about 6 to 10 microns wide) lies on two levels, including a return path under the coils, again insulated by a silicon dioxide layer. The silicon substrate simply serves as a convenient substrate into which the initial silicon dioxide layer can be thermally grown using conventional integrated circuit techniques. The other silicon dioxide layers were formed using conventional CVD (chemical vapor deposition) techniques where silane is oxidized at an elevated temperature. The resulting devices (chips) were mounted in a conventional in-line integrated circuit package as shown in Fig. 5. (However it is envisioned that ultimately, vastly larger arrays will be used, requiring special packages.) The chips were encapsulated in a high grade commercially available polymer.

Commercially-available finite-element magnetic field software (MSG-MAGGIE) is being used to model the system and to test improved designs beyond the present demonstration vehicle. Devices have been tested using standard cracks 0.003 inches wide and a few mils deep. These have resulted in a signal above noise of about five percent, using a driving signal at one to ten megahertz.

A rastering circuit was developed for this system, but it was ultimately determined to be more useful to use commercially-available computerized impedance meters (such as those manufactured by Hewlett-Packard and others) which can be programmed to vary such factors as sampling time, settling time, frequency, differential signal between any selected set of coils, etc. However, an interface circuit was built using meter-actuated reed relays and multiplexing, to allow activation and indexing of each coil set (one at a time) in order to avoid inhomogenous mutual impedances and magnetic field couplings over the area of the array. These studies are presently in progress and the results look promising.

Actual imaging has not yet been attempted. Rather we are at this point simply plotting out the serial row-column signals and correlating these with crack sizes and other parameters.

III. BASIS OF THE DESIRED EDDY CURRENT EFFECT

According to Ampere's circuital law,

$$\oint \vec{H} \cdot d\vec{L} = NI$$

where the arbitrary closed line integral of the dot product of the magnetic field \vec{H} with the vector differential length $d\vec{L}$ is equal to the ampere turns NI enclosed. Thus in a solenoid, whether of the conventional spreaded-out multi-layer type, or the present single-level coil

type, the magnetic field generated in the central core is based upon the current I times the number of linked turns N . Thus for a given configuration, one need only increase the drive current for increased field for a proportional increased sensitivity.

The generated magnetic field from the primary coil is made to penetrate an adjacent electrically conducting material where cracks (or other inhomogeneties) are being examined, such as a space engine material or structural element where imperfections or fatigue cracks are of interest. According to Lenz's law, if the magnetic field is varying in time, eddy currents will be induced in the various possible conducting paths of the subject material in such directions as to generate magnetic fields opposing the change.

These circulating eddy currents will cause a reflected impedance in the secondary coil of the device (wound inside the primary) which will in general consist of an induced or reflected resistance (R), inductive reactance (X_L) and capacitive reactance (X_C) or an overall complex impedance $Z \angle \Theta$ at a polar angle Θ . We are presently attempting to correlate these electrical parameters with fault analysis.

Of course each interwoven coil set (primary/secondary) will have its own resting impedance when contacted to air or other uniform material, therefore the first issue is to record in memory the reference impedance of each coil (with its associated external wiring/circuit impedance) when in contact with the reference or "perfect" material. Then a deviation from this reference should be indicative of the existence of a crack or other material imperfection. With sufficient resolution one should be able to distinguish various types of imperfections -- even to the extent of eddy current imaging.

One of the major problems which we have found is not so much the construction of identical on-chip devices, but rather the differing stray impedances of the individual wiring harness lines to the off-chip signal processing. Of course the ultimate answer lies in doing all preliminary signal processing on-chip, with appropriate buffering to the outside world. This level of integration, however, awaits a planned future level of effort after the present demonstration vehicle is adequately proven. We have every reason to believe, however, that complete on-chip processing of the row/column serial data can be done using bucket brigade or other standard techniques in the same silicon substrate (which at this point merely serves as a rather arbitrary physical substrate).

With elimination of external and wiring harness impedances, one should be able to eliminate the necessity for initial material referencing. It should then be sufficient to program the differential comparison of adjacent reflected impedances in order to sense the existence of local cracks. However for coil spacings of the order of and less than crack sizes, it will probably be necessary to add an integral term to reference the changing background at this level of resolution (unlike present eddy current probes which are much larger than the crack sizes being detected) to exist somewhere between the two coil sets. In this way one might distinguish the "forest from the trees". In fact, with sufficient chip uniformity and on-chip processing, absolute local values should be sufficiently meaningful. Fortunately, with our flexible software-based approach, we can arbitrarily vary the comparison formats among x-y elements in order to arrive at the most meaningful approaches.

Also, the HMTC sensors group has access to several picture and imaging processing experts; the results are not dependent on the originating signals being eddy currents versus conventional optical signals.

IV. DETECTABLE PARAMETERS

At this point integrated coil impedances run in the range of tens of ohms at one to ten megahertz. A crack in the range of a few mils wide will result in a change of impedance of the order of several percent when the sample is set against the packaged sensor array, which we estimate to be separated from the reference metallic (crack-containing) material by approximately 0.020 inch of encapsulating polymer. Since the field drops off at a rate somewhere between the square and cube of the distance, one should be able to increase the sensitivity by one to two orders of magnitude through closer proximity (say 2 or 3 mils). On the other hand, we wish to minimize the placement sensitivity.

Although the beginning reflected impedance of a given coil set ranges in the tens of ohms, we have found that we can obtain meaningful systematic changes in impedance at least out to the third decimal place when bringing an object in from some distance (say a few tenths of an inch away). Thus one can speculate that one might even be able to resolve such material properties as surface smoothness from grinding or processing, as well as more gross defects such as cracks, merely by segmenting gross changes from the fine and superfine structure in the reflected impedances.

As one would suppose, as one brings a metallic object into the proximity of the micro eddycurrent array, the reflected resistance and inductive reactance increase. However if one uses, for example, the human finger, the resistance component increases also (as one would expect, since eddy currents are being induced in the conducting skin), but the increasing reactive component is capacitive, i.e. $\Delta\theta$ changes size. We interpret this to be due to the basic dielectric nature of the human skin, and the group (along with some physicians and biologists from the University of Cincinnati Medical School Perinatal Research Institute) is contemplating the possible use of this effect for characterizing the very sensitive skin of premature infants for heat and vapor loss characteristics.

Finally, we hope to also ultimately be able to add a third dimension to the crack probing technique by "chirping" the frequency when sampling each coil. The ordinary (inanimate) skin effect, particularly well known to all in the microwave field, would increasingly concentrate the eddy currents toward the surface of materials with increasing frequency. Thus a scan of frequency at each point during column and row rastering, could in principle provide a depth profile of the crack or defect for three-dimensional imaging.

V. POSSIBLE IMPROVEMENTS

Although we are only in the preliminary phases of this work, we can envision several ways to improve the sensitivity up to several orders in magnitude. These includes relatively simple issues such as (1) closer spacing of the coil array to the measurement surface, (2) higher drive current and dense multiple level spiral coils, as well as more involved but "doable" changes such as (3) on-chip processing or even (4) fabrication with high temperature superconductors (which we are contemplating in connection with our High T_c Superconductor Lab). Finally, it should be pointed out that the eddy currents are also induced in the silicon substrate, which merely represent a power loss. The use of deep impurities to increase the resistivity would suppress this loss.

VI. CONCLUSIONS

The present project is yet in its preliminary phases, but real devices have been built and are being evaluated in the form of a demonstration vehicle, particularly for crack detection in metals commonly used for aerospace propulsion systems and structures.

Crack detection results show impedance changes only in the range of a few percent, but improvements are theoretically possible in the range of orders in magnitude through reconfiguration.

It is felt that the potential exists here for three-dimensional imaging, as well as applications to an extended range of possibilities such as surface finishes and perhaps even grain boundaries and other material inhomogeneties.

VII. REFERENCES

- 1 R.C. McMaster(editor), **Nondestructive Testing Handbook**, Volumes 1 & 2, Ronald Press, New York, NY, 1959.
- 2 Institut Dr. Forster, "Applications of Eddy Current Testing in Aircraft Maintenance and Engine Overhaul with Forster Defectoscop S 2.830," Application Notes of Institut Dr. Forster, (1985).
- 3 S.A.Schelkunoff, "The Impedance Concept and Its Application to Problems of Reflection, Refraction, Shielding, and Power Absorption," Bell System Technical Journal, Vol.27 pg.17-48, (1938).
- 4 Y.D.Krampfer & D.D.Johnson, "Flexible Substrate Eddy Current Coil Arrays," Material Evaluation, Vol.46, pg.471-478 (1988).
- 5 C.V.Dodd, W.E.Deeds, J.W.Luquire, & W.G.Spoeri, "Some Eddy Current Problems and Their Integral Solutions," ORNL-4384, Oak Ridge National Lab., (1969).
- 6 T.G.Kincaid, "Eddy Current Printed Circuit Probe Array: Phase IIA," SIGNAMETRICS Report No.10 (Internal Memo), (1988).
- 7 M.J.Moore & F.J.Dodd, "Real-Time Signal Processing in an Ultrasonic Imaging System," Material Evaluation, Vol.40 pg.976-981, (1982).
- 8 S.Middelhoek & A.C.Hoogerwerf, "Smart Sensors: when and where?," Sensors and Actuators, Vol.8, pg.39-48 (1985).
- 9 "Detection Theory and Applications," Special Issue of Proceedings of IEEE, Vol.58, (1970).

- 10 R.Hochschild, "The Theory of Eddy Current Testing in One (Not-So-Easy) Lesson," Nondestructive Testing, Vol.12, pg.31-40 (1954).
- 11 J.Vine, "Impedance of a Coil Placed near a Conducting Sheet," Journal of Electronic Control, Vol.16, pg.569-577 (1964).
- 12 C.V.Dodds & W.E.Deeds, "Analytical Solutions to Eddy Current Coil Problems," Journal of Applied Physics, Vol.39 pg.2829-2838, (1968).
- 13 Z.Haznadar & J.Matjan, "Numerical Calculation of Skin Effect in Systems of Straight Conductors," Elektrotehnika, Zagreb Vol.5, (1970).
- 14 F.R.Bareham, "Choice of Frequency for Eddy-Current Testing," British Journal of Applied Physics, Vol.11 pg.218-222, (1960).
- 15 T.G.Kincaid, "Eddy Current Probe Analysis," SIGNAMETRICS Report No.7 (Internal Memo), (1987).
- 16 P.M.Hall, "Resistance Calculations for Thin Film Patterns," Thin Film Solids, Elsevier, Amsterdam, 1968.
- 17 J.M.Janicke & E.S.Sealey, Magnetics, The Magnetics Handbook, RFL Industries, Inc., Boonton, NJ, 1982.
- 18 B.A.Auld, F.Muennemann, and D.K.Winslow, "Eddy Current Probe Response to Open and Closed Surface Flaws," Journal Nondestructive Evaluation, Vol.2 pg.1-21, (1981).
- 19 H.L.Libby, Introduction to Electromagnetic Methods, Wiley Press (Interscience), New York, NY, 1971.
- 20 H.W.Ghent, "A Novel Eddy Current Surface Probe," Atomic Energy of Limited, AECL-7518, Chalk River, Ontario, Canada (1981).
- 21 D.A.Daly, S.P.Knight, M.Coulton, & R.Ekholdt, "Lumped Elements in Microwave Integrated Circuits," IEEE Transactions of Microwave Theory, Vol.15 pg.713-721, (1967).
- 22 H.N.Nerwin, "A Survey of Telemetry Techniques Applicable to Nondestructive Testing," Material Evaluation, Vol.24 pg.373-377, (1966).

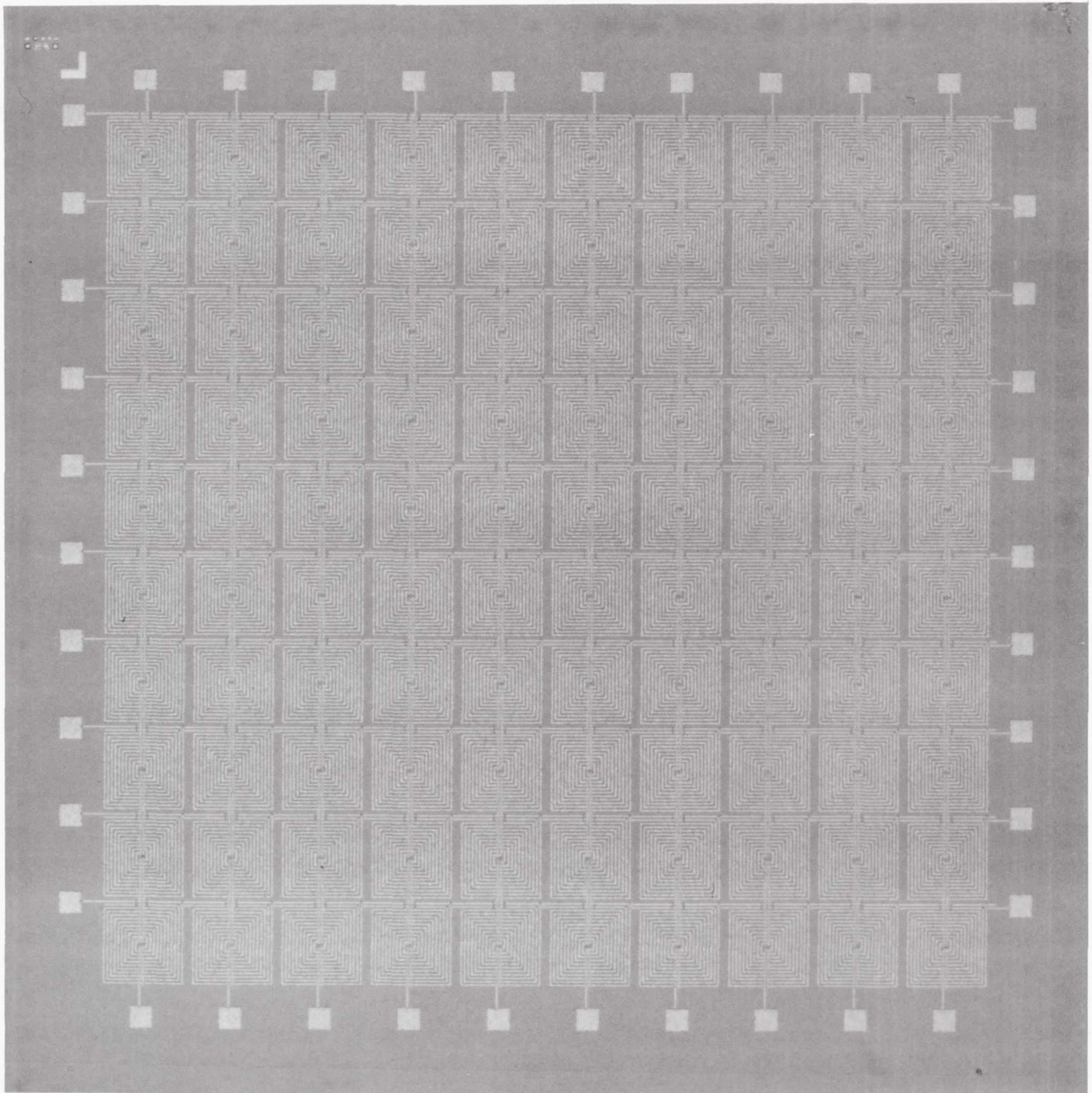


Fig. 1 10 x 10 eddy current coil array on a silicon chip, approximately 1/4 inch square. Each flat coil set consists of a primary for micro eddycurrent generation and a secondary for sensing reflected complex impedance. Each row and column may be externally addressed. Future models will have all signal conditioning on-chip to avoid the necessity for lead compensation.

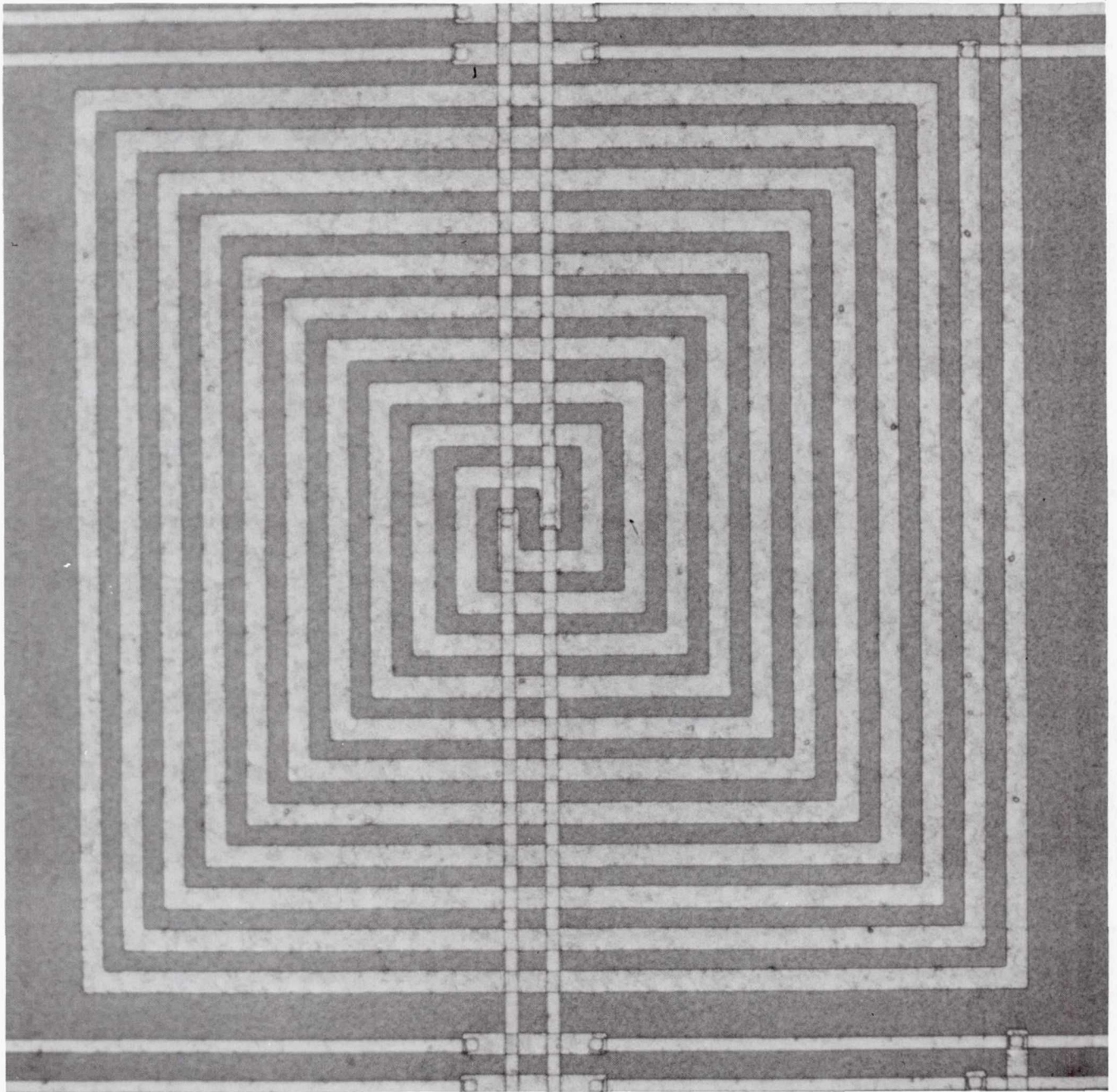


Fig. 2 Expanded view on one of the coil pairs (the two coils have been connected in series in this case for test purposes). The dark lines are aluminum leads, six microns wide in this case, separated by four microns of silicon dioxide.

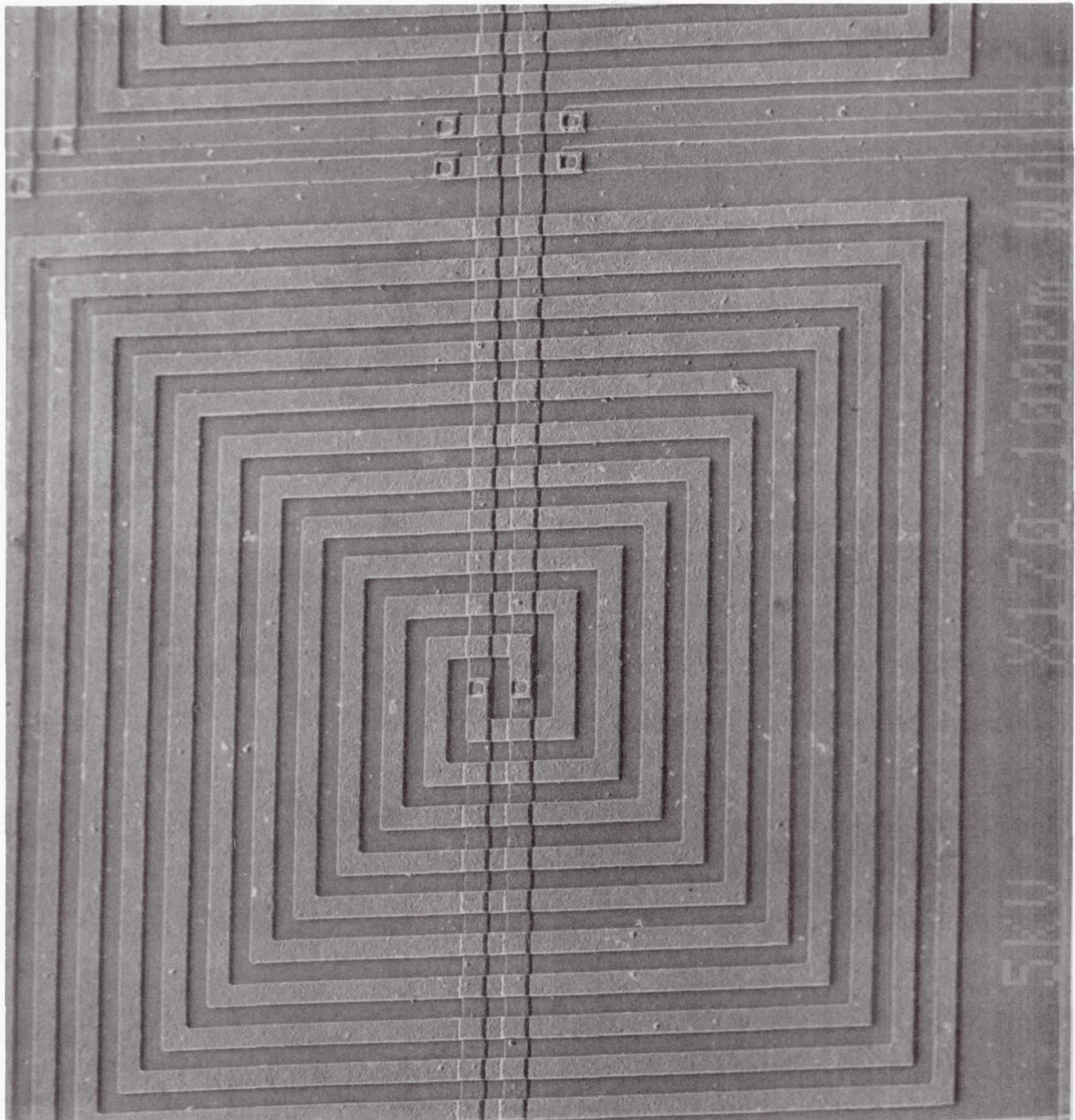


Fig. 3 Scanning electron micrograph of Fig. 2, except in this case the two coils are separated in the form of a primary and a secondary. At the center, each coil connects to a separate aluminum bus (insulated from the top metallization by a silicon device layer) so that all primary and secondary coils can be individually addressed.

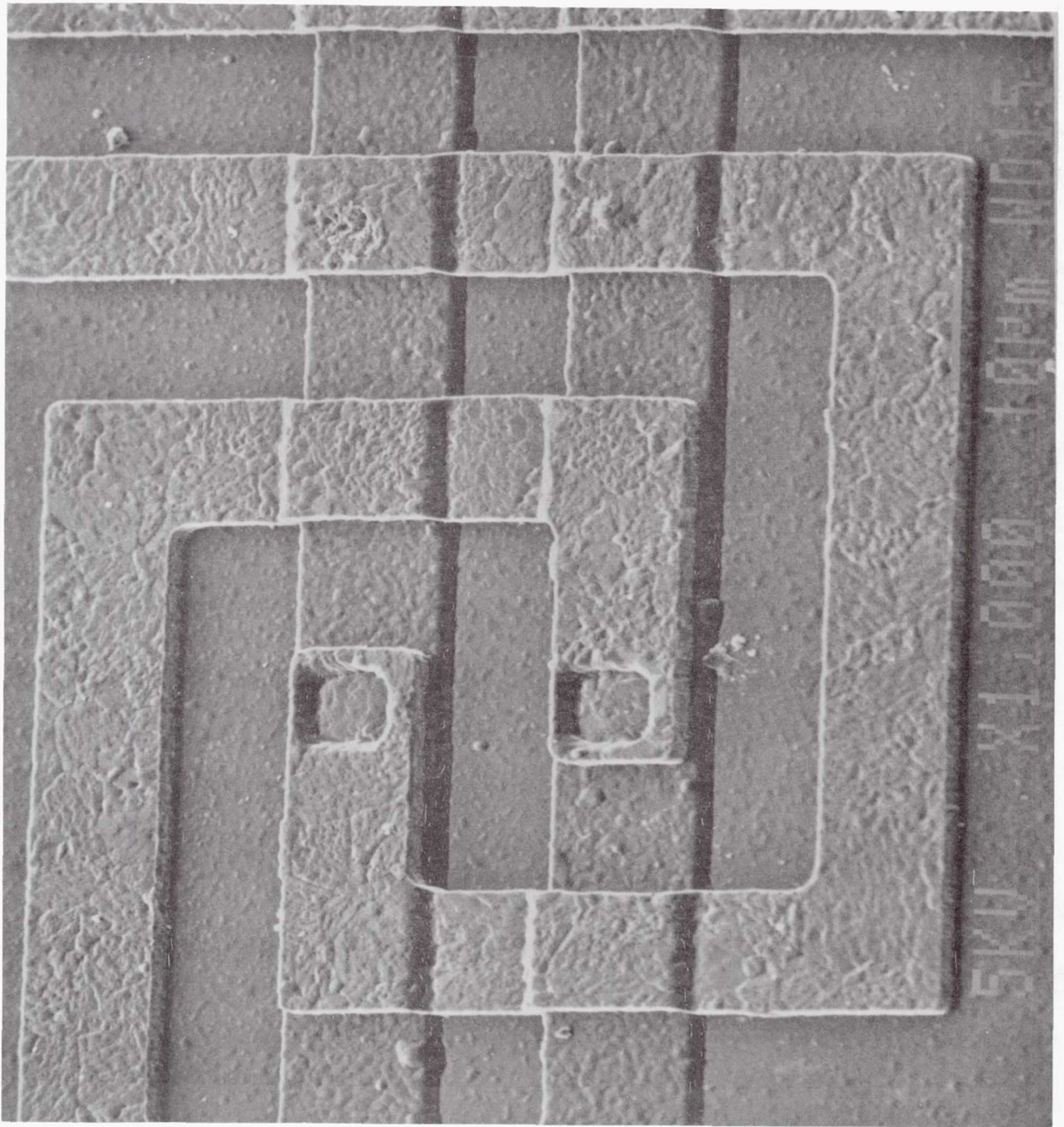


Fig. 4 An expanded view of the center region of Fig. 4, showing the connection of the top side six-micron aluminum leads connected to the lower leads through an intermediate silicon dioxide (about one micron) insulator. Edge definition generally shows a uniformity of two or three tenths of a micron. Note that the last loop can only link about twenty percent of the generating field, but there are five complete loops in the symmetrical primary/secondary coils.

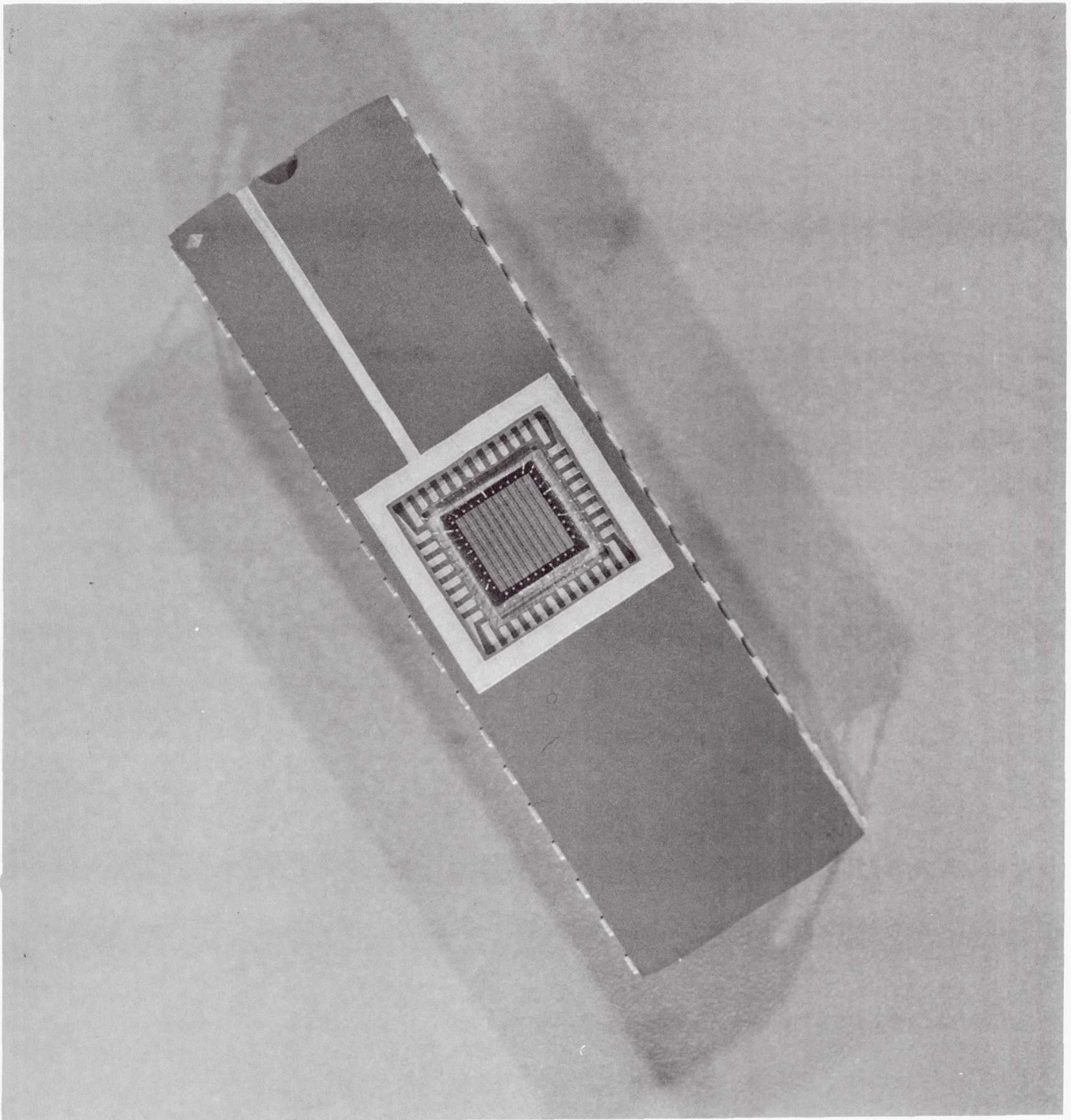


Fig.5 Sensor chip array mounted in a conventional in-line integrated circuit package.

Page intentionally left blank

FOUR DIMENSIONAL RECONSTRUCTION AND ANALYSIS OF PLUME IMAGES

Atam P. Dhawan, Charles Peck III, and Peter Disimile
University of Cincinnati
Cincinnati, Ohio 45221

ABSTRACT

There have been a number of methods investigated and under current investigations for monitoring the health of the Space Shuttle Main Engine (SSME). Plume emission analysis has recently emerged as a potential technique for correlating the emission characteristics with the health of an engine. In order to correlate the visual and spectral signatures of the plume emission with the characteristic health monitoring features of the engine, one has to acquire, store, and analyze the plume emission data in a manner similar to flame emission spectroscopy. The characteristic visual and spectral signatures of the elements vaporized in exhaust plume along with the features related to their temperature, pressure, and velocity can be analyzed once the images of plume emission are effectively acquired, digitized, and stored on a computer. Since the emission image varies with respect to location (the distance from the nozzle) and also with respect to time at a specified planar location, four dimensional visual and spectral analysis needs to be performed on the plume emission data. In order to achieve this objective, we started conducting feasibility research to digitize, store, analyze, and visualize the images of a subsonic jet in a cross flow. The jet structure was made visible using a direct injection flow visualization technique. In this paper, we present the results of time-history based three-dimensional reconstruction of the cross sectional images corresponding to a specific planar location of the jet structure. The experimental set-up to acquire such data is described and 3D displays of time-history based reconstructions of the jet structure are discussed.

Page intentionally left blank

STRUCTURAL DYNAMICS: PROBABILISTIC STRUCTURAL ANALYSIS METHODS

PROGRAM OVERVIEW

Christos C. Chamis and Dale A. Hopkins
NASA Lewis Research Center
Cleveland, Ohio 44135

Deterministic structural analysis methods, as we are seeing, will not be sufficient to properly design critical components in hot structures and particularly, in propulsion structures. Because these structural components are subjected to a variety of complex and severe cyclic loading conditions, including high temperatures and high temperature gradients, most of them are quantifiable only as best engineering estimates. These complex loading conditions subject the material to coupled nonlinear behavior, which depends on stress, temperature, and time. Coupled nonlinear material behavior is non-uniform, very difficult to determine experimentally, and perhaps impossible to describe deterministically. In addition, hot rotating structural components are relatively small. Uncertainties in fabrication tolerances on these components, which are slight variations in thickness, can significantly affect the component structural response. Furthermore, the attachment of components in the structural system generally differs by an indeterminate degree from that assumed for designing the component. These uncertain factors can be grouped into: (1) loading conditions, (2) geometric configuration including supports on which structural analyses are based, and (3) material behavior. In order to formally account for all of these aspects of random nature, we develop probabilistic structural analysis methods where all participating variables are described by appropriate probability functions.

The development of the probabilistic structural analysis methodology is a joint program of NASA Lewis in-house and research sponsored by industry, universities, and support service contractors (ref. 1). Theoretical considerations, computer codes, and their respective applications are described in papers presented in conferences (refs. 2 to 32). Activities and progress up to June 1989 are summarized in reference 33.

The objectives of this session are: (1) to provide a brief description of the fundamental aspects of the quantification process as depicted schematically in figure 1 and (2) to summarize progress since the last structural durability conference in 1989. The methodology to date and that to be developed during the life of the program is presented in the block diagram in figure 2. In this figure the uncertain factors are presented in the top three blocks. This figure outlines the approach required to achieve component/system certification in the shortest possible time for affordable reliability/risk (ref. 34). Two new elements appear in the block diagram (enclosed in dashed lines): (1) uncertainties in human factor and (2) uncertainties in the computer code. We have initiated research to quantify the uncertainties in the human factor as will be discussed in one of the presentations. The progress of the program, which includes relevant sample cases, is summarized and discussed in the presentations listed in figure 3.

REFERENCES

1. Chamis, C.C.: Probabilistic Structural Analysis Methods for Space Propulsion System Components. NASA TM-88861, 1986.
2. Liu, W.K.; Belytschko, T.; and Besterfield, G.H.: A Probabilistic Hu-Washizu Variational Principle. 28th Structures, Structural Dynamics and Materials Conference, Part 1, AIAA, 1987, pp. 252-259.
3. Wirsching, P.H.; Ortiz, K.; and Lee, S.J.: An Overview of Reliability Methods in Mechanical and Structural Design. 28th Structures, Structural Dynamics and Materials Conference, Part 1, AIAA, 1987, pp. 260-267.
4. Nagpal, V.K.; Rubinstein, R.; and Chamis, C.C.: Probabilistic Structural Analysis to Quantify Uncertainties Associated With Turbopump Blades. 28th Structures, Structural Dynamics and Materials Conference, Part 1, AIAA, 1987, pp. 268-274.
5. Chamis, C.C.: Probabilistic Structural Analysis to Evaluate the Structural Durability of SSME Critical Components. Structural Integrity and Durability of Reusable Space Propulsion Systems, NASA CP-2471, 1987, pp. 117-120.
6. Cruse, T.A.: Probabilistic Structural Analysis Methods for Select Space Propulsion System Structural Components (PSAM). Structural Integrity and Durability of Reusable Space Propulsion Systems, NASA CP-2471, 1987, pp. 121-126.
7. Dias, J.B.; Nagtegaal, J.C.; and Nakazawa, S.: The NESSUS Finite-Element Code. Structural Integrity and Durability of Reusable Space Propulsion Systems, NASA CP-2471, 1987, pp. 127-132.
8. Rajagopal, K.R.: Probabilistic Structural Analysis Verification Studies. Structural Integrity and Durability of Reusable Space Propulsion Systems, NASA CP-2471, 1987, pp. 133-138.
9. Burnside, O.H.: Nessus/Expert and Nessus/FPI in the Probabilistic Structural Analysis Methods (PSAM) Program. Structural Integrity and Durability of Reusable Space Propulsion Systems, NASA CP-2471, 1987, pp. 139-144.
10. Wirsching, P.H.: Advanced Probabilistic Method Development. Structural Integrity and Durability of Reusable Space Propulsion Systems, NASA CP-2471, 1987, pp. 145-150.
11. Atluri, S.N.: Stochastic and Hybrid-Stress Plate/Shell Finite Elements for Hot Section Components. Structural Integrity and Durability of Reusable Space Propulsion Systems, NASA CP-2471, 1987, pp. 151-152.
12. Belytschko, T.; and Liu, W.K.: Probabilistic Finite Elements. Structural Integrity and Durability of Reusable Space Propulsion Systems, NASA CP-2471, 1987, pp. 153-160.

13. Shiao, M.; Rubinstein, R.; and Nagpal, V.K.: Probabilistic SSME Blades Structural Response Under Random Pulse Loading. Structural Integrity and Durability of Reusable Space Propulsion Systems, NASA CP-2471, 1987, pp. 161-166.
14. Nagpal, V.K.: Quantifying Uncertainties in the Structural Response of SSME Blades. Structural Integrity and Durability of Reusable Space Propulsion Systems, NASA CP-2471, 1987, pp. 167-174.
15. Newell, J.F.: Composite Load Spectra for Select Space Propulsion Structural Components. Structural Integrity and Durability of Reusable Space Propulsion Systems, NASA CP-2471, 1987, pp. 175-188.
16. Kurth, P.; and Newell, J.F.: Probabilistic Load Model Development and Validation for Composite Load Spectra for Select Space Propulsion Engines. Structural Integrity and Durability of Reusable Space Propulsion Systems, NASA CP-2471, 1987, pp. 189-200.
17. Spencer, B.F., Jr.; and Hopkins, D.A.: An Expert System for Probabilistic Description of Loads on Space Propulsion System Structural Components. 29th Structures, Structural Dynamics and Materials Conference, Part 3, AIAA, 1988, pp. 1262-1266.
18. Wu, Y.T.; and Burnside, O.H.: Validation of the NESSUS Probabilistic Finite Element Analysis Computer Program. 29th Structures, Structural Dynamics and Materials Conference, Part 3, AIAA, 1988, pp. 1267-1274.
19. Shiao, M.C.; Nagpal, V.K.; and Chamis, C.C.: Probabilistic Structural Analysis of Aerospace Components Using NESSUS. 29th Structures, Structural Dynamics and Materials Conference, Part 3, AIAA, 1988, pp. 1275-1282.
20. Millwater, H.; Palmer, K.; and Fink, P.: NESSUS/EXPERT - An Expert System for Probabilistic Structural Analysis Methods. 29th Structures, Structural Dynamics and Materials Conference, Part 3, AIAA, 1988, pp. 1283-1288.
21. Stock, T.A., et al.: Probabilistic Composite Micromechanics. 29th Structures, Structural Dynamics and Materials Conference, Part 3, AIAA, 1988, pp. 1289-1298.
22. Boyce, L.; and Chamis, C.C.: Probabilistic Constitutive Relationships for Cyclic Material Strength Models. 29th Structures, Structural Dynamics and Materials Conference, Part 3, AIAA, 1988, pp. 1299-1306.
23. Boyce, L.; and Chamis, C.C.: Probabilistic Constitutive Relationships for Material Strength Degradation Models. 30th Structures, Structural Dynamics and Materials Conference, Part 4, AIAA, 1989, pp. 1832-1839.
24. McClung, R.C., et al.: An Approximate Methods Approach to Probabilistic Structural Analysis. 30th Structures, Structural Dynamics and Materials Conference, Part 4, AIAA, 1989, pp. 1840-1845.

25. Millwater, H.R.; and Wu, Y.T.: Structural Reliability Analysis Using a Probabilistic Finite Element Program. 30th Structures, Structural Dynamics and Materials Conference, Part 4, AIAA, 1989, pp. 1846-1851.
26. Wu, Y.T.; Millwater, H.R.; and Cruse, T.A.: An Advanced Probabilistic Structural Analysis Method for Implicit Performance Functions. 30th Structures, Structural Dynamics and Materials Conference, Part 4, AIAA, 1989, pp. 1852-1859.
27. Newell, J.F.; Rajagopal, K.R.; and Ho, H.: Probabilistic Structural Analysis of Space Propulsion System Turbine Blades. 30th Structures, Structural Dynamics and Materials Conference, Part 4, AIAA, 1989, pp. 1860-1868.
28. Thacker, B.H.; McClung, R.C.; and Millwater, H.R.: Application of the Probabilistic Approximate Analysis Method to a Turbopump Blade Analysis. 31st Structures, Structural Dynamics and Materials Conference, Part 2, AIAA, 1990, pp. 1039-1047.
29. Millwater, H.R.; Wu, Y.T.; and Fossum, A.F.: Probabilistic Analysis of a Materially Nonlinear Structure. 31st Structures, Structural Dynamics and Materials Conference, Part 2, AIAA, 1990, pp. 1048-1053.
30. Debchaudhury, A., et al.: A Probabilistic Approach to the Dynamic Analysis of Ducts Subjected to Multibase Harmonic and Random Excitation. 31st Structures, Structural Dynamics and Materials Conference, Part 2, AIAA, 1990, pp. 1054-1061.
31. Newell, J.F., et al.: Probabilistic Structural Analysis of Space Propulsion System LOX Post. 31st Structures, Structural Dynamics and Materials Conference, Part 2, AIAA, 1990, pp. 1062-1069.
32. Shiao, M.C.; and Chamis, C.C.: A Methodology for Evaluating the Reliability and Risk of Structures Under Complex Service Environments. 31st Structures, Structural Dynamics and Materials Conference, Part 2, AIAA, 1990, pp. 1070-1080.
33. Chamis, C.C.; and Hopkins, D.A.: Probabilistic Structural Analysis Methods of Hot Engine Structures. NASA TM-102091, 1989.
34. Shiao, M.C.; and Chamis, C.C.: Probability of Failure and Risk Assessment of Propulsion Structural Components. NASA TM-102323, 1990.

Probabilistic Simulation of Component Reliability Using CLS Coupled With PSAM and PMBM

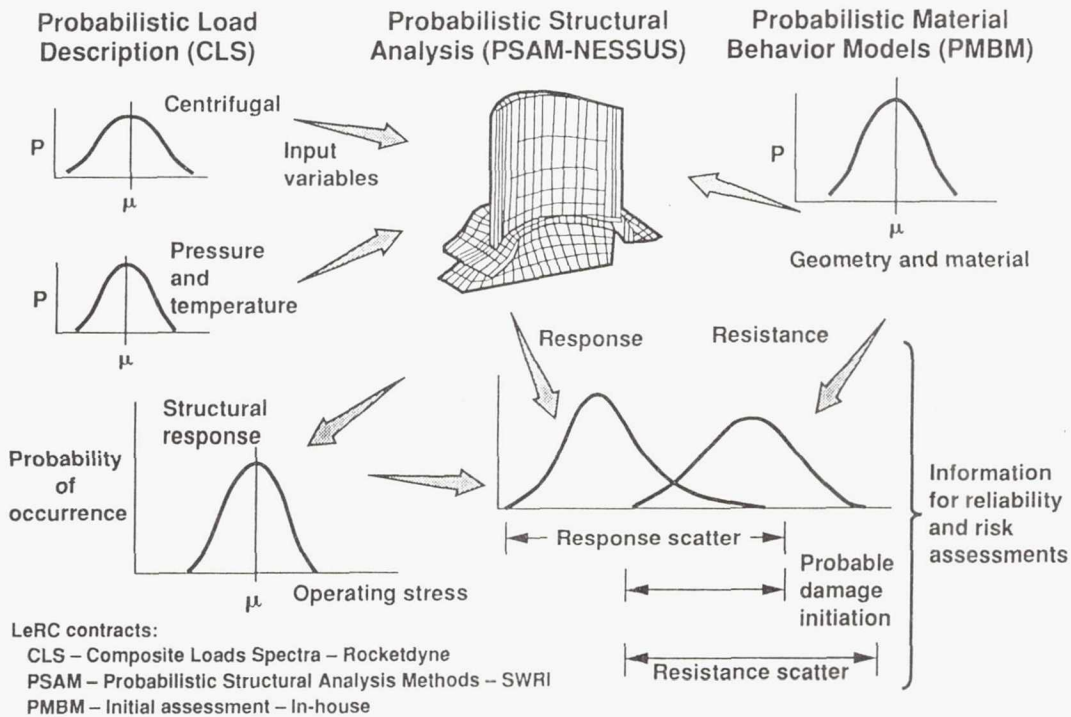


Figure 1

CD-91-52296

Probabilistic Simulation for Assured Structural Certification

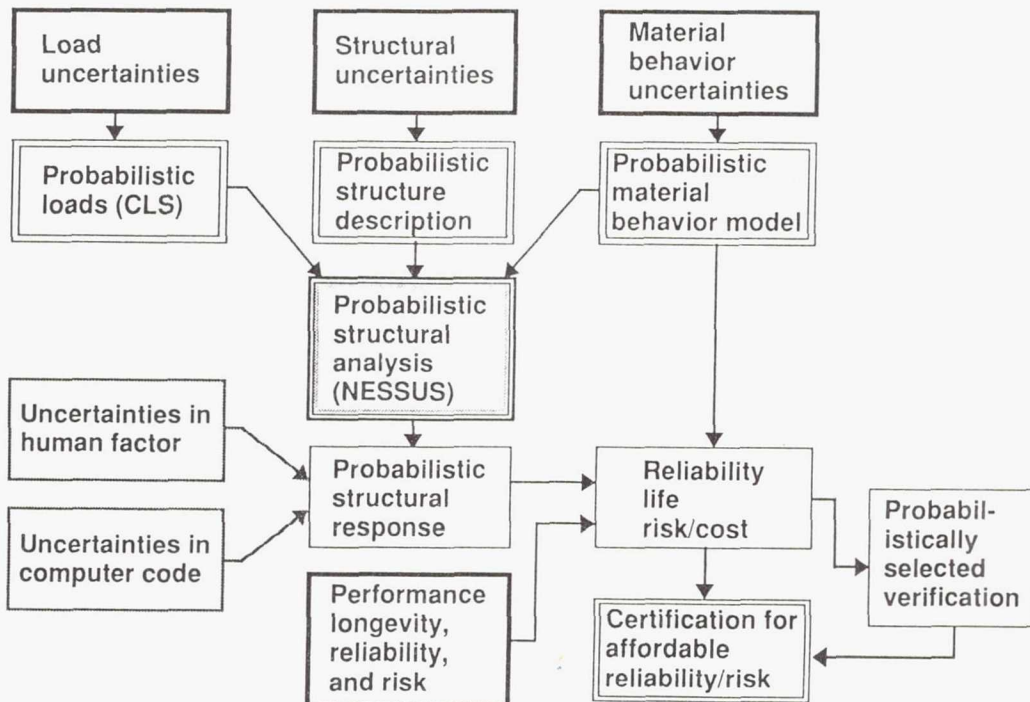


Figure 2

CD-91-52297

Session II – Structural Dynamics: Probabilistic Structural Analysis Methods

- Structural Reliability Methods – Code Development Status
H. Millwater, B. H. Thacker, Y. T. Wu, Southwest Research Institute, San Antonio, Texas; T. A. Cruse, Vanderbilt University, Nashville, Tennessee
- Probabilistic Load Simulation – Code Development Status
J. F. Newell, Rockwell International, Rocketdyne Division, Los Angeles, California
- Probabilistic Evaluation of SSME Structural Components
K. R. Rajagopal, Rockwell International, Rocketdyne Division, Los Angeles, California
- Rocketdyne PSAM – In-House Enhancements/Applications
K. O'Hara, Rockwell International, Rocketdyne Division, Los Angeles, California
- Commercialization of NESSUS – Status
B. H. Thacker, Southwest Research Institute, San Antonio, Texas

Figure 3

CD-91-52298

Session II – Structural Dynamics: Probabilistic Structural Analysis Methods (continued)

- Added Capability for Reliability and Risk – Status
T. A. Cruse, Vanderbilt University, Nashville, Tennessee
- Algorithm Development for Computational Efficiency
Y. T. Wu, Southwest Research Institute, San Antonio, Texas
- Expert System Development for Probabilistic Load Simulation
H. W. Ho, Rockwell International, Rocketdyne Division, Los Angeles, California
- Probabilistic Fracture Finite Elements
W. K. Liu, Northwestern University, Evanston, Illinois
- Coarse Analysis Models Scaling for Improved Accuracy
M. C. Shiao, Sverdrup Technology Inc., Brook Park, Ohio
- Human-Factor in Probabilistic Structural Analysis
A. Shah, Sverdrup Technology Inc., Brook Park, Ohio

Figure 3–Continued

CD-91-52299

STRUCTURAL RELIABILITY METHODS - CODE DEVELOPMENT STATUS

H. Millwater, B. Thacker, and Y.-T. Wu
Southwest Research Institute
San Antonio, Texas 78228

and

T. Cruse
Vanderbilt University
Nashville, Tennessee 37203

The Probabilistic Structures Analysis Methods (PSAM) program integrates state-of-the-art probabilistic algorithms with structural analysis methods in order to quantify the behavior of SSME structures subject to uncertain loadings, boundary conditions, material parameters and geometric conditions. The initial 5-year program focused on advanced software to analyze probabilistic structural response. The second 5-year phase of PSAM is focusing on component and system structural reliability, material resistance, and risk, and on system qualification/certification, and health monitoring.

An advanced, efficient probabilistic structural analysis software program, NESSUS (Numerical Evaluation of Stochastic Structures Under Stress) has been developed as a deliverable for this program. NESSUS contains a number of integrated software components to perform probabilistic analysis of complex structures, see Figure 1. A nonlinear finite element module NESSUS/FEM is used to model the structure and obtain structural sensitivities. Some of the capabilities of NESSUS/FEM are shown in Figure 2. A Fast Probability Integration module NESSUS/FPI estimates the probability given the structural sensitivities. A driver module, PFEM, couples the FEM and FPI modules.

NESSUS, version 5.0, released in January 1991, addresses component reliability, resistance and risk. Recent enhancements include the development and implementation of advanced probabilistic algorithms to compute structural reliability, material resistance models including user defined resistance, and the risk of failure based on the consequences or severity of a failure.

The Advanced Mean Value with iterations (AMV+) algorithm has been shown to be very effective in obtaining accurate and efficient probabilistic solutions. The AMV+ algorithms are intended to minimize the number of finite element calculations needed, yet provide an accurate solution even at very high or low probabilities, i.e. in the tails of the distribution. Figure 3 shows the cumulative distribution function, CDF, of an elastic perfectly plastic cylinder under internal load. The nonlinearity caused by the transition from elastic to plastic material behavior is correctly determined by the AMV+ algorithm. Thus, highly nonlinear problems can be handled with NESSUS.

Material resistance governs the structure's ability to withstand a stress condition. NESSUS 5.0 can treat the traditional reliability problem, defined as $g = R - S$ where R is the resistance and S is the stress, as well as more complicated reliability functions. For example, for fatigue crack growth the reliability function is defined as

$$g = N_f - N_0 = \frac{2[a_f^{(1-n/2)} - a_i^{(1-n/2)}]}{C(2-n)(Y\sigma_{\max}\sqrt{\pi})^n} - N_0, \quad n \neq 2$$

where σ_{\max} is obtained from a finite element model, a_f and a_i are the final and initial crack lengths, C is a crack growth material parameter, n is the Paris crack growth power and Y is a geometry factor. Failure occurs when N_f is less than the design life N_0 . A very general user-defined reliability function option is provided in NESSUS. Figure 4 shows the results of a probabilistic fatigue analysis.

Structural risk with respect to cost is defined as the coupling of the probability of failure and the consequences of failure. The NESSUS/RISK module couples the probability of failure computed by the other NESSUS modules and the consequences of failure. In equation form this is defined as

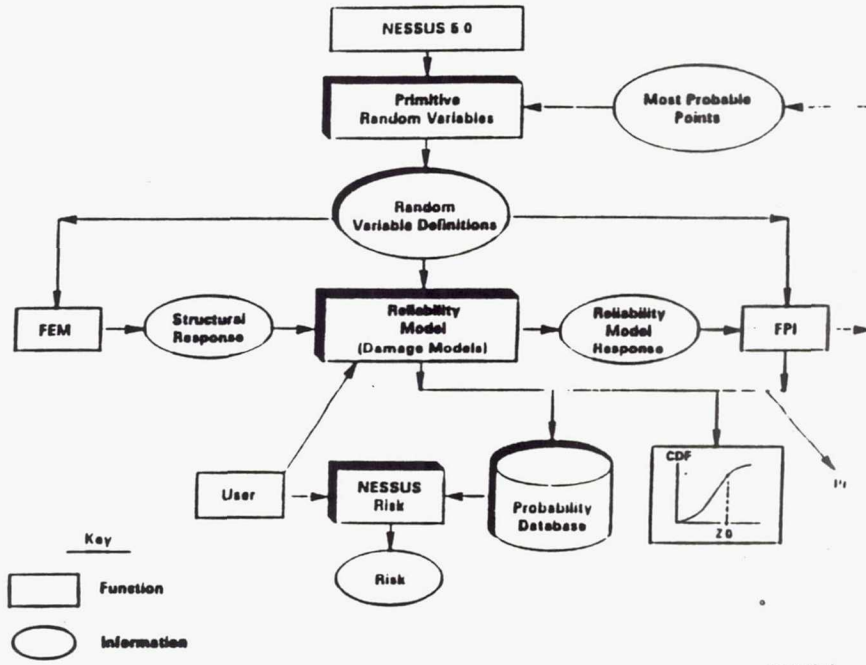
$$\text{Risk} = C_0(x) + P_f(x) C(x) + (1 - P_f(x)) NC(x)$$

where x is the response quantity, $C_0(x)$ is the initial cost, $P_f(x)$ is the probability of failure, $C(x)$ is the cost of failure and $NC(x)$ is the cost of nonfailure or success. A schematic outline of the Risk module is shown in Figure 5. RISK can be run standalone or in conjunction with NESSUS/PFEM.

The capabilities for reliability, resistance and risk are all integrated within NESSUS. Figure 6 shows a schematic of the solution procedure in NESSUS 5.0. The user defines the structure, the resistance model, the random inputs, and the failure consequences. NESSUS computes the probabilistic response including sensitivity factors, and the risk of failure. These results can then be used for decision making by the user.

NESSUS is being extended to system reliability problems. One system reliability analysis method being developed is a probabilistic fault tree approach. In this method, the bottom events are analyzed probabilistically and the probability density functions are integrated upwards to determine the probability distribution of the top event.

NESSUS 5.0 CODE STRUCTURE

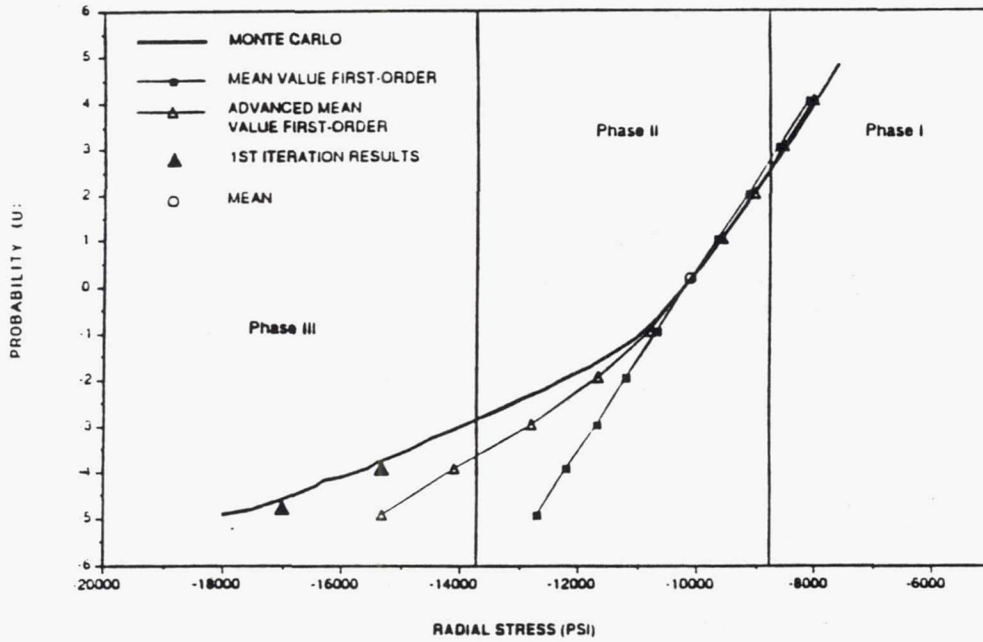


980131-1

NESSUS PROBABILISTIC FINITE ELEMENT CAPABILITIES

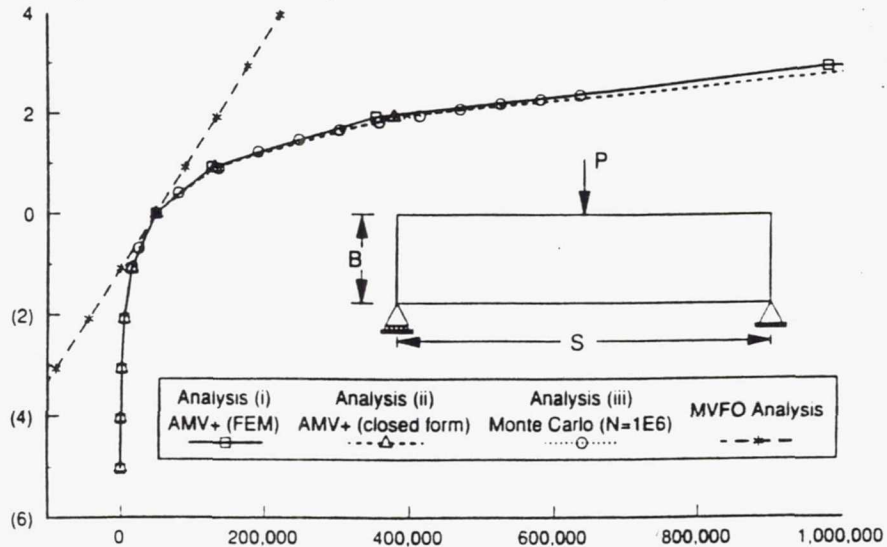
| ANALYSIS TYPES | ELEMENT LIBRARY | RANDOM VARIABLES |
|---------------------|-------------------|----------------------|
| Static | Beam | Geometry |
| Natural Frequency | Plate | Loads |
| Buckling | Plane Stress | Forces |
| Harmonic Excitation | Plane Strain | Pressures |
| Random Vibration | Axisymmetric | Temperatures |
| Transient Dynamics | 3D solid | Material Properties |
| <u>NONLINEAR</u> | Enhanced Elements | Elastic Modulus |
| Material | | Poisson's Ratio |
| Geometry | | Shear Modulus |
| | | Orientation Angle |
| | | Yield Stress |
| | | Hardening Parameters |
| | | Damping |
| | | Initial Conditions |

CDF OF RADIAL STRESS FOR ELASTIC-PLASTIC CYLINDER



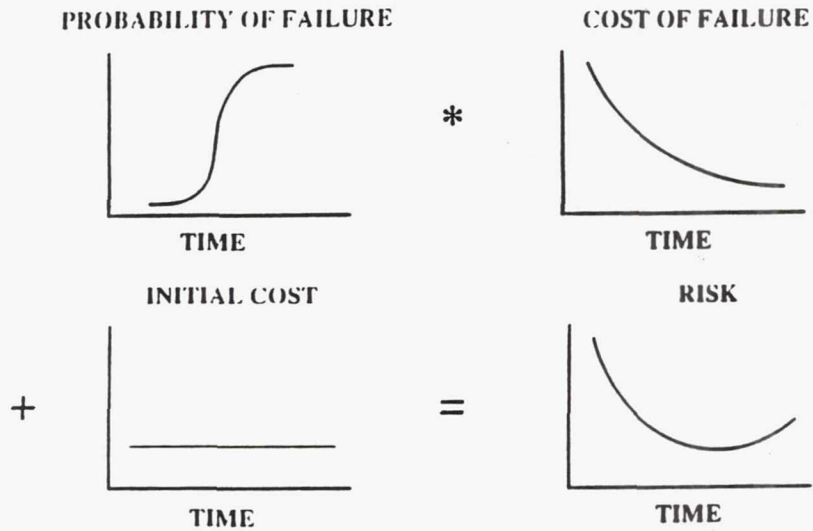
PROBABILISTIC FATIGUE ANALYSIS

CDF (Standard Deviations)

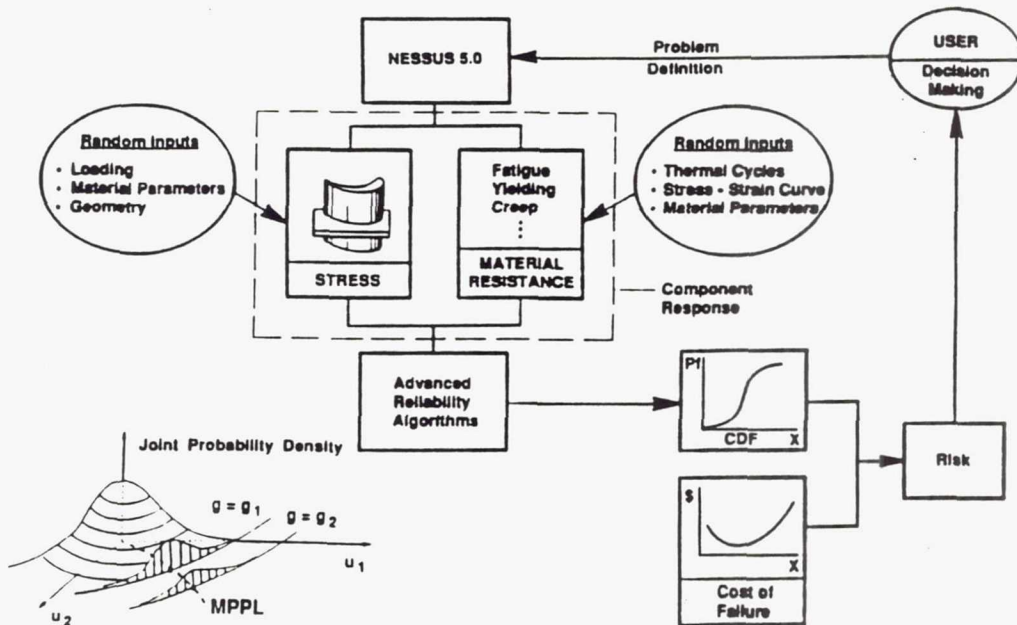


RISK/COST ALGORITHM

$$\text{RISK/COST} = \text{INITIAL COST} + \text{PROBABILITY OF FAILURE} * \text{COST OF FAILURE}$$



NESSUS 5.0 - COMPONENT RELIABILITY, RESISTANCE, AND RISK



Page intentionally left blank

PROBABILISTIC LOAD SIMULATION - CODE DEVELOPMENT STATUS

J.F. Newell and H. Ho
Rockwell International Corp.
Rocketdyne Division
Canoga Park, California 91303

Objective and Approach

The objective of the Composite Load Spectra (CLS) project is to develop generic load models to simulate the composite load spectra that are induced in space propulsion system components. The probabilistic loads thus generated are part of the probabilistic design analysis (PDA) of a space propulsion system that also includes probabilistic structural analyses, reliability and risk evaluations (Figure 1). The development and applications of the project to selected space propulsion system structural components have been carried out under the sponsorship of NASA Lewis Research Center.

Probabilistic load simulation for space propulsion systems demands sophisticated probabilistic methodology and requires large amount of load information and engineering data. The CLS approach is to implement a knowledge-based system coupled with a probabilistic load simulation module. The knowledge-base manages and furnishes load information and expertise and sets up the simulation runs. The load simulation module performs the numerical computation to generate the probabilistic loads with load information supplied from the CLS knowledge base.

CLS Engine Model and Component Load Models Development

A multi-level engine model (Figure 2) was developed for the probabilistic load simulation. It consists of the engine system model at the base of the model, the subsystem (load environment) models and the component load models at higher levels (Figure 3). The engine system model can evaluate 99 system dependent loads, which consist of system performance variables and subsystem interface operating loads, based on a certain engine configuration defined by 64 engine hardware and operational parameters (or primitive variables). The subsystem load environment models generate the boundary information that is used by the local component model. It uses a set of correlated system dependent loads to define the boundary information. The complexity of these subsystem models vary depending on the complexity of the physical model used to define the boundary conditions. The component load models, one for each component load, then use the boundary loads to generate the probabilistic component loads for the corresponding engine operating condition (Figure 4).

The load simulation module provides three probabilistic methods for generating probabilistic loads. They are the Gaussian moment method, the RASCAL (Random Sampling Condensation Algorithm) method and the Monte Carlo method. During the last two years, a correlation field formalism was developed to systematically simulate the correlated component loads. This formalism provides a robust proce-

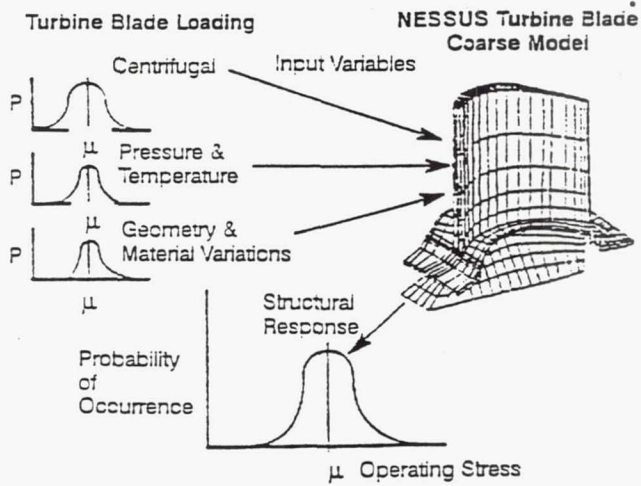
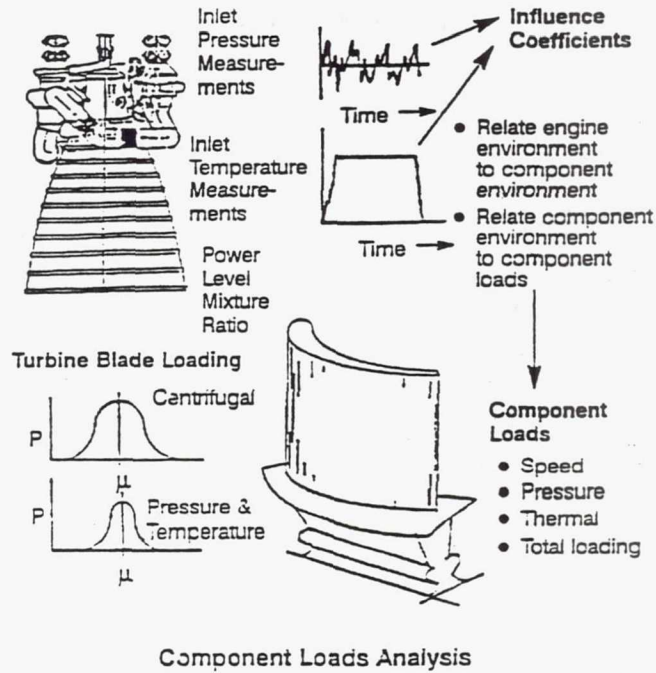
ture to supply simulated probabilistic loads as input to a structural analysis. With the correlated input loads, a probabilistic structural analysis code such as the Probabilistic Structural Analysis Method (PSAM) project's NESSUS can calculate sensitivity information and response distributions of stresses, strains, etc. as functions of engine hardware and operating parameters. Knowledge of this information is better help the design of rocket engine and guide test data requirements and analysis.

Component load models such as static pressure loads and temperature loads were developed as part of the basic CLS contract work. Recent work on the CLS project has emphasized development of generic physical models for loads where no physical models were available, such as acoustic (perturbated flow) related loads. The reason for this emphasis is that during the development phase of the SSME engine the lack of models for the high-energy flow conditions in both propellant and hot-gas systems allowed designs that caused significant problems. An acoustic flow system model (Figure 5) is under development to better define the engine dynamic fluid loads. It has an overall framework for a full system model, but is currently limited to the components applicable to the CLS project. The model is divided into elements; the acoustic waves undergo continuous reflections and transmissions at the element boundaries. The system can have noise sources from elbows (Figure 6), pumps, combustors, valves, etc. The individual sources propagate through system elements acoustically. By superimposing the contributions from all waves passing through a given point in the system, the pressure and velocity at that point can be obtained as a function of time. The pipe bend elbow or flow turning noise model is a good example of a generic flow load model. Acoustic loads are key loads on all four components evaluated by CLS - turbine blade, LOX post, transfer duct and engine system duct.

Another significant effort is the development of a fluid-structural based scaling model to address mechanical vibration as a forced response to fluid loading (Figure 7) rather than a simplistic scaling from overall engine power - the Barrett's approach. This new approach is much more generic and shows real promise in allowing significant better definition of the mechanical vibration environments (Figure 8). When validated, it should be a major improvement to either deterministic or probabilistic load definition. Application of the pressure fluctuation model and the vibration model to rocket engine components is currently underway under production contract work and is being reported in another presentation in this conference.

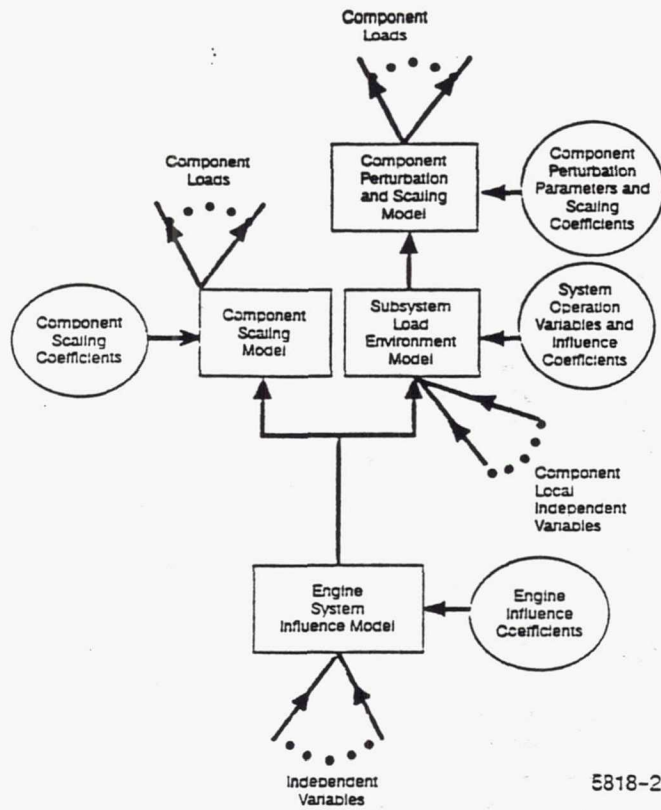
CLS Applications

Applications of the CLS load simulation to component probabilistic structural analysis have been carried out over the years in conjunction with the PSAM project. The most recent ones are the LOX post full cycle thermal strain analysis and the Advanced Launch System (ALS) main combustion chamber (MCC) liner analysis. Details of these efforts are discussed in other talks in this session.



Component Response Analysis 5818-1

Figure 1. Integrated Loads and Response Analysis.



5818-2

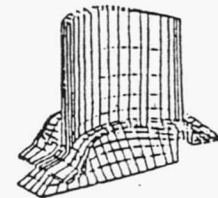
Figure 2. Multi-level Engine Model.

Independent Variables

- Mixture ratio
- Pump cavitation
- Engine inlet
 - Pressures
 - Temperatures

Composite Loads For Each Random Variable

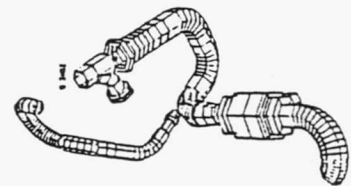
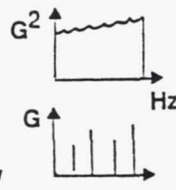
- Pressure
- Temperature
- Speed



Engine Variations

Independent Variables

- Pump power - G
- Engine power - B
- Pump speed



Hardware Variation

Independent Variable

- Heat shield gap

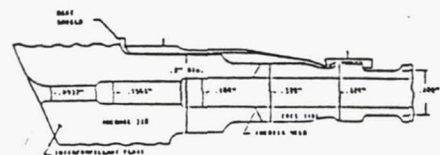
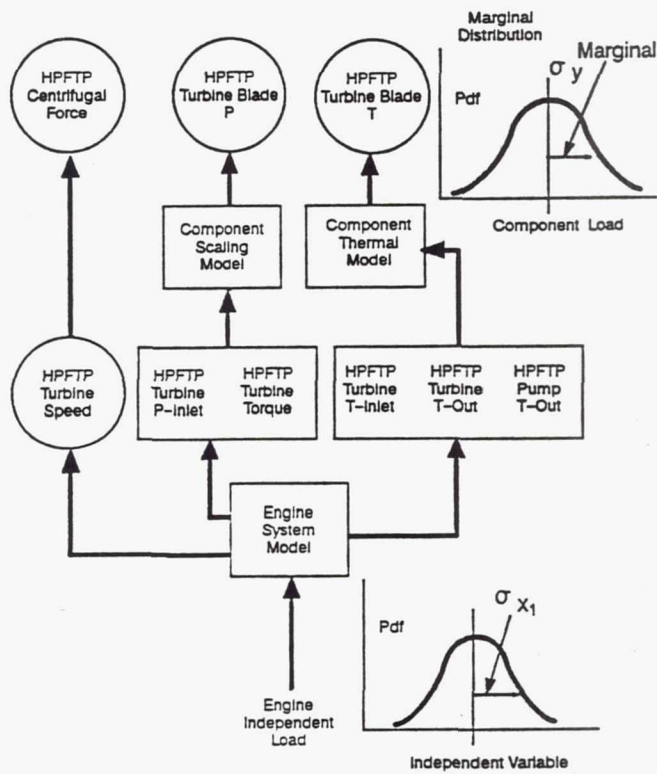


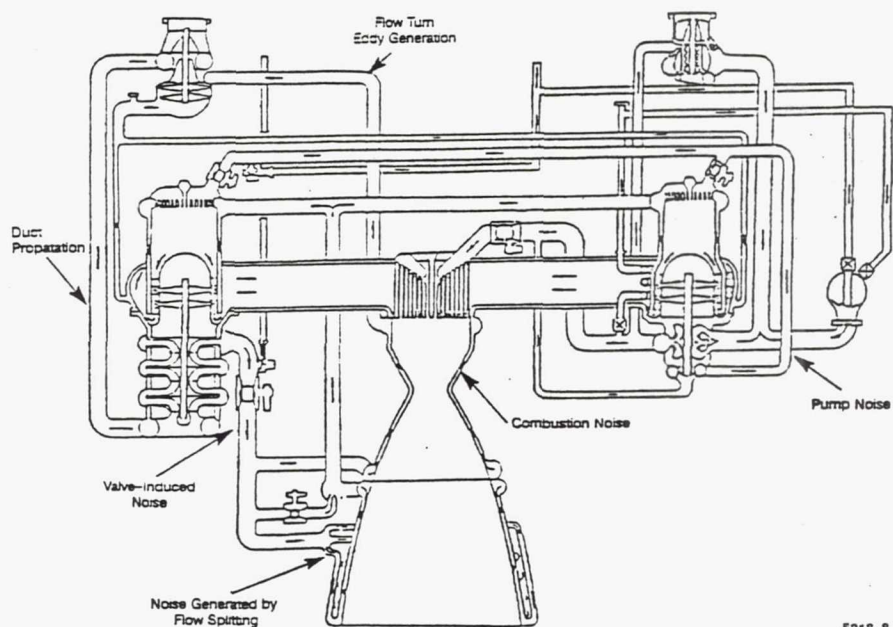
Figure 3. Examples of System, Subsystem and Component Loads.

89c-4-346-5



5818-4

Figure 4. Turbine-Blade Load Component Diagram, showing how a system load spreads throughout all component loads.



5818-8

Figure 5. Flow System Model.

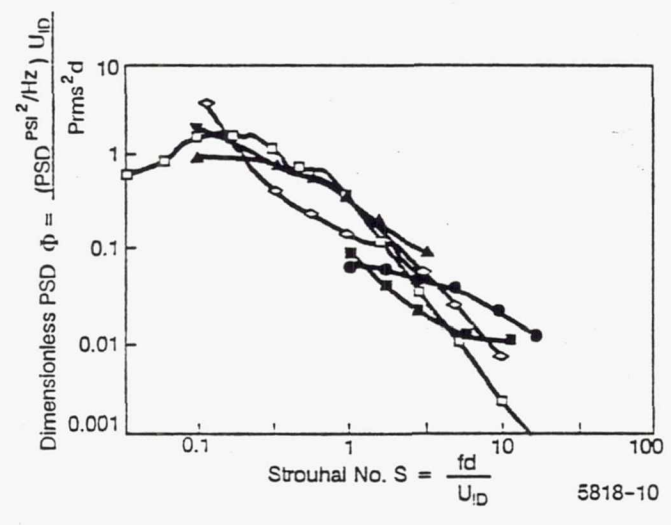
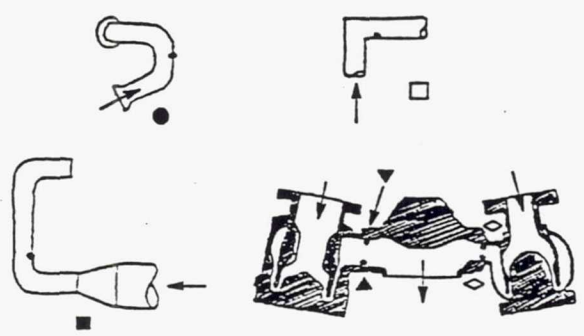


Figure 6. Dimensionless Power Spectral Density for Different Turned Flows.

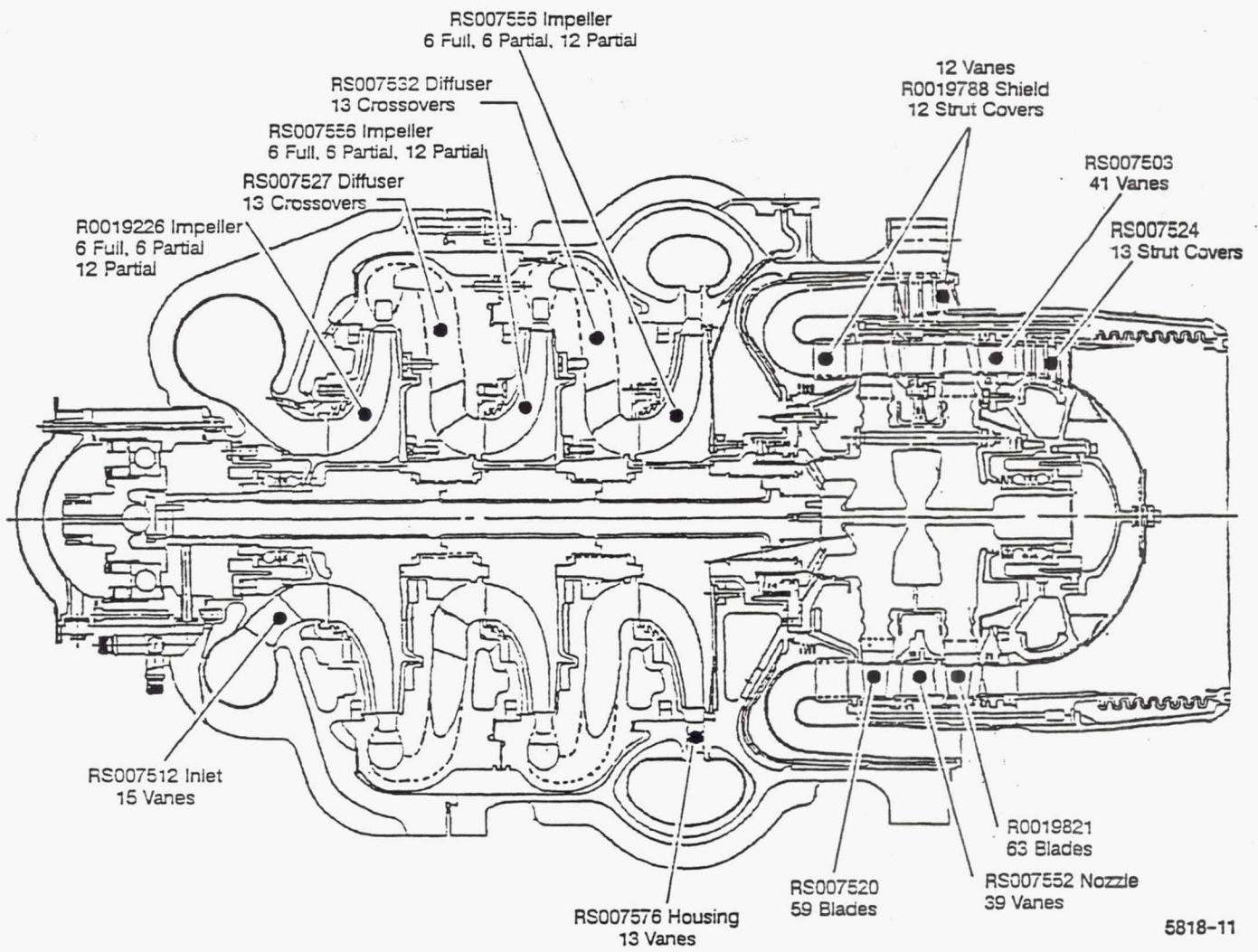
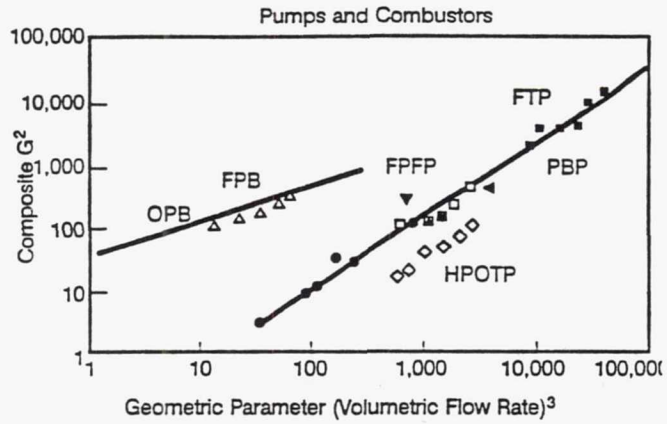
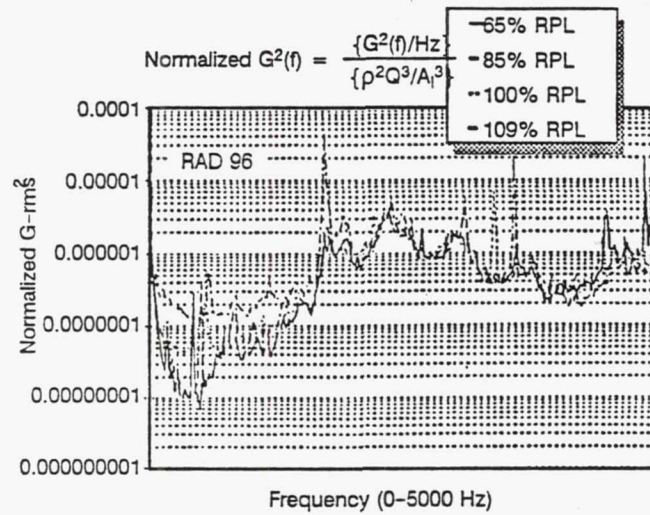


Figure 7. Example Turbopump, showing flow Interruption Drivers and Flow Paths used to calculate fluid power parameters.



a. Fluid Mechanisms Scaling Composite Levels



b. Fluid Mechanisms Scaling Pump Spectra

5818-12

Figure 8. Engine Vibration Scaling Based on Fluid Power Variables.

PROBABILISTIC EVALUATION OF SSME STRUCTURAL COMPONENTS

K.R. Rajagopal, J.F. Newell, and H. Ho
Rockwell International Corp.
Rocketdyne Division
Canoga Park, California 91303

INTRODUCTION

This paper describes the application of CLS and NESSUS family of computer codes to the probabilistic structural analysis of four SSME space propulsion system components. These components are subjected to environments that are influenced by many random variables. The applications consider a wide breadth of uncertainties encountered in practice, while simultaneously covering a wide area of structural mechanics. This has been done consistent with the primary design requirement for each component. This paper discusses the probabilistic application studies using finite element models that have been typically used in the past in deterministic analysis studies.

PROBABILISTIC TURBINE BLADE STATIC AND MODAL ANALYSIS

A high pressure fuel turbopump turbine blade was considered in this study (Figure 1). A total of nineteen random variables were considered in the analysis (Table 1) covering a wide range of parameters encountered in a practical production situation. Results of the analysis predicting expected variation in effective stress response at two different locations is shown Figure 2 and Figure 3 along with the sensitivity factors which are different at each location. This application demonstrates that large scale probabilistic static analysis is feasible and provides valuable information in the form of sensitivities that can help in designing more durable components. (Reference 1).

A knowledge of the variations in the frequencies of the first few modes of a turbine blade is of importance to avoid resonance conditions. Knowing the distribution of the frequencies and speed ranges it is possible to obtain quantitative probability estimates of interference with engine orders. The first ten variables listed in Table 1 were used in this probabilistic analysis.

The results from a mean value first order and the more accurate advanced mean value first order results are shown in Figure 4 for mode 1. It points out the unsymmetrical nature of the distribution and the capability of the probabilistic tools in predicting it. The computed coefficient of variation of the natural frequencies is consistent with the actual experience. If the frequency range is a criteria for acceptance or rejection of blades this analysis technics can then be used to calculate a

target design point that will reduce the rejection rate (Reference 2).

VIBRATION ANALYSIS OF DUCTS SUBJECTED TO UNCERTAIN LOADS

The high pressure oxidizer turbopump discharge duct is used in this study (Figure 5). The duct has three attach points subjected to both random and sinusoidal vibration, a multisupport excitation problem. The variation in the vibratory loads is attributed to engine system duty cycle operation, engine system hardware variations, and local component variations within the turbopump or combustors. A total of thirty eight random variables were used in this analysis (Table 2). A typical result obtained in the form of a cumulative distribution function at a typical node for bending moment in the y direction is shown in Figure 6. The analysis points to a way of designing structures subjected to a large number of excitation sources without exercising undue conservatism (Reference 3).

PROBABILISTIC MATERIAL NONLINEAR ANALYSIS OF LOX POST

A main injector element of SSME is used in this study (Figure 7). The response variable of interest is the cyclic strain range (including the elastic and plastic portions of the stress strain curve). This response quantity is one of the primary drivers in determining Low Cycle Fatigue life of the component. The dominant loading on the component is the differential wall temperature across the Lox Post wall of approximately 1000 degrees rankine. It was the only loading considered in this analysis.

The random variables that affect the local temperature field are shown in Table 3. The probabilistic analysis involved a full two duty cycle incremental nonlinear analysis and constructing a response surface linking effective strain range to random variables. The probabilistic analysis results based on the response surfaces at several locations are shown in Table 4 and the corresponding sensitivity factors in Table 5. The analysis demonstrates a methodology of linking global system variables to local response variables that can eventually be extended to calculate damage, all in a probabilistic domain (Reference 4).

PROBABILISTIC BUCKLING LOAD ANALYSIS

The structural liner in the SSME two duct hot gas manifold design was the subject of this study. The shell is doubly curved with five distinct zones of thicknesses (Figure 8). One of the primary design requirement for the liner is to have adequate margin against buckling failure. Unlike the previous examples cited above this application deals with estimation of the strength variable. As a first step in this process a probabilistic linear buckling analysis was

conducted. A more rigorous material and geometric probabilistic collapse load analysis would be more accurate but the computational effort will also be significantly larger.

In this study the thickness in the five zones of the shell were considered as independent random variables but within each zone, the thickness variation was considered to be fully correlated. The probabilistic analysis method used is a response surface approach. The resulting computed cumulative distribution function is shown in Figure 9. Thus knowing the distribution of the buckling strength and the distribution of differential pressure the probability of buckling failure based on the linear eigen value analysis can easily be calculated.

SUMMARY

Application of the probabilistic analysis tools developed in CLS AND PSAM contracts to a select SSME components has been successfully demonstrated. The scope and size of the application prove the viability and usefulness of the tools and methods developed to practical design in terms of designing more durable components.

REFERENCES

1. Newell, J.F., Rajagopal, K.R., and Ho.H., " Probabilistic Structural Analysis of Space Propulsion System Turbine Blade", 30th AIAA Structures, Structural Dynamics and Materials Conference, Mobile, Alabama, April 1989.
2. Southwest Research Institute, University of Arizona, Rocketdyne, and Joao B.Dias, " Probabilistic Structural Analysis For Select Space Propulsion System Components ", 4th Annual Report, October 1988.
3. DebChaudhury, A., Rajagopal, K.R., Ho.H., and Newell, J.F., "A Probabilistic Approach to the Dynamic Analysis of Ducts Subjected to Multibase Harmonic and Random Excitation", 31st AIAA structures, Structural Dynamics, and Materials Conference, LongBeach, California, April 1990.
4. Newell, J.F., Rajagopal, K.R., Ho.H., and Cunniff, J.M., "Probabilistic Structural Analysis of Space Propulsion System Lox Post", 31st AIAA Structures, Structural Dynamics, and Materials Conference, LongBeach, California, April 1990.
5. Southwest Research Institute, University Of Arizona, Rocketdyne, and Joao B.Dias, " Probabilistic Structural Analysis Methods For Select Space Propulsion System Components", 5th Annual Report, October 1989.

TABLE I
LIST OF RANDOM VARIABLES USED IN
TURBINE BLADE ANALYSIS

| RANDOM VARIABLE NO | DESCRIPTION | TYPE | FEM QUANTITIES AFFECTED | MEAN | STANDARD DEVIATION | |
|--------------------|--|-----------------------------|-------------------------|------------------------------|-------------------------------|---------------------------|
| 1 | MATERIAL AXIS ABOUT Z | MATERIAL AXIS VARIATIONS | MATERIAL | -0.087266 RADIANS | 0.067544 RADIANS | |
| 2 | MATERIAL AXIS ABOUT Y | | ORIENTATION | -0.034907 RADIANS | 0.067544 RADIANS | |
| 3 | MATERIAL AXIS ABOUT X | | ANGLES | +0.052360 RADIANS | 0.067544 RADIANS | |
| 4 | ELASTIC MODULUS | ELASTIC PROPERTY VARIATIONS | ELASTIC CONSTANTS | 18.38E6 PSI (126.22E9 Pa) | 0.4595E6 PSI (3.168E9 Pa) | |
| 5 | POISSON'S RATIO | | | 0.386 | 0.00965 | |
| 6 | SHEAR MODULUS | | | 18.63E6 PSI (128.45E9 Pa) | 0.46575E6 PSI (3.223E9 Pa) | |
| 7 | MASS DENSITY | MASS VARIATIONS | MASS | 0.805E-3 | 0.493E-5 | |
| 8 | GEOMETRIC LEAN ANGLE ABOUT X | GEOMETRY VARIATIONS | NODAL | 0.0 | 0.14 DEGREES | |
| 9 | GEOMETRIC TILT ANGLE ABOUT Y | | COORDINATES | | 0.0 | 0.14 DEGREES |
| 10 | GEOMETRIC TWIST ANGLE ABOUT Z | | | | 0.0 | 0.30 DEGREES |
| 11 | MIXTURE RATIO LIQUID HYDROGEN/ LIQUID OXYGEN | INDEPENDENT LOAD | | 6.00 | 0.02 | |
| 12 | FUEL INLET PRESSURE | DEPENDENT LOADS ARE | PRESSURE | 30.00 PSI (2.068E5 Pa) | 5.00 PSI (.344E5 Pa) | |
| 13 | OXIDIZER INLET PRESSURE | | | TEMPERATURE | 100.00 PSI (6.894E5 Pa) | 26.00 PSI (1.793E5 Pa) |
| 14 | FUEL INLET TEMPERATURE | TURBINE BLADE | CENTRIFUGAL | 38.5° R (21.39° K) | 0.5° R (0.278° K) | |
| 15 | OXIDIZER INLET TEMPERATURE | | PRESSURE TEMPERATURE | LOAD | 167.0° R (92.78° K) | 1.33° R (0.739° K) |
| 16 | HPFP EFFICIENCY | AND SPEED | | 1.00 | 0.008 | |
| 17 | HPFP HEAD COEFFICIENT | | | | 1.0237 | 0.008 |
| 18 | COOLANT SEAL LEAKAGE FACTOR | LOCAL GEOMETRY | TEMPERATURE | 1.00 | 0.1 | |
| 19 | HOT GAS SEAL LEAKAGE FACTOR | FACTORS | | | 1.0 | 0.5 |

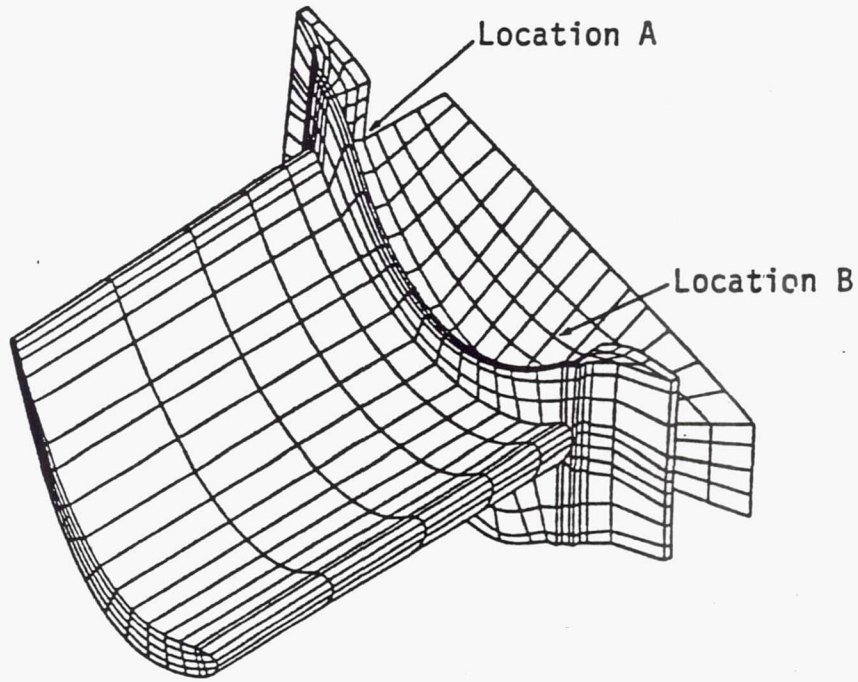


Figure 1. Turbine Blade Finite Element Model

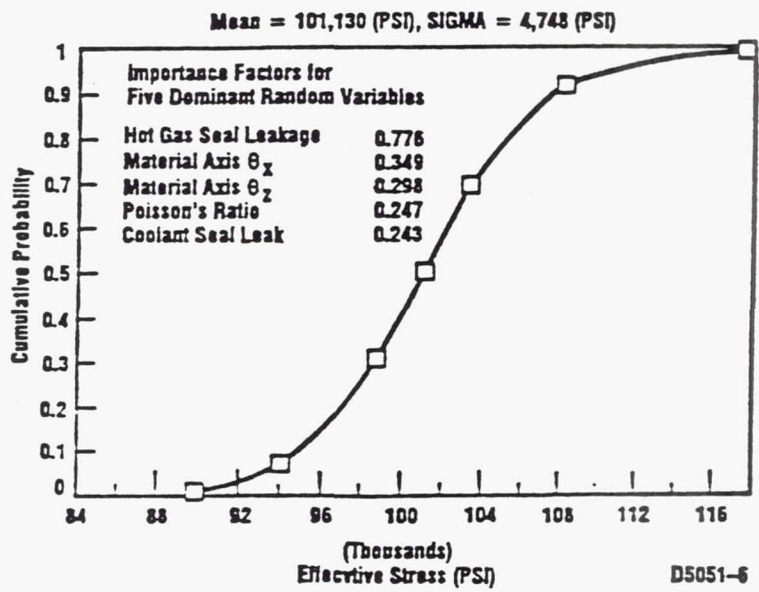


Figure 2. CDF For Effective Stress at Location A

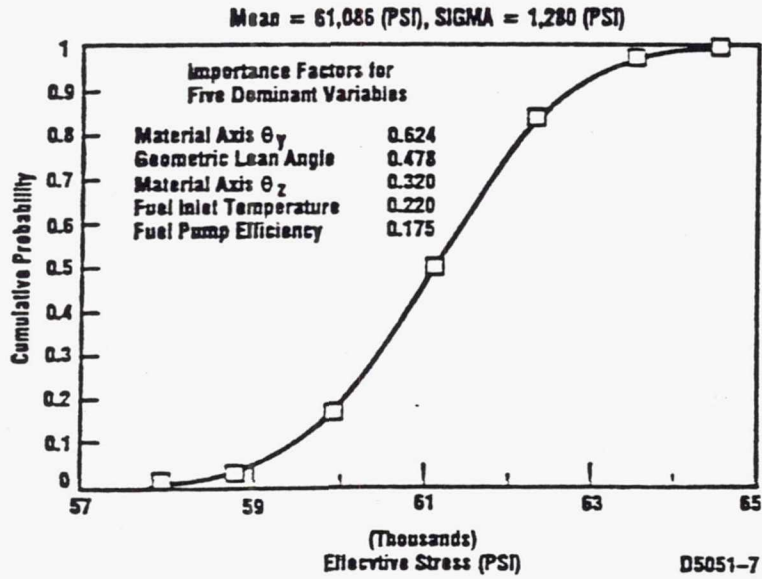


Figure 3. CDF For Effective Stress at Location B

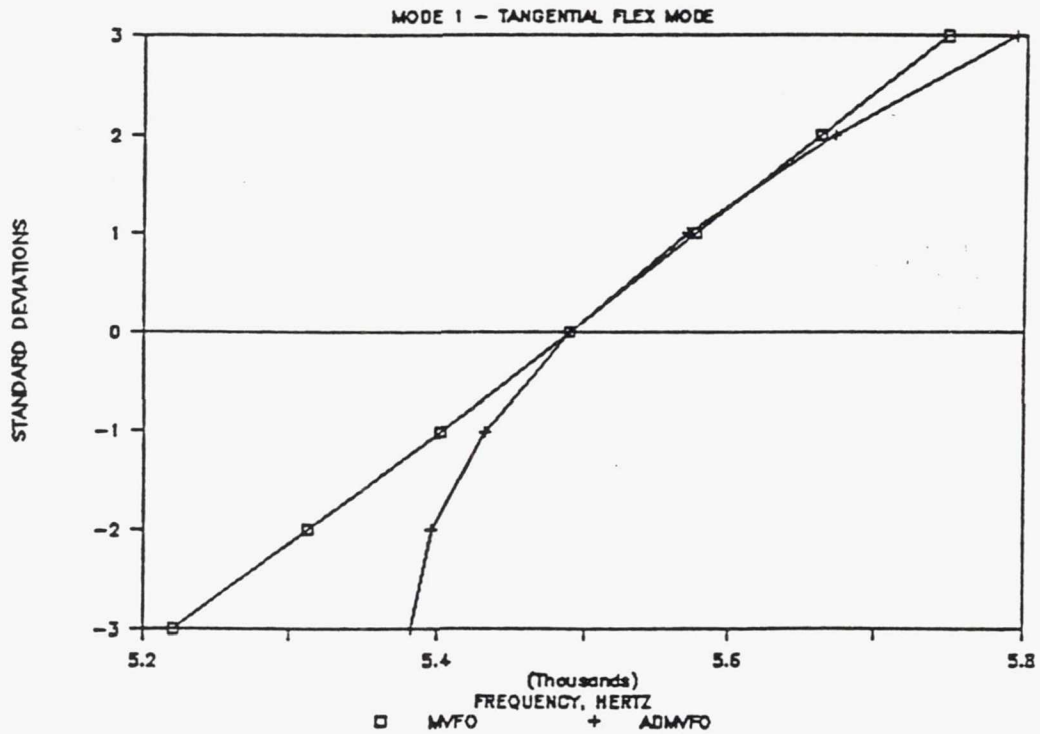


Figure 4. CDF For Mode 1 Frequency Using MVFO and ADMVFO

**Table 2. HPOTP Discharge Duct Analysis
Random Variable Statistics**

| Sequence No. | Random Variable Description | Mean | CV | Dist. Type |
|--------------|-------------------------------|---------|-------|------------|
| 1) | Zone G - X axis, PSD power | 222.0 | 0.73 | Log Normal |
| 2) | Zone G - Y axis, PSD | 73.5 | 0.808 | Log Normal |
| 3) | Zone G - Z axis, PSD | 73.5 | 0.808 | Log Normal |
| 4) | Zone A - X axis, PSD | 22.5 | 0.20 | Log Normal |
| 5) | Zone A - Y axis, PSD | 54.0 | 0.20 | Log Normal |
| 6) | Zone A - Z axis, PSD | 69.5 | 0.2 | Log Normal |
| 7) | Oxidizer Pump Speed | 2940.53 | 0.014 | Log Normal |
| 8) | Fuel Pump Speed | 3707.08 | 0.01 | Log Normal |
| 9) | Damping | 0.033 | 0.15 | Normal |
| | Zone A Main Injector | | | |
| | Oxidizer Pump Sine Amplitudes | | | |
| 10) | X direction 1N | 0.30 | 0.4 | Log Normal |
| 11) | 2N | 0.30 | 0.15 | Log Normal |
| 12) | 4N | 1.5 | 0.3 | Log Normal |
| 13) | Y direction 1N | 0.60 | 0.5 | Log Normal |
| 14) | 2N | 0.70 | 0.40 | Log Normal |
| 15) | 4N | 2.6 | 0.3 | Log Normal |
| 16) | Z direction 1N | 0.5 | 0.45 | Log Normal |
| 17) | 2N | 0.70 | 0.20 | Log Normal |
| 18) | 4N | 0.70 | 0.20 | Log Normal |
| | Fuel Pump Sine Amplitudes | | | |
| 19) | X Direction 1N | 0.35 | 0.3 | Log Normal |
| 20) | Y Direction 1N | 0.80 | 0.35 | Log Normal |
| 21) | Z Direction 1N | 1.20 | 0.3 | Log Normal |
| | Zone G - Oxidizer Turbopump | | | |
| | Oxidizer Pump Sine Amplitudes | | | |
| 22) | X Direction 1N | 1.35 | 1.0 | Log Normal |
| 23) | 2N | 1.50 | 0.5 | Log Normal |
| 24) | 3N | 1.10 | 0.45 | Log Normal |
| 25) | 4N | 11.0 | 0.25 | Log Normal |
| 26, 27) | Y&Z Direction 1N | 1.9 | 0.9 | Log Normal |
| 28, 29) | 2N | 1.6 | 0.6 | Log Normal |
| 30, 31) | 3N | 0.75 | 0.3 | Log Normal |
| 32, 33) | 4N | 5.5 | 0.6 | Log Normal |
| | Fuel Pump Sine Amplitudes | | | |
| 34) | X Direction 1N | 0.65 | 0.35 | Log Normal |
| 35, 36) | Y&Z Direction 1N | 0.45 | 0.4 | Log Normal |
| 37, 38) | Y&Z Direction 2N | 0.45 | 0.4 | Log Normal |

Note: 1) Power units are in g^2
 2) Pump speed units are in radians/second
 3) Sinusoidal amplitude units are in g

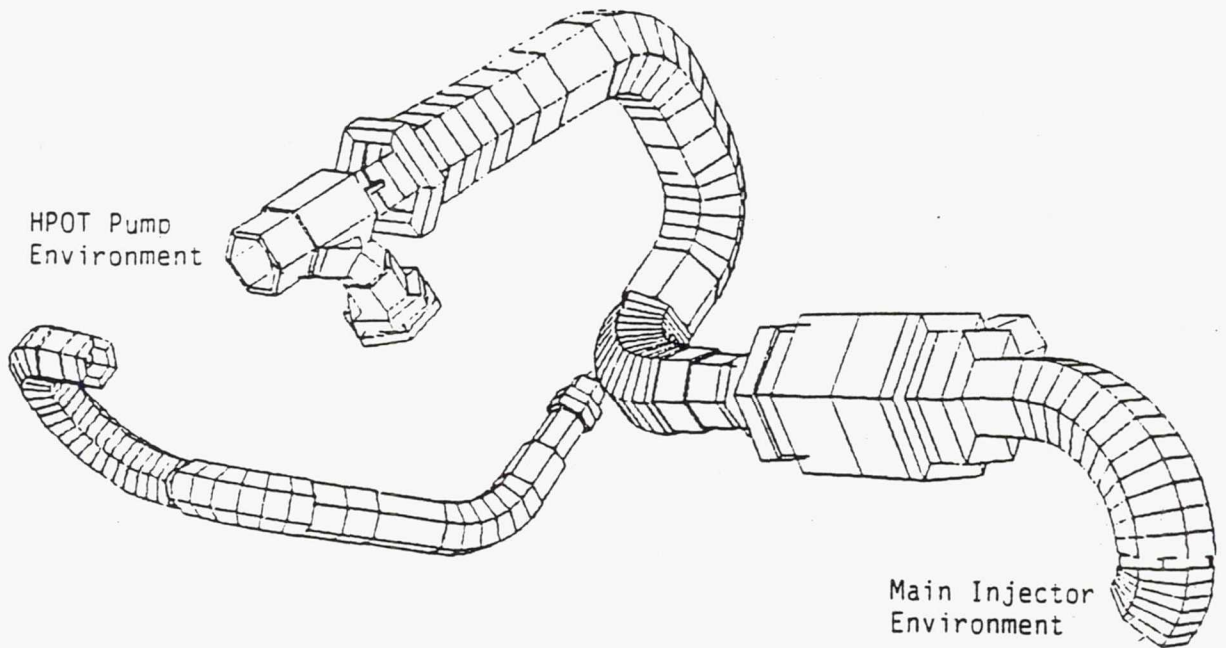


FIGURE 5. DUCT MODEL WITH ELBOWS, VALVES, ATTACHMENTS AND SECONDARY LINES.

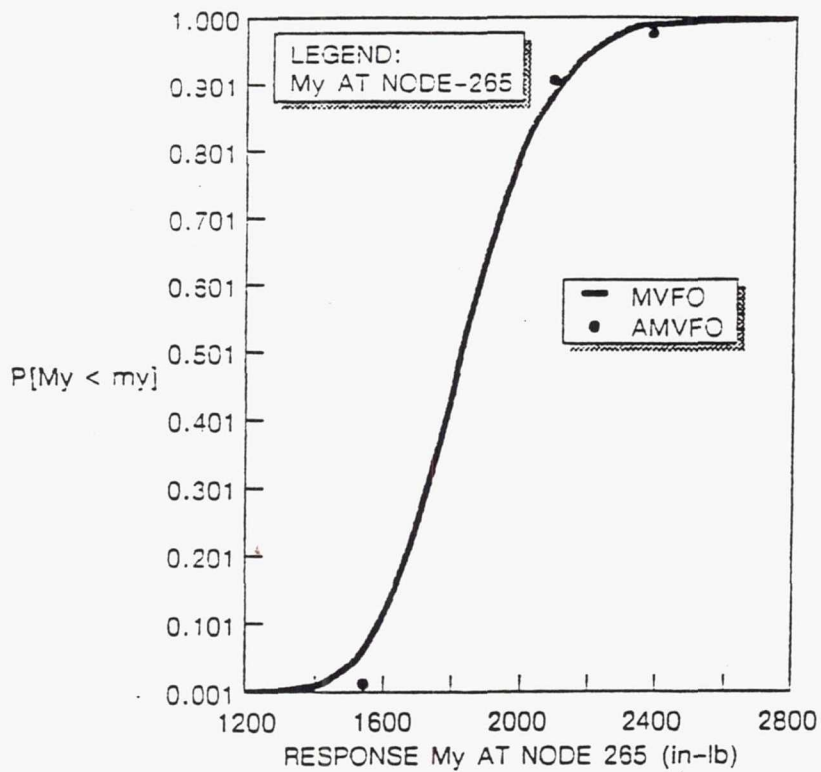
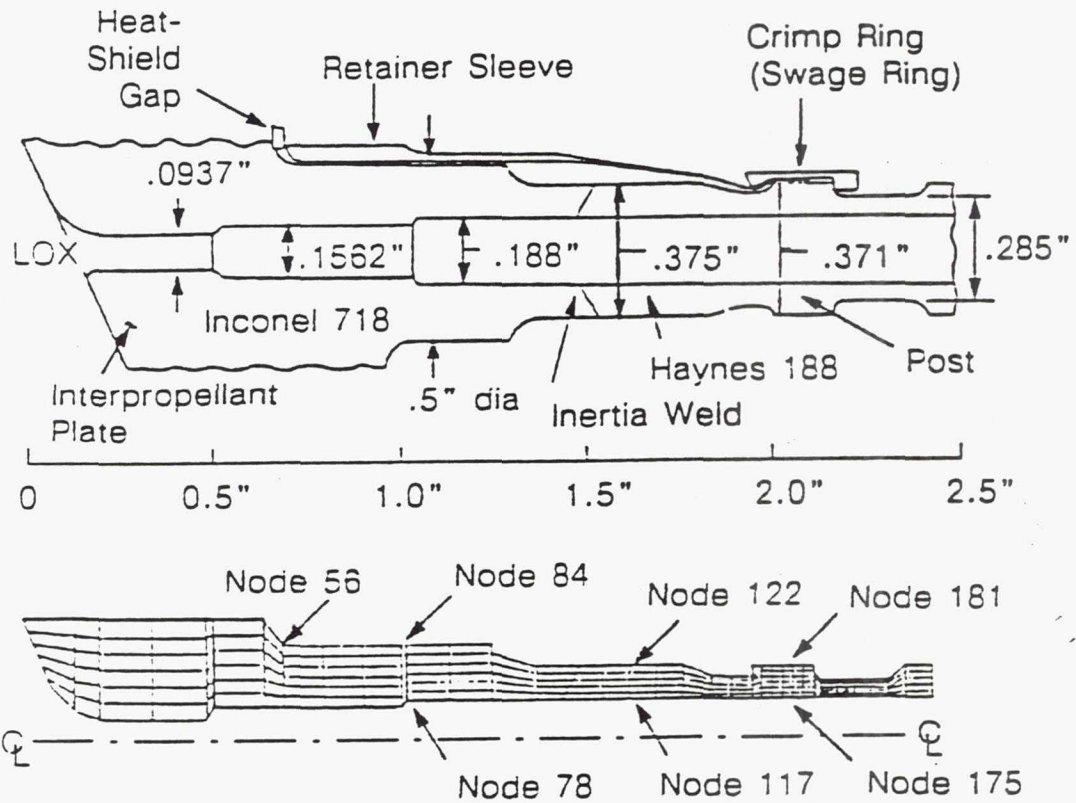


FIGURE 6. CDF OF A RESPONSE BASED ON MVFO AND AMVFO METHODS.



LOX-Post Axisymmetric Model

FIGURE 7. LOX POST AND ITS AXISYMMETRIC FINITE ELEMENT MODEL.

TABLE 3
RANDOM VARIABLES USED IN LOX-POST ANALYSIS

| Random Variable | Mean | Standard Deviation | Distribution |
|-----------------------------|----------|--------------------|--------------|
| Material yield stress (ksi) | 175.0 | 8.75 | Normal |
| Hot-gas temperature (R) | 1654.70 | 26.6407 | Normal |
| Coolant temperature (R) | 191.643 | 4.21019 | Normal |
| Hot-gas flowrate (lbm/sec) | 167.249 | 1.0928 | Normal |
| Coolant flowrate (lbm/sec) | 929.918 | 4.31211 | Normal |
| Mixture ratio | 0.948012 | 0.0184211 | Normal |
| Heat-shield-gap factor | 0.47 | 0.235 | Lognormal |
| Hot-gas film coefficient | 1.0 | 0.1 | Normal |
| Coolant film coefficient | 1.0 | 0.08 | Normal |

TABLE 4
SUMMARY STATISTICS FOR EFFECTIVE STRAIN RANGE
FOR THE LOX POST

| Node | Median | Mean | Standard Deviation | Coefficient of Variation |
|------|----------|----------|--------------------|--------------------------|
| 56 | 0.004143 | 0.004821 | 0.0002613 | 0.054 |
| 78 | 0.006759 | 0.008360 | 0.0002275 | 0.027 |
| 84 | 0.002114 | 0.004175 | 0.0001661 | 0.040 |
| 117 | 0.002990 | 0.004757 | 0.0001454 | 0.031 |
| 122 | 0.001186 | 0.003831 | 0.0001473 | 0.038 |
| 175 | 0.002949 | 0.005135 | 0.0001430 | 0.028 |
| 181 | 0.002296 | 0.002401 | 0.00006408 | 0.027 |

TABLE 5
SENSITIVITY* FACTORS FOR THE EFFECTIVE
STRAIN RANGE FOR THE LOX POST

| Random Variable | Node 56 | Node 78 | Node 84 | Node 117 | Node 122 | Node 175 | Node 181 |
|--------------------------|---------|---------|---------|----------|----------|----------|----------|
| Hot-gas temperature | 0.455 | 0.796 | 0.771 | 0.802 | 0.793 | 0.860 | 0.786 |
| Coolant temperature | 0.014 | 0.026 | 0.024 | 0.023 | 0.023 | 0.019 | 0.022 |
| Hot-gas flowrate | 0.062 | 0.075 | 0.111 | 0.070 | 0.074 | 0.045 | 0.108 |
| Coolant flowrate | 0.000 | 0.003 | 0.002 | 0.002 | 0.002 | 0.001 | 0.003 |
| Mixture ratio | 0.022 | 0.034 | 0.034 | 0.035 | 0.034 | 0.028 | 0.031 |
| Shield-gap factor | 0.793 | 0.115 | 0.071 | 0.028 | 0.003 | 0.011 | 0.017 |
| Hot-gas film coefficient | 0.399 | 0.587 | 0.620 | 0.590 | 0.603 | 0.507 | 0.605 |
| Coolant film coefficient | 0.002 | 0.031 | 0.042 | 0.024 | 0.026 | 0.005 | 0.052 |

*Range between 0 and 1. Larger values indicate a greater influence of the random variable on the response.

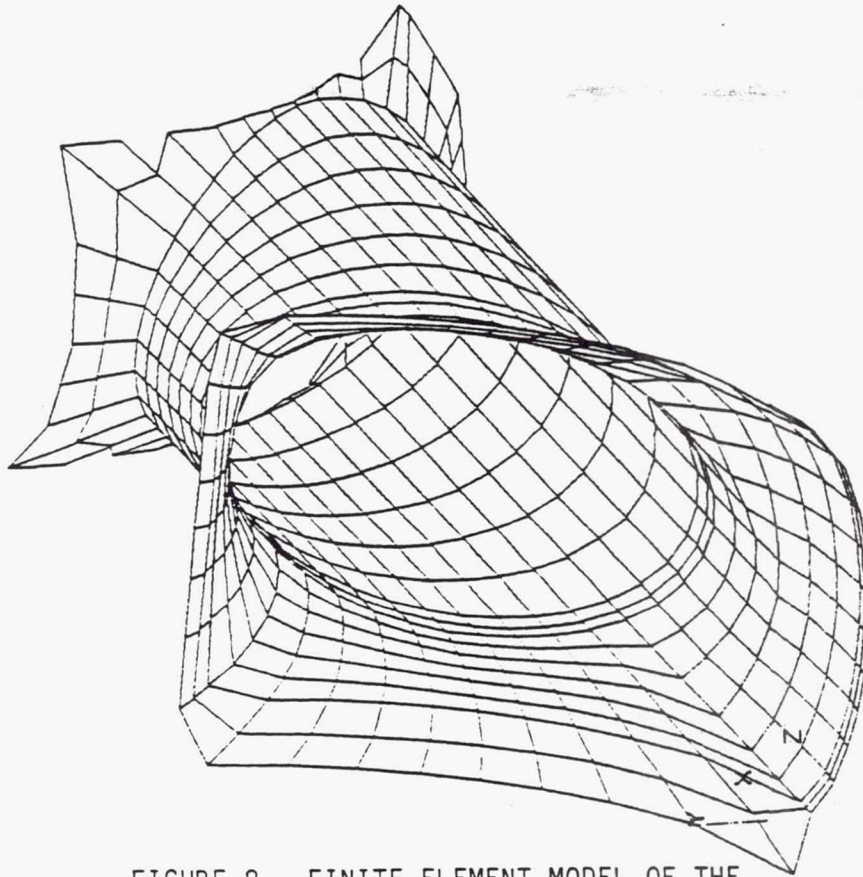


FIGURE 8. FINITE ELEMENT MODEL OF THE STRUCTURAL LINER.

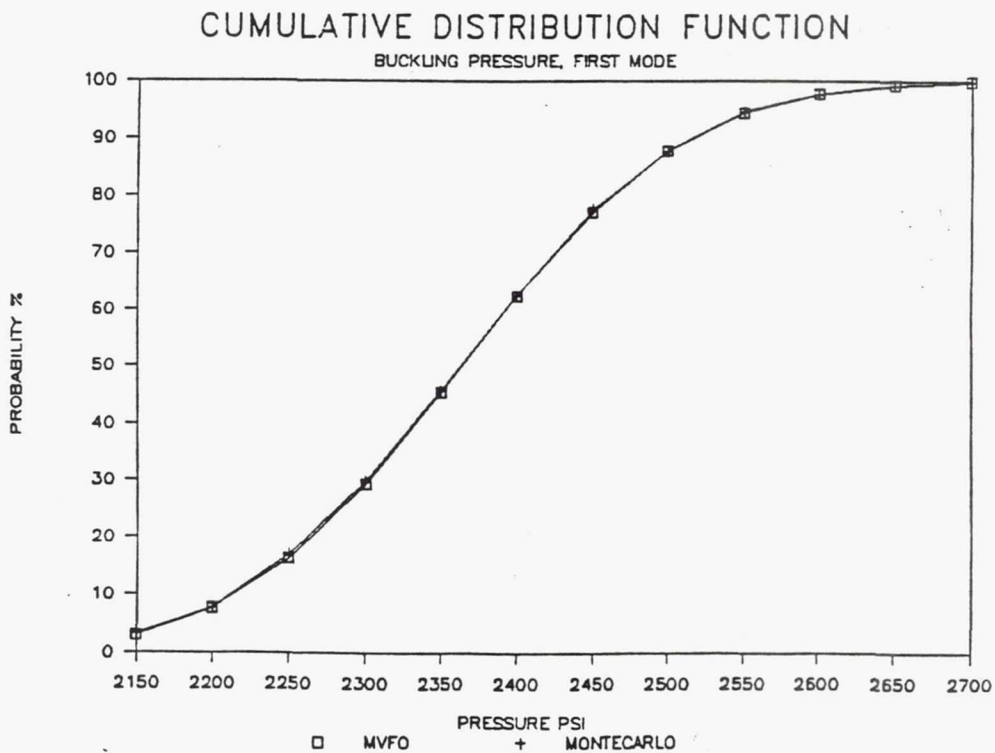


FIGURE 9. CDF OF THE FIRST BUCKLING MODE PRESSURE.

Page intentionally left blank

ROCKETDYNE PSAM - IN HOUSE ENHANCEMENT/APPLICATION

J.F. Newell, K.R. Rajagopal, and K. O'Hara
Rockwell International Corp.
Rocketdyne Division
Canoga Park, California 91303

Rocketdyne has embarked on the development of the Probabilistic Design Analysis (PDA) Process for Rocket engines. This will enable engineers a quantitative assessment of calculated reliability during the design process. The PDA will help choose better designs, make them more robust and help decide on critical tests to help demonstrate key reliability issues to aid in improving the confidence of the engine capabilities. Rocketdyne's involvement with the Composite Loads Spectra (CLS) and Probabilistic Structural Analysis Methodology (PSAM) contracts started this effort and are key elements in our on-going developments. Internal development efforts and hardware applications complement and extend the CLS and PSAM efforts. The completion of the CLS option work and the follow-on PSAM developments will also be integral parts of this methodology. A brief summary of these internal efforts to date follows.

METHODS/CODE DEVELOPMENTS

The CLS loads work has spawned method developments or extensions in thermal analysis and fluid dynamics. The CLS thermal loads approach addresses loading from a scaling of deterministic responses based on specific temperature variations of critical points or temperature profiles in the hardware for the key independent load variables. A more general methodology has been developed at Rocketdyne to allow a full scale probabilistic thermal analysis by essentially substituting the SINDA thermal code for the NESSUS FEM module along with its own modeling input techniques. This adds a general solution to the thermal problem for separate thermal assessments or as another tool for developing thermal models for CLS and NESSUS. (Figure 1).

The CLS acoustics loads work is limited to defining a generic systems modeling approach and developing specific modes for the components in the CLS study. The development of other source inputs and modeling elements like pumps, combustors and valves are needed to make such an overall systems model viable. In house work is addressing these needs as they arise for specific hardware problems as well as maturing the CLS developed acoustics source-propagations code.

Resistance models for Rocketdyne specific applications have been developed to allow reliability assessment for specific hardware and applications. These include models for strength, fatigue and fracture mechanics. Production oriented codes for preliminary design use have been developed to allow both sensitivity assessment and reliability calculations and also furnish a simple presentation of these results. (Figure 2)

PDA APPLICATIONS

The CLS, PSAM and in house developed methodologies are being used and tested against specific hardware and related tasks as they evolve. Examples of PDA applications include its use as: a evaluation tool to develop a criteria for flaw acceptance by dye penetrant for specific hardware (Figure 3); analysis of the accumulated fatigue damage for a turbopump bearing carrier; a turbopump

stator vane study to relate geometric tolerance variations to vane natural frequencies, engine duct analysis to determine acoustic transfer functions and fluctuation loads on elbows (Figure 4), and the development of a single flight reliability methodology basis using a reliability requirement.

Support to JPL's certification/reliability analysis of specific hardware components has also been accomplished on eight engine parts. This effort has also added to Rocketdyne's analysis capabilities for probabilistic damage assessment. A critical need to effectively use PDA is to calibrate this methodology against deterministic factor of safety approaches. Work in this area is an on-going effort at Rocketdyne (Figure 5).

RELIABILITY BASED DESIGN ANALYSIS

An overall approach on how to design for reliability is evolving at Rocketdyne. New engine programs such as ALS and NASP are planning on require quantitative reliability assessment of the engine during the design process. An initial design methodology has been developed and proposed for use on the ALS engine (Figure 6). An example of a combustion chamber liner was completed to demonstrate the use of this methodology. This effort included an FMEA, reliability allocation to specific hardware elements including the liner, the use of CLS to develop the loads and PSAM to evaluate the structural response and an in-house damage assessment code (Figure 7, 8, 9). The effort used the approximate modeling approach rather than a detail finite element assessment so that the work could focus on the overall methodology aspects.

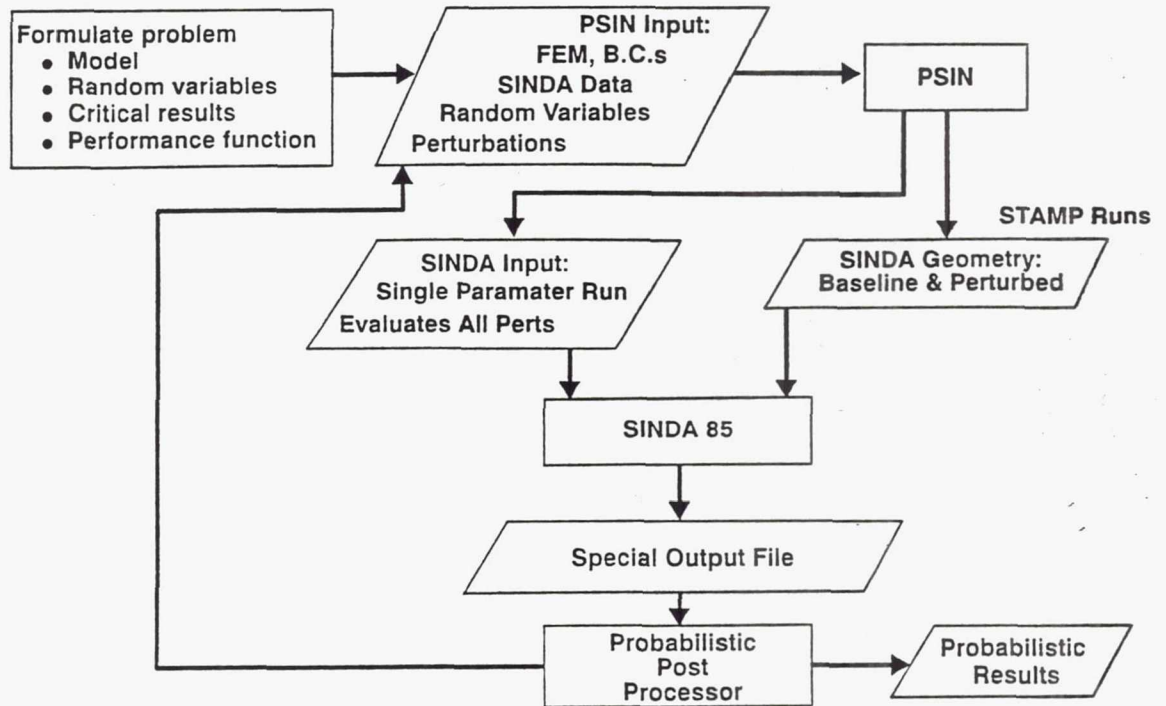
CHALLENGES

The main challenges are to move this technology from a research tool to a production tool and to further developments in the overall methodology. Calibration of PDA against deterministic methodologies is required to gain confidence in how to properly use and understand its application to hardware. Training analysts in its use and getting acceptance of PDA from program management and customers are further key efforts in integrating the technology to production hardware. Joint efforts between engineering, reliability, quality and manufacturing organizations are required to implement these techniques in new or on-going programs.

REFERENCES

1. Newell, J.F., Ho, H.O., Romine, W.D., Depsky, J.S., Rajagopal, K.R., Rocketdyne Division, Rockwell International Corporation, Canoga Park, California, "Probabilistic Design and Analysis Applied to Thermal Loading Environments and Thermal Responses", SAE 1991 Aerospace Atlantic Conference, Dayton, Ohio.
2. Newell, J.F., Ho, H.O., Rocketdyne Division, Rockwell International Corporation, Canoga Park, California, "Probabilistic Load Modeling for Rocket Turbomachinery Components", 3rd ASME-JSME Thermal Engineering Joint Conference and ASME-JSME JSES Solar Energy Conference, Reno, California.
3. O'Hara, K.J., Rockwell International Corporation, Canoga Park, California, "Liquid Propulsion System Reliability 'Design for Reliability'", AIAA/ASME/SAE/ASEE 25th Joint Propulsion Conference, Monterey, California.

Thermal Response Using Finite Element Model



91d-32-60
017

Figure 1. Sinda/Probabilistic Assessment Implementation.

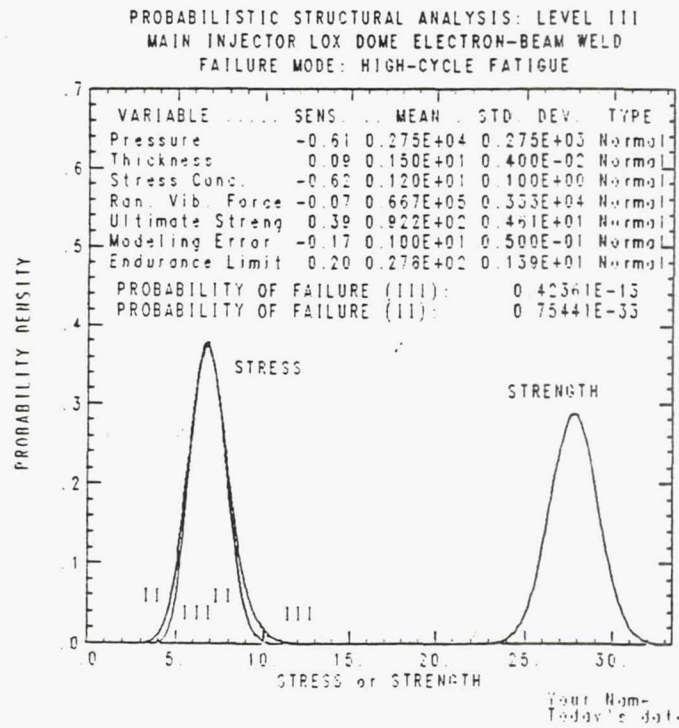


Figure 2. Example Levels-II and -III Results for PROBABILISTIC.

SIMULATION DESIGN

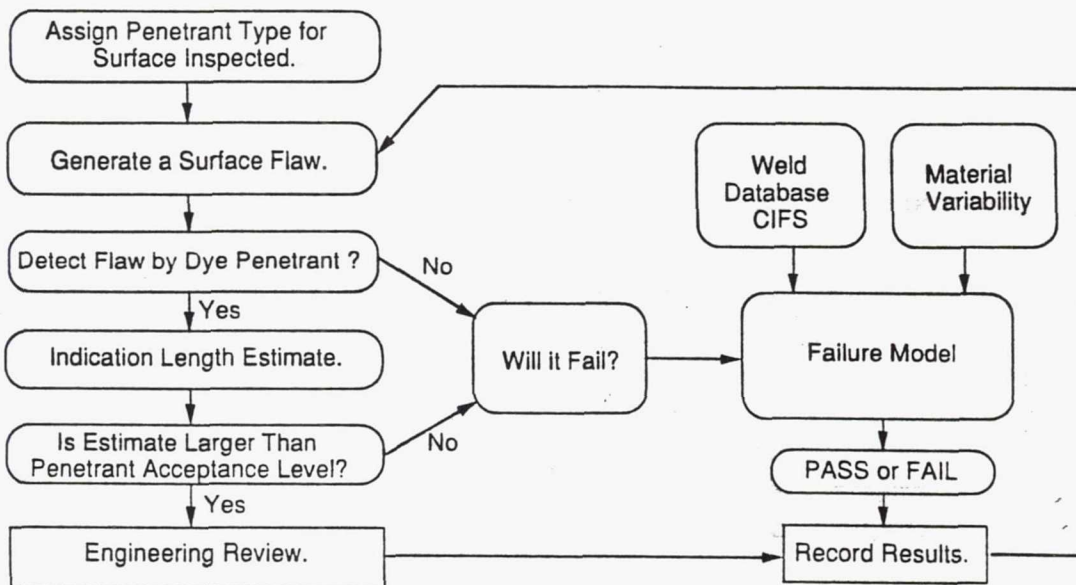
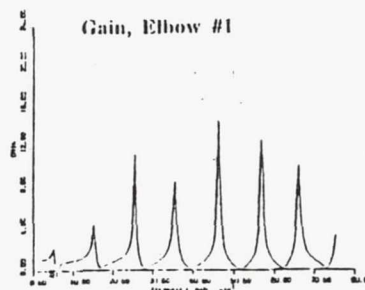
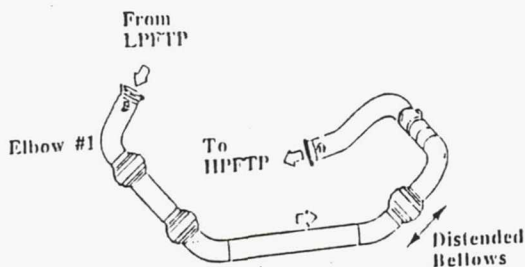


Figure 3. Flaw Acceptance by Dye - Penetrant Inspection.

NOISE PROPAGATION & ACOUSTIC MODES ANALYSIS

(C) Transfer Function Analysis: Gain & Phase

(i) Problem Diagnosis



(ii) Design Tool

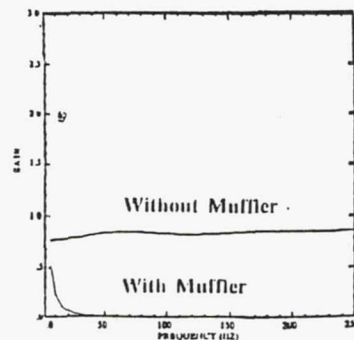
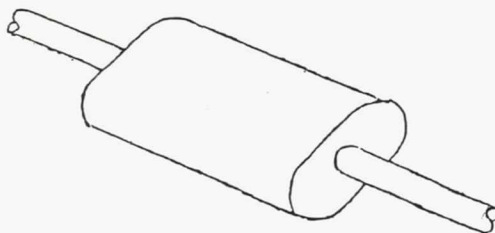
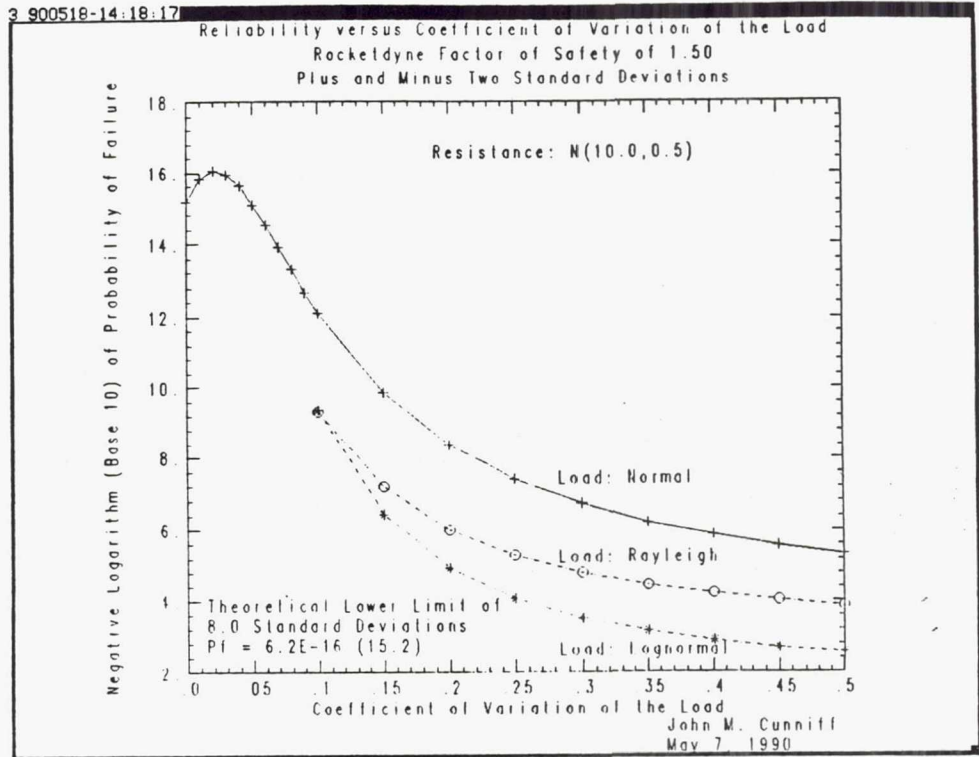


Figure 4. Duct Analysis Acoustic Transfer Function Analysis.

3 900518-14:18:17



3 900522-07:30:19

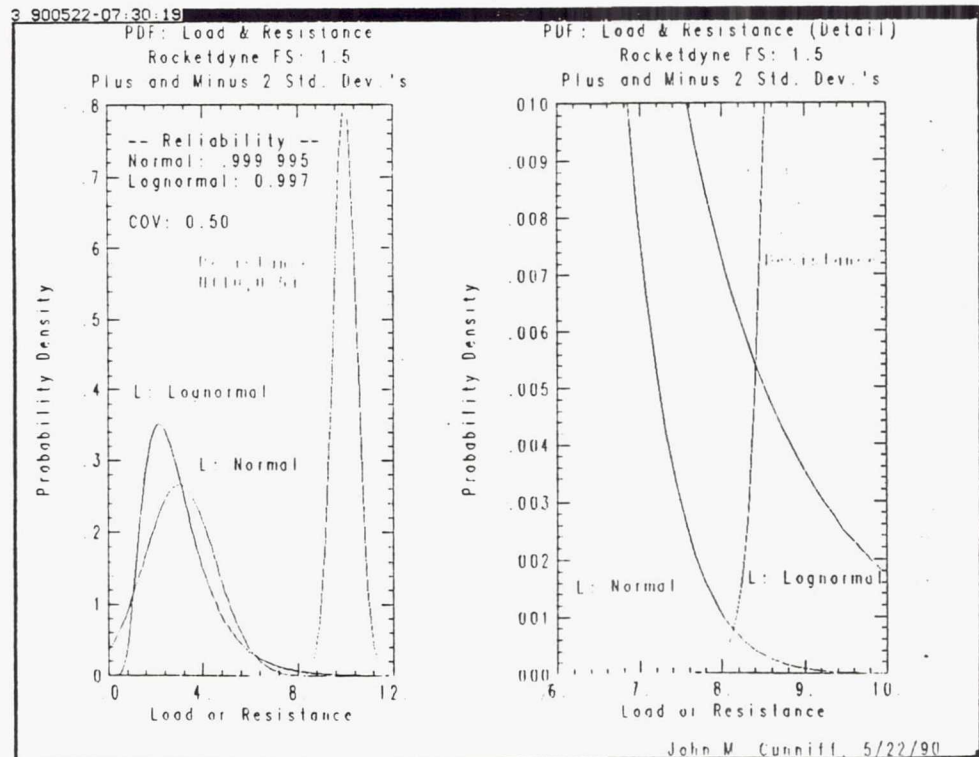
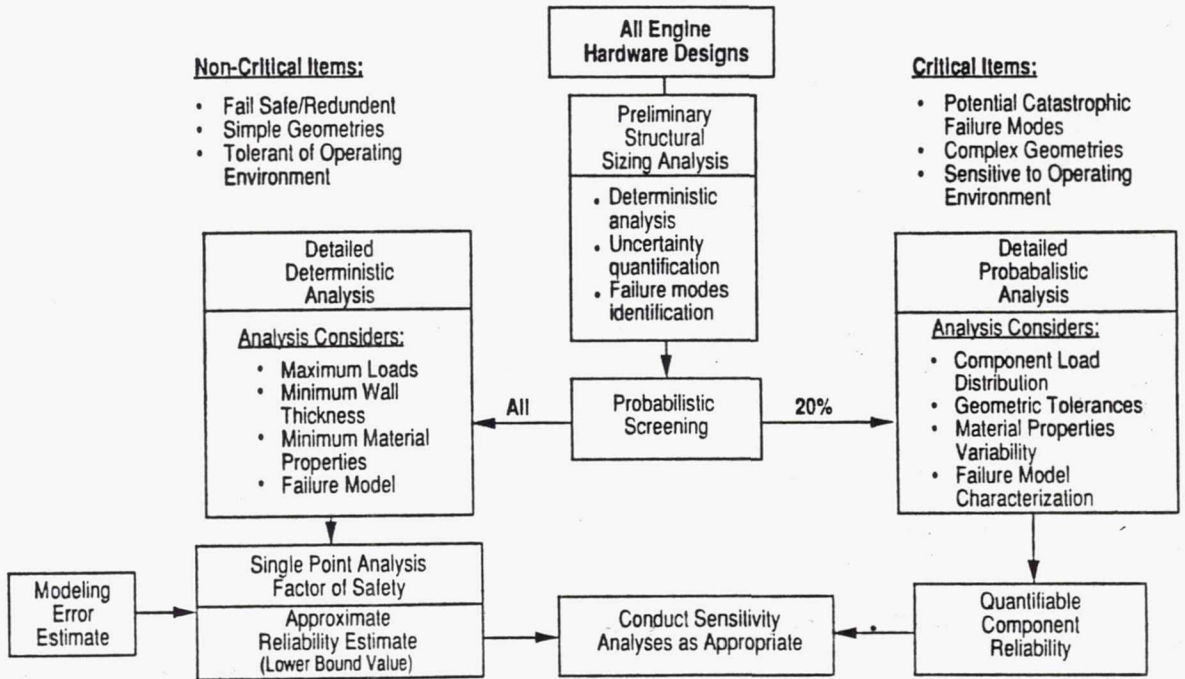


Figure 5. Reliability vs. Factor of Safety of 1.5.

DESIGN METHODOLOGY

Analysis Flow Schematic



PROBABILISTIC ANALYSIS METHODOLOGY

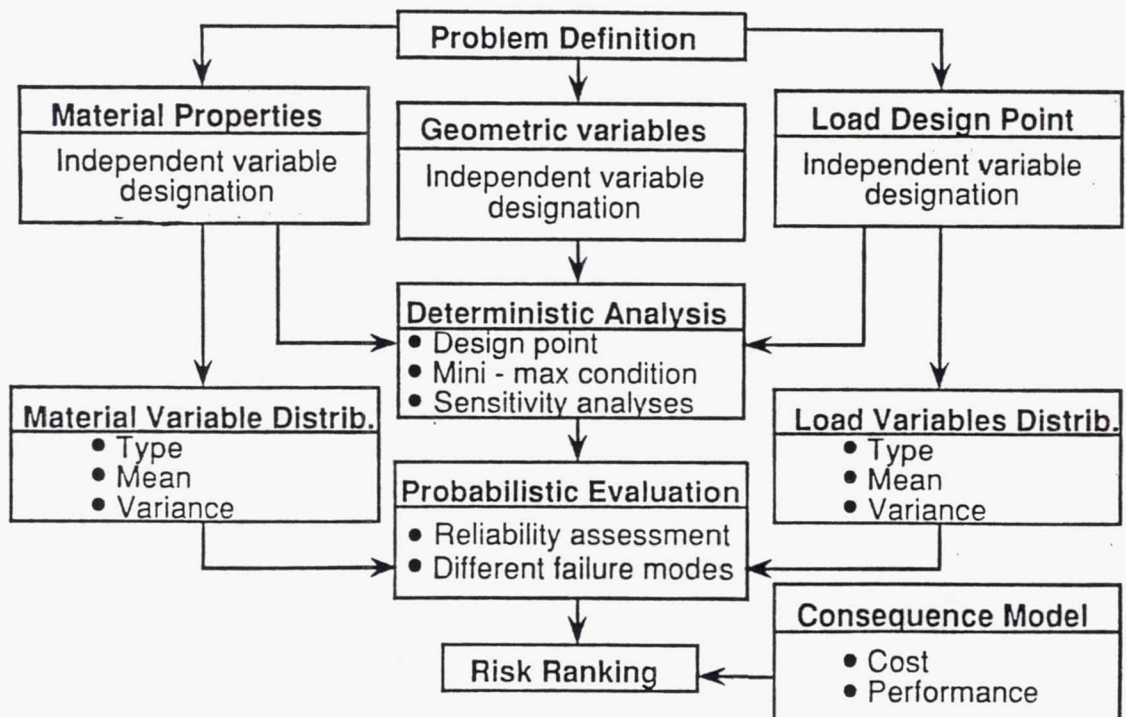


Figure 6. Probabilistic Design & Analysis Methodology Outline.

Application to Main Combustion Chamber Liner

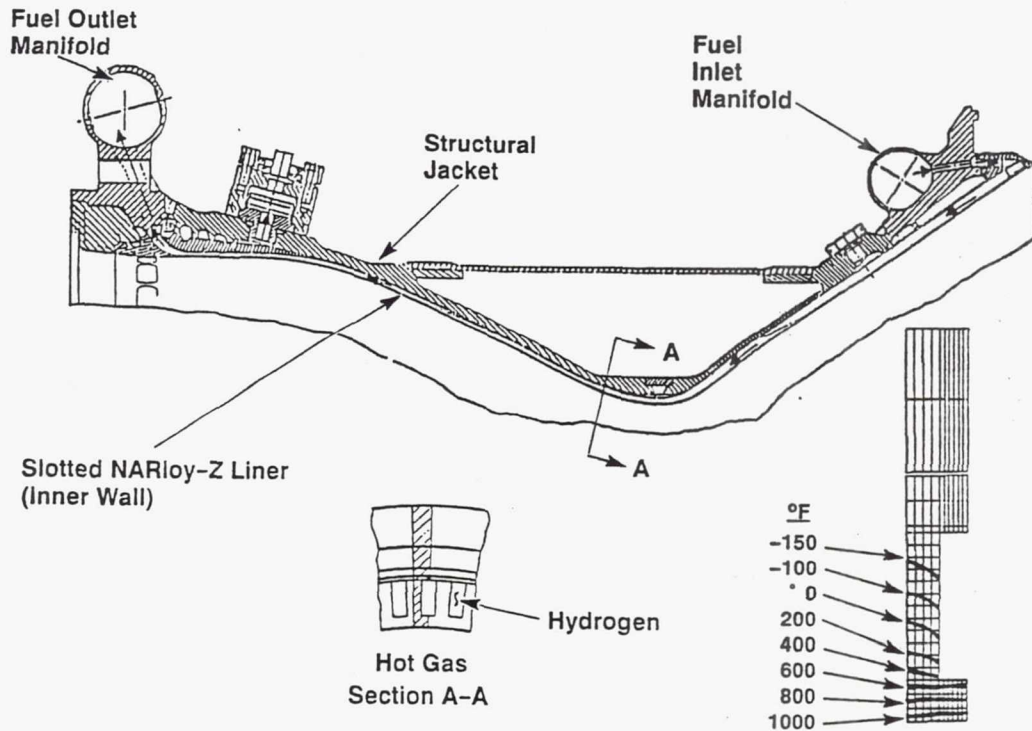


Figure 7. Typical Main Combustion Chamber Geometry.

91d-32-57
017

Probabilistic Analysis of the MCC Liner

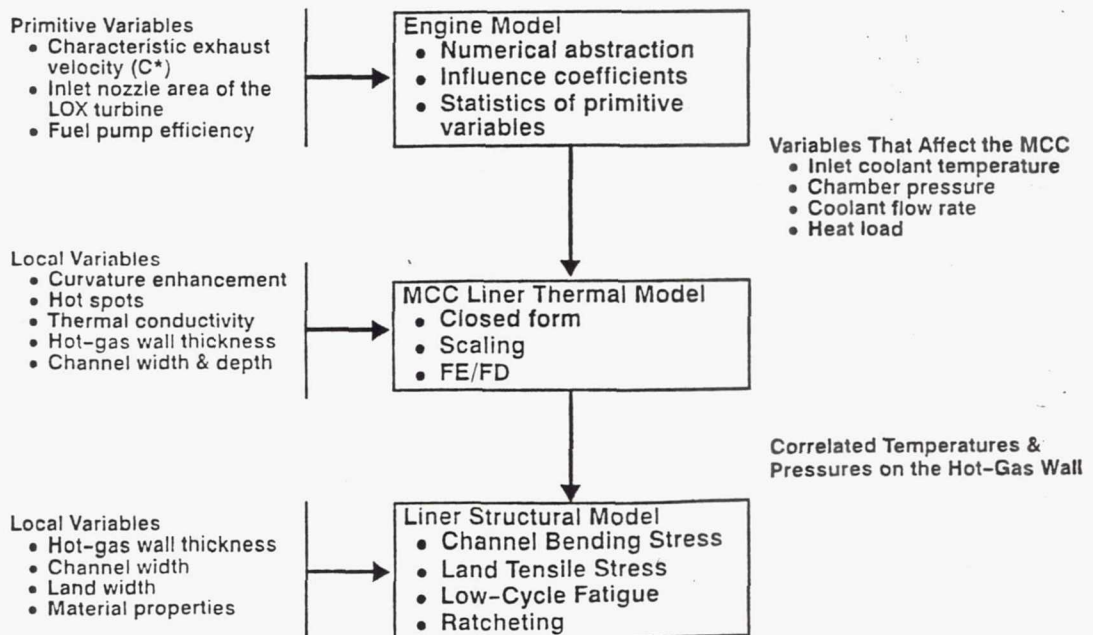


Figure 8. Probabilistic Analysis of the MCC Liner.

Probabilistic Analysis of MCC Liner (Ratcheting Failure Rate at a Hot Spot)

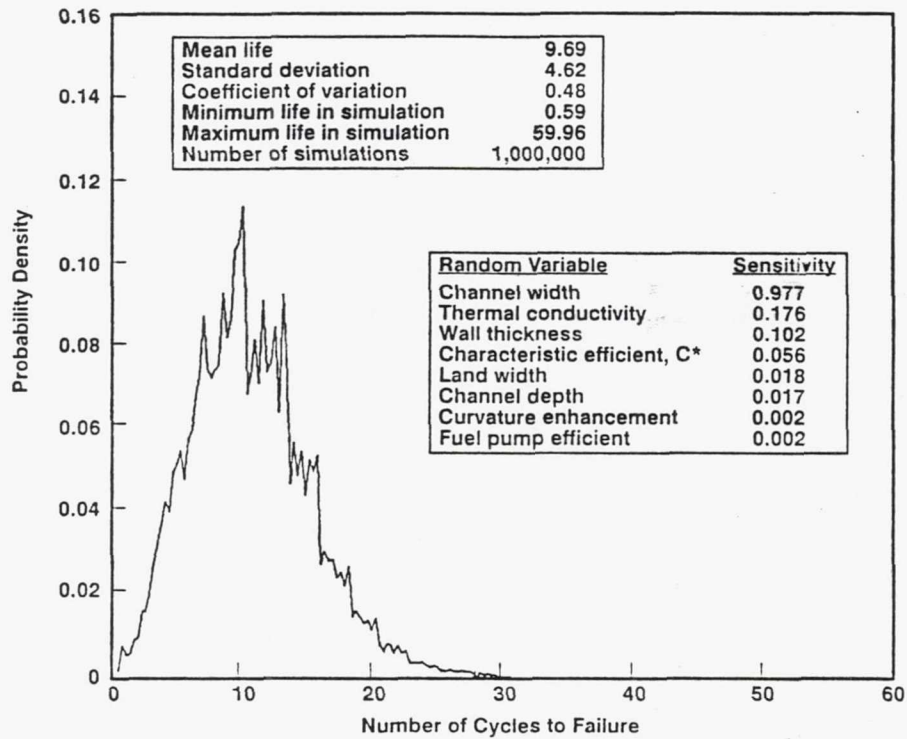


Figure 9. Ratcheting Failure Mode Response.

91d-32-59
017

COMMERCIALIZATION OF NESSUS - STATUS

Ben H. Thacker and Harry R. Millwater
Southwest Research Institute
San Antonio, Texas 78228

In 1988, Southwest Research Institute initiated a plan to commercialize the NESSUS probabilistic structural analysis software. The goal of the on-going commercialization effort is to begin the transfer of PSAM developed technology into industry and to develop additional funding resources in the general area of structural reliability. Initially, this goal will be met through code license support. This paper reports on the status of the on-going NESSUS commercialization effort at SwRI.

The SwRI/NESSUS™ Software System is a general purpose probabilistic finite element computer program employing state-of-the-art methods for predicting stochastic structural response due to random loads, material properties, part geometry, and boundary conditions. NESSUS can be used to assess structural reliability, to compute probability of failure, to rank the input random variables by importance, and to provide a more cost-effective design than traditional deterministic methods.

NESSUS continues to be developed by Southwest Research Institute (SwRI) for the National Aeronautics and Space Administration under the Probabilistic Structural Analysis Methods (PSAM) contract NAS3-24389 (1985-1989, 1990-1994). The goal is to develop a general probabilistic structural analysis methodology to assist in the certification of critical components in the next generation space shuttle main engine.

Near the end of the first five-year PSAM effort, discussions with numerous firms indicated that there was an interest in applying the NESSUS computer program to design concerns that were believed to be significantly affected by random, or uncertain, variables. This, in combination with our belief that reliability based design and certification by analysis is a promising new technology area led to our decision to promote the application of NESSUS on a commercial basis.

Some Aspects of the Commercialization Effort

The NESSUS code was developed as a research code with attention given to the development of capabilities specifically required for the PSAM program, including a reasonable user interface. To support commercial interests in this technology, we are implementing new capabilities and expanding existing capabilities in NESSUS to take the code from a purely research environment to a design application environment. To date, nearly all of the SwRI developed enhancements have been implemented in the NASA version of NESSUS.

The NESSUS Software System is developed on a network of Apollo Workstations running the Domain/SR10.2 operating system. A Configuration Management (CM) system has been implemented in order to track incremental versions, provide automated source code change tracking, and provide a means for re-constructing past versions of the NESSUS code. A family of specially tailored shell scripts have been developed and are used to manage the CM system.

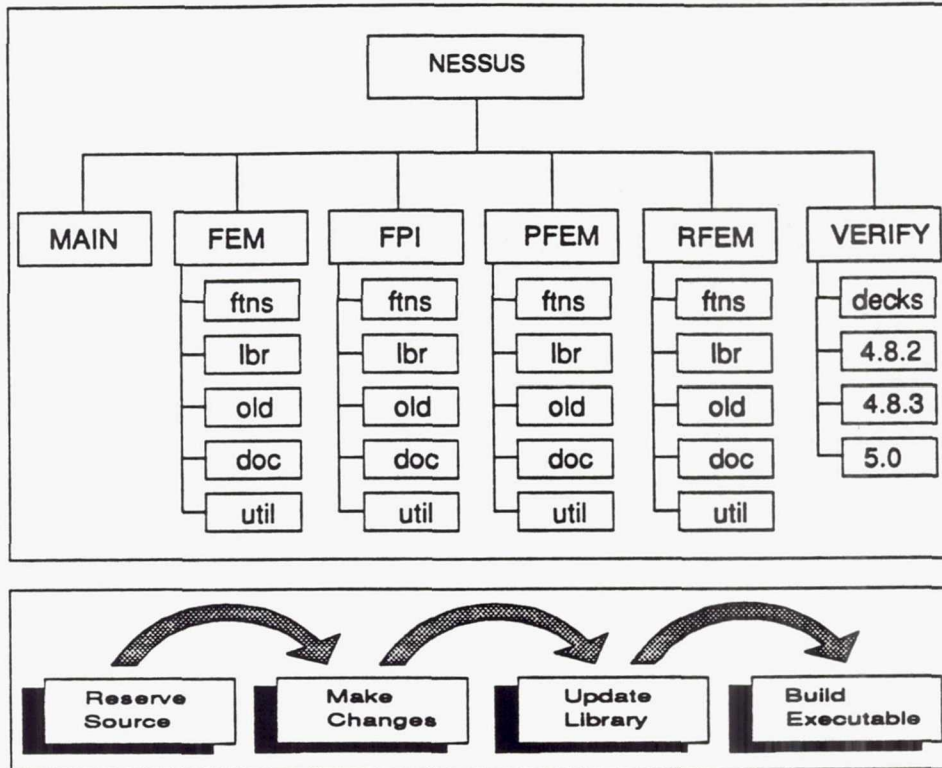
All of the existing NESSUS documentation has been improved and several new manuals written. The existing manuals (NESSUS/FEM, FPI, and PRE User's Manuals) were reviewed for errors and cleaned-up. Several new manuals were developed: NESSUS Demonstration Manual, VAX/Cray/Apollo/Sun Installation Guides, NESSUS/FEM Systems Manual, and the P/NESSUS Users Manual. The demonstration manual contains a detailed tutorial for performing a probabilistic analysis with NESSUS, NESSUS/FEM validation problems, and NESSUS/PFEM probabilistic validation problems. The NESSUS/FEM Systems manual, primarily for SwRI use, serves as a programmers/developers guide. The installation manuals explain how to install and execute NESSUS on the different computer systems, compile and link in user-programmed subroutines, and run a set of validation problems to check the installation.

Graphical pre- and post-processing capabilities for NESSUS are provided by P/NESSUS. P/NESSUS is designed to be used in conjunction with the commercially available PATRAN¹ software and provides for a data exchange process between NESSUS and PATRAN. Specific options are available in P/NESSUS to translate (1) a PATRAN finite element model to a NESSUS input deck, (2) a NESSUS input deck to a PATRAN finite element model, (3) a NESSUS post file to a PATRAN finite element model, and (4) a NESSUS perturbation data base to PATRAN results files. In (4), deterministic and perturbed solution data is translated for incremental, modal and harmonic analysis types.

SwRI is currently working with several clients interested in applying NESSUS to specific design problems. Future work that has been identified by industry as important include better input and output organization, graphics capabilities, better documentation, more extensive FEM modeling capabilities, and interfacing to third party commercial FE codes.

¹ PATRAN is a registered trademark of PDA Engineering

NESSUS CONFIGURATION MANAGEMENT SYSTEM



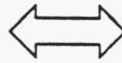
EXTENDED DOCUMENTATION DEVELOPED

- Software QA Plan Developed
 - Controls for Software Development and Validation
- P/NESSUS Graphics Translator
- Promotional Flyer
- Logo
- Documentation
 - NESSUS Demonstration Manual
 - VAX/CRAY/Apollo/Sun Installation Guides
 - NESSUS/FEM Systems Manual
 - P/NESSUS Users Manual

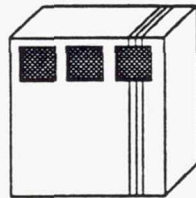
P/NESSUS Links PATRAN and NESSUS

PATRAN Geometry to/from NESSUS

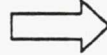
Coordinates
Elements
Boundary Conditions
Material Properties
Loads/Pressures/Temperatures



Graphic Workstation
Running PATRAN



Compute Server
Running NESSUS



NESSUS Results to PATRAN

Stresses/Strains
Displacements
Incremental/Modal/Spectral
Deterministic/Perturbed

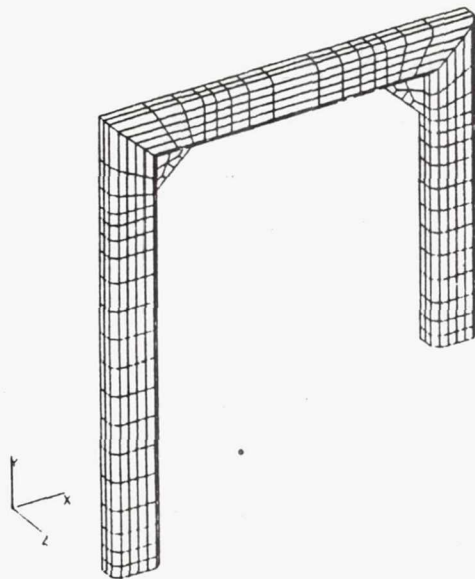


SOFTWARE ENHANCEMENTS

-
- NESSUS/FPI Extended User Interface
 - All Output Re-written to be Better Organized
 - All Input Keyword Driven with Column Independent Data Input
 - PATRAN Graphics Interface (P/NESSUS) Developed
 - Probabilistic Storage File Being Developed to Store Probabilistic Information
 - PFEM Output Organization

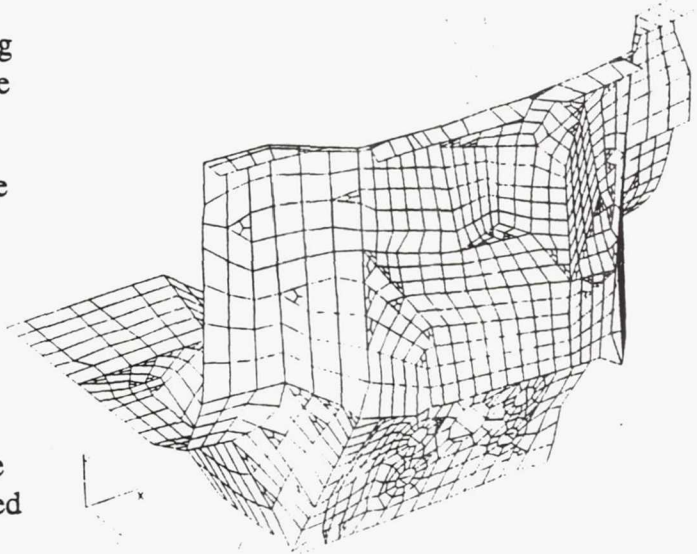
APPLICATIONS - Probabilistic Analysis of a Roll Over Protection System (ROPS)

- ROPS Certified by Meeting Strict SAE Legal Criteria on Deflection Envelop
- All Heavy Earthmoving Equipment Must Meet Criteria
- NESSUS Used to Determine the Probability of Exceeding Design Envelop for Deflections



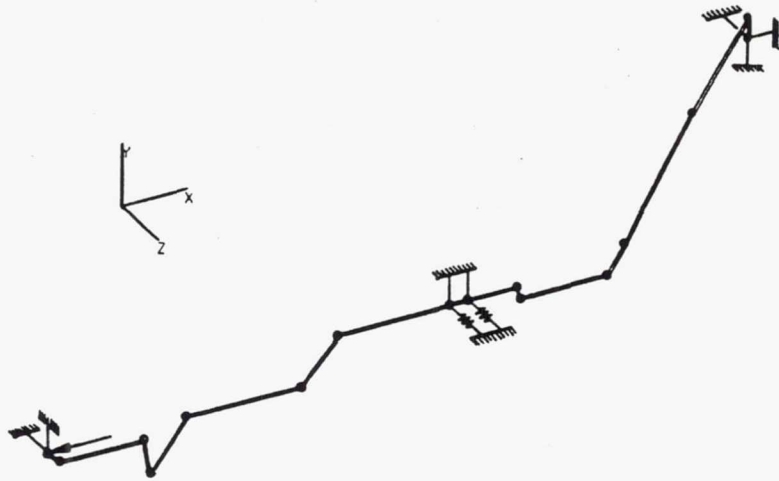
APPLICATIONS - Automobile Shock Tower Analysis

- Shock Tower Structure Carries Loading from Shock Absorption System into the Main Automobile Frame
- Durability Requirements Set Due to the Dynamic (Random) Nature of the Loading
- NESSUS was used to Compute the Probability of Not Meeting a Required Design Life (Unreliability)
- Random Variables that Contributed the Most to the Unreliability were Identified and Suggestions for Redesign Made



APPLICATIONS - Automobile Door Latch Mechanism

-
- Mechanism Studied Serves as a Key Connecting Rod in the Automobile Door Latching System
 - Door Latch Mechanism Required to Operate Within Certain Deformation and Force Constraints
 - Using a Simple Beam Model, NESSUS Predicts the Variation in Deformation and Force Responses Due to Variations in Material Properties and Connecting Clip Spring Stiffness
 - Several Variables Identified that Contributed the Most to the Variation in Deflections and Clip Forces



NESSUS Commercialization Benefits PSAM

-
- Mutual Sharing of Developed Technology
 - Better Support for NASA Engineers
 - More Robust User Interface and Documentation
 - Technology Transfer into Other Industries Helps to Identify and Strengthen Code Weaknesses
 - Visibility - Projects Good Image of NASA's Foresight in Developing Probabilistic Structural Analysis Methods

SYSTEM RELIABILITY AND RISK ASSESSMENT TASK GOALS & STATUS

T.A. Cruse and S. Mahadevan
Vanderbilt University
Nashville, Tennessee 37235

The major focus for continued development of the NESSUS codes is in support of system testing and certification of advanced propulsion systems. Current system certification procedures place a major emphasis on design methodology and on system testing. However, as a result of the standard certification effort, no specific levels of system reliability and confidence can be made. Experience in past system development and reliability is used as a guide to determine which tests and how much test time are required for system certification.

Propulsion system testing has evolved over the years from tests designed to show success (benign testing), to tests designed to reveal reliability issues before service use (accelerated testing). Such test conditions as performance envelope corners, high rotor imbalance, power dwells, and overspeed tests are designed to "shake-out" problems that can be associated with low and high cycle fatigue, creep and stress rupture, bearing durability, and the like. Passing these tests by some defined margin of time is intended to indicate a safe operational margin for shorter-term service use of the propulsion system.

Subsystem testing supports system certification by standing as an early evaluation of the same durability and reliability concerns as for the entire system. These tests have to be successful before the full system testing can be initiated. Analysis in support of design is often confirmed in subsystem testing. However, as in system testing for certification, little has been done to quantify just how much reliability has been demonstrated by these standard forms of design analysis, component, and subsystem tests.

The NESSUS software system is being further developed to support the definition of rigorous subsystem and system test definition and reliability certification. The approach taken is a building-block approach, wherein the foundation is constructed before the penthouse - full certification support. The first level of required analysis is that of component reliability (NESSUS 5.0). This analysis has defined the full range of component reliability modeling capabilities, including the consequences of component failure (risk). The NESSUS 5.0 code allows the user great flexibility in choosing critical structural performance and reliability measures, including the impact of reliability of on performance and availability measures.

Current NESSUS 6.0 effort focuses on a variety of issues related to the integration of component reliability information to a system level. In this case, system refers to an assembly of structural components. The current paper outlines the principal technical issues related to system reliability, including key technology issues such as failure mode synergism, sequential failure mechanisms, and fault tree definition. An approach is given to the development of an automatic means for system reliability calculations that includes a definition of the most probable failure

sequences, as well as the probability of system failure. Critically, the proposed method also preserves the sensitivity linkage of each event to all precursor primitive system variables that contribute to system failure. The proposed approach represents a major advance in system reliability, and builds on the available NESSUS analysis strategies.

Quantification of system reliability and sensitivity factors for sequential failures is an essential ingredient in system certification. It is critical to be able to identify failure sequences and to link each with the driving system variables in order to assess critical test conditions and confidence levels for certification. It is also believed that the proposed strategies will provide, for the first time, a basis for a system certification with quantification of reliability measures, as well as a means for defining critical reliability testing requirements. Sensitivity information can be used in a direct manner to define lower confidence intervals on certification testing results.

The paper reports on the proposed solution algorithms which build on previous NESSUS code structures to define the most probable failure sequence(s). Additionally, the paper defines potential approximation schemes for the definition of failure sequences in a cost effect manner. This task is one of the most critical in terms of technology advance for NESSUS 6.0.

SYSTEM RELIABILITY AND RISK ISSUES

1. Component reliability under interaction of all failure modes
2. Conditional dependence between reliabilities of two components
3. Effect of component unreliability on system performance
4. Effect of component unreliability on system availability
5. Effect of component unreliability on life cycle cost
6. System certification requirements

DISCRETE VS. CONTINUUM SYSTEMS RELIABILITY

- Present methods → Series/parallel combination of discrete component reliabilities
- Structural redundancy, correlation of failure modes etc. have been considered
 - No consideration of sequential damage
- Propulsion systems → Little or no redundancy
- Sequential damage distributed in the continuum
 - Interaction of failure modes and synergism
 - *New strategies required for system reliability computation*

SYSTEM RELIABILITY COMPUTATIONS NEEDED FOR CERTIFICATION ANALYSIS

- (1) Probability of failure of an individual component due to interacting multiple failure modes (e.g., creep and LCF)
- (2) Probability of failure of one component due to failure of another component (e.g., plastic deformation of hot gas seal → causes hot gas leakage → causes reduced thermomechanical fatigue life of another component)
- (3) Probability of failure of the system due to failure of multiple components (e.g., fatigue fracture of disk due to combination of cracking in firtrees, rim slots, snap fillets, and bore region)
- (4) Probability of failure of multiple components due to a system condition (e.g., temperature, rotor speed)

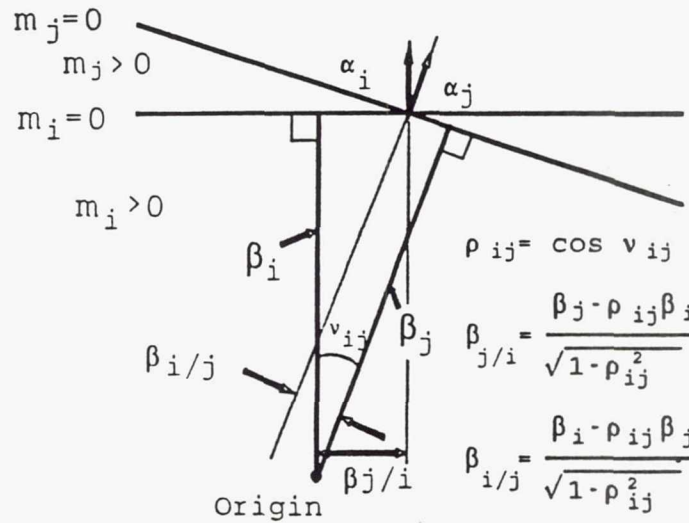
FOUR LEVELS OF COMPUTATIONAL COMPLEXITY ADDRESS SYSTEM RELIABILITY ISSUES

1. Level 0: Independent components/failure modes
2. Level I: Correlations among component failures
Series/parallel combinations
Fault tree analysis
3. Level II: Global response surface approach to find joint failure probability
4. Level III: Conditional dependencies between component failures based on sensitivity information and system reanalysis

↓

Alternate System Reliability Method

DITLEVSEN'S APPROXIMATION FOR CONDITIONAL RELIABILITY BASED ON FIRST ORDER SENSITIVITY MODELS



DEFICIENCIES IN DITLEVSEN'S METHOD FOR SYSTEM CERTIFICATION MODELING

1. Applicable to systems with discrete components
2. Does not account for progressive, synergistic damage processes
3. Similar to linear structural analysis
 - Based on first-order approximation of limit state
 - Component reliabilities are first found independently and then combined
 - Does not recognize sequential failure
 - Does not account for drastic modifications in structural behavior due to failure
4. Possible improvements
 - Importance Sampling
 - Formulation of Conditional Limit States
 - Proposed Alternative Method

**PROPOSED ALTERNATE SYSTEM RELIABILITY METHOD
ADDRESSES SEQUENTIAL FAILURE MODES**

0. Define system and non-system failure modes.
1. $\iota=0$. Determine the reliability of all components.
 - Analyze system model with all random variables.
 - Use perturbation and FPI to find MPP for each failure mode for each component.
2. System failure = Combination of individual system failures
+ Conditional effect of other non-system failures

Update system reliability result as each system failure mode is encountered.

Proceed to step 3 with non-system modes.
3. $\iota = \iota + 1$. Impose each non-system failure condition.

Compute conditional probability of each remaining mode.
 - Perturb the system at the imposed failure condition.
 - Similar to AMV procedure.

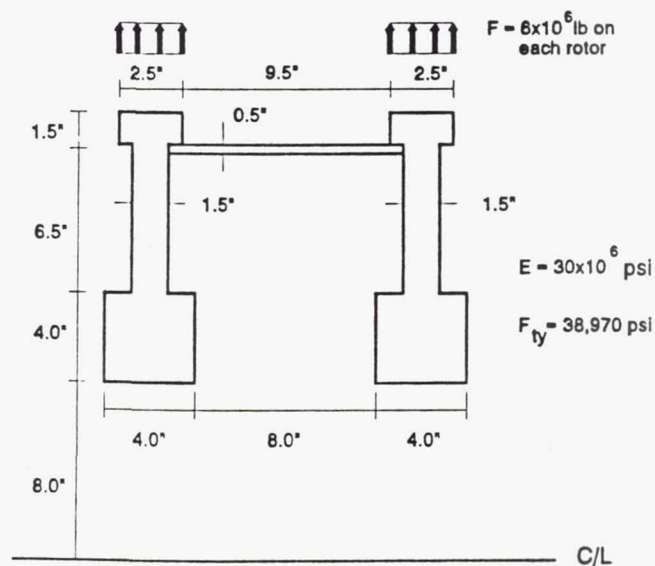
**PROPOSED ALTERNATE SYSTEM RELIABILITY METHOD
ADDRESSES SEQUENTIAL FAILURE MODES (CONTINUED)**

4. Repeat steps 2 and 3 until convergence in system reliability result.
5. Define the most probable failure sequence.
6. Define sensitivity of "top-event" to component and system primitive variables (certification issue).

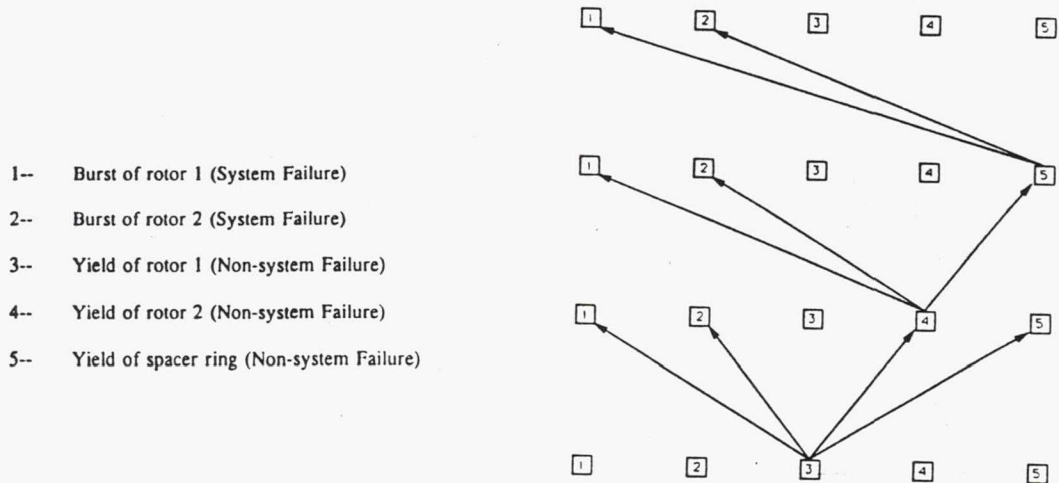
PROPOSED SYSTEM RELIABILITY METHOD PROVIDES UNIQUE TECHNOLOGY ADVANCES

1. Rigorously identifies the most probable failure sequence
 - Construction of fault-tree (bottom-up approach)
2. Also supports top-down approach
 - Sensitivities of various system failure modes to individual component failure modes computed and stored
 - Easy identification of the most probable damage, its location and extent that causes system failure
 - Reanalysis after each failure condition ensures that no component failure mode is missed
 - Definition to nonlinear structural analysis
 - Modification in structural behavior after each failure is accounted for

EXAMPLE



ONE POSSIBLE SEQUENCE OF REANALYSES

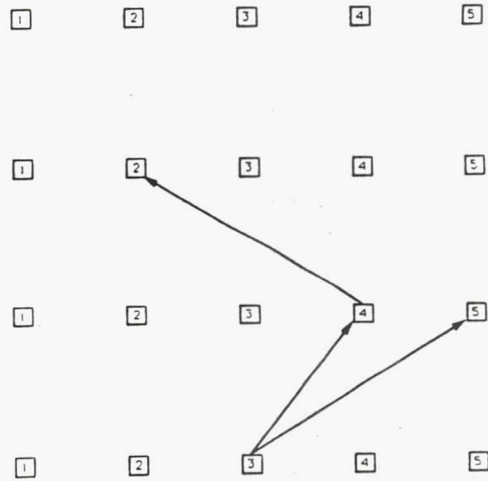


PROPOSED STRATEGIES TO REDUCE COMPUTATIONS

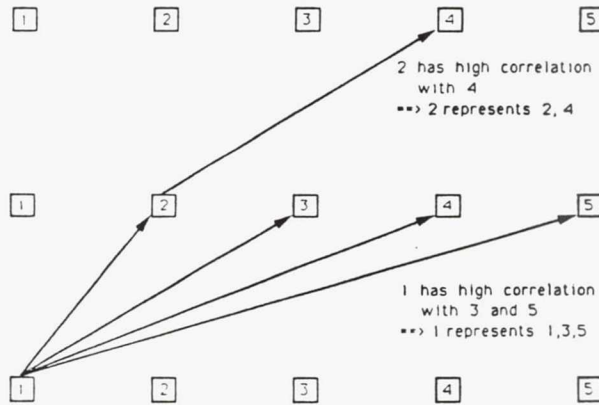
1. Follow the path whose failure modes have highest probability in each step
 - Useful to construct most probable sequence
 - Unsafe for overall system reliability result
2. Use cut-off values for updated failure probabilities
3. Use cut-off values for conditional probabilities
 - PNET Method (Ang)
4. Construct a first-order fault-tree based on sensitivities at $t = 0$ (individual component reliability analyses), and pursue significant paths.

STRATEGIES 1 AND 2

- 1-- Burst of rotor 1
- 2-- Burst of rotor 2
- 3-- Yield of rotor 1
- 4-- Yield of rotor 2
- 5-- Yield of spacer ring



PNET METHOD



$$P(\text{system failure}) = P(1 \cup 2 \cup 3 \cup 4 \cup 5)$$

$$= P(1 \cup 2)$$

PROGRAMMING REQUIREMENTS DEFINED

1. User needs to identify all the failure modes
 - system and non-system
2. Code to compute reliabilities for all failure modes at first.
3. Options for most probable failure sequence:
 - Code constructs a first-order fault tree
 - AMV-type reanalysis and refinement for dominant paths
 - User is allowed to explore a chosen sequence
4. Store and receive
 - MPP for each failure mode
 - Sensitivities of each failure mode to random variables
 - Conditional probability of each failure mode to previous modes in a sequence
5. Output
 - System reliability update at each step
 - Subsystem conditional failure probabilities at each step
 - Most probable failure sequence

APPLICATION TO PROPULSION SYSTEM CERTIFICATION

1. Compute reliability effects on system performance, life cycle cost, and availability
2. Link system reliability analysis with CLS (Composite Load Spectrum)
 - Sensitivity information regarding loads and performance
 - e.g., hot gas seal leakage
3. System reliability analyses include failed conditions
 - Need to recompute sensitivity information
4. Definition of system certification testing requirements
 - Sensitivity information needed to determine
 - (i) confidence bounds
 - (ii) accelerated testing parameters
5. System reliability analysis can account for "unknown-unknowns"
 - design and assembly errors
 - sequential failure nodes
 - functional failures

PROBABILISTIC STRUCTURAL ANALYSIS ALGORITHM DEVELOPMENT FOR COMPUTATIONAL EFFICIENCY

Y.-T. Wu
Southwest Research Institute
San Antonio, Texas 78228

The PSAM (Probabilistic Structural Analysis Methods) program, funded by NASA Lewis Research Center, is developing a probabilistic structural risk assessment capability for the SSME components. PSAM is currently in the seventh year of a two-phase, ten-year contract. An advanced probabilistic structural analysis software system, NESSUS (Numerical Evaluation of Stochastic Structures Under Stress), is being developed as part of the PSAM effort to accurately simulate stochastic structures operating under severe random loading conditions.

A central part of the NESSUS system is a finite element analysis (FEA) module. FEA is generally known to be computer intensive. Thus, the conventional Monte Carlo method, which requires a large number of simulations (i.e., a large number of deterministic computer runs), is too time-consuming to be practical for probabilistic FEA analysis. One of the major challenges in developing the NESSUS system is the development of the probabilistic algorithms that provide both efficiency and accuracy. The main probability algorithms developed and implemented in the NESSUS system are efficient, but approximate in nature. In the last six years, the algorithms have improved very significantly.

In probabilistic FEA analysis, a good index for measuring the computational efficiency is the number of deterministic solutions required for the user-selected performance function. To minimize this number, denoted as M , the first approach taken by PSAM was to generate a response surface over a "wide" range (say, ± 3 standard deviations for each random variable). Once the response surface is generated, a fast probability integration (FPI) algorithm [Ref. 1] can be used. In practice, when the number of random variables is not small, M might be too large, and the FEA part tends to dominate the total computational time. Moreover, the response surface approach does not generally provide sufficient accuracy unless an expensive iterative procedure is applied to update the response surface at focused regions [Ref. 2].

To improve the efficiency, the concept of FPI was applied directly to guide the FEA to develop a good approximate performance function. The basic concept is to use the initial information from the conventional mean value first order (MVFO) solutions to identify regions that are probabilistically more likely for the given performance function values, then move the FEA to these regions. MVFO requires $(n + 1)$ deterministic solutions, where n is the number of random variables, and provides approximate mean and standard deviation for the performance function. However, in probabilistic structural analysis, it is more desirable and often necessary to have knowledge in the whole distribution function (CDF). The advanced mean value (AMV) method was developed to provide the guidance for the FEA "move," and for efficiently generating performance CDF based on the MVFO solution [Refs. 3, 4]. The AMV method has been found to be quite effective for a wide variety of engineering problems. Further procedures requiring more M were also developed to improve the accuracy of the AMV method. In summary, $M = n + 7$ is believed to be the minimum number required to obtain reasonably accurate probabilistic output that includes the performance CDF, and the probabilistic sensitivity factors for the input random variables.

In addition to the AMV-based methodology development, the probability algorithms have also been improved for problems with closed-form performance functions. The original FPI algorithm [Ref. 1] has proved to provide a good approximate solution. However, the drawback is that it tends to run into numerical problems when the input random variables are highly non-normal or have very large coefficient of variations. To solve the problem and to further improve the accuracy, the FPI algorithm has been enhanced recently by combining the linearization concept developed in the original FPI with the fast convolution method [Ref. 5]. The fast convolution theorem provides an exact CDF solution if the performance function can be expressed by a sum of random variables. The combined analysis procedure includes three steps: (1) establish a linear or quadratic performance function based on the AMV-based procedure, (2) transform the quadratic function into a linear function (if the function is quadratic), (3) apply the convolution theorem to compute the performance CDF. In the last step, a procedure based on the discrete, fast Fourier transform (FFT) technique has been developed to speed up the convolution calculations. In summary, the current NESSUS probabilistic analysis procedure combines the AMV-based method with the fast convolution method. The AMV-based procedure generates linear or quadratic performance functions, and the fast convolution method takes the polynomial performance functions and generates probability solutions.

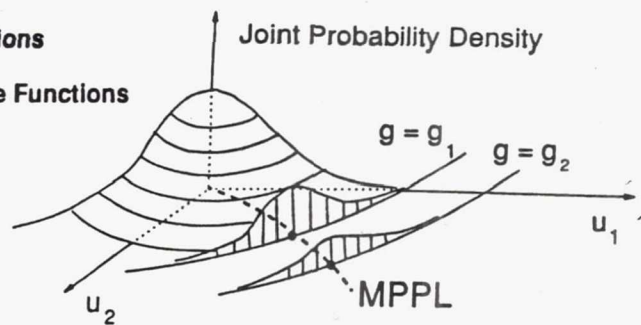
The PSAM program is moving into the area of system risk assessment. The methodology currently under development includes system reliability analysis that deals with multiple failure modes and multiple components. Here, the challenge is to accurately and efficiently evaluate probabilities associated with joint and conditional events. An efficient adaptive importance sampling method is being implemented in the NESSUS system. The method was originally developed for probabilistic rotordynamics analysis under a project funded by the NASA Marshall Space Flight Center [Ref. 6]. It is anticipated that other system reliability analysis tools will be developed and implemented in the NESSUS system based on a fault-tree type analysis framework.

References

1. Wu, Y.-T. and Wirsching P.H., "A New Algorithm for Structural Reliability Estimation," *Journal of Engineering Mechanics*, ASCE, Vol. 113, No. 9, pp. 1319-1336, September 1987.
2. Y.-T. Wu and P.H. Wirsching, "Advanced Reliability Methods for Fatigue Analysis," *Journal of Engineering Mechanics*, ASCE, Vol. 110, No. 4, April 1984.
3. Wu, Y.-T., O.H. Burnside, and T.A. Cruse, "Probabilistic Methods for Structural Response Analysis," *Computational Mechanics of Reliability Analysis*, W.K. Liu and T. Belytschko (eds.), Elmepress International, Ch. 7, 1989.
4. Wu, Y.-T., H.R. Millwater, and T.A. Cruse, "An Advanced Probabilistic Structural Analysis Method for Implicit Performance Functions," *AIAA Journal*, Vol. 28, No. 9, pp. 1663-1669, 1990.
5. Wu, Y.-T. and T.Y. Torng, "A Fast Convolution Procedure for Probabilistic Engineering Analysis," *Proceedings of the First International Symposium on Uncertainty Modeling and Analysis*, IEEE, December 1990.
6. Y.-T. Wu, T.Y. Torng, H.R. Millwater, A.F. Fossum, and M.H. Rheinfurth, "Probabilistic Methods for Rotordynamics Analysis," *Proceedings of the SAE Aerospace Atlantic 1991 Conference*, April 1991, (to appear).

Establish CDF Using Fast Probability Integration Algorithm

- Define Limit-State
- Approximate Performance Function
At One or More Probability Significant Regions
- Compute Probability Based on Approximate Functions



ADVANCED MEAN VALUE (AMV) METHOD

- Conventional Mean Value First-Order (MVFO) method

First-order Taylor's series expansion at mean values:

$$Z = a_0 + \sum a_i X_i (\equiv Z_1)$$

Valid for small standard deviations.

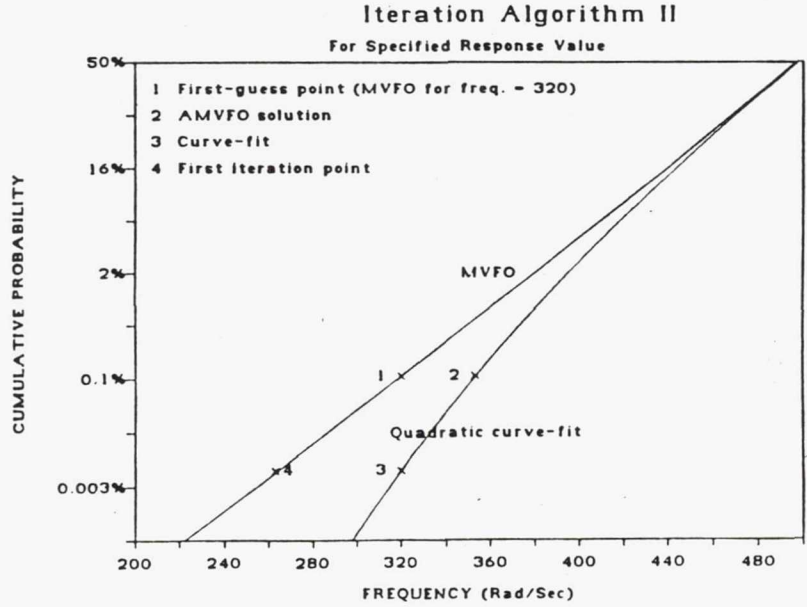
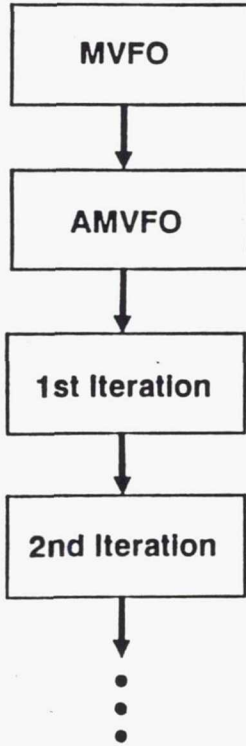
- Advanced Mean Value (AMV) First Order Method

$$Z^* = Z_1 + H(Z_1)$$

Features:

- $H(Z_1)$ introduced to minimize truncation error.
- Iteration procedure available to find $H(Z_1)$.
- Can be used to detect non-monotonic functions.

AMV - Based Iteration Procedure

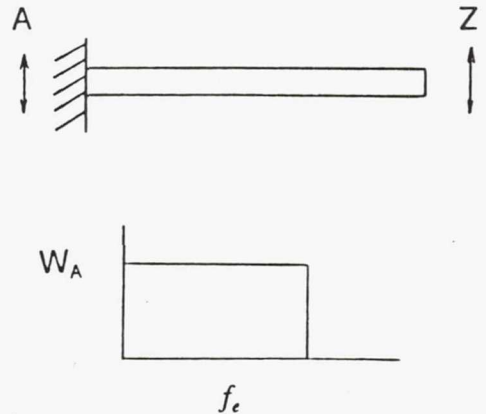


AMV EXAMPLE: RANDOM VIBRATION

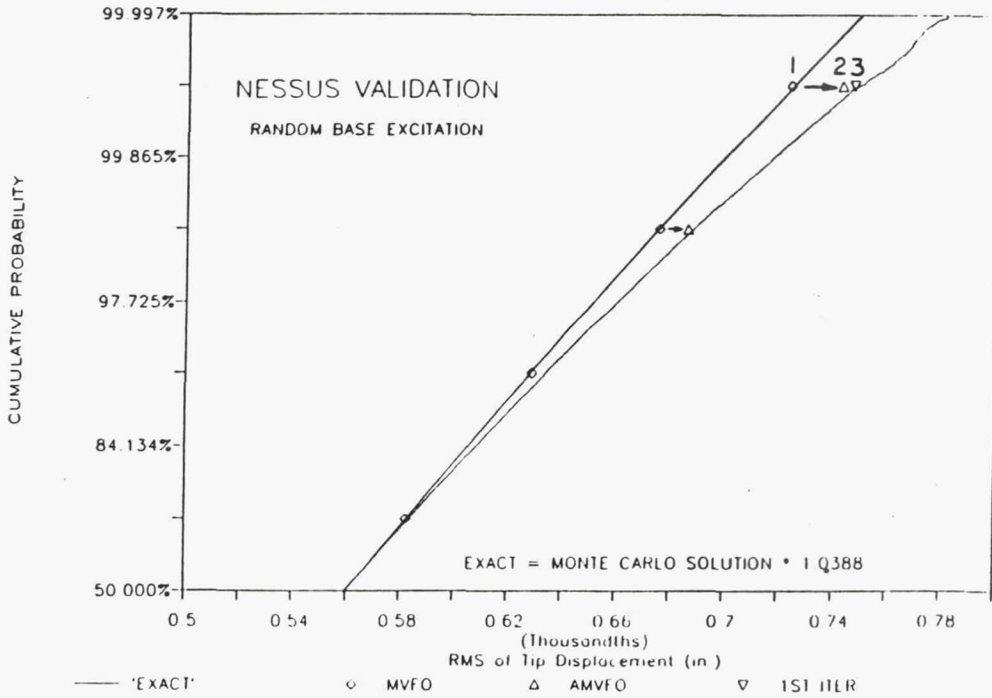
Monotonic Performance Function

$$RMS = \sqrt{\frac{1.707L^6W_A\rho^{1.5}}{E^{1.5}t^3\xi}}$$

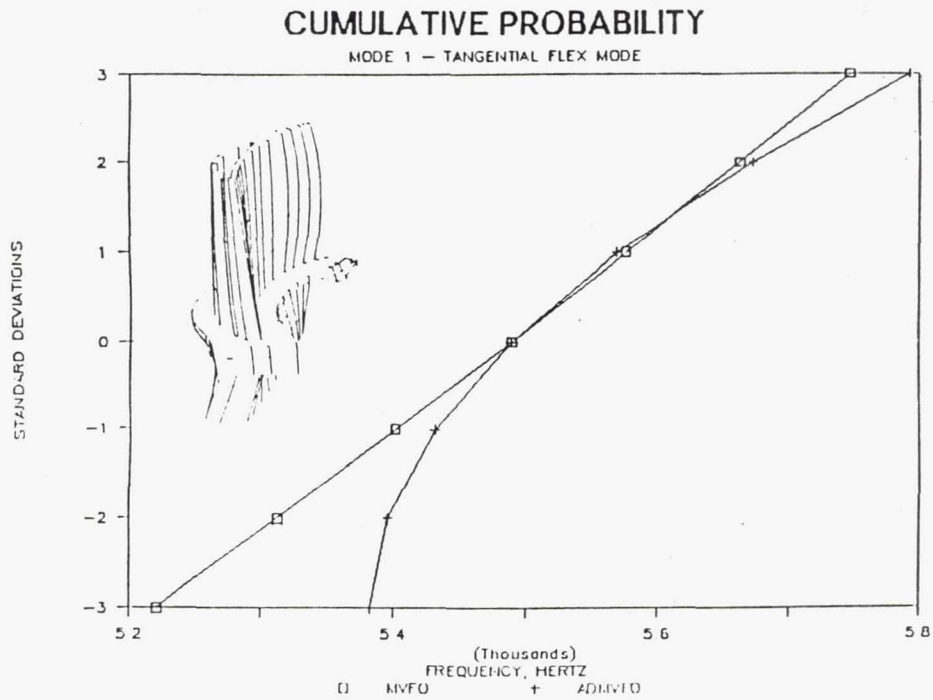
| Variable | Mean | COV | Distribution |
|----------------|---|------|--------------|
| E | 10E+6 lb/in ² | 0.03 | Lognormal |
| L | 20.0 in. | 0.01 | Normal |
| t | 0.98 in. | 0.01 | Normal |
| ξ | 0.05 | 0.10 | Lognormal |
| W _A | 1.0 in/sec ² -rad | 0.10 | Lognormal |
| ρ | 2.5E-4 lb-sec ² /in ⁴ | 0.02 | Normal |



AMV EXAMPLE: RANDOM VIBRATION



Turbine Blade Verification Example



Fast Convolution Procedure

1. Dependent Non-normal RVs to Independent Std. Normal RVs.
2. Find Most Probable Point and Construct Second-order Approx.
3. Eliminate Product Terms by Orthogonal Transformation.
4. Transform to Linear Polynomial.
5. Apply Convolution Theorem.

Fast Convolution

- SUM OF INDEPENDENT RANDOM VARIABLES

$$Z = X_1 + X_2 + \dots + X_i + \dots + X_n$$

- CHARACTERISTIC FUNCTION

$$\Phi(\omega) = \int_{-\infty}^{\infty} f(x)e^{i\omega x} dx$$

$$\Phi_Z(\omega) = \Phi_{X_1}(\omega)\Phi_{X_2}(\omega)\Phi_{X_n}(\omega)$$

- USE FAST FOURIER TRANSFORM TO COMPUTE $\Phi(\omega)$
- USE INVERSE FFT TO COMPUTE PDF OF Z
- * FOR NON-LINEAR Z, USE MPP, QUADRATIC APPROXIMATION AND LINEARIZATION

Linearization

$$g_2(\mathbf{u}) = a_o + \sum_{i=1}^n a_i(u_i - u_i^*) + \sum_{i=1}^n b_i(u_i - u_i^*)^2 + \sum_{i=1}^n \sum_{j=1}^{i-1} c_{ij}(u_i - u_i^*)(u_j - u_j^*)$$

• QUADRATIC APPROXIMATION AND LINEARIZATION

$$g(X) \cong a_o + \sum_{i=1}^n a_i x_i + b_i x_i^2$$

$$c_o = a_o - \frac{1}{4} \sum_{i=1}^n \frac{a_i^2}{b_i}$$

$$g(Y) = c_o + \sum_{i=1}^n b_i Y_i$$

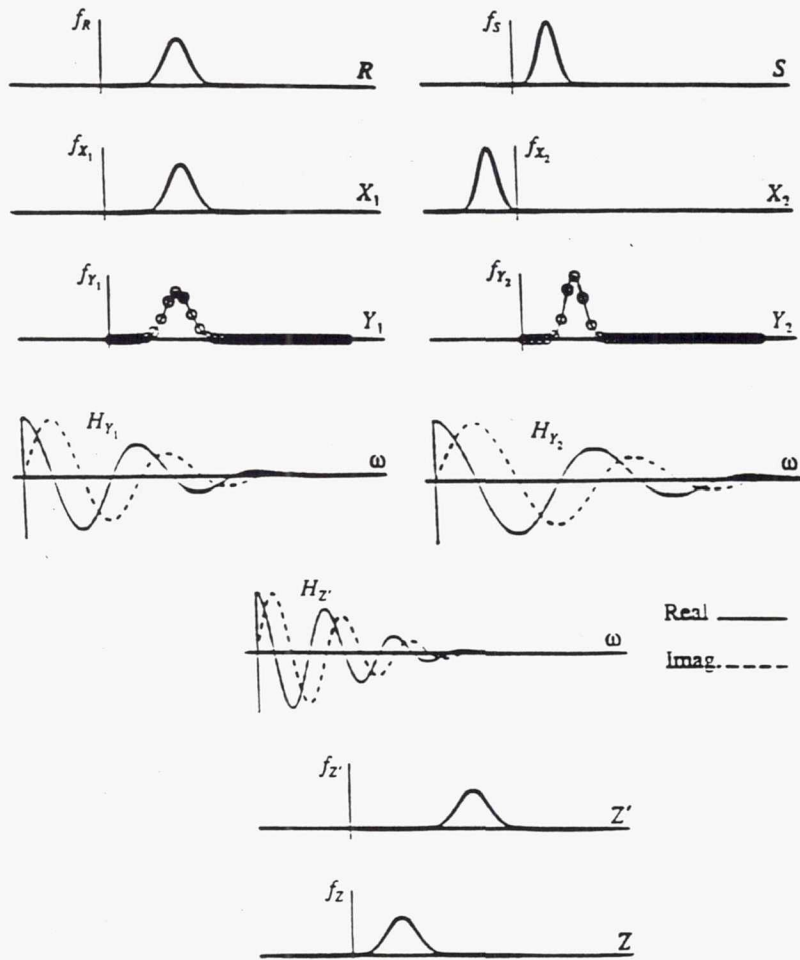
$$Y_i = \left[X_i + \frac{a_i}{2b_i} \right]^2 = [X_i + A_i]^2$$

• LOG-TRANSFORMATION

$$g(X) \cong a_o + \sum_{i=1}^n a_i \ln x_i + b_i (\ln x_i)^2$$

Fast Convolution Example

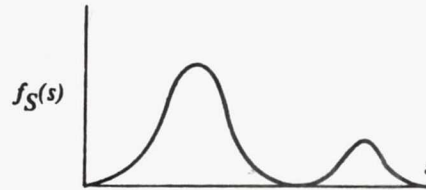
$$Z = R - S$$



Fast Convolution Validation Problem

Random variable S has bi-modal pdf:

$$f_S(s) = \left(\frac{a}{b}\right) \phi\left(\frac{s-\mu_1}{\sigma_1}\right) + \left(\frac{b-a}{b}\right) \phi\left(\frac{s-\mu_2}{\sigma_2}\right)$$



Limit state function:

$$g = R - S = 0$$

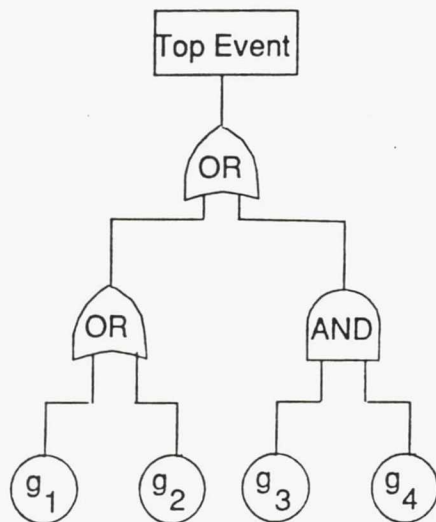
Strength: $R \sim \text{Lognormal} \sim (20., 5.)$

Stress: $S \sim \text{Bi-modal} \sim (\mu_1, \mu_2, \sigma_1, \sigma_2) = (10, 2, 40, 2)$

Probability of failure:

| a | b | Exact | Previous Method | Improved Method |
|----|-----|----------|-------------------|-----------------|
| 19 | 20 | 6.331E-2 | 8.29E-2 | 6.285E-2 |
| 99 | 100 | 2.307E-2 | Numerical Problem | 2.347E-2 |

SYSTEM RELIABILITY ANALYSIS METHODOLOGY

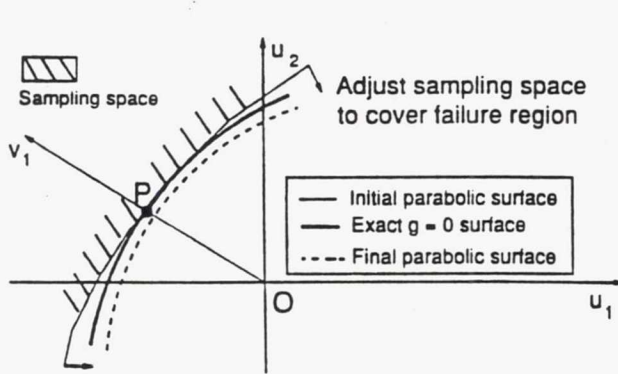


→ COMPUTE:

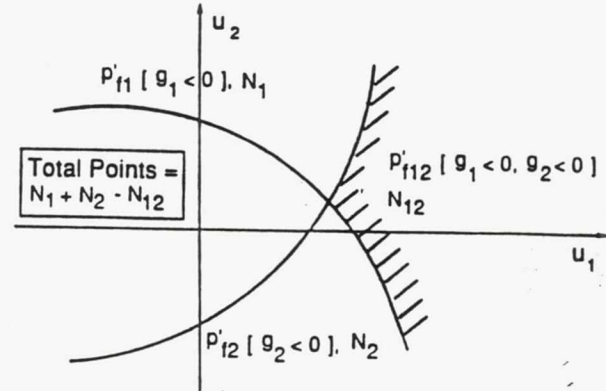
$$P[(g_1 < 0) \cup (g_2 < 0) \cup ((g_3 < 0) \cap (g_4 < 0))]$$

ADAPTIVE IMPORTANCE SAMPLING METHOD FOR SYSTEM RELIABILITY ANALYSIS

METHODOLOGY



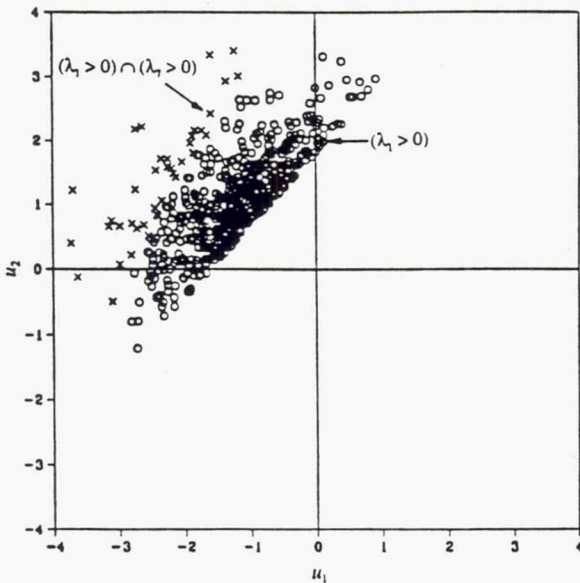
The Concept of the Curvature-Based Adaptive Importance Sampling Method



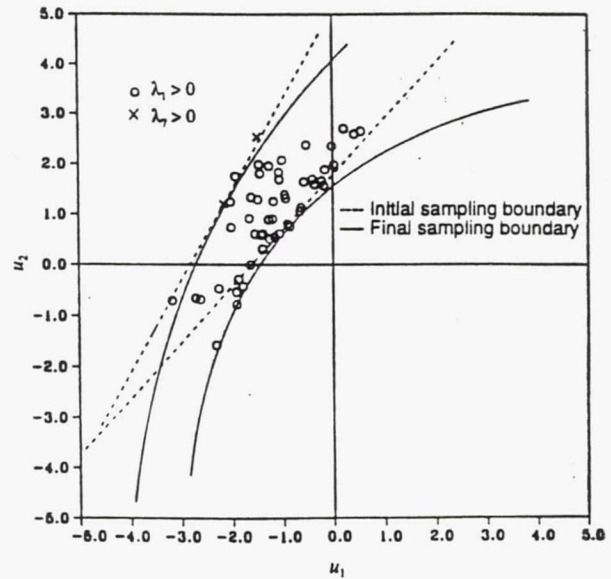
The Concept of Generating Importance Sampling Points for Multiple Limit States

ADAPTIVE IMPORTANCE SAMPLING METHOD FOR SYSTEM RELIABILITY ANALYSIS

ROTORDYNAMICS EXAMPLE



Probability of Instability Sampling Points for $\lambda_1 > 0$ and $\lambda_2 > 0$ in the u -Space (5000 Monte Carlo Samples)



Curvature-Based Importance Sampling Points for $\lambda_1 > 0$ and $\lambda_2 > 0$ in the u -Space

EXPERT SYSTEM DEVELOPMENT FOR PROBABILISTIC LOAD SIMULATION

H. Ho and J.F. Newell
Rockwell International Corp.
Rocketdyne Division
Canoga Park, California 91303

The Composite Load Spectra Load Expert System LDEXPT

A knowledge-based system LDEXPT using the intelligent database paradigm has been developed for the Composite Load Spectra (CLS) project to simulate the probabilistic loads of a space propulsion system. The knowledge-base approach provides a systematic framework of organizing the load information and facilitate the coupling of the numerical processing and symbolic (information) processing. It provides an incremental development environment for building generic probabilistic load models and book-keeping the associated load information.

Large volume of load data is stored in the database and can be retrieved and updated by a built-in database management system. The database system standardizes the data storage and retrieval procedures. It helps maintain data integrity and avoid data redundancy. The intelligent database paradigm provides ways to build expert system rules for shallow and deep reasoning and thus provides expert knowledge to help users to obtain the required probabilistic load spectra.

Expert System Development

Considerable investigation has been given to the load simulation and expert system implementation issues during the development of the expert system. The first important issue even before the construction of the program was the load simulation using a probabilistic method versus a deterministic method. In a deterministic analysis, several worst-case variable limits are often used together in a calculation to produce a worse-case load. The result is maybe too conservative and is typically inconsistent with the real situation. On the other hand, the load generated from a probabilistic method will not be an unrealistic maximum value. If the correlation between loads is accounted for there will be no inconsistency in the simulated loads.

A system model was required to simulate the operational condition of the system so correlated component loads could be synthesized for a space propulsion system. The issue was that of building a detail physical model versus a heuristic system model. Detail physical models are developed for steady state performance calculations and for transient solutions as system operation tools. These models require significant computer resources and solution time and are inappropriate for probabilistic solution schemes requiring hundreds or thousands of solutions to develop distributional responses of component loads. Whereas a heuristic model was doable, has sufficient accuracy and requires minimal computing time. The CLS system model of the expert system is such a heuristic model : a multi-

level engine model that employs the influence model technique, scaling and perturbation method that are anchored with results from available deterministic models and test data.

A crucial implementation issue for CLS was the choice of a knowledge-base approach over that of a pure procedural approach. A pure procedural approach for a load simulation program was not impossible. However, a modular structural approach would be much more difficult to implement. There would be problems in data maintenance and data redundancy. It would be more difficult to automate the complete load simulation process in a consistent way and could end up with codes that require considerable manual work in between different tasks.

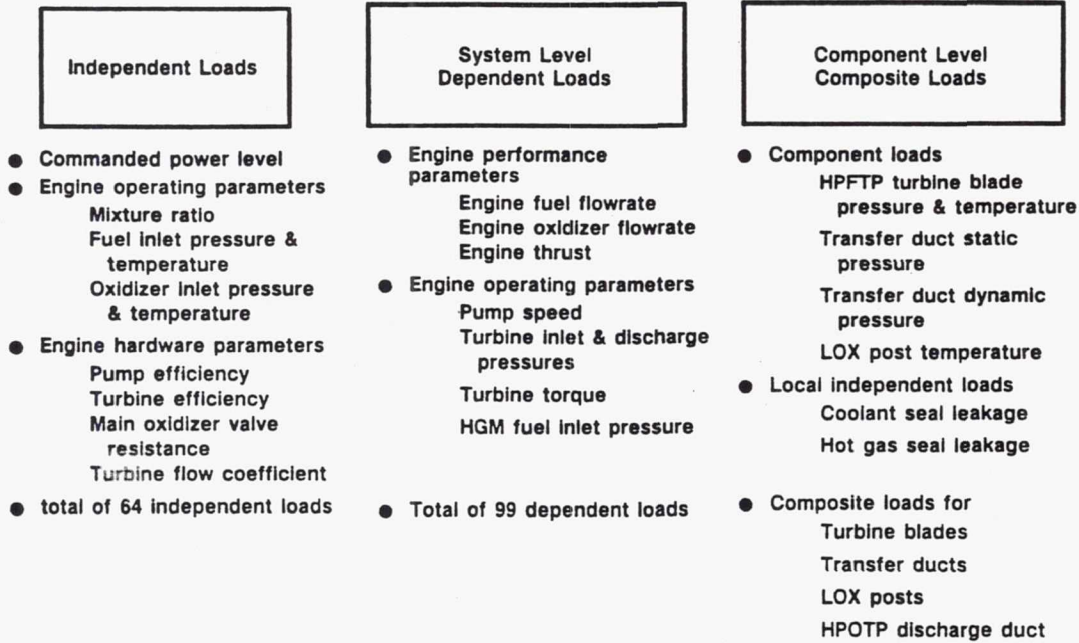
A knowledge-base approach with the intelligent database paradigm provided a natural knowledge representation to load simulation. The knowledge representation is object-oriented. The object can be a real object such as a component -- the LOX (liquid-oxygen) post or a conceptual object such as a dependent load -- the HPFTP (high pressure fuel turbopump) turbine inlet pressure. With this representation, modular incremental development was facilitated as new components and their associated loads were added to the program. If a generic load model already exists for the new component, then only the new load information and associated data are required to be added to the knowledge base and no new model is required.

The knowledge base approach employed in CLS does not dwell on a pure rule-based system. In this implementation, the symbolic processing is coupled with the numeric processing to achieve the objective of synthesizing the probabilistic loads. Intelligence is achieved by coupled rules with clever algorithms (for deep reasoning). Tremendous knowledge and expertise have been incorporated in the knowledge base of the composite load spectra program. Further development on the expert system is being pursued in the option phase of the contract to exploit the knowledge base to provide tutorial on rocket engine loads.

Future Development

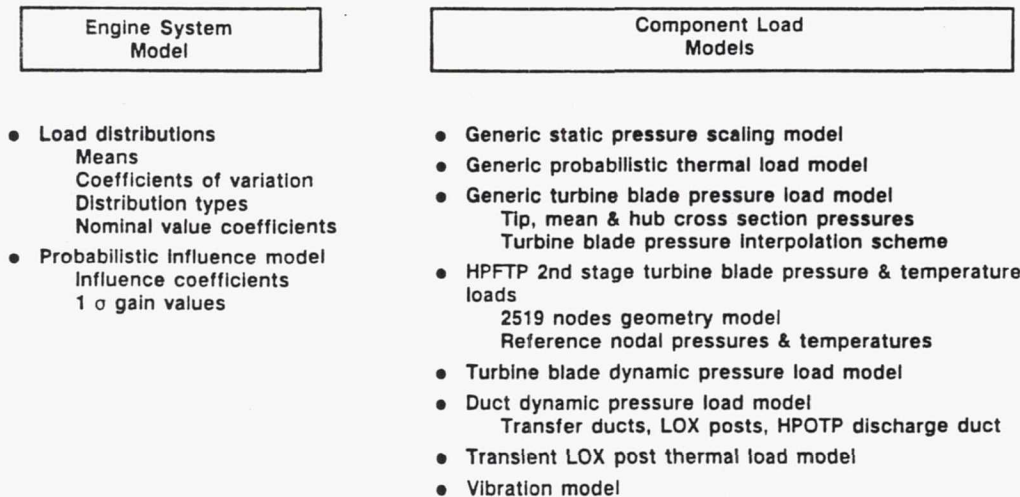
A development task that can be benefitted from the existing vast amount of knowledge on the rocket engine loads is to develop a simple hypertext tool to provide tutorials on rocket engine loads. It is perceived that the expert system will be able to answer simple questions such as what are the important component local variables required to simulate the thermal load of the LOX post.

Composite Load Spectra
Load Expert System Version 3.0
Load Model Knowledge Base



89c-4-339-30

Composite Load Spectra
Load Expert System Version 3.0
Load Model Knowledge Base



Composite Load Spectra
Load Expert System Version 3.0

**Expert System
Characteristics**

- Intensive numerical computation
- Large volume of data
- Coupled symbolic & numeric computation
- Deep reasoning
- Modular

What Has CLS Done Right

- Stay with FORTRAN
- Have a data base system
- Decision tree inference
- Couple rules with computational routines
- Rules modules
- Working memory for communication b/n rules

89c-4-339-32

**Composite Load Spectra
Important Issues**

Probabilistic Load Simulation Issues

- Probabilistic Method vs Deterministic Method
- Heuristic Engine Model vs Physical Engine Model
- Correlation Field vs Random Variation Loads

Expert System Implementation Issues

- Knowledge-Based System vs Procedure Approach
- Symbolic Processing vs Numeric Processing
- Intelligent Database System vs Pure Ruled-based System

Page intentionally left blank

PROBABILISTIC FRACTURE FINITE ELEMENTS

W.K. Liu, T. Belytschko, and Y.J. Lua
Northwestern University
Evanston, Illinois 60201

The Probabilistic Fracture Mechanics (PFM) is a promising method for estimating the fatigue life and inspection cycles for mechanical and structural components. Since failure process depends on random defects and may be influenced by random variables, the probabilistic aspects of the problem should be taken into account. The main sources of uncertainty are attributed to the randomness in defect sizes, growth law parameter, loads, and material properties.

The Probabilistic Finite Element Method (PFEM), which is based on second-moment analysis developed by Liu et al. [1-2], has proved to be a promising, practical approach to handle problems with uncertainties. As the PFEM provides a powerful computational tool to determine first- and second- moment of random parameters, the second-moment reliability methods can be easily combined with PFEM to obtain measures of the reliability of the structural system. The fusion of the PFEM and reliability analysis for brittle fracture and fatigue has been reported by Besterfield et al. [3-4]. In order to model the crack-tip singularity, an enriched element is employed. As the stress intensity factors are directly included as unknowns along with the nodal displacements, this approach simplifies the development of the sensitivity analyses which are required in the first-order reliability methods. In addition to the uncertainties in loads, material properties and component geometry, the randomness in the crack length, crack location and orientation and fatigue crack growth parameters are also considered. Based on the first-order reliability analysis, a constrained optimization problem to calculate the reliability index for brittle fracture and fatigue has been formulated. The performance of this method is demonstrated through the Mode I fatigue crack growth reliability analysis (see Figs.1-2).

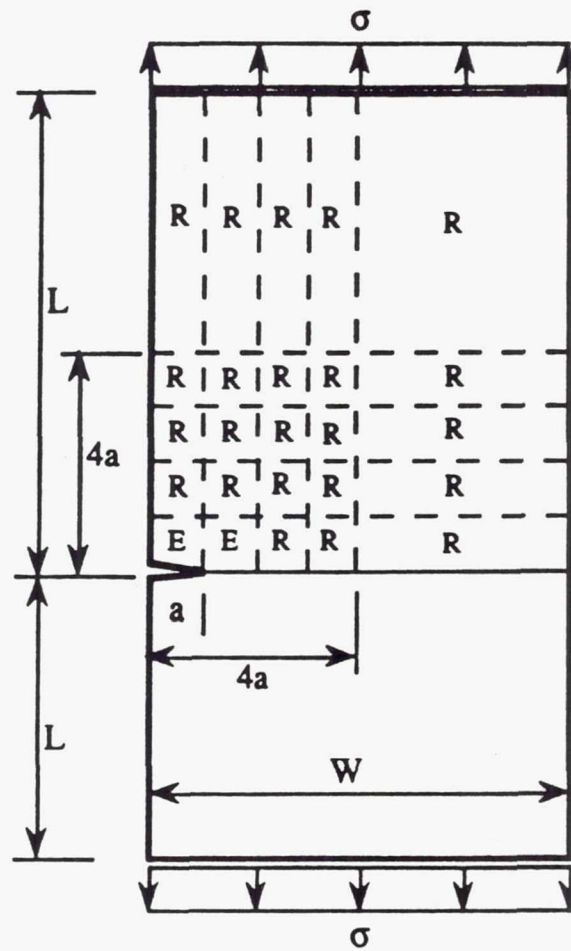
The method is also being applied to fatigue crack growth. Due to the combined effects of external loading, unsymmetrical component geometry and crack geometry, cracks rarely grow in a straight line. In a finite element method, a scheme for remeshing is required during the crack growth. In order to avoid the numerical complexity in remeshing and provide highly accurate solutions in both crack path and the relation between the crack length and stress intensity factors, an alternative approach based on the Boundary Integral Equation Method (BIEM) is developed for a multi-region embedded with a crack. The applicability of this method is demonstrated by the following two problems: 1) a rectangular plate with a circular hole under simple tension, where a crack emanates from the hole at the maximum stress point (see Figs 3a-3b), 2) a rectangular plate with an inclined edge crack under simple tension (see Figs 4a-4b). The first-order reliability analysis for a curved fatigue crack emanated from a hole is also formulated by a constrained optimization problem. The effects of uncertainty on the crack path and fatigue life are investigated. The Monte Carlo simulation is employed to check the accuracy of the first-order reliability analysis.

Uncertainties in the material properties of advanced materials such as polycrystalline alloys, ceramics and composite are commonly observed from experimental tests. This is mainly attributed to intrinsic microcracks, which are randomly distributed as a result of the applied load and the residual stress. In order to quantify the inherent statistical distribution, a stochastic damage model (see Fig.5) has been proposed most recently by Lua et al. [5-6]. The model, based on macrocrack-microcrack interaction, incorporates uncertainties in locations, orientations and numbers of microcracks. Due to the high concentration of microcracks near the macro-tip, a higher order analysis based on traction boundary integral equations is formulated first for an arbitrary array of cracks. The effects of uncertainties in locations, orientations and numbers of microcracks at a

macro-tip are analyzed quantitatively in [5-6] by using the BIEM in conjunction with the computer simulation of the random microcrack array. The statistical nature of the fracture toughness is compared to the Neville function in Figs. 6a and 6b for both dilute and highly concentrated microcracks. This model can also serve as a semi-empirical tool for predicting the fracture toughness based on a statistical characterization of the geometric parameters of microcracks, which can be obtained experimentally.

REFERENCES

- [1] W. K. Liu, T. Belytschko, and A. Mani, Random field finite elements. *Int. J. Numer. Methods Eng.* **23**, 1831-1845 (1986).
- [2] W. K. Liu, G. H. Besterfield and T. Belytschko, Variational approach to probabilistic finite elements. *J. Eng. Mech. ASCE*, **114**, 2115-2133 (1988).
- [3] G. H. Besterfield, W. K. Liu, M. Lawrence, and T. Belytschko, Brittle fracture reliability by probabilistic finite elements. *J. Eng. Mech. ASCE*, **116**, 642-659 (1990).
- [4] G. H. Besterfield, W. K. Liu, and T. Belytschko, Fatigue crack growth reliability by probabilistic finite elements, to appear in *Computer Method in Applied Mechanics and Engineering*.
- [5] Y. J. Lua, W. K. Liu and T. Belytschko, A stochastic damage model for the rupture prediction of a multi-phase solid: Part I: Parametric studies, submitted to *Int. J. Fracture Mech.*.
- [6] Y. J. Lua, W. K. Liu and T. Belytschko, A stochastic damage model for the rupture prediction of a multi-phase solid: Part II: Statistical approach, submitted to *Int. J. Fracture Mech.*.



| Parameter | Mean | Standard Deviation | Percent |
|--|-----------------------|-----------------------|---------|
| Length (L) | 10.0 in | 0.0 | 0.0 |
| Width (W) | 4.0 in | 0.0 | 0.0 |
| Thickness (t) | 1.0 in | 0.0 | 0.0 |
| Young's Modulus (E) | 30,000.0 ksi | 0.0 | 0.0 |
| Poisson's Ratio (ν) | 0.3 | 0.0 | 0.0 |
| Applied Stress (t) | 12.0 ksi | 3.0 ksi | 25.0 |
| Initial Crack Length (a_1) | 0.01 in | 0.01 in | 100.0 |
| Final crack Length (a_f) | 0.1 in | 0.01 in | 10.0 |
| Fatigue Parameter (D) | 1.0×10^{-10} | 3.0×10^{-11} | 30.0 |
| Fatigue Parameter (n) | 3.25 | 0.08 | 2.5 |
| Note: 1 in. = 0.0254 m 1 ksi = 6.89 kPa | | | |

Figure 1. Problem Statement for Single Edge-Cracked Beam with an Applied Load.

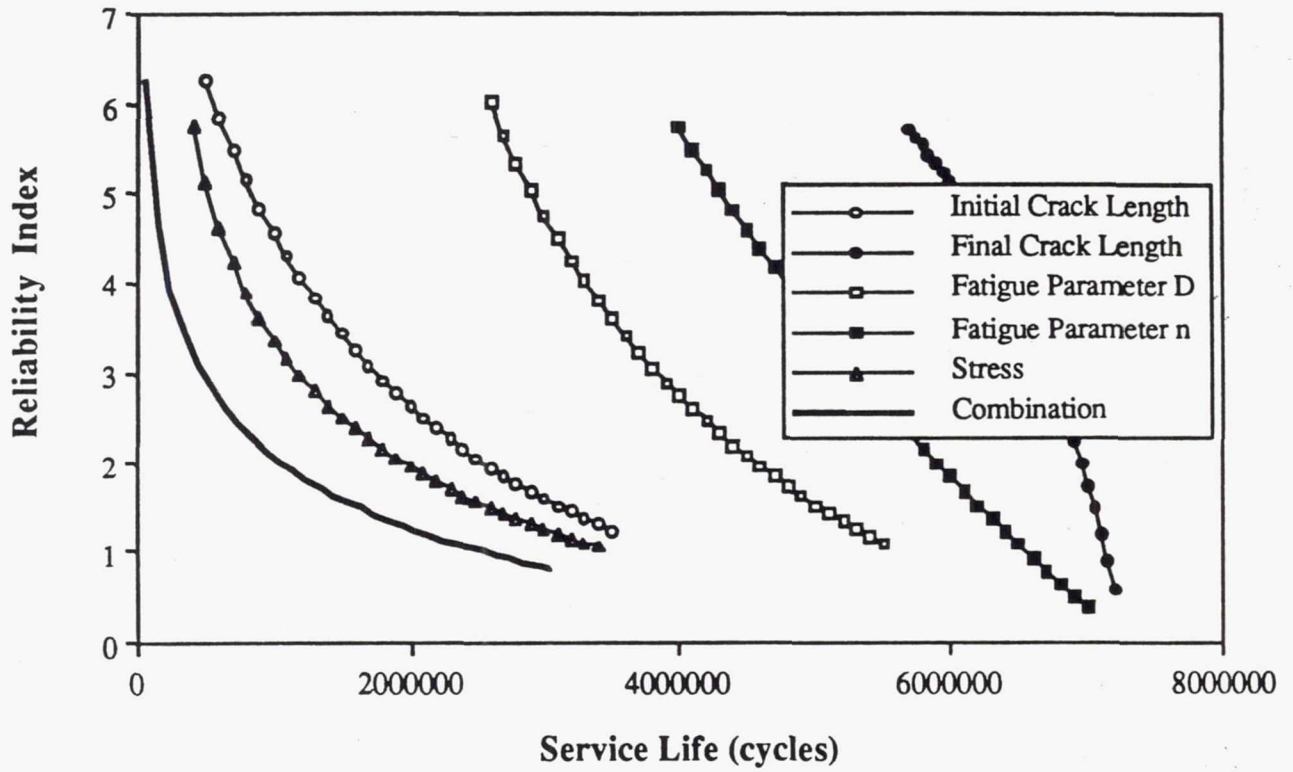


Figure 2. Reliability Index for the FEM Solution Comparing the Effects of Uncertainty in the Individual Variables and their Combined Effect.

Material Constants: $\mu=80,000$ ksi, $\nu=0.25$

Crack Path: Straight Line (Pure Mode I)

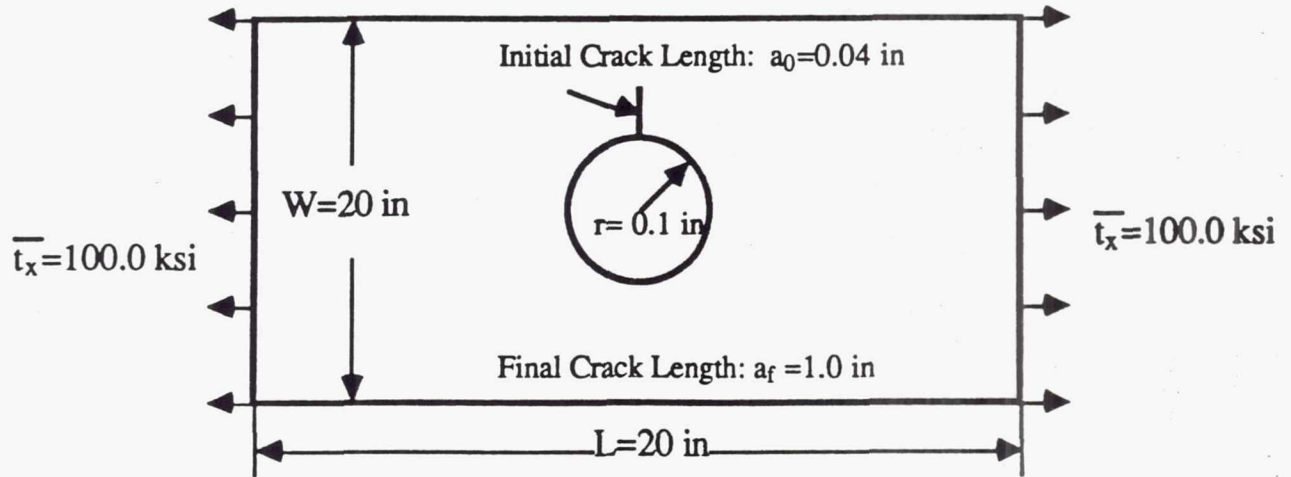


Figure 3a. Problem Statement for a Rectangular Plate with a Crack Emanating from a Hole under Uniaxial Tension.

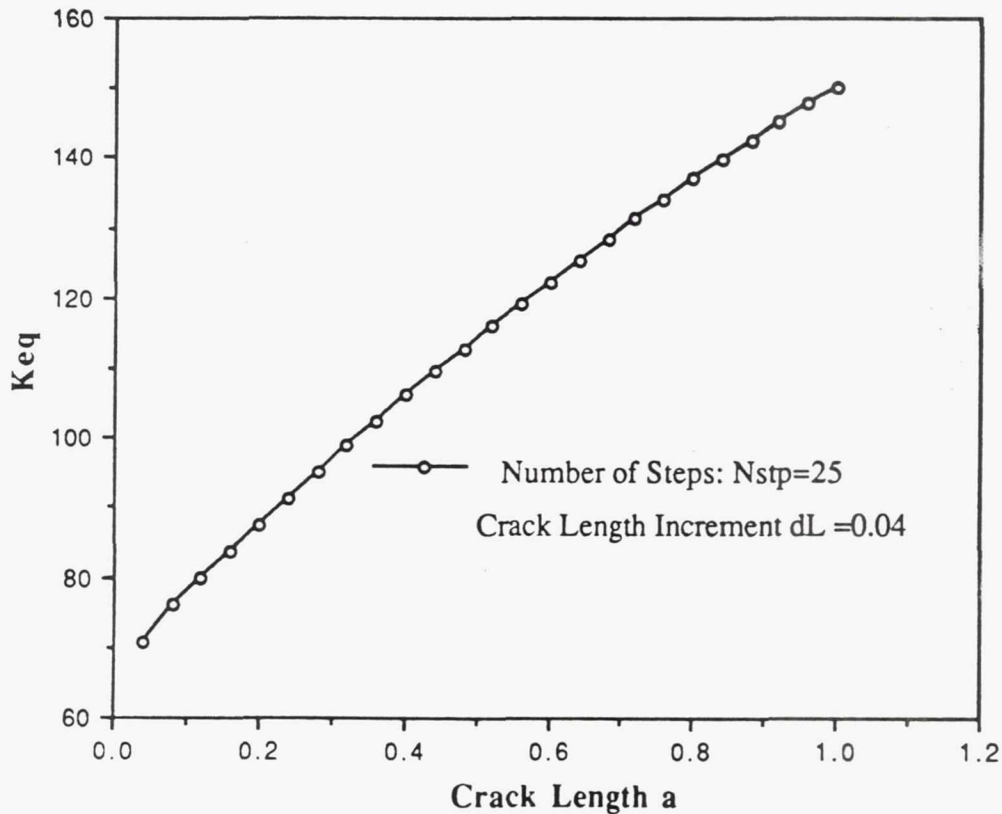


Figure 3b. Relation between the Equivalent Stress Intensity Factor Keq and the Crack Length for the Problem of a Rectangular Plate with a Crack Emanating from a Hole under Uniaxial Tension.

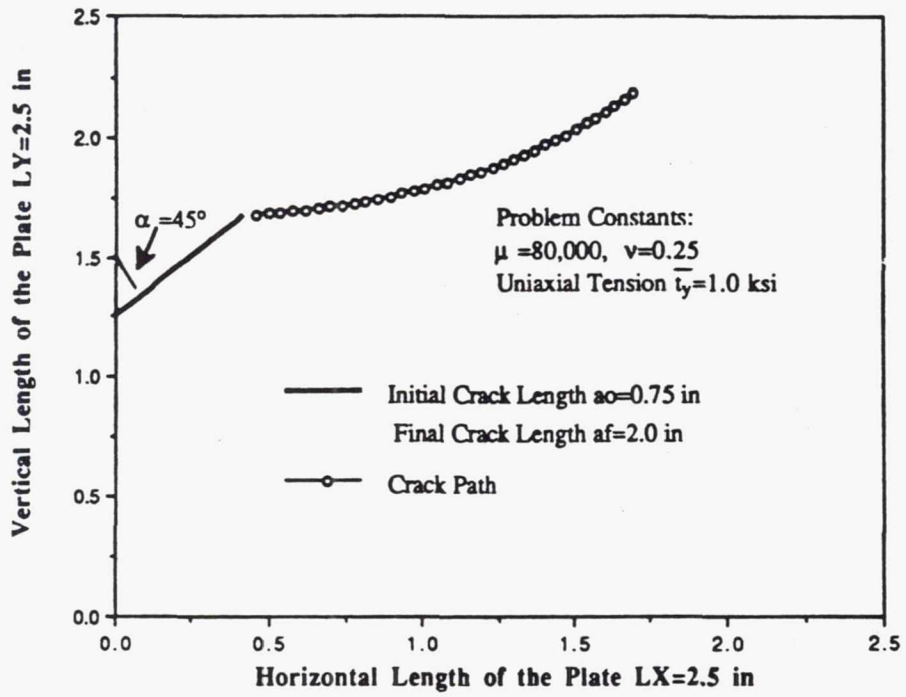


Figure 4a. Crack Path for an Inclined Edge-Cracked Plate under Uniaxial Tension.

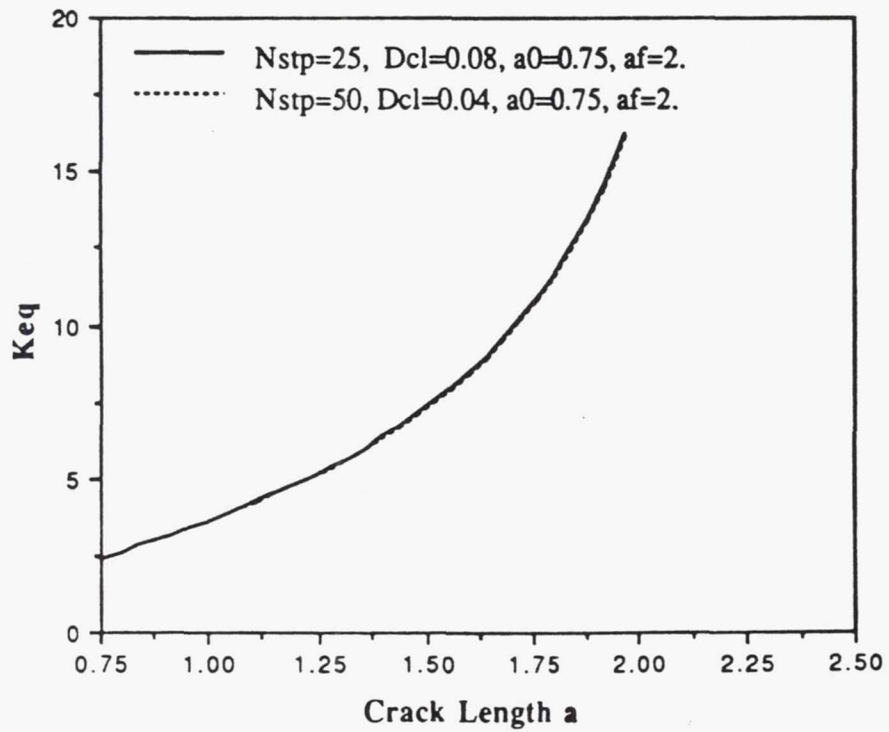


Figure 4b. Relation between the Equivalent Stress Intensity Factor K_{eq} and Crack Length a for an Inclined Edge-Cracked Plate under Uniaxial Tension.

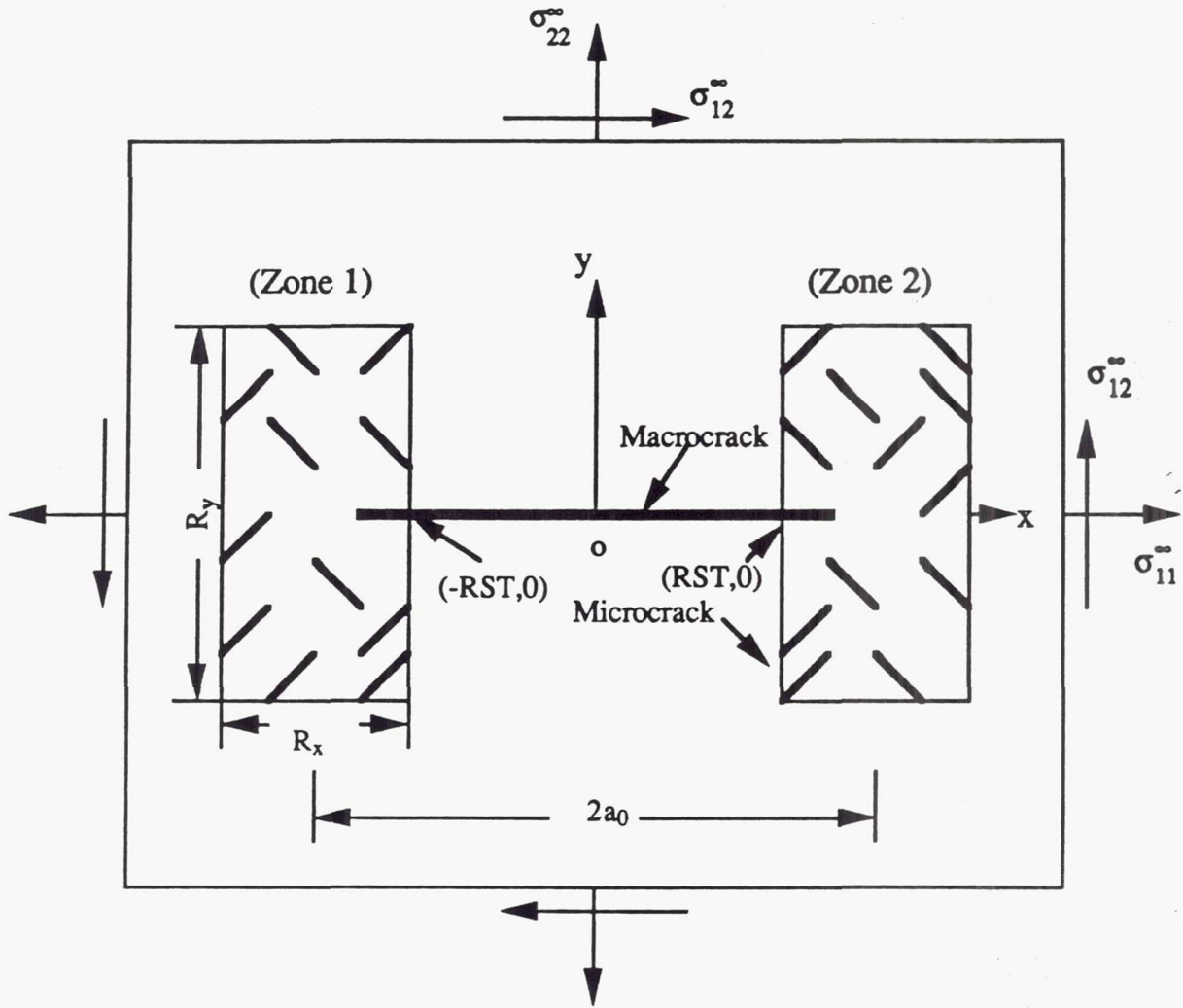


Figure 5. A Damage Saturation Model for a Brittle Multi-Phase Solid.

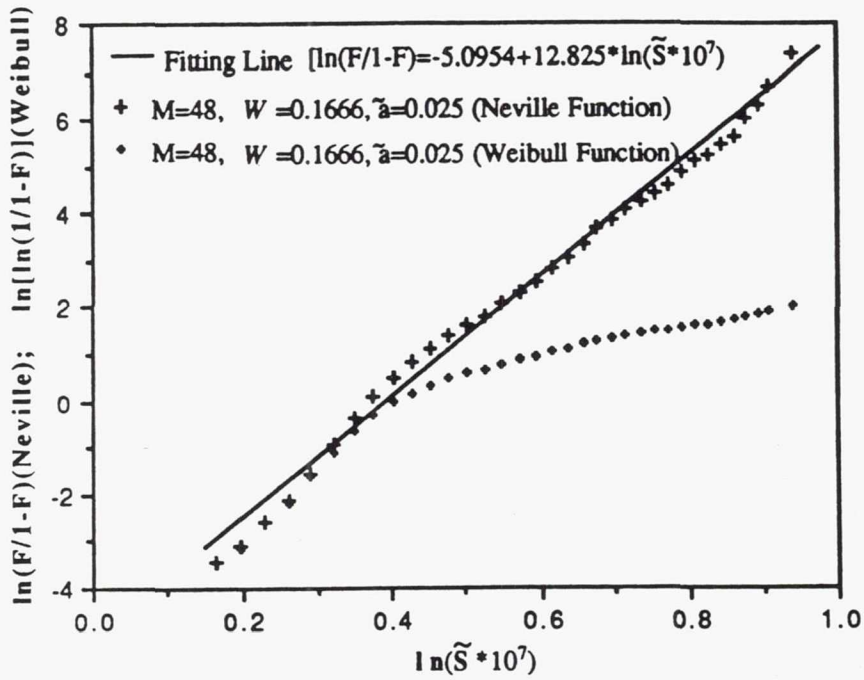


Figure 6a. Neville and Weibull Plots of the Intensity of Strain Energy Density \tilde{S} for Low Microcrack Concentration $W = 0.1666$.

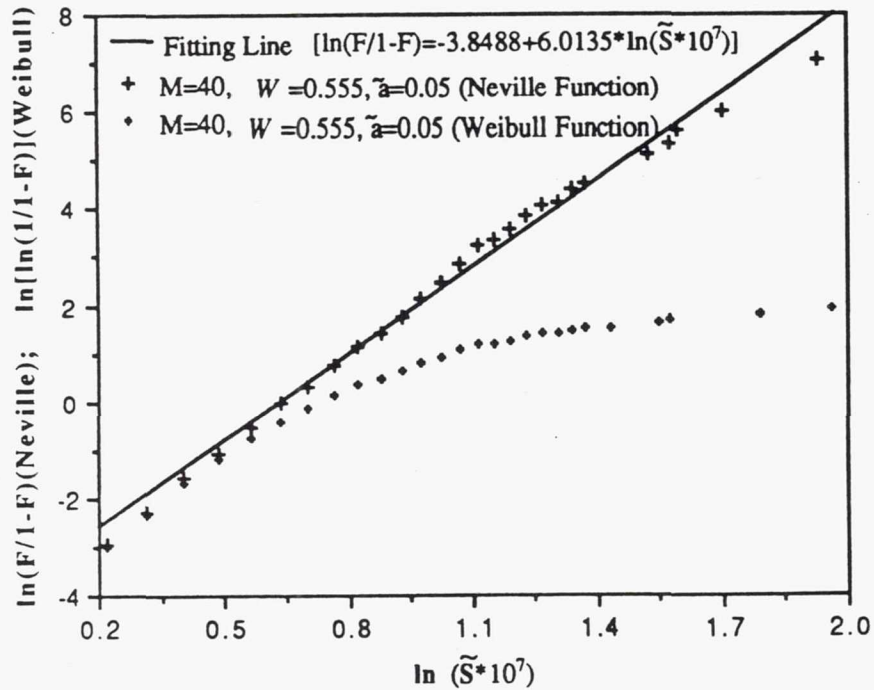


Figure 6b. Neville and Weibull Plots of the Intensity of Strain Energy Density \tilde{S} for Microcrack Concentration $W = 0.5555$.

MAPPING METHODS FOR COMPUTATIONALLY EFFICIENT AND ACCURATE STRUCTURAL RELIABILITY

Michael C. Shiao
Sverdrup Technology, Inc.
Lewis Research Center Group
Brook Park, Ohio 44142

and

Christos C. Chamis
NASA Lewis Research Center
Cleveland, Ohio 44135

The structures community has recognized that uncertainties in the structural parameters as well as in the service environments need to be considered in evaluating structural integrity and reliability. Probabilistic structural analyses are formal methods to include those uncertainties. However, these methods are inherently computational intensive because of the large number of deterministic analyses required to accurately simulate the effect of the uncertainties on the desired structural response (such as stress, displacement, and frequency) required for structural reliability assessment. Moreover, modern structures are often analyzed by finite element methods. Probabilistic structural analyses using finite element models can be economical when relatively coarse meshes are employed. Finite element analyses using coarse meshes not only raise questions regarding the convergence to the deterministic values, but also significantly alter the true probabilistic distributions of the structural responses.

It is important, therefore, to evaluate the influence of mesh coarseness on the accuracy of structural reliability. Several alternatives were recently examined at Lewis. The objectives of this presentation are to briefly describe these alternatives and to demonstrate their effectiveness. The results show that special mapping methods can be developed by using (1) deterministic structural responses from a fine (convergent) finite element mesh, (2) probabilistic distributions of structural responses from a coarse finite element mesh, (3) the relationship between the probabilistic structural responses from the coarse and fine finite element meshes, and (4) probabilistic mapping. The structural responses from different finite element meshes are highly correlated. Using this correlation together with the probabilistic potential energy variation principle (ref. 1) that determines the mean and standard deviation of a structural response for a given finite element mesh, one can obtain the linear relationships shown in equation (1):

$$X_f = A X_c + B \quad (1)$$

where X_f and X_c are the random responses from fine and coarse meshes, respectively, and A and B are constants. Three relationships are derived for three different mapping methods. Shift mapping considers only the first moment correction: A in equation (1) is equal to 1, and B is the

difference between the deterministic responses from fine and coarse meshes. Shift mapping states that the shapes of the probabilistic distribution functions of structural responses are the same for different meshes, but their mean values vary. Ratio mapping is from a second moment correction: A in equation (1) is the ratio of fine and coarse mesh deterministic responses, and B is equal to zero. Ratio mapping represents not only the fact that the mean values are different but also that the scatters around the mean can be either wider or narrower. Therefore, only the reduced response variables are considered to be the same. Mixed mapping is the average of shift and ratio mapping. Once this relationship is developed, probabilistic mapping can be applied.

Four examples were studied to verify this methodology. The computer code NESSUS (Numerical Evaluation of Stochastic Structures Under Stress) (ref. 2) was used to perform the probabilistic structural analyses. In the first example, a cantilever plate subjected to lateral pressure was analyzed. Plate thickness and the uniform pressure were considered to be random variables. In the second example, a buckling analysis of a simply supported composite plate was performed. The random variables were the coefficients of the stiffness matrix for the stress resultants/generalized strains relations. The probabilistic distributions of those coefficients were computed by the computer code PICAN (Probabilistic Integrated Composite Analyzer). In the third example, a cantilever plate subjected to thermal and mechanical loads was analyzed. Three random fields (uncertainties) were considered - thickness, modulus, and temperature. Each field consisted of correlated nodal random variables, and the loads at the free edge were also considered to be random. The structural parameters, such as modulus and strength, deteriorated under the aggressive service environments. These effects were characterized by the Multi-Factor Interaction Model (ref. 3). In this example, even with a poor mesh (16 percent error in the deterministic response), the probabilistic distribution of the response and the structural reliability using ratio mapping compare very well with those using fine finite element mesh. In addition, the ratio of the computational time using coarse and fine mesh was about 1:20. In the final example, a tapered cantilever plate with variable thickness was studied. The uncertainties considered were the same as in the previous example. In each example, only the maximum effective stresses from coarse and fine meshes using different mapping methods were compared. From examples 1 and 2, we verified the equality of the ratios r_1 and r_2 as defined in the viewgraph "Comparisons Between Probabilistic Distributions from Different Mapping Methods, Cantilever Plate Subjected to Uniform Load." This is essential to the derivation of the ratio mapping. We also found that (1) the shift mapping works well only with a good coarse mesh; (2) ratio mapping, which provides very accurate probabilistic distribution and the structural reliability even with a very coarse mesh, is highly recommended; and (3) results from mixed mapping always lie between those from shift and ratio mapping.

In conclusion, mapping methods were developed to perform probabilistic structural analyses by using coarse finite element meshes. High accuracy was achieved, and computational time was saved. Therefore, the dilemma experienced using either coarse or fine meshes for the probabilistic structural analyses was resolved.

REFERENCES

1. Liu, W.K.; Mani, A.; and Belytschko, T.: Finite Element Methods in Probabilistic Mechanics. Probabilistic Engineering Mechanics, vol. 2, no. 4, Dec. 1987, pp. 201-213.
2. Probabilistic Structural Analysis Methods for Select Propulsion System Components (PSAM). Vols. 1-3, NASA CR-185125-Vol-1,-2,-3, 1989.
3. Shiao, M.C.; and Chamis, C.C.: A Methodology for Evaluating the Reliability and Risk of Structures Under Complex Service Environments. 31st Structures, Structural Dynamics and Materials Conference, part 2, AIAA, 1990, pp. 1070-1080.

Presentation Outline

- Background
- Objective
- Mathematical foundation and derivation
- Numerical examples
- Concluding remarks

CD-91-52188

Background

- Probabilistic structural analysis using convergent finite element mesh is computationally inefficient
 - Large amount of CPU time is needed
 - Long turn-around time is expected
- Probabilistic structural analysis using coarse finite element mesh may not provide accurate results
- Accuracy can be improved by
 - Shifting the mean
 - Adjusting the scatter around the mean

CD-91-52189

Objective

Develop methods to increase the efficiency and to improve the accuracy of probabilistic structural analysis using coarse finite element mesh

CD-91-52190

Mathematical Foundation for Various Mapping Methods

- Probabilistic structure responses from different finite element meshes are highly correlated
- Mean and standard deviation are determined by probabilistic potential energy variation principle (Liu, Mani, and Belytschko (ref. 1))

$$E(X) = X^0 - \sum_{k=1}^N (X_k'' \sigma_k^2)$$

$$\sigma_X^2 = \sum_{k=1}^N (X_k')^2 \sigma_k^2$$

where

X probabilistic structural response for given mesh

X^0 deterministic value

X_k' $\partial X / \partial U_k$ where U_k is k^{th} independent random variable

X_k'' $\partial^2 X / \partial U_k^2$

σ_k standard deviation of U_k

CD-91-52191

Probabilistic Relationship for Shift Mapping First Moment Correction

From

$$X_f - E(X_f) = X_c - E(X_c)$$

$$X_f = X_c - X_c^0 + X_f^0 + \sum_{k=1}^N (X_c)''_k \sigma_k^2 - \sum_{k=1}^N (X_f)''_k \sigma_k^2$$

Since

$$\sum_{k=1}^N (X_c)''_k \sigma_k^2 - \sum_{k=1}^N (X_f)''_k \sigma_k^2 \text{ is small,}$$

$$X_f \cong X_c - X_c^0 + X_f^0$$

- X_f and X_c are the probabilistic structural responses from fine and coarse finite element meshes.

CD-91-52192

Probabilistic Relationship for Ratio Mapping

Second Moment Correction

From

$$\frac{X_f - E(X_f)}{\sigma_{X_f}} = \frac{X_c - E(X_c)}{\sigma_{X_c}}$$

Letting

$$r_1 = \frac{X_f^o}{X_c^o} \quad \text{and} \quad r_2 = \sqrt{\frac{\sum (X_f)_k^2 \sigma_k^2}{\sum (X_c)_k^2 \sigma_k^2}}$$

$$X_f = r_2 X_c - r_2 (X_c^o - \sum (X_c)_k^2 \sigma_k^2) + (X_f^o - \sum (X_f)_k^2 \sigma_k^2)$$

Since

$$r_1 \equiv r_2$$

$$X_f \equiv \frac{X_f^o}{X_c^o} X_c$$

CD-91-52193

Probabilistic Relationship for Mixed Mapping

Combined First and Second Moment Mapping

Letting

$$X_f \equiv \frac{1}{2} (\text{shift mapping}) + \frac{1}{2} (\text{ratio mapping})$$

$$X_f \equiv \frac{1}{2} \left[1 + \frac{X_f^o}{X_c^o} \right] X_c + \frac{X_f^o - X_c^o}{2}$$

CD-91-52194

Probabilistic Response Can Be Accurately Predicted Using Coarse Finite Element Mesh By—

- (1) Computing the convergent deterministic response
- (2) Computing the probabilistic distribution of the response using coarse finite element mesh
- (3) Determining the probabilistic relationship between the coarse and fine finite element responses
- (4) Computing the true probabilistic distribution of the response using the results obtained from steps (1) to (3)

CD-91-52195

Probability of Damage Initiation

$$P_f = P(\sigma \geq s)$$

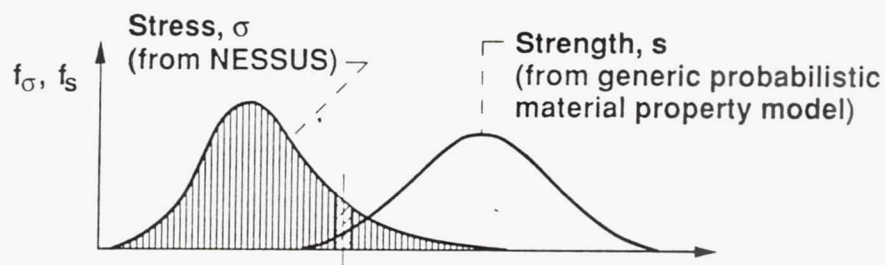
where

P_f probability

σ stress

s strength

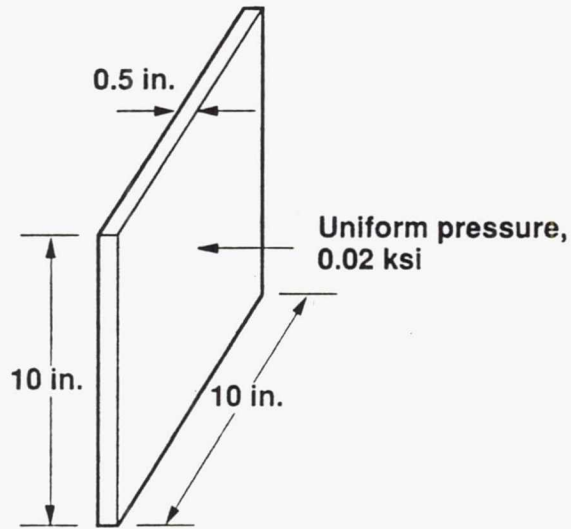
$$P_f = \int_{-\infty}^{\infty} \left(\int_{-\infty}^x f_s(s) ds \right) f_{\sigma}(x) dx$$



CD-91-52196

Probabilistic Stress Analysis of Cantilever Plate

- Uncertainties (random variables): plate thickness, lateral pressure

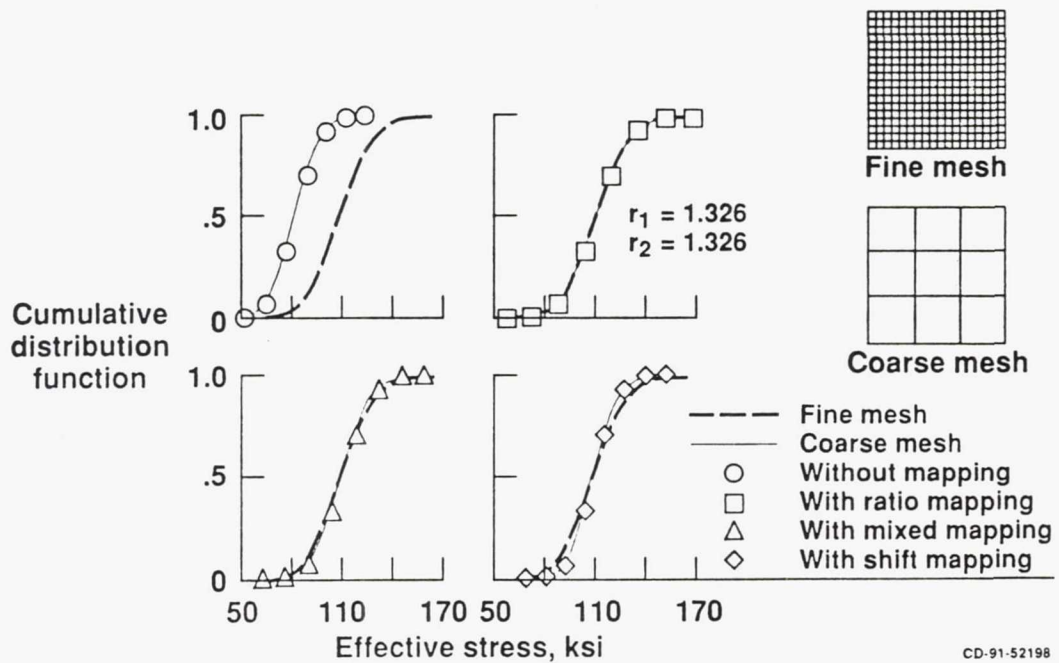


Geometry and Load

CD-91-52197

Comparisons Between Probabilistic Distributions From Different Mapping Methods

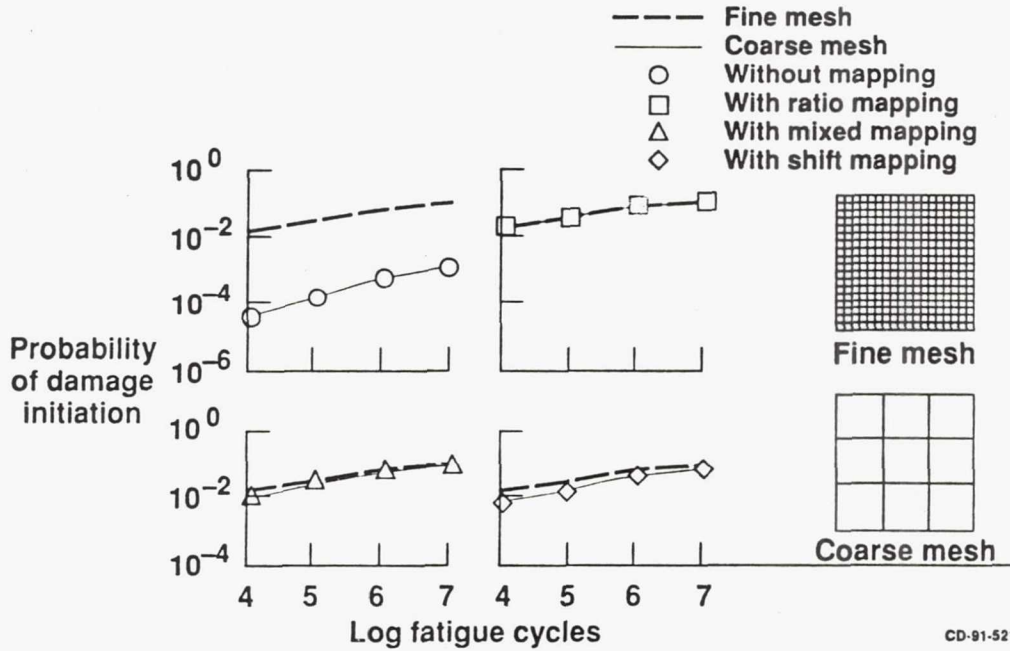
Cantilever Plate Subjected to Uniform Load



CD-91-52198

Comparisons Between Structural Reliabilities From Different Mapping Methods

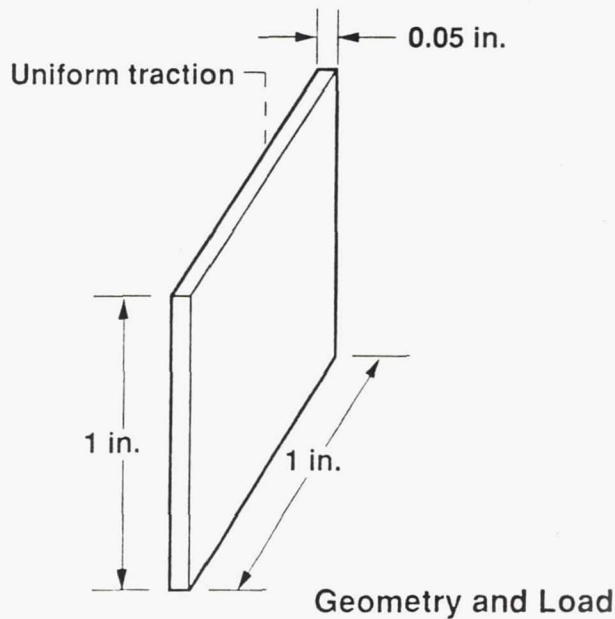
Cantilever Plate Subjected to Uniform Load



Probabilistic Buckling Analysis of a Simply Supported Composite Plate

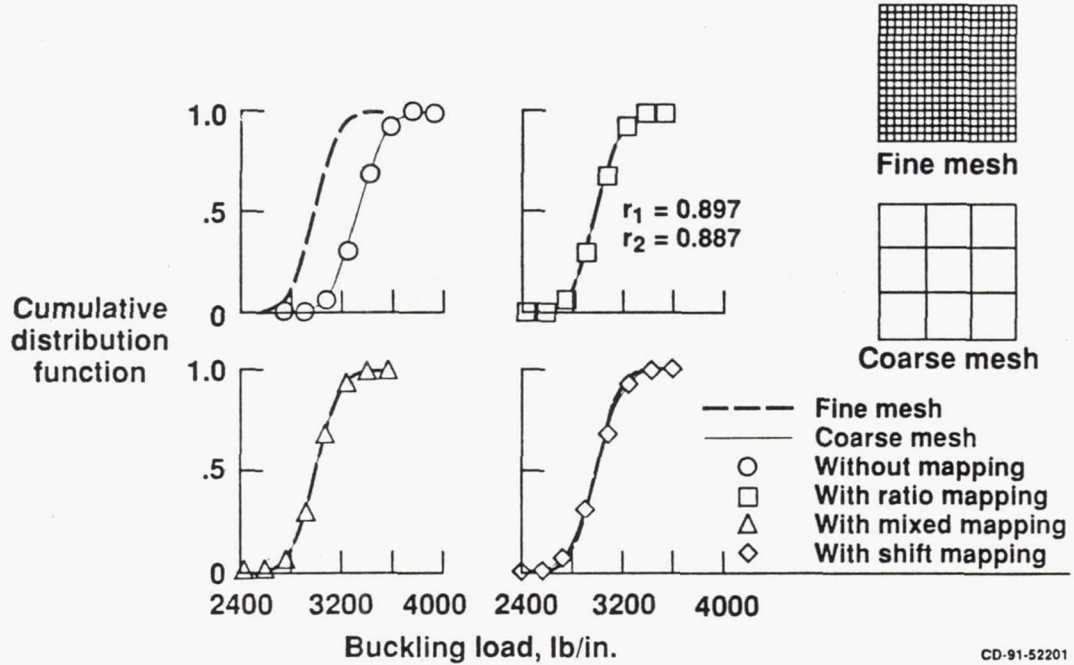
- Uncertainties (random variables): coefficients in [D] matrix

$$([M_x \ M_y \ M_{xy}]^T = [D] [K_x \ K_y \ K_{xy}]^T)$$



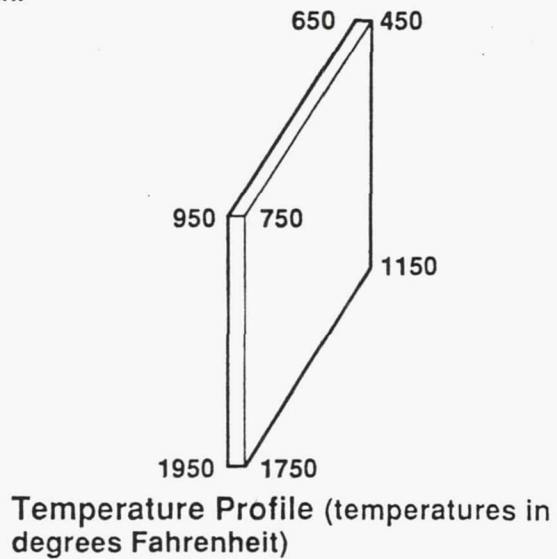
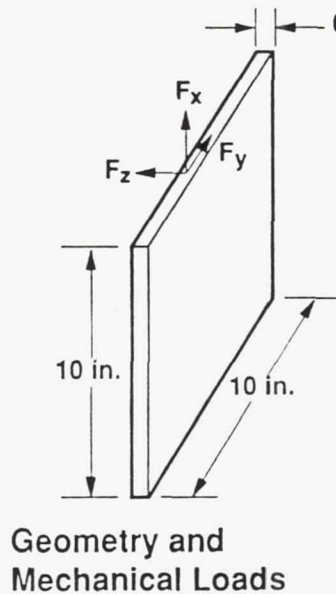
Comparisons Between Probabilistic Distributions From Different Mapping Methods

Buckling Analysis of Composite Plate



Probabilistic Stress Analysis of Cantilever Plate Subjected to Thermal and Mechanical Loads

- *Uncertainties (random fields):* thickness, modulus, temperature, and thermal and mechanical loads



CD-91-52202

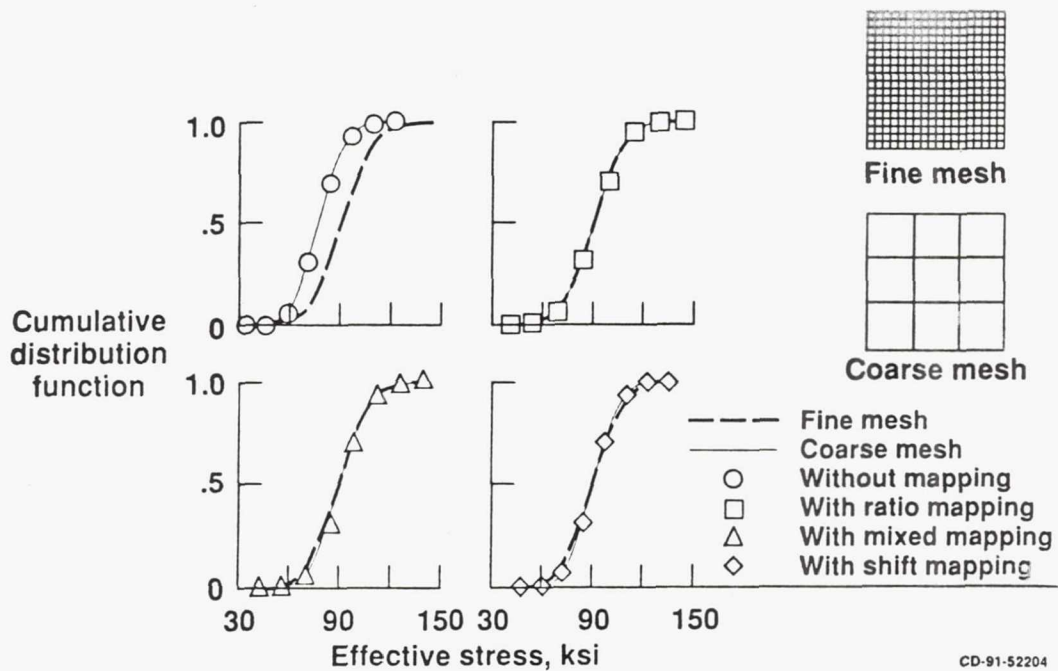
Deterministic Stress Analyses Using Different Finite Element Meshes

| Nodes | Deterministic stress | Error, percent | CPU time, sec |
|----------------|----------------------|----------------|---------------|
| 16 (4 by 4) | 75.4 | 16 | 0.9 |
| 25 (5 by 5) | 81.0 | 9 | 1.2 |
| 36 (6 by 6) | 83.9 | 6 | 1.7 |
| 49 (7 by 7) | 85.6 | 4 | 2.2 |
| 64 (8 by 8) | 86.7 | 3 | 2.9 |
| 81 (9 by 9) | 87.5 | 2 | 3.5 |
| 100 (10 by 10) | 88.1 | 1.5 | 4.5 |
| 361 (19 by 19) | 89.4 | 0 | 19.1 |

CD-91-52203

Comparisons Between Probabilistic Distributions From Different Mapping Methods

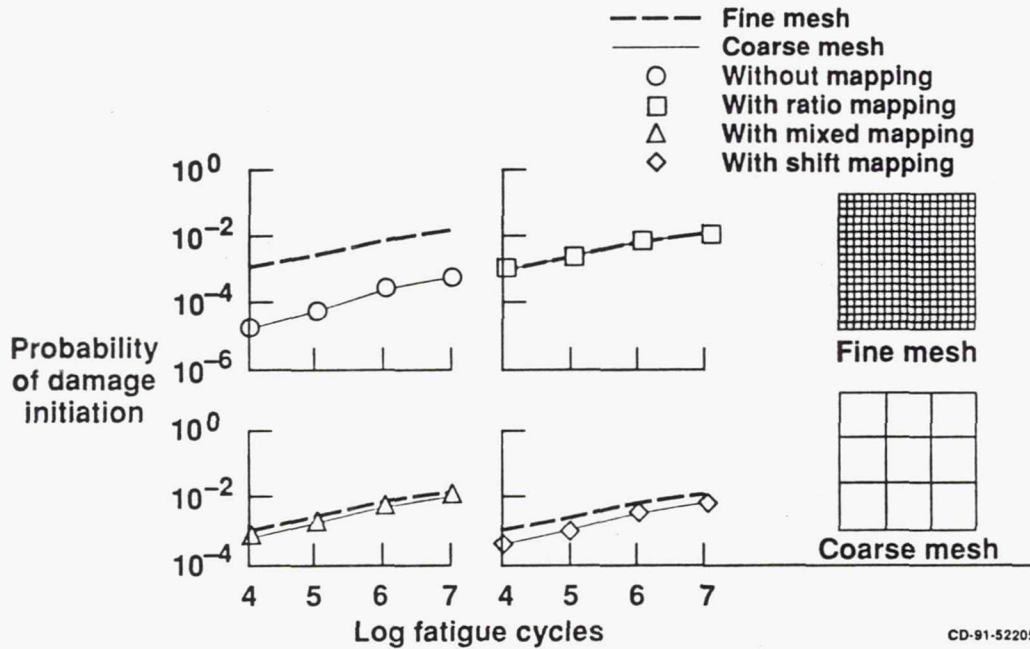
Cantilever Plate Subjected to Thermal and Mechanical Loads



CD-91-52204

Comparisons Between Structural Reliabilities From Different Mapping Methods

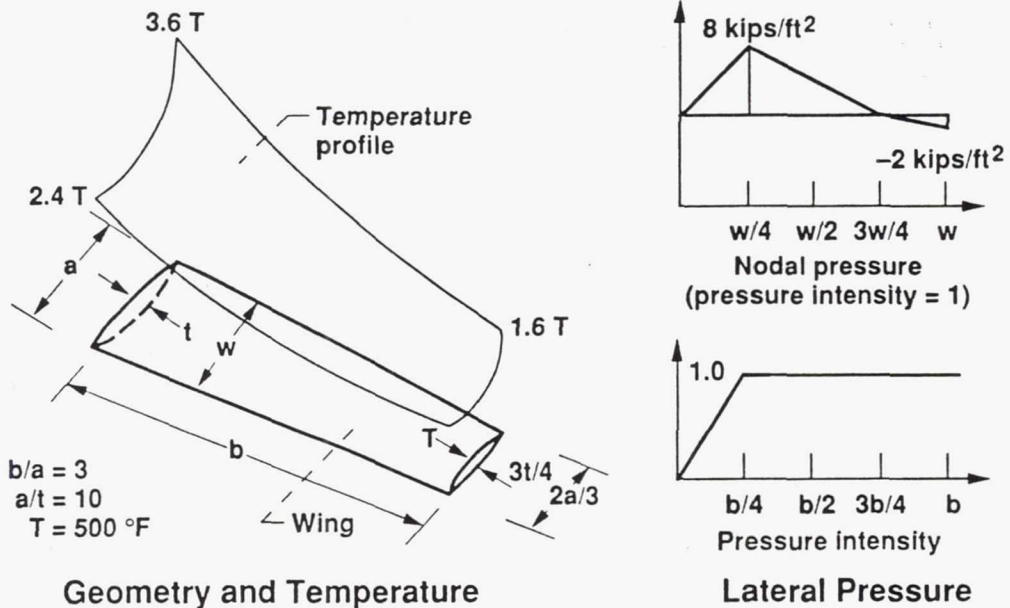
Cantilever Plate Subjected to Thermal and Mechanical Loads



CD-91-52205

Probabilistic Stress Analysis of Tapered Cantilever Plate

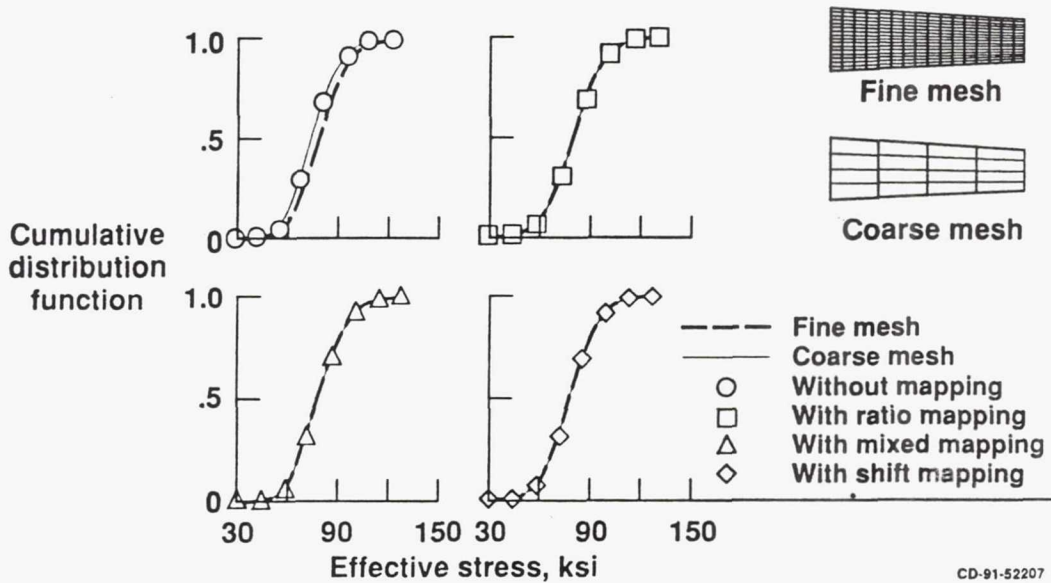
- Uncertainties (random fields): thickness, modulus, temperature, and thermal and mechanical loads



CD-91-52206

Comparisons Between Probabilistic Distributions From Different Mapping Methods

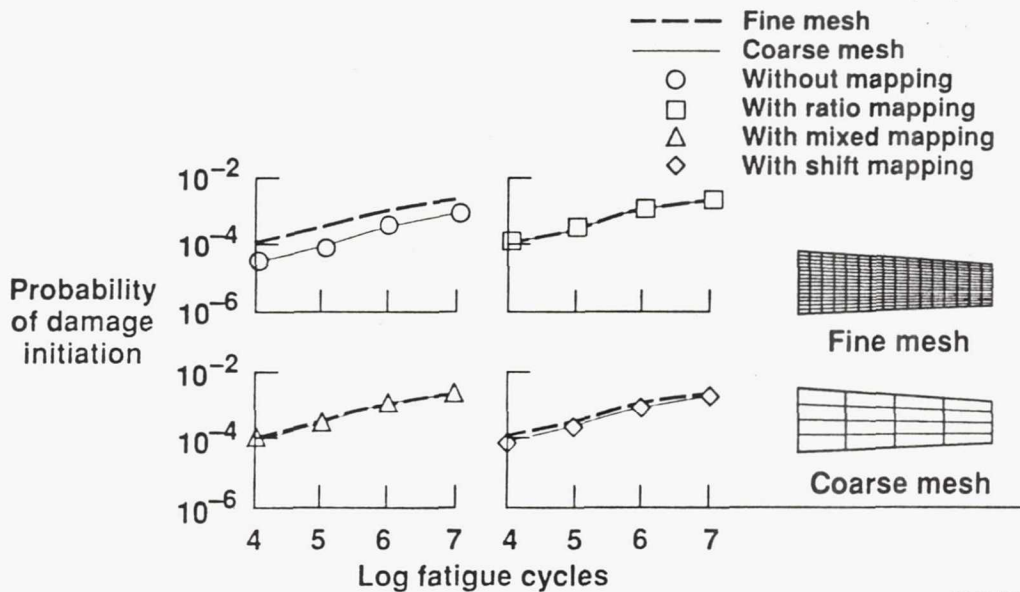
Tapered Cantilever Plate Subjected to Thermal and Mechanical Loads



CD-91-52207

Comparisons Between Structural Reliabilities From Different Mapping Methods

Tapered Cantilever Plate Subjected to Thermal and
Mechanical Loads



CD-91-52208

Concluding Remarks

Mapping methods have been developed—

- (1) To improve the accuracy of structural reliability
using coarse finite element meshes**
- (2) To save computational and turn-around time**
- (3) To evaluate reliability of large structural systems**

CD-91-52209

PROBABILISTIC SIMULATION OF THE HUMAN FACTOR IN STRUCTURAL RELIABILITY

Ashwin R. Shah
Sverdrup Technology, Inc.
Lewis Research Center Group
Brook Park, OH 44142

and

Christos C. Chamis
NASA Lewis Research Center
Cleveland, OH 44135

Many structural failures have occasionally been attributed to human factors in engineering design, analyses, maintenance and fabrication processes. The human factor is intertwined in all engineering activities to develop durable, safe and reliable products. Every facet of engineering process (planning, designing, manufacturing, inspection, maintenance, communication and coordination between different engineering disciplines) is heavily governed by human factors and the degree of uncertainty associated with them. Factors such as societal, physical, professional, psychological and many others introduce uncertainties that significantly influence the reliability of human performance. Quantifying human factors and associated uncertainties in structural reliability require (i) identification of the fundamental factors that influence human performance and (ii) models to describe the interaction of these factors.

For the purpose of an initial simulation, the fundamental factors assumed to affect human performance are: (i) health, (ii) home life, (iii) marital status, (iv) work load, (v) job satisfaction, (vi) professional status. It is ludicrous to presume that these are the only factors that influence human performance; however, they constitute a reasonable initial set. Since, these factors have tremendous variability on a timely basis, human performance also inherits the uncertainty associated with this variability. Therefore, it is more appropriate to simulate human performance from a probabilistic standpoint. Many researchers describe uncertainties of fundamental (primitive) factors in many different ways such as probability density function, stochastic process, fuzzy set approach, etc. Generally, these models are based on subjective information and description. An approach is being developed at Lewis to quantify the uncertainties associated with the human performance. This approach consist of a multi factor model in conjunction with direct Monte-Carlo simulation.

The objective of this presentation is to briefly describe the approach, present some initial results and interpret their implications. The Multi Factor Interaction Model (MFIM) similar to the one for material degradation developed by Boyce and Chamis is adopted to simulate human factor uncertainty. MFIM is based on the concepts of ultimate(maximum), current and reference level of each primitive factor effect. The contribution of a particular factor on the overall human performance is governed by the exponent assigned to it. The magnitude of an exponent can be determined by synthesizing any available data or

subjective expert opinion. MFIM for human performance, HP can be described mathematically as:

$$HP = \prod_{j=1}^k \left(\frac{HF_{u_j} - HF_j}{HF_{u_j} - HF_{o_j}} \right)^{p_j}$$

where

HF_{u_j} , HF_j and HF_{o_j} are ultimate, current and reference values of human performance due to an individual primitive factor j respectively.

p_j - Exponent corresponding to primitive factor j

k - total number of effects.

The approach developed herein models each term of the human factor uncertainty in the form of a probability density function and couples MFIM with the Monte-Carlo simulation to obtain cumulative distribution function of human performance. The effect of the exponent magnitude in the MFIM is evaluated by using different values and range of the exponents. The statistical distributions of exponents for each case of simulation is selected randomly from a desired range. The variation of human performance due to different range of exponent magnitude at different probability levels are plotted in the form of a bar chart. The cumulative distribution functions (CDF) of human performance are also plotted. Since, the quantification is in the form of CDFs, it is easy to incorporate it in the reliability algorithms.

Further work on probabilistic simulation of human performance is under progress. The research in several areas such as incorporating into the probabilistic structural analysis and risk assessment is under progress. The current paper describes the primary objectives, problems, analytical models and simulation techniques relevant to the prediction of human performance and its impact on structural reliability.

References:

1. Boyce, L. and Chamis C.C., "Probabilistic Lifetime Strength of Aerospace Materials Via Computational Simulation", 31st Structures, Structural Dynamics and Materials Conference, Long Beach, CA April 1990.

PRESENTATION OUTLINE:

- o **BACKGROUND**
- o **OBJECTIVE**
- o **APPROACH**
- o **SIMULATION PROCESS**
- o **RESULTS**
- o **CONCLUDING REMARKS**
- o **FUTURE EFFORT**

BACKGROUND:

- o **ATTRIBUTES TO ENGINEERING FAILURES**
 - MANUFACTURING
 - MATERIAL
 - OPERATION
 - MAINTENANCE
 - INSPECTION
 - HUMAN FACTOR
- o **UNCERTAINTIES ASSOCIATED WITH HUMAN FACTOR PLAYS SIGNIFICANT ROLE IN ENGINEERING ACTIVITY**

OBJECTIVE:

DEVELOP A METHODOLOGY TO SIMULATE HUMAN FACTOR UNCERTAINTY AND QUANTIFY THE HUMAN PERFORMANCE PROBABILISTICALLY

APPROACH:

o FUNDAMENTAL HUMAN FACTORS AFFECTING HUMAN PERFORMANCE

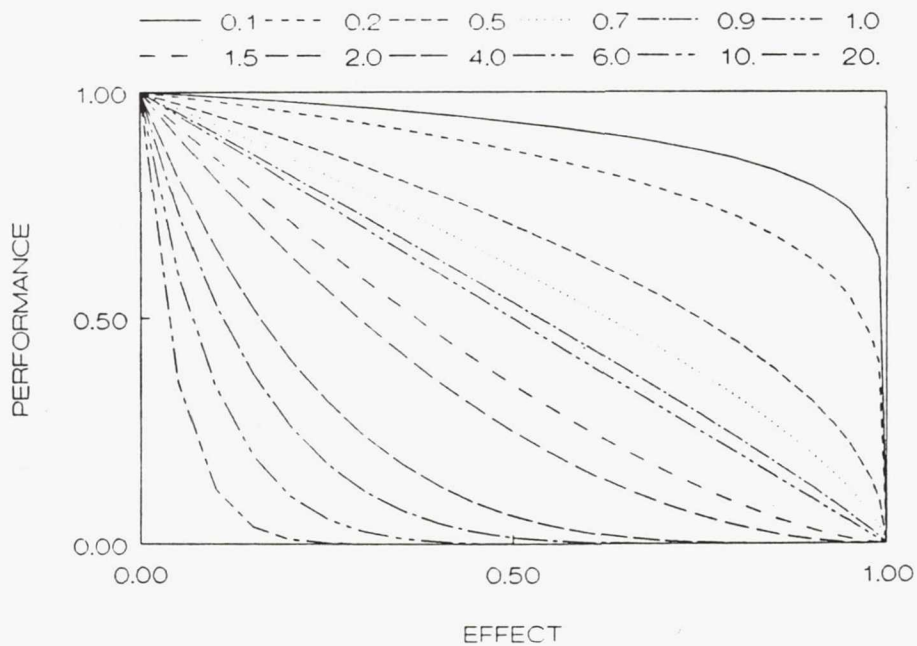
- PROFESSIONAL STATUS
- HOME LIFE
- JOB SATISFACTION
- HEALTH
- MARITAL STATUS
- WORK LOAD

o HUMAN PERFORMANCE, P IS EVALUATED BY USING MULTI-FACTOR INTERACTION MODEL FOR HUMAN FACTORS, HF:

$$P = \prod_{j=1}^k \left(\frac{HF_{w_j} - HF_l}{HF_{w_j} - HF_{o_j}} \right)^{p_j}$$

- o HF_j and p_j ARE CONSIDERED TO BE RANDOM AND NORMALLY DISTRIBUTED**
- o MONTE-CARLO SIMULATION IS USED FOR PROBABILISTIC ANALYSIS**

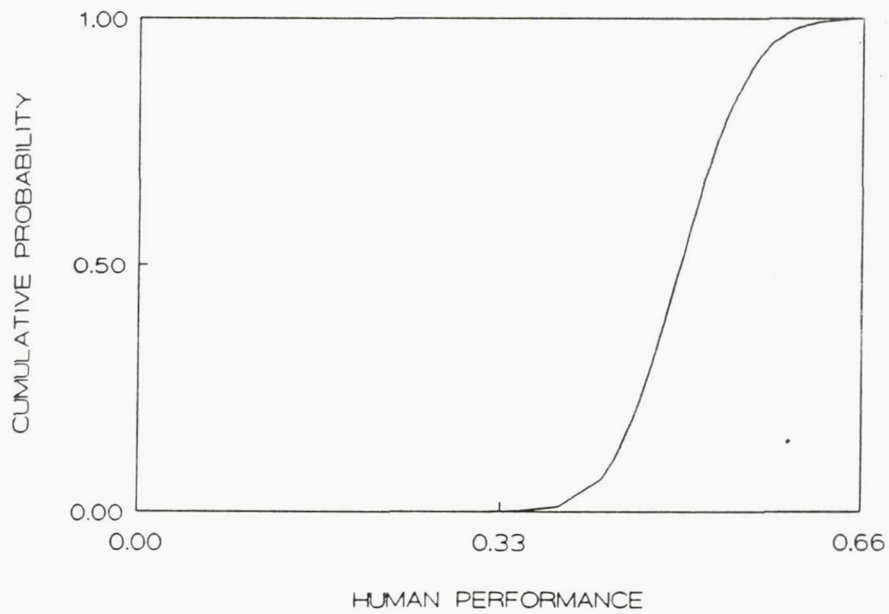
EFFECT OF VARIATION IN EXPONENT



**FUNDAMENTAL HUMAN FACTOR DISTRIBUTIONS:
EXPONENT BETWEEN RANGE (0-1)**

| Primitive Variable | | Mean | Coefficient of Variation (%) |
|----------------------|----------|-------|------------------------------|
| Professional Status | Final | 1.0 | 0.0 |
| | Current | 0.30 | 33.3 |
| | Exponent | 0.267 | 10.0 |
| Home Life | Final | 1.00 | 0.0 |
| | Current | 0.25 | 20.0 |
| | Exponent | 0.013 | 10.0 |
| Job Satisfaction | Final | 1.00 | 0.0 |
| | Current | 0.40 | 25.0 |
| | Exponent | 0.176 | 10.0 |
| Health | Final | 1.0 | 0.0 |
| | Current | 0.2 | 20.0 |
| | Exponent | 0.964 | 10.0 |
| Marital Satisfaction | Final | 1.0 | 0.0 |
| | Current | 0.30 | 26.7 |
| | Exponent | 0.252 | 10.0 |
| Work Load | Final | 1.0 | 0.0 |
| | Current | 0.35 | 22.9 |
| | Exponent | 0.466 | 10.0 |

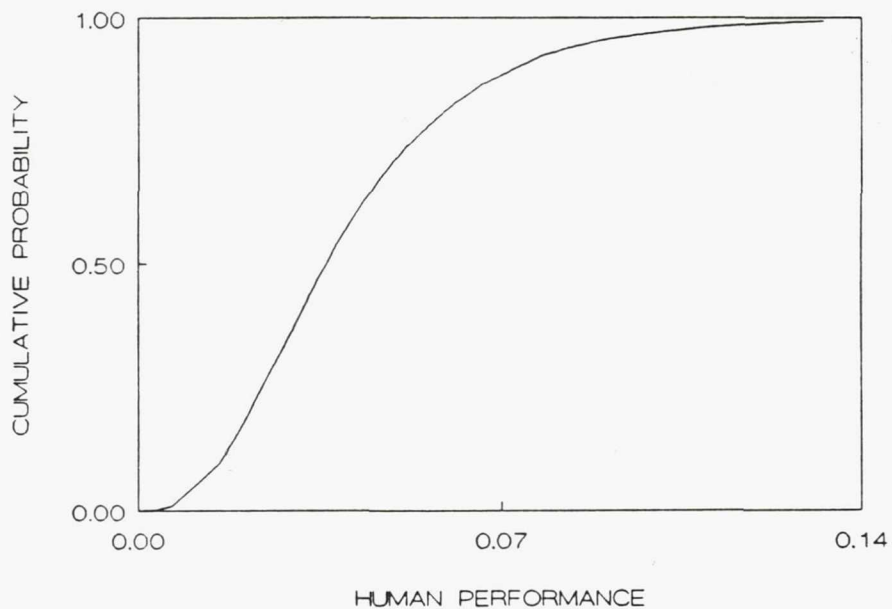
**CDF OF HUMAN PERFORMANCE
RANDOM EXPONENTS BETWEEN (0-1)**



**FUNDAMENTAL HUMAN FACTOR DISTRIBUTIONS:
EXPONENT BETWEEN RANGE (0-3)**

| Primitive Variable | | Mean | Coefficient of Variation (%) |
|----------------------|----------|-------|------------------------------|
| Professional Status | Final | 1.0 | 0.0 |
| | Current | 0.30 | 33.3 |
| | Exponent | 1.85 | 10.0 |
| Home Life | Final | 1.00 | 0.0 |
| | Current | 0.25 | 20.0 |
| | Exponent | 1.691 | 10.0 |
| Job Satisfaction | Final | 1.00 | 0.0 |
| | Current | 0.40 | 25.0 |
| | Exponent | 2.703 | 10.0 |
| Health | Final | 1.0 | 0.0 |
| | Current | 0.2 | 20.0 |
| | Exponent | 0.099 | 10.0 |
| Marital Satisfaction | Final | 1.0 | 0.0 |
| | Current | 0.30 | 26.7 |
| | Exponent | 0.852 | 10.0 |
| Work Load | Final | 1.0 | 0.0 |
| | Current | 0.35 | 22.9 |
| | Exponent | 1.005 | 10.0 |

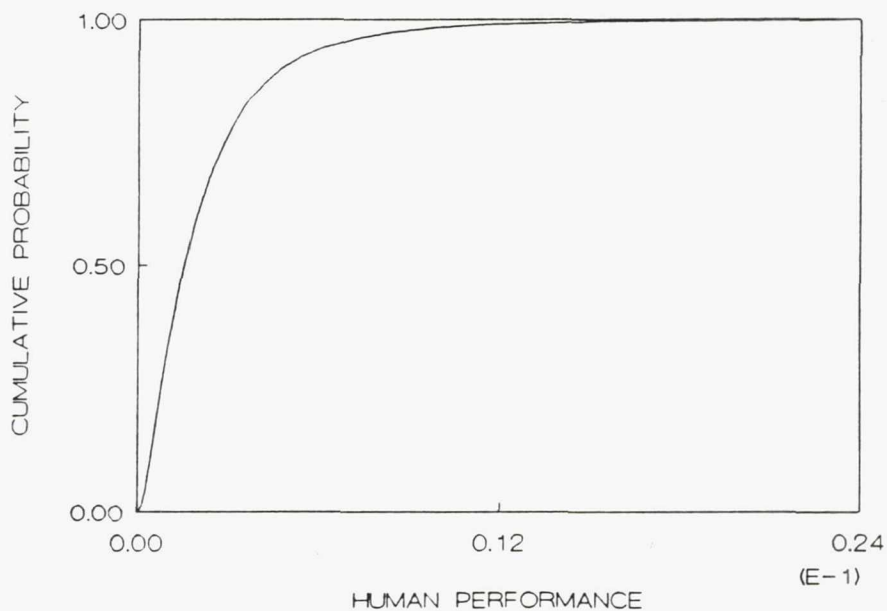
**CDF OF HUMAN PERFORMANCE
RANDOM EXPONENTS BETWEEN (0-3)**



**FUNDAMENTAL HUMAN FACTOR DISTRIBUTIONS:
EXPONENT BETWEEN RANGE (0-5)**

| Primitive Variable | | Mean | Coefficient of Variation (%) |
|----------------------|----------|-------|------------------------------|
| Professional Status | Final | 1.0 | 0.0 |
| | Current | 0.30 | 33.3 |
| | Exponent | 4.007 | 10.0 |
| Home Life | Final | 1.00 | 0.0 |
| | Current | 0.25 | 20.0 |
| | Exponent | 1.923 | 10.0 |
| Job Satisfaction | Final | 1.00 | 0.0 |
| | Current | 0.40 | 25.0 |
| | Exponent | 1.926 | 10.0 |
| Health | Final | 1.0 | 0.0 |
| | Current | 0.2 | 20.0 |
| | Exponent | 3.912 | 10.0 |
| Marital Satisfaction | Final | 1.0 | 0.0 |
| | Current | 0.30 | 26.7 |
| | Exponent | 2.897 | 10.0 |
| Work Load | Final | 1.0 | 0.0 |
| | Current | 0.35 | 22.9 |
| | Exponent | 3.597 | 10.0 |

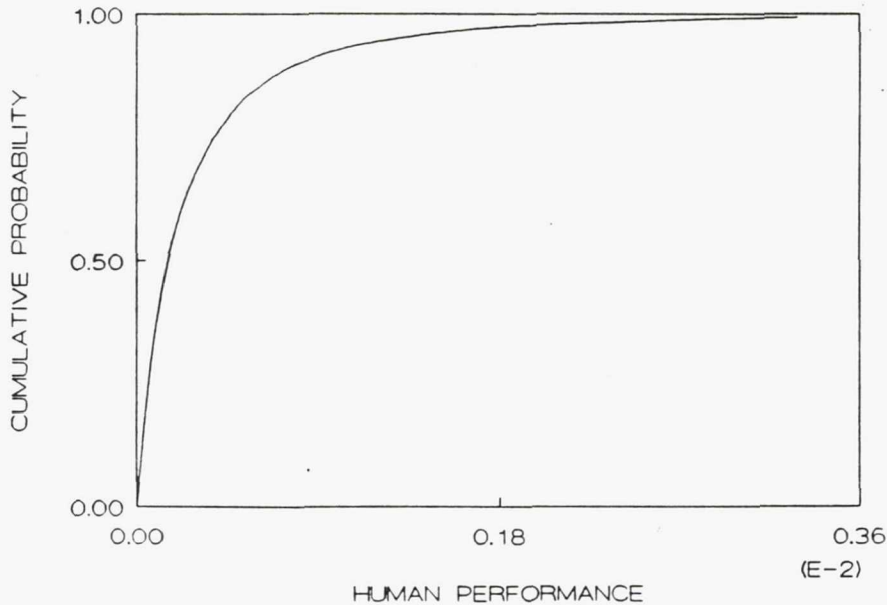
**CDF OF HUMAN PERFORMANCE
RANDOM EXPONENTS BETWEEN (0-5)**



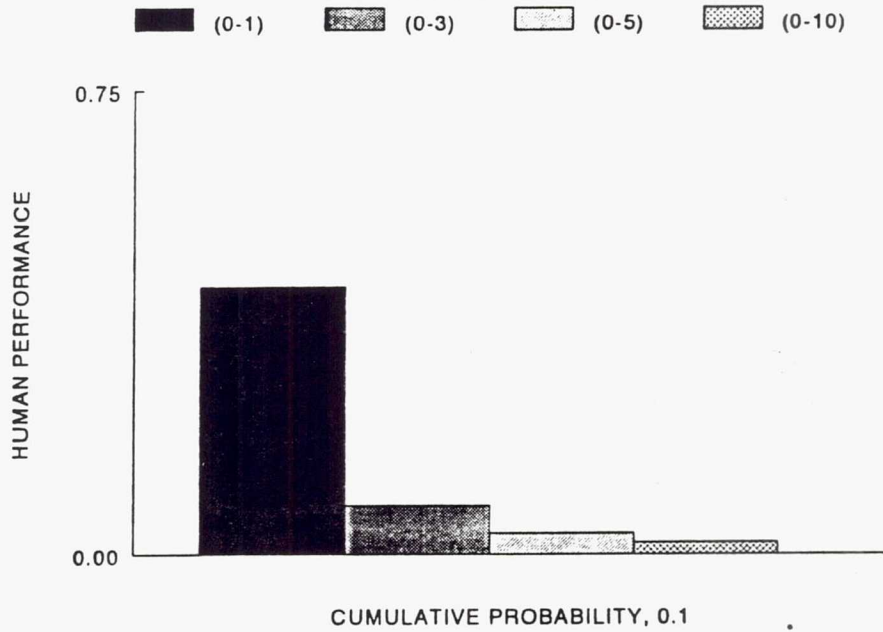
**FUNDAMENTAL HUMAN FACTOR DISTRIBUTIONS:
EXPONENT BETWEEN RANGE (0-10)**

| Primitive Variable | | Mean | Coefficient of Variation (%) |
|----------------------|----------|-------|------------------------------|
| Professional Status | Final | 1.0 | 0.0 |
| | Current | 0.30 | 33.3 |
| | Exponent | 5.431 | 10.0 |
| Home Life | Final | 1.00 | 0.0 |
| | Current | 0.25 | 20.0 |
| | Exponent | 6.903 | 10.0 |
| Job Satisfaction | Final | 1.00 | 0.0 |
| | Current | 0.40 | 25.0 |
| | Exponent | 0.518 | 10.0 |
| Health | Final | 1.0 | 0.0 |
| | Current | 0.2 | 20.0 |
| | Exponent | 1.737 | 10.0 |
| Marital Satisfaction | Final | 1.0 | 0.0 |
| | Current | 0.30 | 26.7 |
| | Exponent | 3.301 | 10.0 |
| Work Load | Final | 1.0 | 0.0 |
| | Current | 0.35 | 22.9 |
| | Exponent | 6.826 | 10.0 |

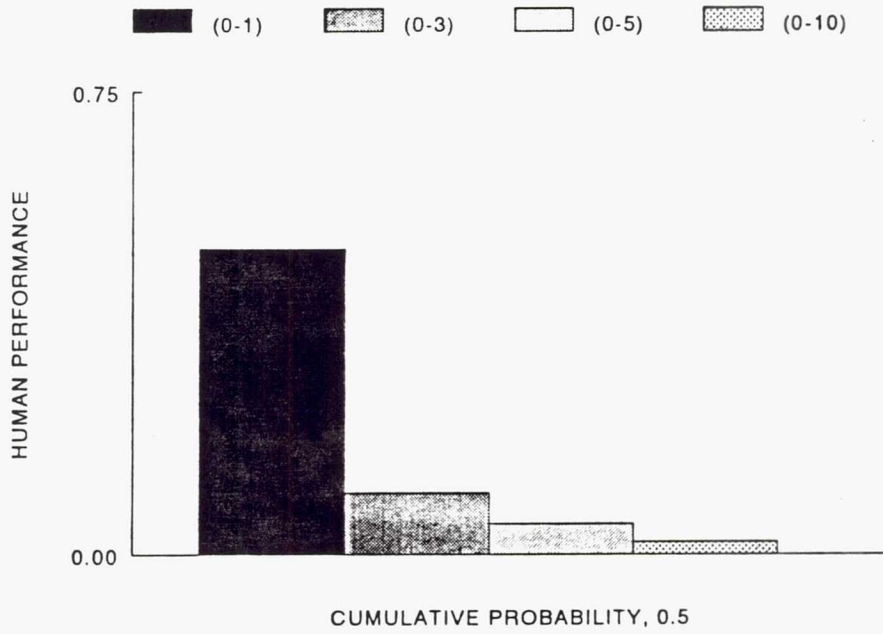
**CDF OF HUMAN PERFORMANCE
RANDOM EXPONENTS BETWEEN (0-10)**

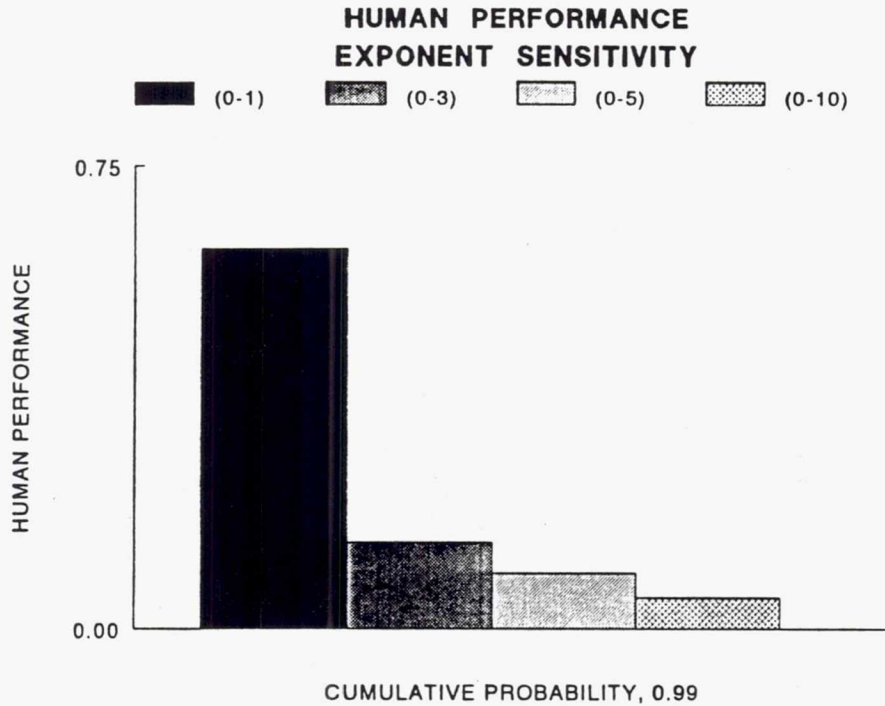


HUMAN PERFORMANCE EXPONENT SENSITIVITY



HUMAN PERFORMANCE EXPONENT SENSITIVITY





CONCLUSION:

- o METHODOLOGY TO QUANTIFY HUMAN PERFORMANCE UNCERTAINTY IS INITIATED
- o MULTI-FACTOR INTERACTION MODEL CAN BE USED TO SIMULATE HUMAN FACTOR UNCERTAINTIES
- o METHODOLOGY DEVELOPED IS CONSISTENT WITH RELIABILITY ALGORITHM DEVELOPED AT LEWIS RESEARCH CENTER

FUTURE EFFORT:

- o EXTENSION OF THE MULTI-FACTOR INTERACTION MODEL TO INCLUDE ADDITIONAL FACTORS THAT INFLUENCE HUMAN PERFORMANCE
- o INCORPORATION OF THE HUMAN FACTOR UNCERTAINTIES INTO PROBABILISTIC STRUCTURAL ANALYSIS AND RISK ASSESSMENT

OVERVIEW OF THE FATIGUE/FRACTURE/LIFE PREDICTION WORKING GROUP PROGRAM AT THE LEWIS RESEARCH CENTER

Michael A. McGaw
NASA Lewis Research Center
Cleveland, Ohio 44135

The objective of the Fatigue/Fracture/Life Prediction Working Group at Lewis is to develop and verify constitutive and life prediction models for materials typically used in hot gas path components of reusable space propulsion systems over the range of relevant operating environments. The efforts at Lewis have centered on the development of crack initiation life prediction methods, while the efforts of our counterpart group located at the Marshall Space Flight Center have centered on the development of cyclic crack propagation and fracture life prediction methods.

The tasks presently active in this program are shown in figure 1. This program is a blend of in-house, contract and grant research. Substantial progress has been made in many areas over the past year; many of the papers to be presented in this session document this progress.

Also included in this session are two papers from the Materials Working Group (Gayda, et. al., and Arya, et. al.), as well as a paper from the Instrumentation and Controls Working Group (Lorenzo, et. al.). The latter paper addresses a topic recently receiving a great deal of attention: rocket engine health monitoring and controls, specifically, the introduction of Life Extending Controls, an interdisciplinary activity showing the application of life prediction methodologies in new areas.

**LeRC FATIGUE/FRACTURE/LIFE
PREDICTION
WORKING GROUP**

PROGRAM SUMMARY

**MACROSCOPIC EFFECTS OF HIGH PRESSURE HYDROGEN ON
CONSTITUTIVE AND LIFE MODELS**

- * Establish validity of structural durability models developed under the program

HCF/LCF INTERACTION UNDER MISSION-RELATED LOADING

- * Interspersed HCF and LCF loadings
- * TMF interaction with HCF loadings
- * Cumulative creep-fatigue interactions

**APPLICATION OF CONSTITUTIVE AND LIFE MODELS IN
STRUCTURAL ANALYSIS**

- * Apply models developed to SSME components

THERMAL RATCHETTING DAMAGE ANALYSIS

- * Interaction of ratchet strains with TMF and HCF
- * Application to Main Combustion Chamber materials

ADVANCED CONCEPT MATERIALS MODELS DEVELOPMENT

- * Metal matrix composites modeling: material constitutive and life models

CREEP-FATIGUE DAMAGE ANALYSIS PROCESSOR

- * Integrate constitutive and life prediction models, as well as relevant materials properties data into a damage analysis and life assessment computer code

MULTIAXIAL LIFE PREDICTION

- * Develop multiaxial life prediction models applicable to components exhibiting complex multiaxial states of stress

ROCKET ENGINE LIFE MODELING

- * Develop SSME component durability models in terms of engine performance variables for use in health monitoring and controls studies

LeRC FATIGUE/FRACTURE/LIFE
PREDICTION
WORKING GROUP

PROGRAM DELIVERABLES

* VALIDATED MATERIAL CONSTITUTIVE AND LIFE
PREDICTION MODELS

* MATERIAL PROPERTIES DATABASE

* STRUCTURAL MATERIAL DURABILITY COMPUTER CODES

Page intentionally left blank

CUMULATIVE FATIGUE DAMAGE BEHAVIOR OF MAR M-247

Michael A. McGaw and Gary R. Halford
NASA Lewis Research Center
Cleveland, Ohio 44135

and

Sreeramesh Kalluri
Sverdrup Technology, Inc.
Brook Park, Ohio 44142

Cumulative Fatigue Damage Analysis is the term used to describe the assessment of fatigue lives of metallic materials under variable amplitude or block loading. A linear life-fraction rule, known as the Palmgren-Miner Linear Damage Rule (LDR) is the standard model currently used in engineering design for assessing cumulative fatigue-damage. In recent years, it has been discovered that engineering metals and alloys exhibit pronounced nonlinear cumulative fatigue damage behavior under certain conditions of loading. Conditions for which pronounced nonlinearity and subsequent fatigue life degradation might exist can now be identified readily using engineering models developed at the Lewis Research Center of NASA. The models reflect the accumulation of fatigue damage through the nonlinear sequence of microcrack initiation, microcrack growth, macrocrack initiation, macrocrack growth, and eventual fracture. Despite the extreme complexity of the physical mechanisms of fatigue, relatively simple engineering models have evolved. They are proving useful in guiding the evaluation of the cumulative fatigue damage behavior of materials tested in laboratory environments.

The simplest and most common laboratory test procedure for evaluating cumulative damage behavior is the two-level loading sequence in which low-cycle fatigue (LCF) is applied for a portion of the expected LCF life followed by high-cycle fatigue (HCF) loading until failure. Analysis of hundreds of two-level loading experimental results from the literature has led to the development of several simple engineering models, including: the Double Linear Damage Rule (DLDR), the Damage Curve Approach (DCA), and the Double Damage Curve Approach (DDCA). Each has its regime of utility, but all three give rise to essentially the same numerical results. Another common attribute in these models is the recognition that the degree of nonlinearity in damage accumulation depends solely upon relative life levels of the extreme cycles. In other words, LCF/HCF lives of $10^2/10^5$ or $10^4/10^7$ will exhibit equal degrees of nonlinearity and hence equal degrees of fatigue life degradation.

The object of this study was to examine the room temperature fatigue and nonlinear cumulative fatigue damage behavior of the cast nickel-base superalloy, MAR M-247. This is the bill-of-material for the turbine housings and inlet guide vanes of both the oxidizer and fuel turbopump designs from the Alternate Turbopump Development (ATD) program. Pratt & Whitney Corp. (West Palm Beach group) is performing this program under contract to NASA Marshall Space Flight Center. Through a small cooperative agreement with NASA Lewis Research Center, a casting of MAR M-247 was obtained from Pratt & Whitney Corp. The casting was

produced using the MICROCAST-X process of the Howmet Corp. and had been HIPed and heat treated according to engineering use specifications from the ATD program requirements. Axial fatigue specimens possessing a half-inch uniform gage section were machined from this casting.

The fatigue test matrix carried consisted of single-level, fully reversed ($R = -1$, either load or strain control) fatigue experiments (fig. 1). Duplicate tests were performed at each of three test conditions. The mechanical test parameters were chosen to establish two lower-life LCF levels (N_{1A} & N_{1B}) and one higher-life HCF level (N_2) for use in the two-level loading experiments. Two-level block loading experiments (in which higher amplitude strain or load cycling, corresponding to lower life levels, N_{1A} and N_{1B}) were conducted for various life fractions, followed by load cycling (corresponding to a higher fatigue life level, N_2) to failure (fig. 2). In these tests, LCF life fractions (n_{1A}/N_{1A} and n_{1B}/N_{1B}) of approximately 0.1, 0.2, and 0.3 were applied and the HCF life remaining in the second loading level was observed. Two series of tests were performed: one of the two baseline fatigue LCF life levels was used in the first loading block, and the HCF baseline loading level was used in the second block in each series. For each series, duplicate tests were performed at each applied LCF life fraction.

The results of the baseline fatigue characterization tests are shown in figure 3. The lowest life tests were performed under strain control at 10 cpm, $\Delta\epsilon_t = 1.0$ percent. A small amount of inelastic strain range, on the order of 0.1 percent, was observed. The balance of the tests was performed under load control, at 100 Hz, and nominally elastic behavior was observed. These results agreed with results obtained by Pratt & Whitney (ref. 2).

The results of the two-level loading experiments are shown as cumulative fatigue damage interaction plots (figs. 4 and 5). In figure 4, the LCF life level, N_{1A} corresponding to the first loading block was approximately 7000 cycles to failure. The second load level corresponded to approximately 10^7 cycles to failure (N_2). These life levels result from a consideration of the average of the fatigue lives obtained in the baseline fatigue characterization. Also shown in the figure are predicted results based on a linear damage approach, and two nonlinear cumulative damage approaches, the Double Linear Damage Rule (ref. 1) and the Damage Curve Approach (ref. 1). As can be observed, for the three duplicated test conditions employed in this series, MAR M-247 exhibits a very strong nonlinear cumulative interaction behavior. This behavior is predicted qualitatively based on the DCA and DLDR approaches. By contrast, predictions according to the LDR approach are in error by nearly a factor of 8 on the unconservative side with respect to the experimental results (the remaining HCF life is overpredicted by a factor of 33).

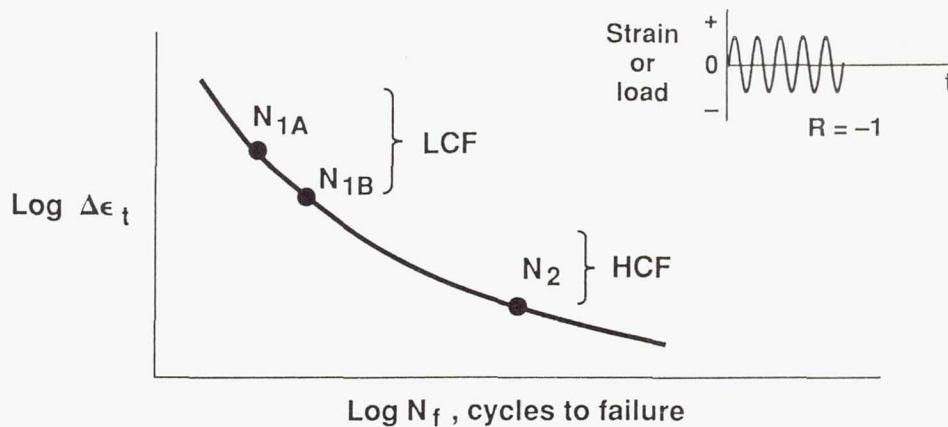
In figure 5, the LCF life level, N_{1B} corresponding to the first block of loading was approximately 340,000 cycles to failure. The second loading level was as before. The experimental results are again shown with predictions made according to both linear and nonlinear cumulative damage approaches. Nonlinear cumulative fatigue damage behavior is again exhibited. Predictions by the DCA and DLDR models again are qualitatively correct for all but two of the results shown in this figure. The cumulative fatigue damage results in this figure do show a bifurcation in behavior that has not previously been observed. The re-

maining HCF lives are either shorter than expected, or substantially greater, possibly indicating that the samples are from two separate populations of differing grain size, hardness, strength, etc. There is presently no physical evidence to explain the behavior. The specimens are to be thoroughly examined at MSFC using fractographic and metallographic techniques in anticipation of explaining the duality in behavior.

References

1. Manson, S.S.; Halford, G.R.: Practical Implementation of the Double Linear Damage Rule and Damage Curve Approach. Intern. J. Fracture, vol. 17, no. 2, Apr. 1981, pp. 169-192.
2. Heine, J.: Pratt & Whitney Aircraft, West Palm Beach group, private communication.

Approach: Baseline Fatigue Behavior

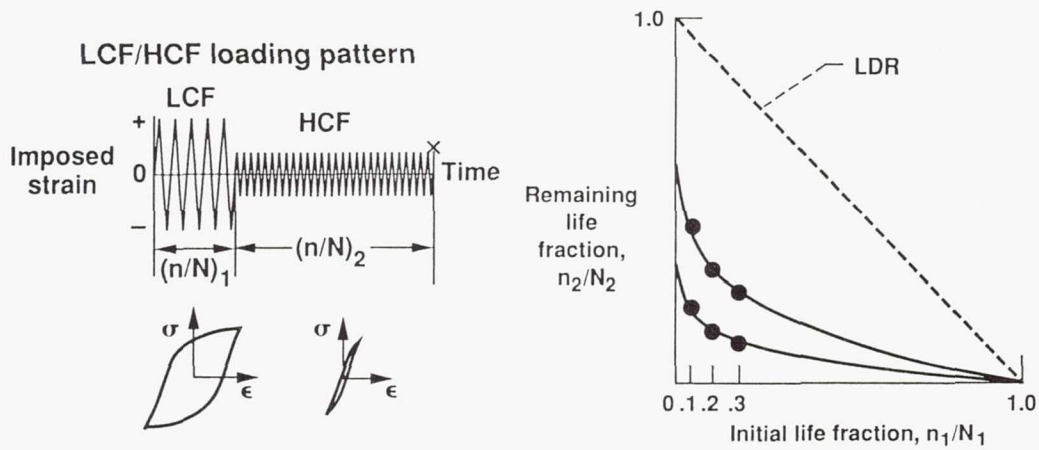


- Establish base life levels for HCF/LCF interaction study
- Two LCF life levels, one HCF life level
- Replicate tests at each condition

CD-91-52290

Figure 1

Approach: HCF/LCF Interaction Behavior



- Two-level block loading tests run
- Three applied LCF life fractions designed to bracket maximum expected nonlinear interaction
- Duplicate tests at each condition

CD-91-52291

Figure 2

Results: Baseline Fatigue Behavior MAR M-247 in Air at Room Temperature

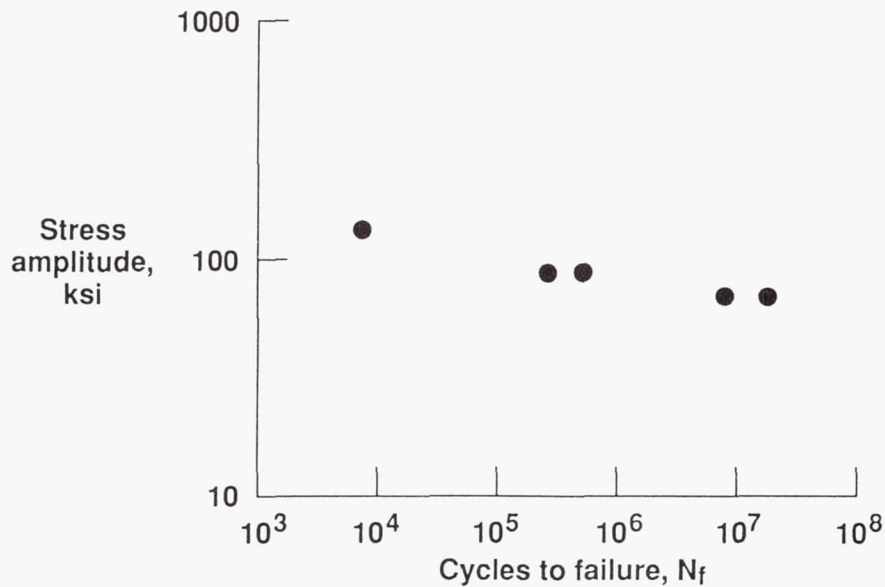
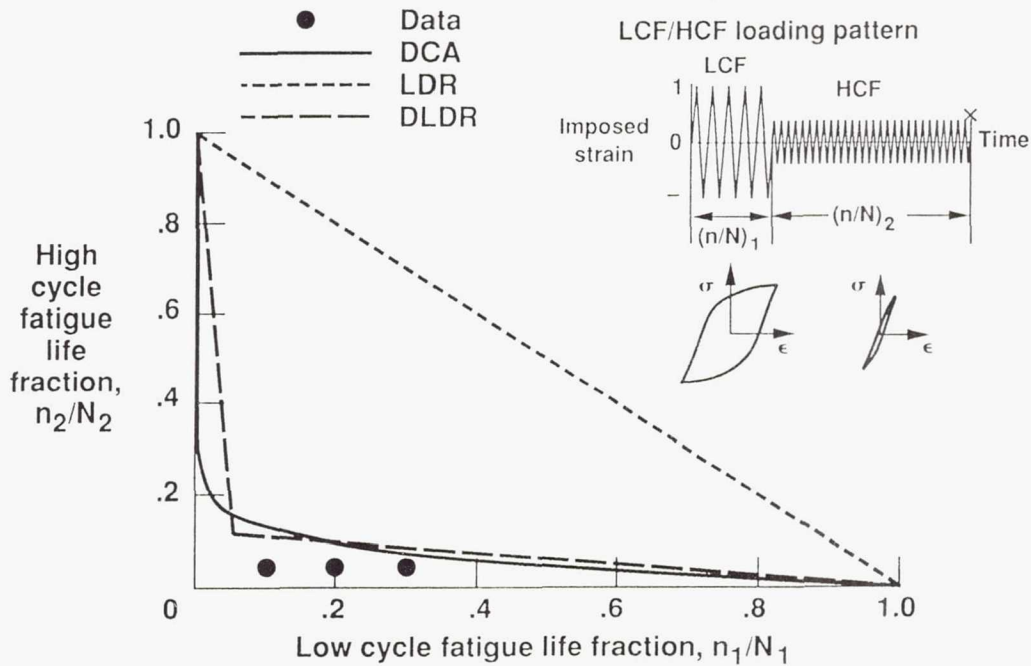


Figure 3

CD-91-52292

Results: LCF/HCF Interaction Behavior

MAR M-247 Fatigue Interaction; $N_1 = 6764$; $N_2 = 11\,136\,861$

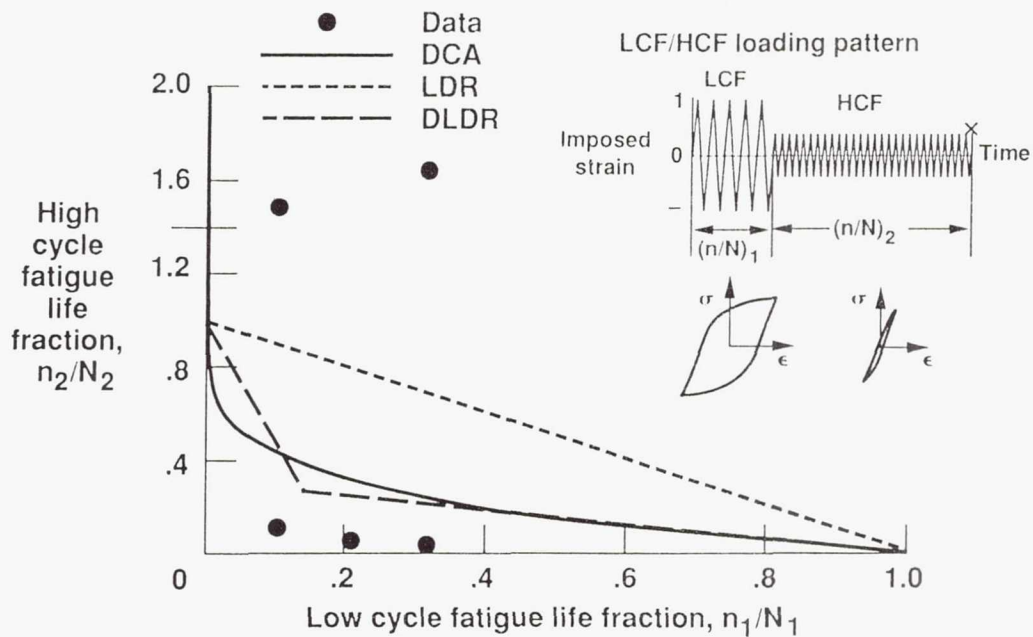


CD-91-52293

Figure 4

Results: LCF/HCF Interaction Behavior

MAR M-247 Fatigue Interaction; $N_1 = 342\,016$; $N_2 = 11\,136\,861$



CD-91-52294

Figure 5

Page intentionally left blank

THE EFFECT OF POROSITY AND γ - γ' EUTECTIC CONTENT ON THE LOW CYCLE FATIGUE BEHAVIOR OF HYDROGEN-CHARGED PWA 1480

John Gayda, Robert L. Dreshfield, and Timothy P. Gabb
NASA Lewis Research Center
Cleveland, Ohio 44135

Single crystal superalloys such as PWA 1480 are being considered for turbopump blades in the main engines of the space shuttle. As fatigue resistance in a hydrogen environment is a key issue in this application, a study of the effect of porosity and γ - γ' eutectic content on the fatigue life of a hydrogen-charged PWA 1480 single crystal was performed. Porosity and eutectic have been linked to fatigue initiation in previous studies, and therefore reduction of either or both may be one means to improve fatigue life of PWA 1480 when hydrogen is present.

To reduce levels of porosity and eutectic alone or in combination, [001] single crystals of PWA 1480 were given various thermomechanical treatments. A eutectic solution treatment at 1290 °C was employed to reduce eutectic content, while porosity was reduced by hot isostatic pressing (HIP). To reduce porosity and eutectic content, a duplex thermomechanical treatment was used in which PWA 1480 was first given a eutectic solution at 1290 °C and then HIPed. After processing, fatigue specimens were machined, heat treated, and subsequently charged in high-pressure gaseous hydrogen. The hydrogen level increased from less than 5 to 400 ppm by weight after charging.

Room temperature, strain-controlled fatigue tests were run on all material conditions in an air environment. Hydrogen charging was found to reduce the fatigue life of PWA 1480 containing normal levels of porosity and eutectic (standard microstructure) by more than one order of magnitude. Initiation sites in hydrogen charged PWA 1480 were easily identified by (001) facets on the fracture surface. Each facet usually initiated at a central pore which was often closely associated with a γ - γ' eutectic. Material given the eutectic solution treatment was found to have a significant decrease in eutectic content; however, a small amount of incipient melting occurred producing an appreciable increase in the number of large pores. This microstructure showed a greater life degradation than the standard microstructure in the presence of hydrogen. HIPing at 1280 °C was found to reduce the size and frequency of larger pores and also halved the amount of γ' eutectic. The HIPed material showed a slight improvement in fatigue life over material with the standard microstructure in the presence of hydrogen.

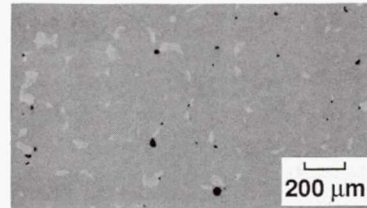
The longest fatigue life of hydrogen-charged PWA 1480 was obtained with material given the eutectic solution and then HIPed. The porosity and eutectic content of this material was significantly lower than any of the other conditions tested. Further, the degree of facet formation on the fracture surface of tested specimens was also greatly reduced. The reduction in porosity level achieved by this duplex thermomechanical treatment suggests that closure of porosity is more readily achieved if eutectic content is minimized before HIPing.

Objective and Material

PWA 1480 single-crystal superalloy

- Orientation, [001]
- Fine aging γ' , 60 vol. %
- Coarse eutectic, 2 vol. %
- Porosity, 0.3 vol. %

Study the effect of γ - γ' eutectic and porosity on the fatigue life of a single-crystal, nickel-base superalloy in the presence of hydrogen

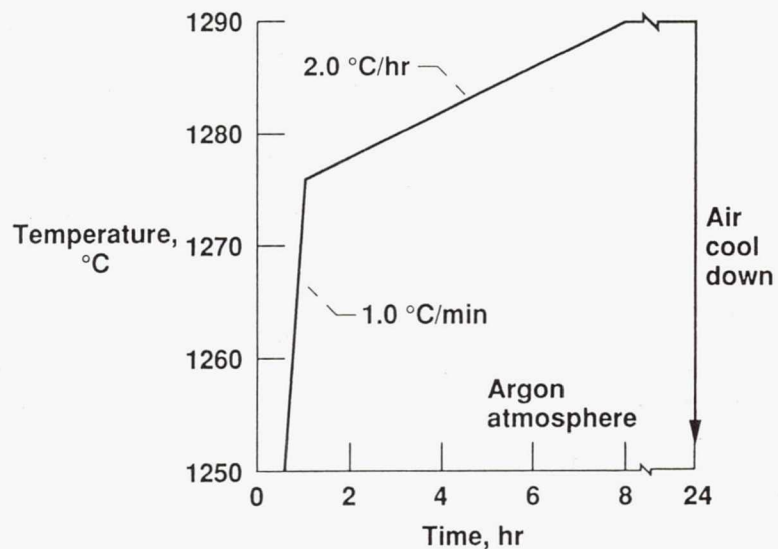


Chemical composition by weight

| | |
|------------|--------|
| 9.4 Cr | 11 Ta |
| 4.7 Al | 5.2 W |
| 1.0 Ti | 4.8 Co |
| Balance Ni | |

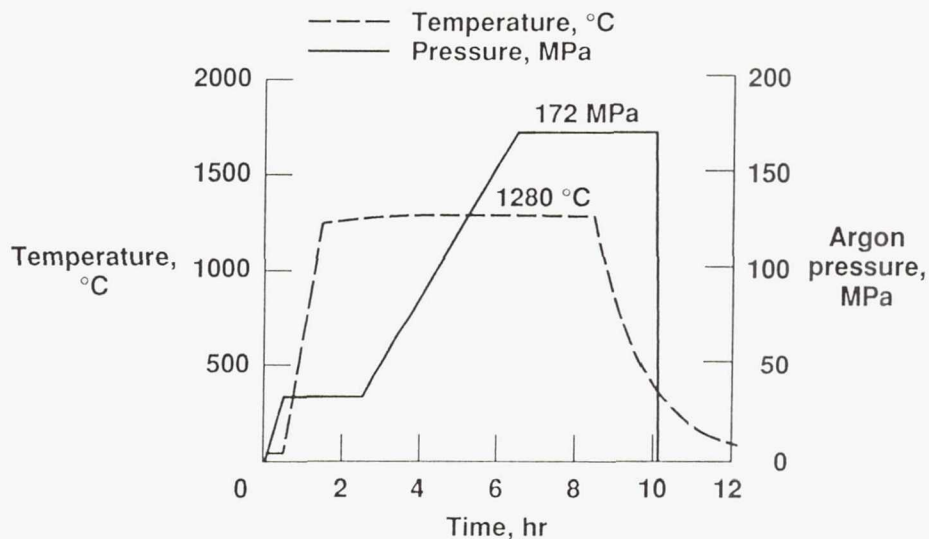
CD-91-52301

1290 °C Eutectic Solution Treatment Used to Reduce γ' Eutectic Content



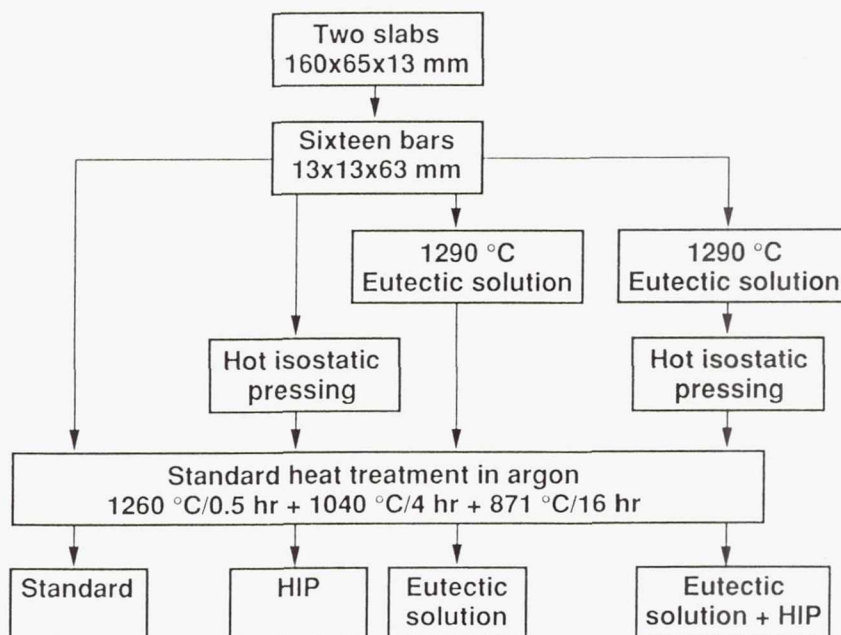
CD-91-52302

Hot Isostatic Pressing (HIP) Used to Reduce Porosity



CD-91-52303

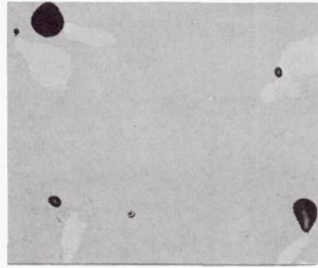
Processing Flowchart



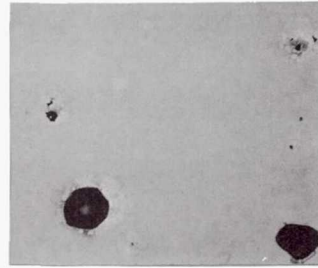
CD-91-52304

γ - γ' Eutectic Morphology After Processing

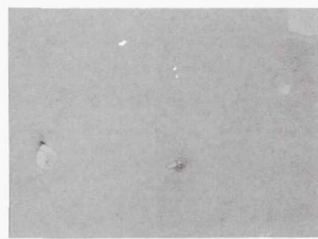
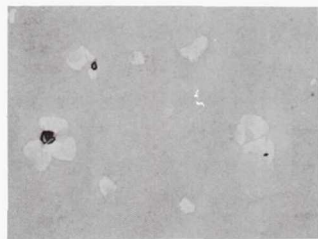
Standard treatments (2.3 vol. % eutectic) Eutectic solution (0.5 vol. %)



HIP (1.0 vol. %)

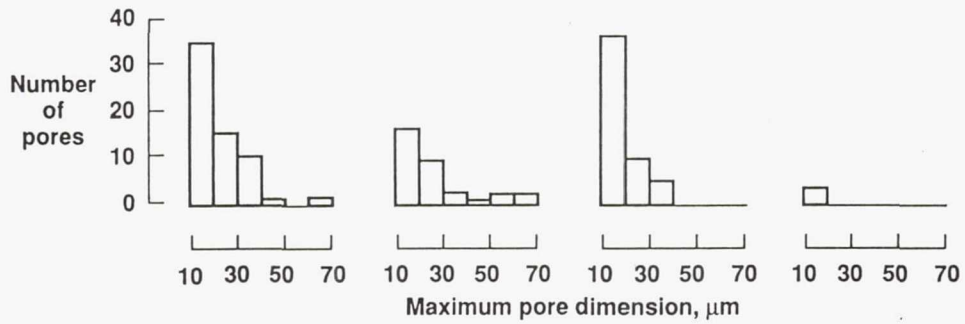
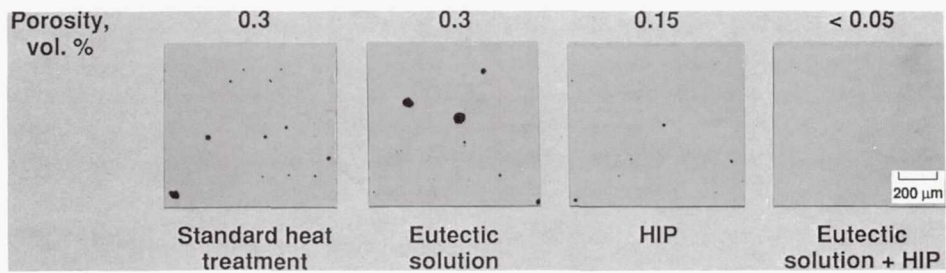


Eutectic solution + HIP (< 0.1 vol. %)



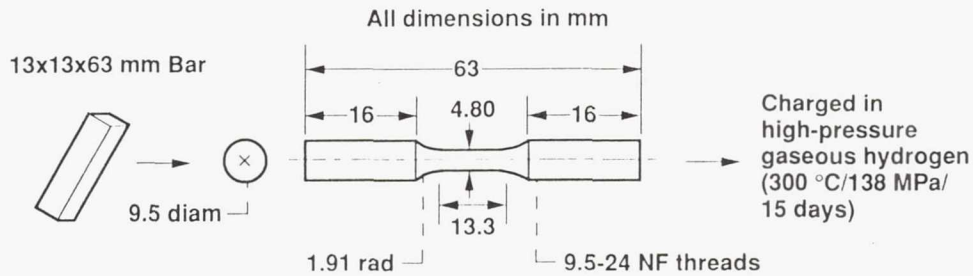
CD-91-52305

Porosity Distributions After Processing



CD-91-52306

Machining, Charging, and Testing Procedures



Tensile test

- Room temperature
- Strain rate, 0.1 %/sec

Fatigue test

- Or
- Room temperature
 - Strain control
 - Sine wave, 0.1 Hz
 - Maximum strain/minimum strain = -1

CD-91-52307

Tensile Properties of PWA 1480

Uncharged (< 5 ppm by weight of hydrogen)

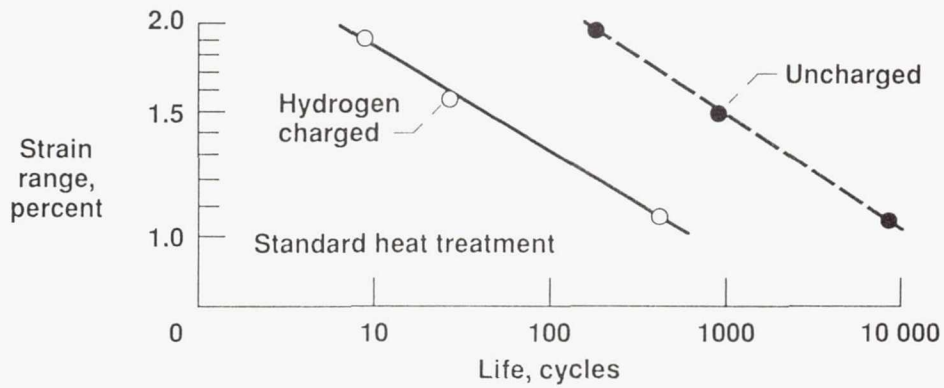
| Heat treatment | Yield strength, MPa | Ultimate strength, MPa | Elongation, percent | Reduction in area, percent |
|----------------|---------------------|------------------------|---------------------|----------------------------|
| Standard | 1041 | 1241 | 7.6 | 8.4 |

Hydrogen charged (400 ppm by weight)

| Heat treatment | Yield strength, MPa | Ultimate strength, MPa | Elongation, percent | Reduction in area, percent |
|-------------------------|---------------------|------------------------|---------------------|----------------------------|
| Standard | 936 | 1048 | 2.6 | 7.3 |
| Eutectic solution | 1060 | 1083 | 1.7 | 6.9 |
| HIP | 960 | 1069 | 3.0 | 6.8 |
| Eutectic solution + HIP | 952 | 1117 | 3.2 | 4.2 |

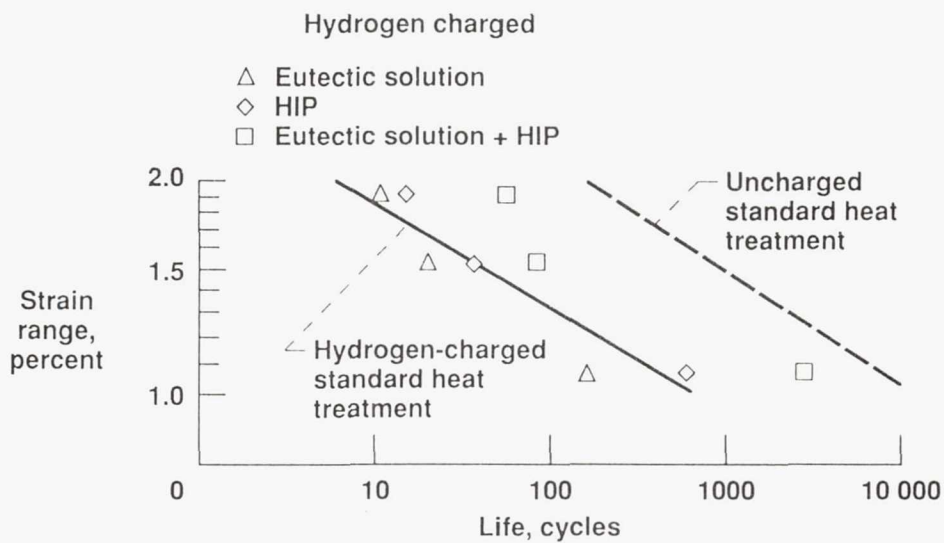
CD-91-52308

Hydrogen Charging Severely Degrades Fatigue Life of [001] PWA 1480



CD-91-52309

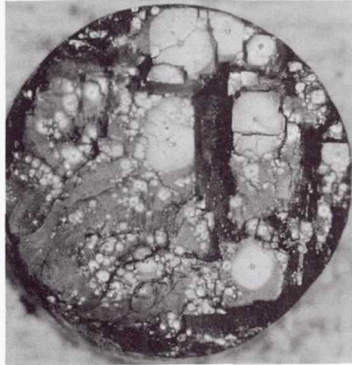
The Microstructure With the Least Amount of Porosity and Eutectic Exhibits the Best Fatigue Life When Hydrogen is Present



CD-91-52310

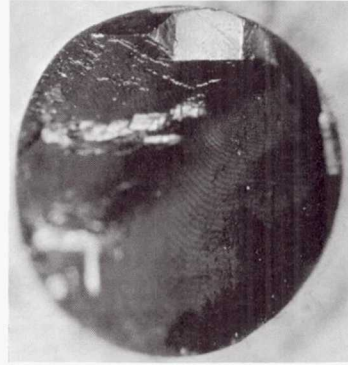
Fracture Surfaces of Fatigue Tests Run at $\Delta\varepsilon = 1\%$ of Hydrogen-Charged PWA 1480

Eutectic Solution



Multiple (001) facet initiations at
10 - 100 μm pores
Shortest life ($N_F = 166$)

Eutectic Solution + HIP



Single (001) facet initiation at
15 μm pore
Longest life ($N_F = 2750$)

Uncharged PWA 1480 Does Not Exhibit Any (001) Facets on
Fracture Surface of Fatigue Specimens

CD-91-52311

Summary and Conclusions

- Hydrogen charging greatly reduces the fatigue life of PWA 1480.
- The reduction of fatigue life in the presence of hydrogen was minimized by a duplex thermomechanical treatment consisting of a eutectic solution at 1290 °C, followed by hot isostatic pressing. This treatment produced the greatest reduction in size and amount of eutectic and porosity.
- It is suggested that the 1290 °C eutectic solution treatment preconditions PWA 1480 such that pores are more easily closed by hot isostatic pressing.

CD-91-52312

Page intentionally left blank

CONSTITUTIVE AND DAMAGE MATERIAL MODELING IN A HIGH PRESSURE HYDROGEN ENVIRONMENT

D. A. Russell and L. G. Fritzscheier
Rocketdyne Division
Rockwell International
Canoga Park, California 91303

Numerous components operating in reusable space propulsion systems such as the Space Shuttle Main Engine (SSME) are exposed to high pressure gaseous hydrogen environments. Shown (Figure 1.0) is the SSME Powerhead. Flow areas and passages in the fuel turbopump, fuel and oxidizer preburners, main combustion chamber and injector assembly contain high pressure hydrogen either high in purity or as hydrogen rich steam. As can be seen, this includes many components such as turbine disks and blades, impellers, housings, ducts, etc. Accurate constitutive and damage material models applicable to high pressure hydrogen environments are therefore needed for engine design and analysis. Existing constitutive and cyclic crack initiation models have been evaluated only for conditions of oxidizing environments. The purpose of this effort (Figure 2.0) is to evaluate these models for applicability to high pressure hydrogen environments.

Material behavior is known to be significantly affected by high pressure hydrogen environments (Figure 3.0). For the materials typically employed in rocket engine applications, hydrogen environment embrittlement is most severe near room temperature (Ref. 1). Tensile ductility and notched bar ultimate tensile strength reductions are typically reduced by the hydrogen environment. The room temperature embrittlement effects increase with increasing pressure (Ref. 2). Although the room temperature tensile properties of the superalloys are relatively insensitive to strain rate effects, hydrogen environment embrittlement is strain rate sensitive. Low cycle fatigue lives, especially crack initiation lives, are also reduced by the hydrogen environment (Ref. 3). Thermal activation and time dependent deformation (creep) also become important as temperature increases (Ref. 4). Indications are that the presence of hydrogen can accelerate creep effects by enhancing dislocation mobility (Ref. 5).

The program flow chart (Figure 4.0) is shown for each material. Constitutive modeling effort precedes life modeling. Therefore constitutive test results can be utilized to provide a preliminary projection of crack initiation results, ductility normalized, (Ref. 6) as well as identify target test values for σ , ϵ , $\dot{\epsilon}$, etc. During life testing, specimen constitutive response will be measured to provide an added database for constitutive model verification including any modifications. The experimental phase will begin with the selected isotropic material, followed by the anisotropic material. Both helium and hydrogen testing will be performed to obtain contrasting inert and aggressive environment test results.

Alloy and material model selections as well as test conditions have been defined. Currently, existing data is being surveyed and compiled to provide initial estimates for model constants and to guide test details. Inconel 718 was selected as the isotropic material due to its extensive usage on the SSME, its susceptibility to Hydrogen Environment Embrittlement (HEE) and the existence of service-related hydrogen assisted cracking. PWA 1480 was selected as the single crystal material, due mainly to its development for potential usage on the SSME as a blade material and its known susceptibility to HEE. The nominal properties of

these two materials are presented (Figure 5.0) along with the test specimen geometry (Figure 6.0). The maximum test temperatures and pressures (Figure 7.0) correspond to maximum usage on the SSME. Due to the known enhanced HEE effects at room temperature ambient temperature testing shall also be performed.

Recent emphasis on constitutive model development has concentrated on unified viscoplastic models wherein plastic, creep and relaxation strains are treated as one strain component, the inelastic strain. Constitutive model characterization tests (Figure 8.0) will be carried out at both room and elevated temperature in helium and hydrogen environments. The Walker model was chosen for the isotropic material, Inconel 718 and Walker's anisotropic model was selected for PWA 1480 (Figure 9.0, Refs. 7, 8, 9). A modification based on Valanis' material time scale has been developed in-house to extend these rate dependent models into the rate independent (low temperature) regime (Figure 10.0).

Recent crack initiation model development has emphasized life prediction in oxidizing environments under such loading complexities as thermomechanical fatigue, cyclic creep, multiaxial and variable amplitude loading. For assessment in a hydrogen environment, the total strain version of strain range partitioning (TS-SRP) (Refs. 10, 11) was selected for constant amplitude loading conditions. Isothermal testing will be performed to determine the four basic inelastic strain-range life relations, PP, PC, CP, CC as well as the elastic strain-range life relation (Figure 11.0). Due to the preponderance of thermal gradient driven strain cycling of SSME hardware, the most important non-isothermal loop types to consider are out-of-phase PP and PC. To better simulate the impact of thermal mechanical fatigue (TMF), out-of-phase bithermal testing will be performed in PP cycling (Figure 12.0). Reasonable estimates of strain cycle history relative to TMF can be obtained where free thermal expansion strains can be easily subtracted from the total strain.

Cumulative damage will be assessed via the advanced NASA-developed models, Damage Curve Approach (Figure 13.0) and Double Linear Damage Rule (Ref. 12). The nature of these models is to accumulate damage nonlinearly with high-low load sequences being more damaging than low-high. Isothermal tests will be run to provide baseline data and a bithermal LCF test followed by HCF is planned as a verification experiment.

The experimental program as proposed shall include uniaxial monotonic, cyclic (both isothermal and bithermal), creep and relaxation tests to investigate the applicability of these chosen models and to provide a basis for necessary modifications (Figure 14) arising from model deficiencies should they occur.

*Work performed under NASA contract NAS3-26130

REFERENCES

1. Fritzemeier, L. G.; and Chandler, W. T.: "Hydrogen Embrittlement - Rocket Engine Applications", in Superalloys, Supercomposites and Superceramics, Tien, J. K. and Caulfield, T., Editors, Academic Press Inc., San Diego, 1989.
2. Jewett, R. P.; Walter, R. J.; Chandler, W. T.; and Fromberg, R. P.: "Hydrogen - Environment Embrittlement of Metals", NASA CR-2163, Final Report to NAS8-19(C), 1971.
3. Fritzemeier, L. G.; Walter, R. J.; Meisels, A. P.; and Jewett, R. P.: in "Hydrogen Effects on Material Behavior", Moody, N. R. and Thompson, A. W., Editors, pp. 941-954, 1990.
4. Mucci, J.; and Harns, J. A.: Final Report to NAS8-30744, Exhibits B and C, 1976.
5. Robertson, I. M.; and Birnbaum, H. K.: Acta Met., Vol. 34, No. 3, pp. 353-366, 1986.
6. Halford, G. R.; Saltsman, J. F.; and Hirschberg, M. H.: "Ductility Normalized - Strainrange Partitioning Life Relations for Creep-Fatigue Life Predictions", NASA TM-73737, 1977.
7. Walker, K. P.: "Research and Development for Nonlinear Structural Modeling with Advanced Time-Temperature Dependent Constitutive Relationships", NASA CR-165533, November 1981.
8. Walker, K. P.; and Jordan, E.: "Biaxial Constitutive Modeling and Testing of Single Crystal Superalloy at Elevated Temperature", Engineering Science Software, Inc., Report No. ESS-SCD-8512, September 1985.
9. Chang, K. J.; and Newell, J. F.: "A Material Time Application to Viscoplasticity Theories", in STRUCENG & FEMCAD - Structural Engineering and Optimization, Zarkd, J. and Ohtmer, O., Editors, November, 1990.
10. Saltsman, J. F.; and Halford, G. R.: "Life Prediction of Thermomechanical Fatigue Using Total Strain Version of Strainrange Partitioning (SRP) -- A proposal, NASA TP 2779, February 1988.
11. Manson, S. S.; and Zab, R.: "A Framework for Estimation of Environmental Effect in High Temperature Fatigue", in Proc. of Conf. Environmental Degradation of Engineering Materials, October, 1977.
12. Manson, S. S.; and Halford, G. R.: "Practical Implementation of the Double Linear Damage Rule and Damage Curve Approach for Treating Cumulative Fatigue Damage", NASA TM 81517, April 1980.

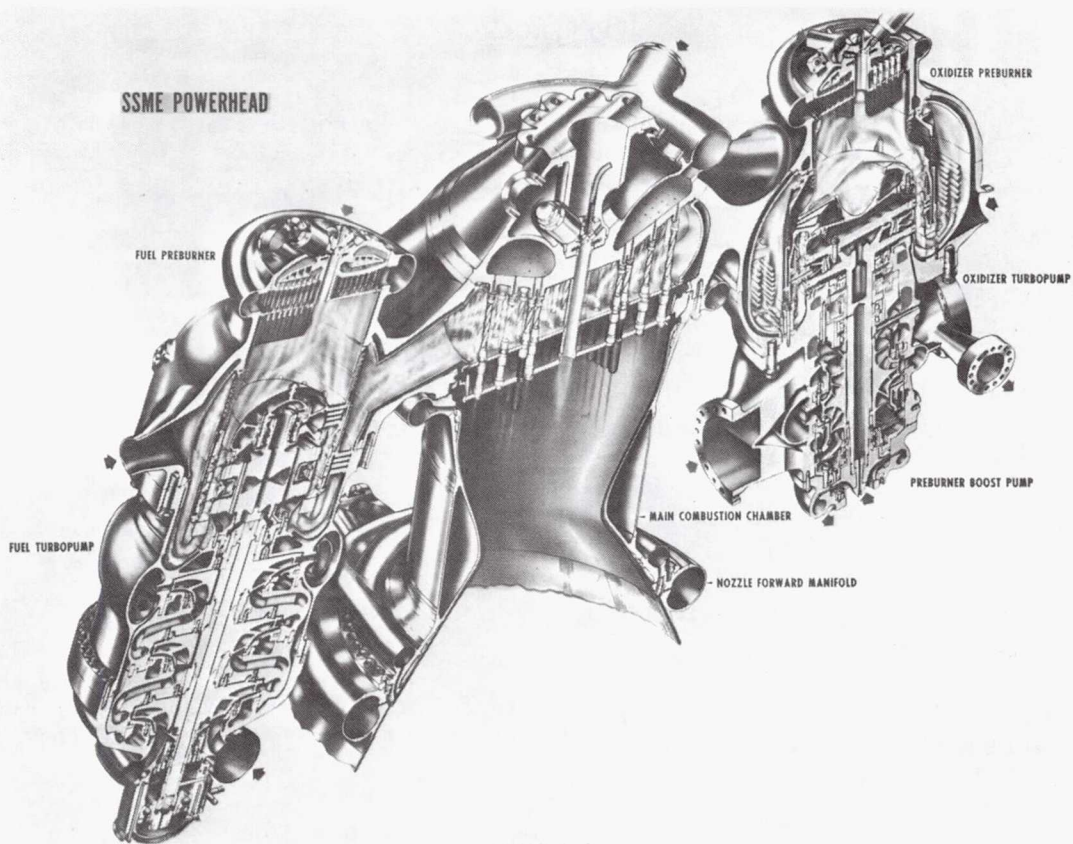
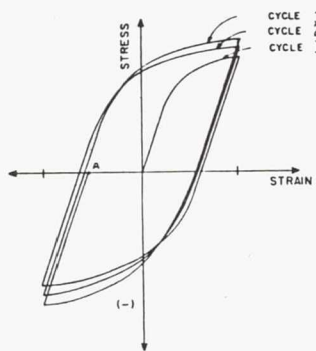


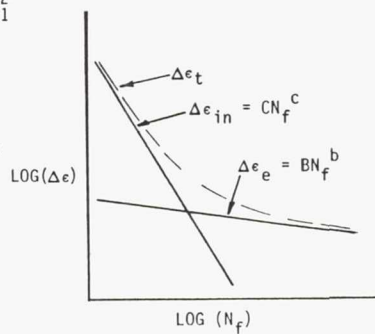
FIGURE 1.0
COMPONENTS EXPOSED TO HIGH PRESSURE HYDROGEN

- DETERMINE REGIMES OF MATERIAL BEHAVIOR ALTERED BY HIGH PRESSURE H₂
- EVALUATE EXISTING MATERIAL MODELS FOR HIGH PRESSURE H₂ APPLICABILITY
- PROPOSE MODEL MODIFICATIONS AS REQUIRED

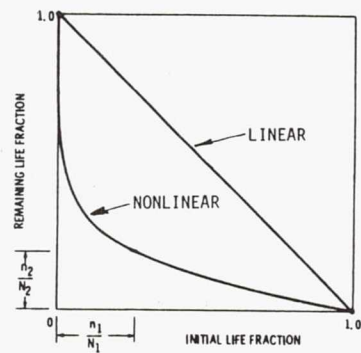
$$\Delta\epsilon_e = B \left(\frac{\Delta\epsilon}{C} \right)^{b/c} \frac{IN}{c}$$



CONSTITUTIVE MODEL



LIFE MODEL



CUMULATIVE DAMAGE MODEL

FIGURE 2.0
MATERIAL MODELING TASK OBJECTIVES

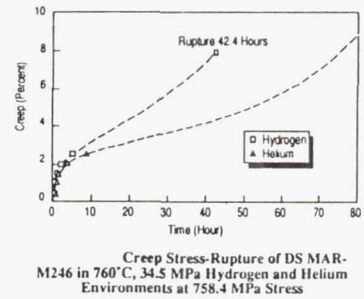
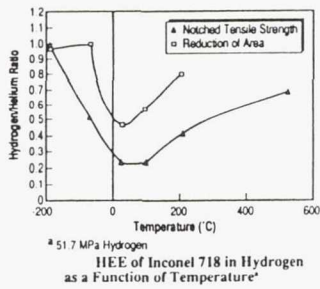
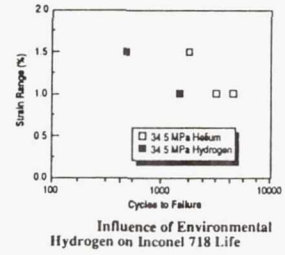
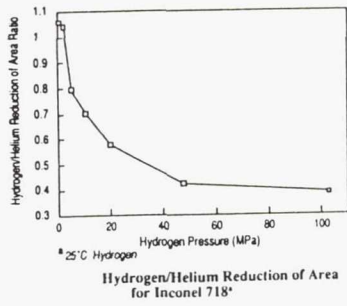


FIGURE 3.0 MATERIAL ISSUES RELATED TO HIGH PRESSURE HYDROGEN

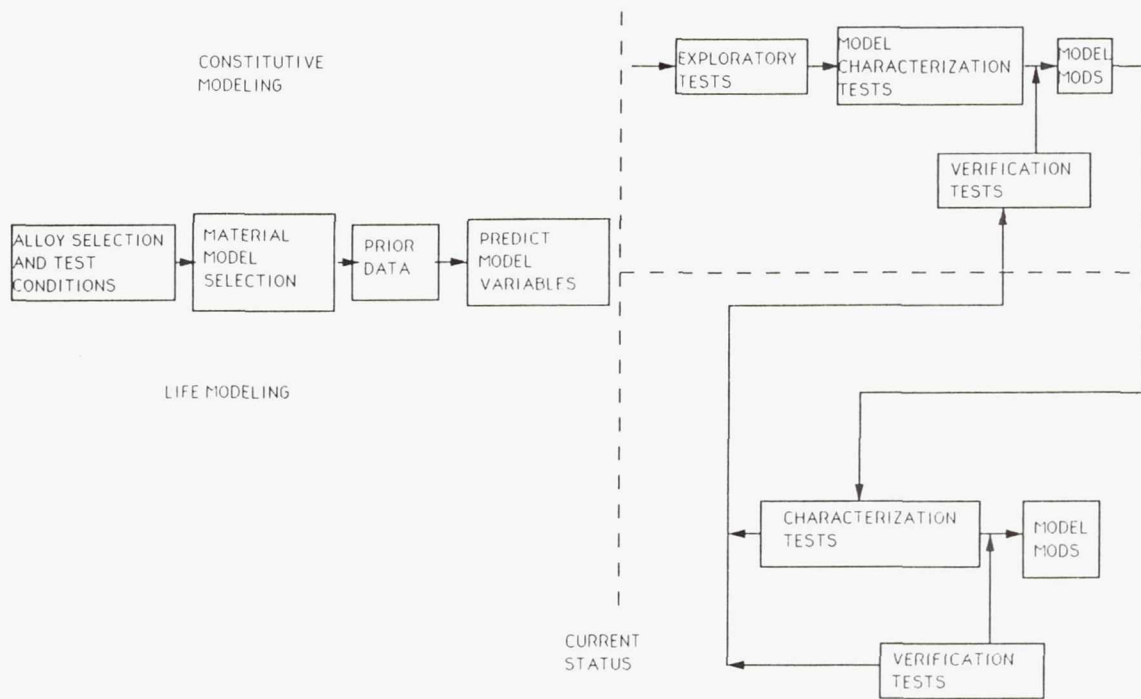


FIGURE 4.0 PROGRAM FLOW (EACH MATERIAL) H2 AND HE TESTING

ISOTROPIC MATERIAL
INCONEL 718

SINGLE CRYSTAL MATERIAL
PWA 1480

NOMINAL COMPOSITION (WEIGHT PERCENT)

CR - 19 MO - 3
NB + T2 - 5 TI - 1.0
AL - 0.5 FE - 18.5
NI - BAL.

NOMINAL COMPOSITION (WEIGHT PERCENT)

CR - 10 CO - 5
W - 4 TI - 1.5
TA - 12 AL - 5
NI - BAL.

HEAT TREATMENT

1900°F/30 MIN/AIR COOL
1400°F/10 HRS/FURNACE COOL TO
1200°F/HOLD TO 20 HOURS TOTAL

HEAT TREATMENT AND PROCESSING
(TYPICAL TIMES AND TEMPERATURES)

2350°F/4 HOURS/AIR COOL
HOT ISOSTATIC PRESS/4 HOURS/2350°F/15 KSI
1975°F/4 HOURS
1600°F/32 HOURS

TENSILE PROPERTIES (TYPICAL), KSI

| | RT | | 650°C |
|-----------------|-----|-----|-------|
| | HE | H2 | HE |
| F _{TY} | 160 | 160 | 140 |
| F _{TU} | 185 | 185 | 160 |
| ELONG. % | 20 | 11 | 20 |

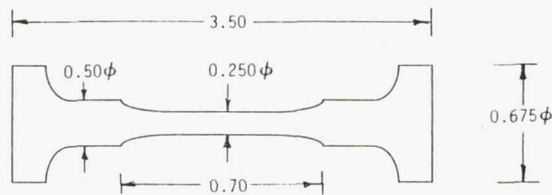
TENSILE PROPERTIES (TYPICAL) <001>, KSI

| | RT | | 870°C |
|-----------------|-----|-----|-------|
| | HE | H2 | HE |
| F _{TY} | 145 | 140 | 100 |
| F _{TU} | 165 | 150 | 140 |
| ELONG. % | 5.4 | 2.5 | 12 |

FIGURE 5.0
MATERIAL SELECTIONS

SPECIMEN DIMENSIONS

HTFV Button Head Fatigue Sample



H₂ VESSEL DESCRIPTION/INSTRUMENTATION DESCRIPTION

- 10,000 PSI/1800°F FATIGUE SYSTEM
- INTERNAL LOAD AND ON-SPECIMEN STRAIN CAPABILITY
- SELF COMPENSATING (TEMP., PRESSURE, ENVIRONMENT) CAPACITANCE EXTENSOMETER
- FULL COMPUTER TEST CONTROL AND DATA MANAGEMENT

FIGURE 6.0
TEST SPECIMEN AND VESSEL DESCRIPTION

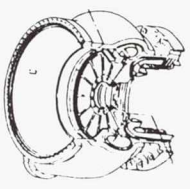
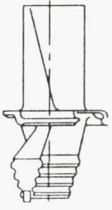
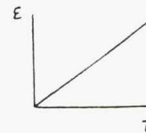
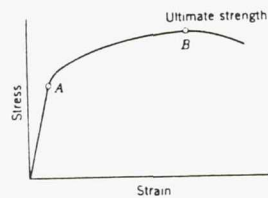
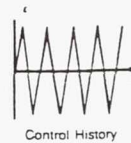
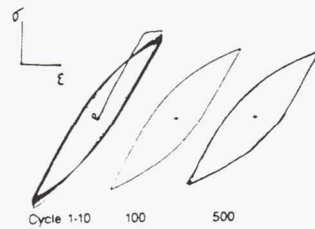
| ISOTROPIC MATERIAL - INCONEL 718 | SINGLE CRYSTAL MATERIAL - PWA 1480 |
|--|---|
| <ul style="list-style-type: none"> • MAXIMUM USAGE (SSME) • TURBINE HOUSING AND OUTLET MANIFOLD <ul style="list-style-type: none"> • PRESSURE = 24-34 MPA • HOT GAS TEMP = 650° C • PUMP INLET TO OUTLET <ul style="list-style-type: none"> • PRESSURE = 50 MPA • TEMP = 20° C • MINIMUM TEMP <ul style="list-style-type: none"> • 20° C | <ul style="list-style-type: none"> • MAXIMUM USAGE (SSME) • HIGH PRESSURE TURBOPUMP BLADES <ul style="list-style-type: none"> • PRESSURE = 34.5 MPA • TEMP = 870° C • MINIMUM TEMP <ul style="list-style-type: none"> • 20° C |
|  |  |

FIGURE 7.0
TEST TEMPERATURES AND PRESSURES

Monotonic Tensile Tests



Cyclic Tests



Creep/Relaxation Tests

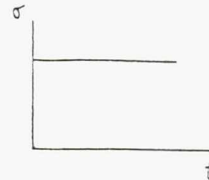
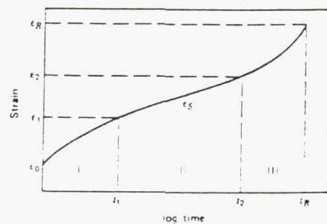


Figure 8.0
CONSTITUTIVE MODEL CHARACTERIZATION TESTS

ISOTROPIC CONSTITUTIVE MODEL

Material Selected: INCO-718

Model Selected: Walker's Isotropic Model

Modification: Employ Material Time Concept

Formulation:

$$\dot{(\cdot)} = \frac{d}{dz}(\cdot); \quad \text{and} \quad \dot{z} = \frac{dz}{dt}$$

• **The Flow Rule:**

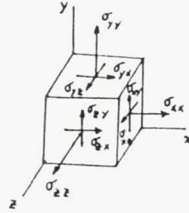
$$\dot{\epsilon}_{ij}^p = \left(\frac{\|\frac{3}{2}\dot{S} - \dot{\Omega}\|}{K} \right)^n \left(\frac{3}{2}S_{ij} - \Omega_{ij} \right)$$

• **The Evolution Equations:**

$$\begin{aligned} K &= K_1 - K_2 e^{-n_1 R} \\ \dot{\Omega}_{ij} &= (n_1 + n_2) \dot{\epsilon}_{ij}^p + \epsilon_{ij}^p \frac{\partial n_1}{\partial \theta} \dot{\theta} - \left(\Omega_{ij} - \dot{\Omega}_{ij} - n_1 \epsilon_{ij}^p \right) \left(\dot{G} - \frac{1}{n_2} \frac{\partial n_2}{\partial \theta} \dot{\theta} \right) \end{aligned}$$

• **The Hooke's Law:**

$$\begin{aligned} \dot{\sigma}_{ij} &= 2\mu (\dot{\epsilon}_{ij} - \dot{\epsilon}_{ij}^p) + \lambda \delta_{ij} \dot{\epsilon}_{kk} \\ &= 2\mu (\dot{\epsilon}_{ij} - \dot{\epsilon}_{ij}^p) + \lambda \delta_{ij} \dot{\epsilon}_{kk} \end{aligned}$$



SINGLE CRYSTAL CONSTITUTIVE MODEL

Material Selected: PWA-1480

Model Selected: Walker's Single Crystal Model

Modification: Employ Material Time Concept

Formulation:

$$\dot{(\cdot)} = \dot{(\cdot)} \frac{dz}{dt}$$

• **The Flow Rule:** on the r^{th} slip system of the 12 octahedral and 6 cubic systems (π_r , below is the Schmid shear stress on the slip plane)

$$\dot{\gamma}_r = \left(\frac{|\pi_r - \omega_r|}{K_r} \right)^{p-1} \left(\frac{\pi_r - \omega_r}{K_r} \right)$$

• **The Evolution Equations for ω_r and K_r**

$$\dot{\omega}_r = \rho_1 \dot{\gamma}_r - \rho_2 |\dot{\gamma}_r| \omega_r - \rho_3 |\omega_r|^{m-1} \omega_r$$

$$\dot{K}_r = \left\{ \sum_{k=1}^{12} [\beta|q + (1-q)\delta_{rk}] - \eta(K_r - \bar{K}) \right\} |\dot{\gamma}_r| - h(K_r - \bar{K})^t$$

• **The Inelastic Strain Rate:**

$$\dot{\epsilon}_{ij}^p = \sum_{r=1}^{12} a_{ij}^r \dot{\gamma}_r + \sum_{r=1}^6 b_{ij}^r \dot{\gamma}_r$$

• **The Hooke's Law:**

$$\dot{\sigma}_{ij} = D_{ijkl} \left\{ \dot{\epsilon}_{kl} - \sum_{r=1}^{12} (\dot{\epsilon}_{kl}^p)^{\text{oct}} - \sum_{r=1}^6 (\dot{\epsilon}_{kl}^p)^{\text{cubic}} \right\}$$

Figure 9.0 WALKER'S UNIFIED CONSTITUTIVE MODELS

Basic Ideal

- Material experiences deformation and remembers its deformation history.
- Thus, the **time** felt by material should also include the effect of deformation.

Expression of the Material Time Increment

$$dz = \sqrt{\lambda_{ijkl} \epsilon_{ij} \epsilon_{kl} + g dt^2}$$

where λ_{ijkl} and g are material parameters.

Proposed Use of the Material Time

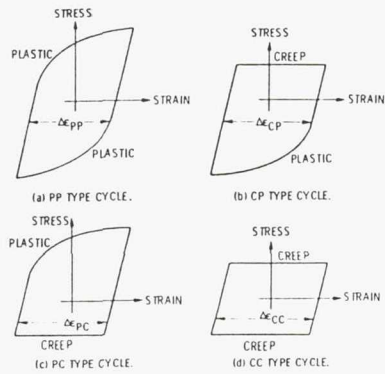
Change the time derivatives in a viscoplastic formulation into derivatives with respect to the material time.

- * It reduces to the original viscoplastic formulation when λ_{ijkl} is null and $g = 1$ (used for high temperature cases)
- * It has no rate dependence while plasticity remains when λ_{ijkl} is constant and $g = 0$ (applicable for low temperatures)

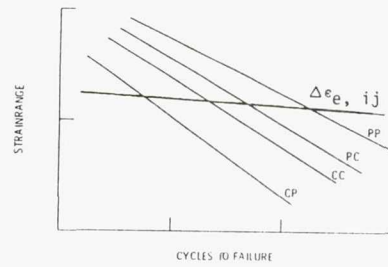
Figure 10.0 THE MATERIAL TIME CONCEPT

INELASTIC SRP CYCLE
TYPES/IDEALIZED LOOPS

($R_e = -1.0$)



TYPICAL PARTITIONED STRAIN
RANGE-LIFE RELATIONS



INTERACTION DAMAGE RULE:

$$\sum \frac{F_{ij}}{N_{ij}} = \frac{1}{N_{f0}}, \quad ij = pp, pc, cp, cc$$

FIGURE 11.0
DAMAGE MODEL TS-SRP (ISOTHERMAL)
 $R_e = -1.0$ AND $R_e = 0.0$ (PP)

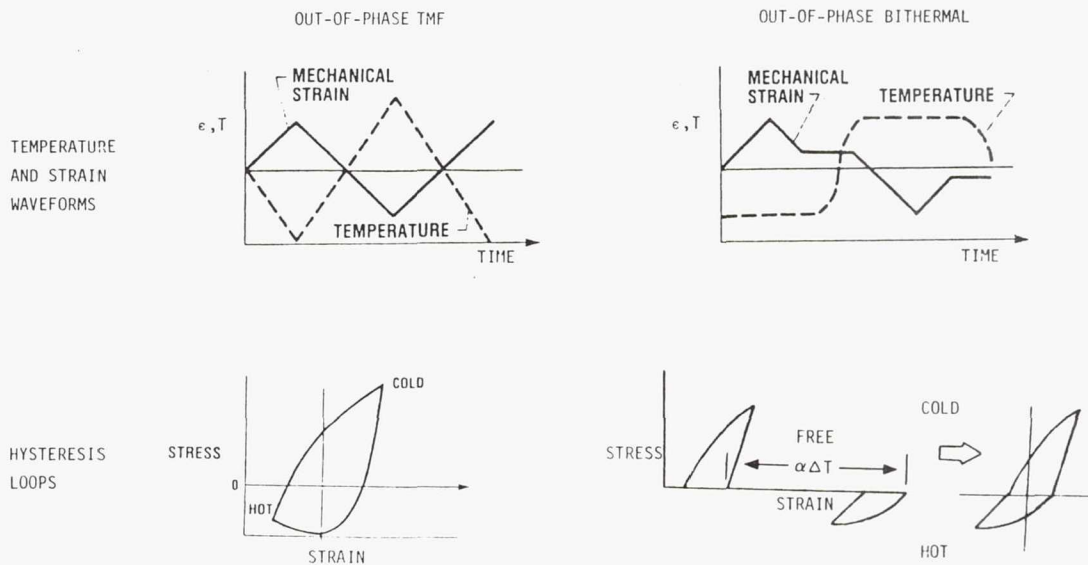
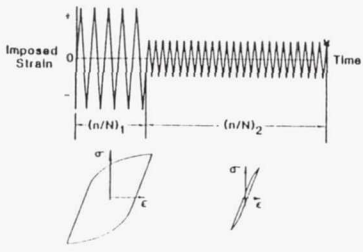


FIGURE 12.0
COMPARISON BETWEEN BITHERMAL AND TMF CYCLING

TWO STEP LOADING PATTERN



TWO LEVELS OF LOADING

N_1 & N_2

$$\frac{n_2}{N_2} = 1 - \left[\frac{n_1}{N_1} \right] \left[\frac{N_1}{N_2} \right]^\alpha$$

INITIAL LIFE FRACTION

REMAINING LIFE FRACTION

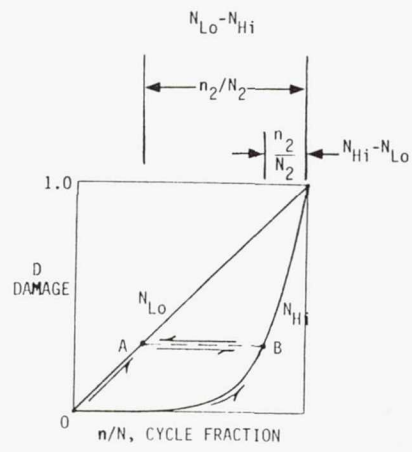


FIGURE 13.0
DAMAGE CURVE APPROACH

SECONDARY ORIENTATION EFFECTS IN A SINGLE CRYSTAL SUPERALLOY UNDER MECHANICAL AND THERMAL LOADS

Sreeramesh Kalluri and Ali Abdul-Aziz
Sverdrup Technology, Inc.
Lewis Research Center Group
Brook Park, Ohio 44142

and

Michael A. McGaw
NASA Lewis Research Center
Cleveland, Ohio 44135

The nickel-base single crystal superalloy PWA 1480 is a candidate blading material for the advanced turbopump development (ATD) program of the space shuttle main engine (SSME). In advanced liquid propellant rocket engines such as the SSME, the turbine blades are subjected to severe thermal gradients, both along the span and through the thickness during startup and shutdown cycles. In addition, the blades are subjected to centrifugal (arising from the very large rotational speeds) and vibratory loads. In order to improve thermal fatigue resistance of the blades, the single crystal superalloy PWA 1480 is grown along the low modulus [001] crystal orientation by a directional solidification process. Unless a seed crystal is used during the solidification process, the secondary crystal orientation [010] tends to be randomly oriented with respect to the geometry of the turbine blade (ref. 1). Since cubic single crystal materials such as PWA 1480 exhibit anisotropic elastic behavior (ref. 2), the stresses developed within the single crystal superalloy due to mechanical and thermal loads are likely to be affected by the exact orientation of the secondary crystallographic direction with respect to the geometry of the turbine blade.

The effects of secondary crystal orientation on the elastic response of single crystal PWA 1480 superalloy were investigated by using a square plate (25.4-mm side) with a thickness of 3.2 mm. This was accomplished by a parametric study in which the secondary crystallographic orientation was offset with respect to the geometric axes of the square plate from 0° to 90° in increments of 10°. The primary orientation of the square plate was assumed to be along the [001] crystallographic direction. The square plate was subjected to mechanical, thermal, and combined thermal and mechanical loads; the elastic stresses developed within the single crystal PWA 1480 plate were computed with elastic finite-element stress analysis for each combination of loading condition and secondary orientation angle.

Temperature-dependent elastic constants and the thermal coefficient of expansion for single crystal PWA 1480 were determined by the engineering division of Pratt & Whitney, United Technologies Corporation under the NASA Lewis Research Center Contract NAS3-23939 (ref. 3). The elastic stiffness matrices for different secondary orientation angles were computed by using the simplified method of Lieberman and Zirinsky (ref. 4). The commercially available MARC code was used to conduct the elastic stress analyses (ref. 5). The finite-element model of the square plate consisted of 500 8-noded,

isoparametric elements. The elastic stresses developed within a few selected elements in the finite-element mesh under mechanical, thermal, and combined thermal and mechanical loads, and the variation of these elastic stresses with the secondary orientation angle are presented.

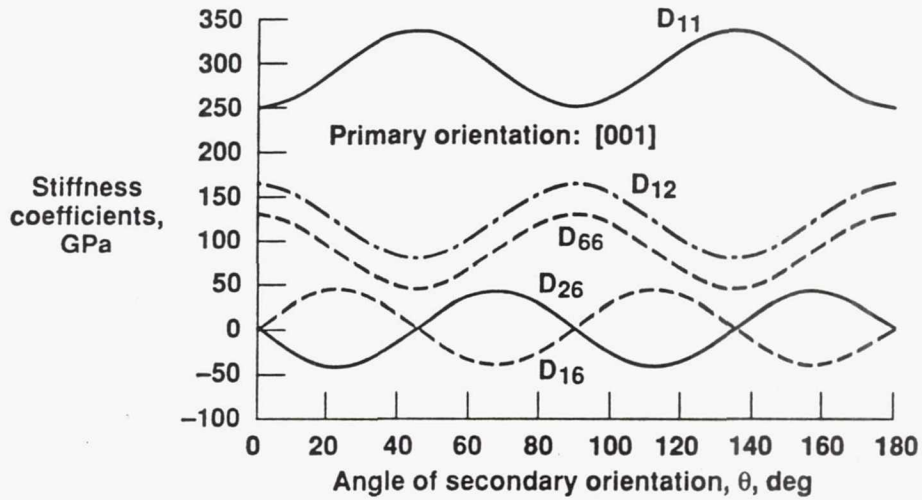
Results of the parametric study indicated that the variations in the stress components with the secondary orientation angle were dependent on the type of loading (mechanical, thermal, or combined) imposed on the square plate. It was also found that, for a case involving thermal gradient through the thickness of the square plate, the secondary orientation angle of 0° minimizes thermal stresses whereas the secondary orientation angle of 45° maximizes the thermal stresses.

REFERENCES

1. Duhl, D.N., "Single Crystal Superalloys", Superalloys, Supercomposites and Superceramics, J.K. Tien and T. Caulfield, eds., Academic Press, Inc., 1989, pp. 149-155.
2. Nye, J.F., "Physical Properties of Crystals, Their Representation by Tensors and Matrices", Clarendon Press, Oxford, 1957, pp. 131-149.
3. Swanson, G.A., Linsak, I., Nissley, D.M., Norris, P.P., Meyer, T.G., and Walker, K.P., "Life Prediction and Constitutive Models for Hot Section Anisotropic Materials Program, Second Annual Status Report", NASA CR-179594, 1987.
4. Lieberman, D.S., and Zirinsky, S., "A Simplified Calculation for the Elastic Constants of Arbitrarily Oriented Single Crystals", Acta Cryst., 9, 1956, pp. 431-436.
5. MARC General Purpose Finite Element Analysis Program, Vol. A: User Information Manual; Vol. B: Marc Element Library; Vol. F: Theoretical Manual. MARC Analysis Corporation, Palo Alto, CA, 1988.

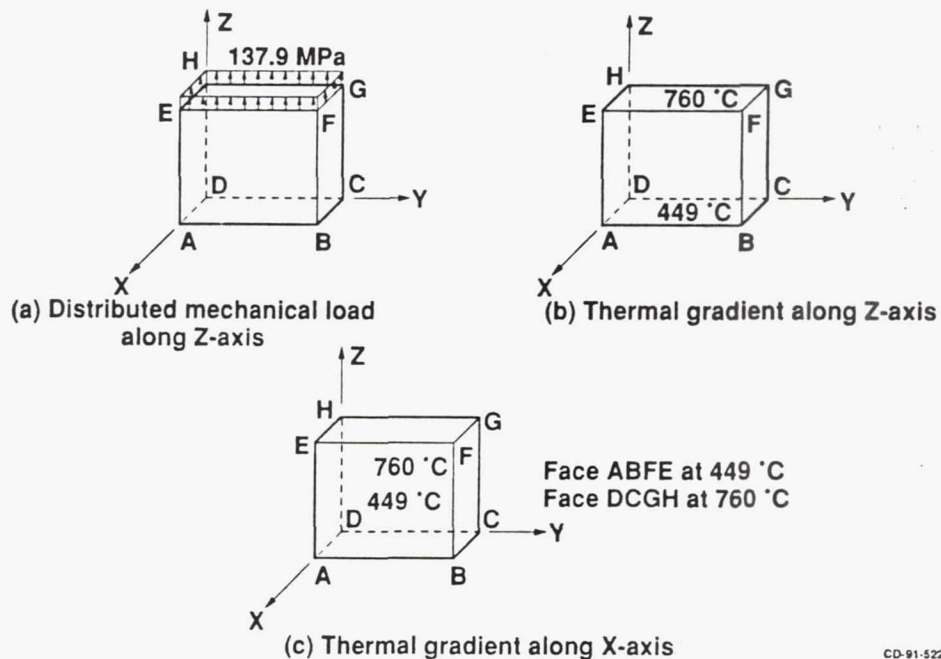
Elastic Stiffness Coefficients of PWA 1480 SC at 38 °C

($C_{11} = 250$ GPa; $C_{12} = 163$ GPa; $C_{44} = 129$ GPa)



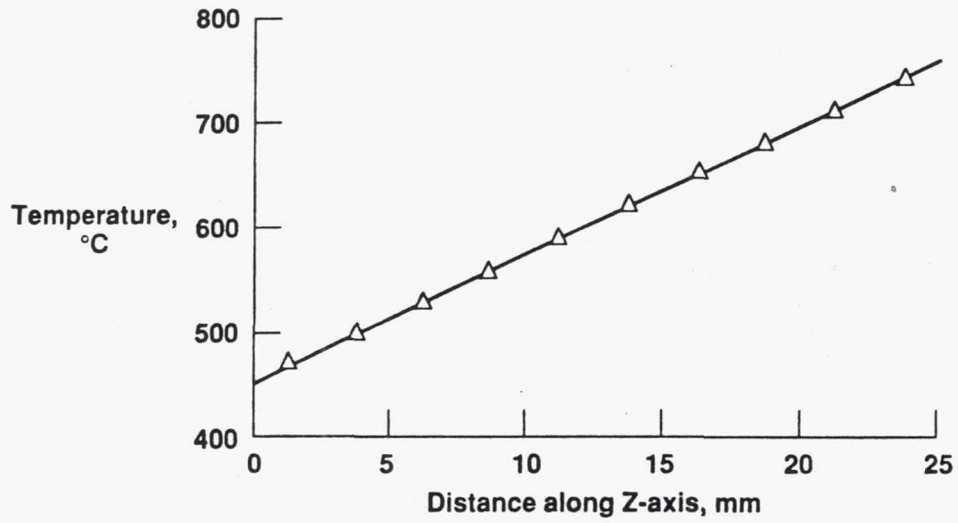
CD-91-52240

Mechanical and Thermal Loads Imposed on the Single Crystal PWA 1480 Square Plate



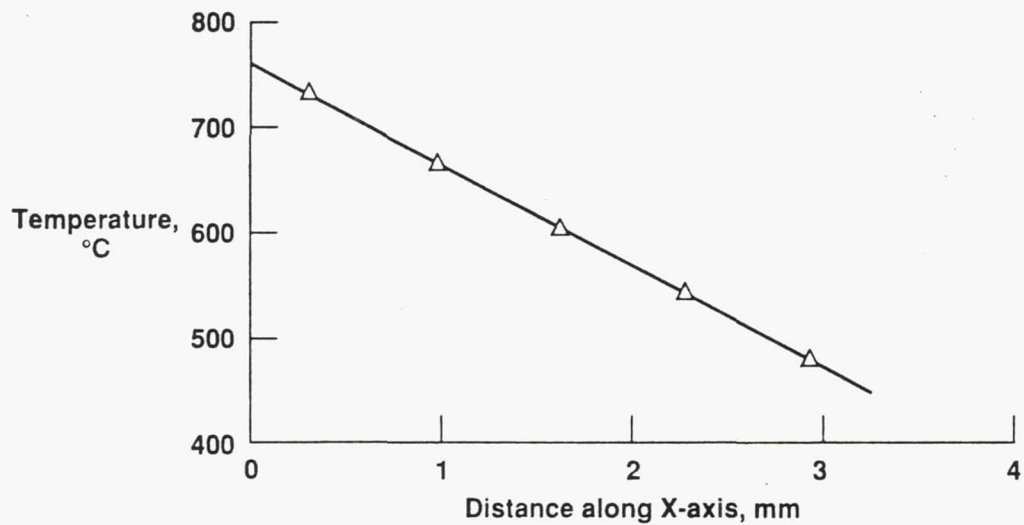
CD-91-52241

Imposed Thermal Gradient Along Z-Axis



CD-91-52242

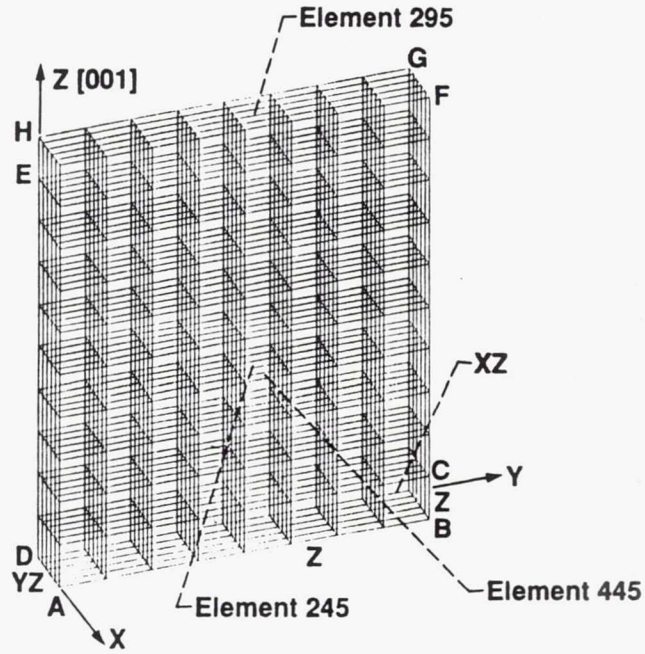
Imposed Thermal Gradient Along X-Axis



CD-91-52243

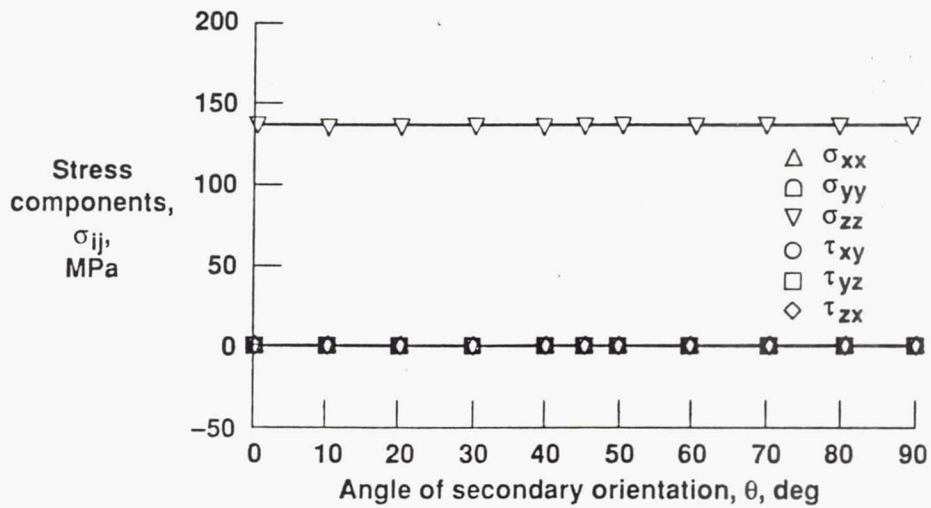
Finite-Element Mesh

500 8-Noded Isoparametric Elements



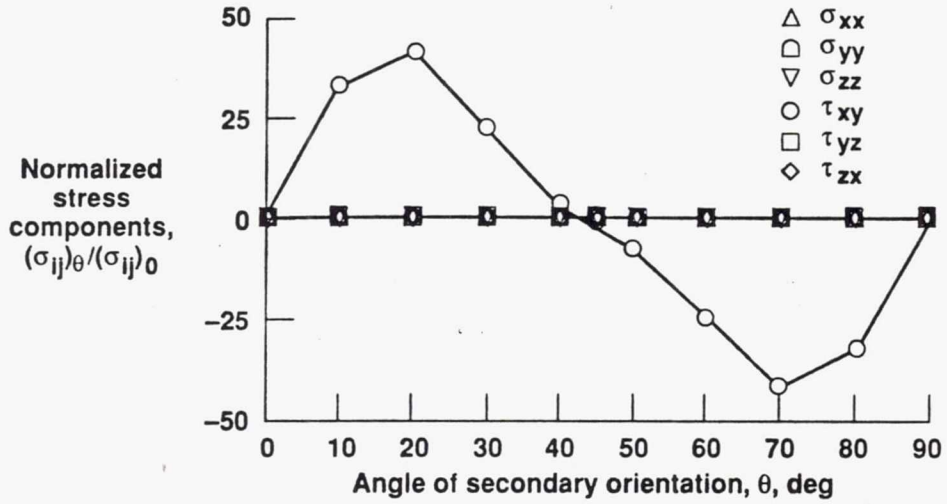
CD-91-52244

Mechanical Loading: Element 245



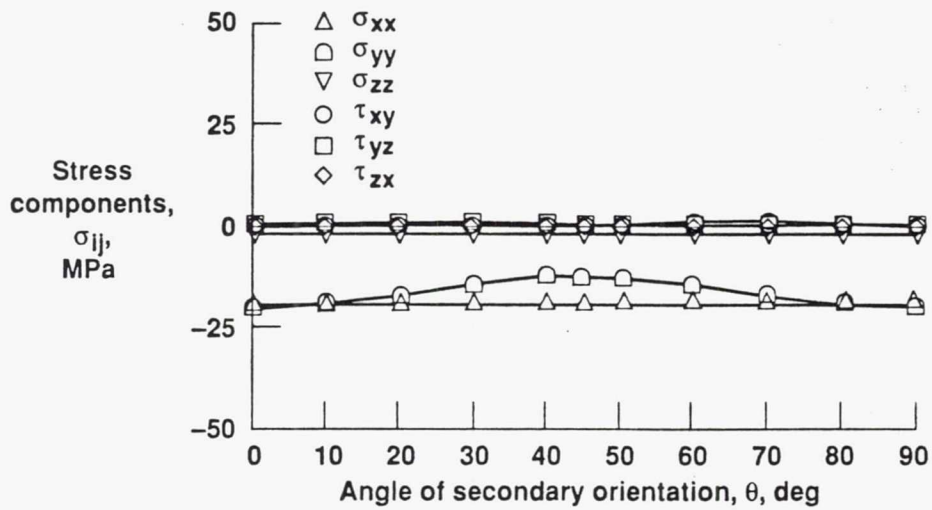
CD-91-52245

Mechanical Loading: Element 245



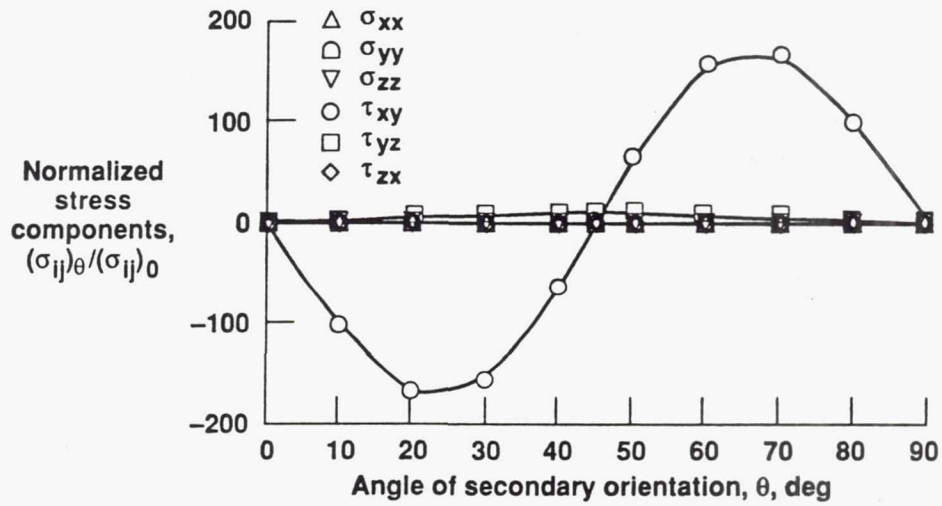
CD-91-52246

Thermal Loading in Z-Direction: Element 295



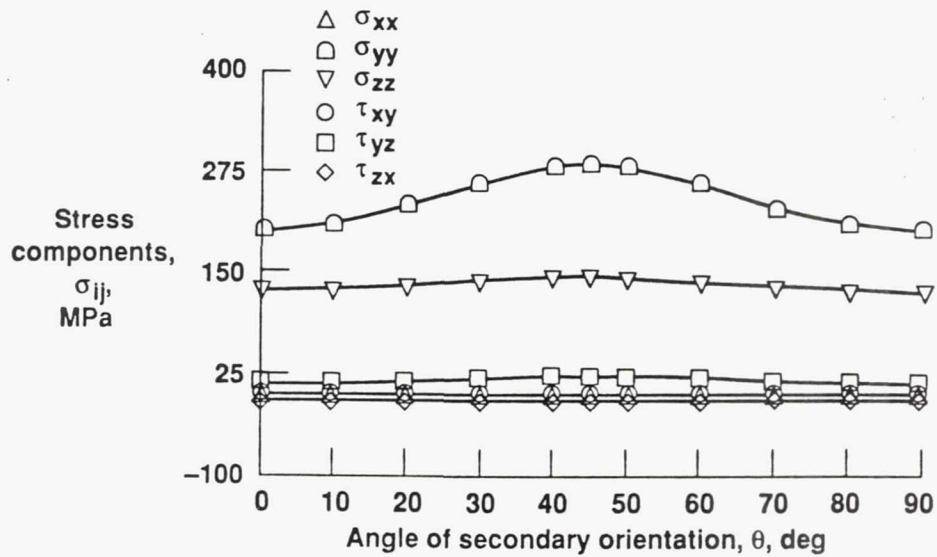
CD-91-52247

Thermal Loading in Z-Direction: Element 295



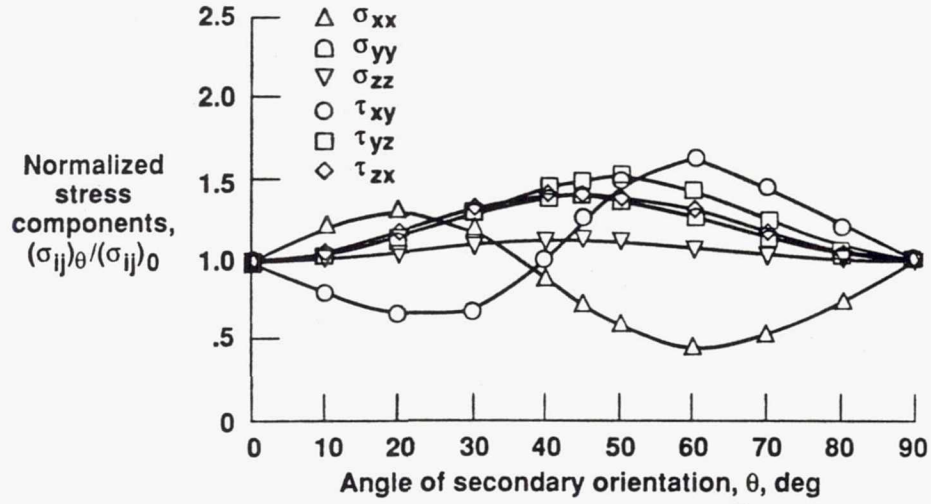
CD-91-52248

Thermal Loading in X-Direction: Element 445



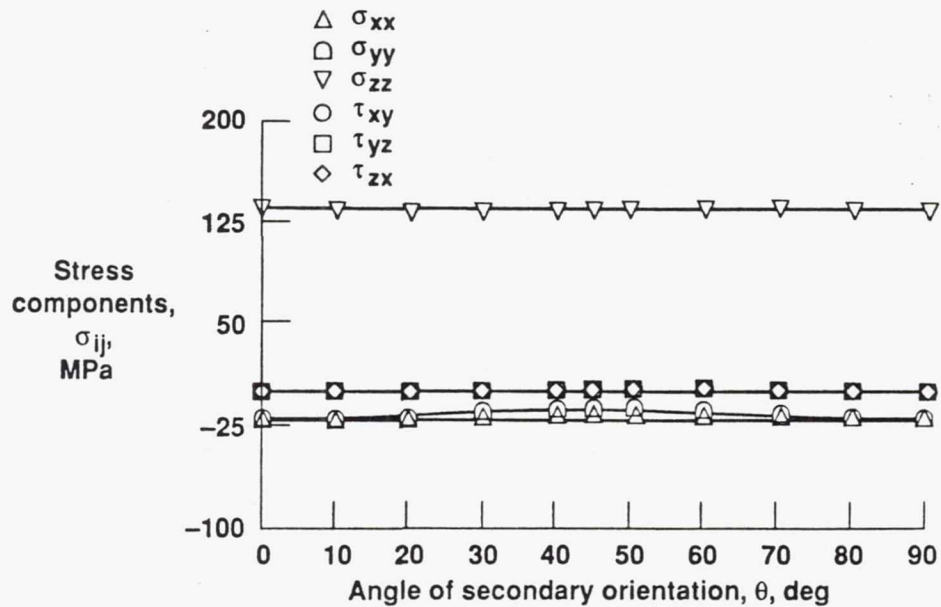
CD-91-52249

Thermal Loading in X-Direction: Element 445



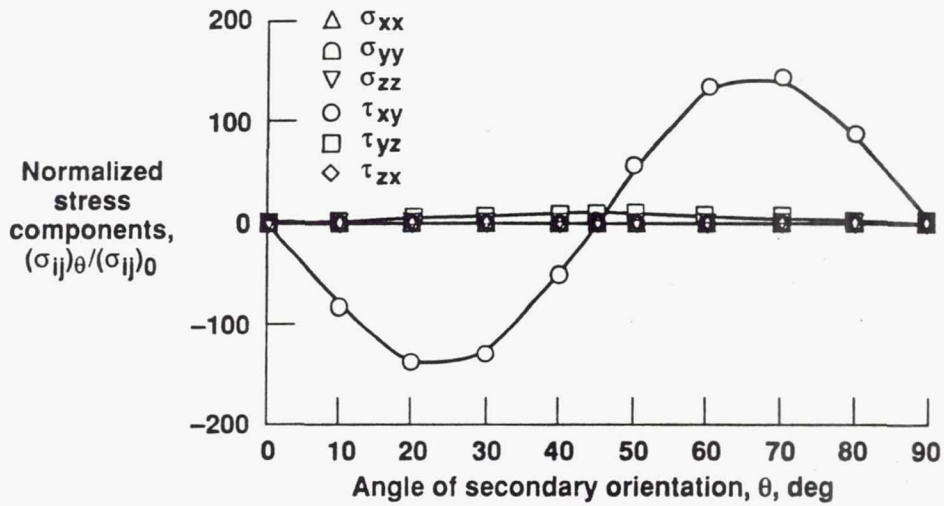
CD-91-52250

Thermal and Mechanical Loading in Z-Direction: Element 295



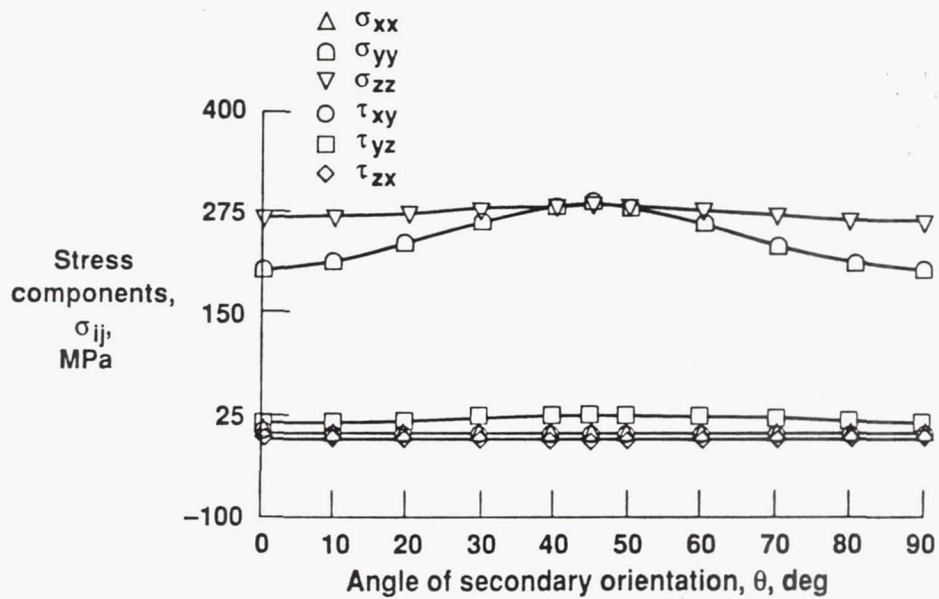
CD-91-52251

Thermal and Mechanical Loading in Z-Direction: Element 295



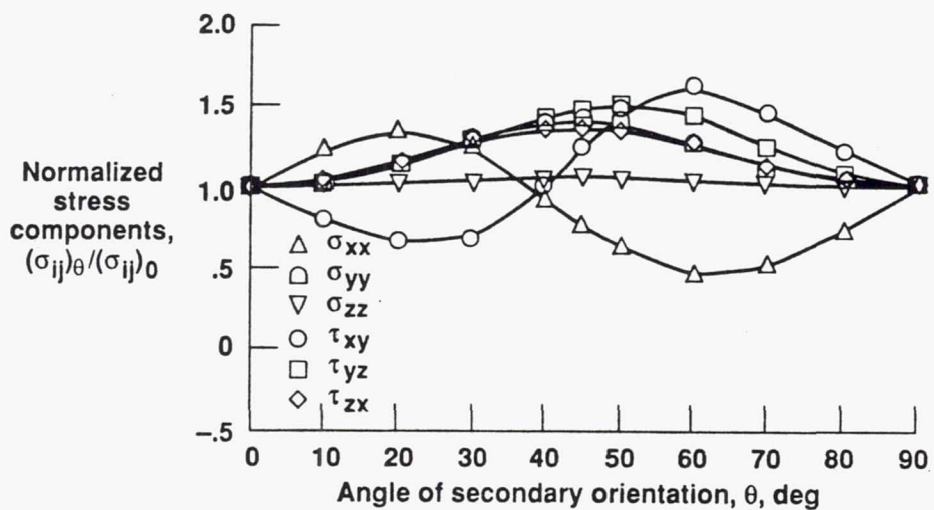
CD-91-52252

Combined Thermal (X-Direction) and Mechanical (Z-Direction) Loading: Element 445



CD-91-52253

Combined Thermal (X-Direction) and Mechanical (Z-Direction) Loading: Element 445



CD-91-52254

A MODEL FOR PREDICTING HIGH-TEMPERATURE FATIGUE FAILURE OF A W/Cu COMPOSITE

M.J. Verrilli, Y.-S. Kim,^{*} and T.P. Gabb
NASA Lewis Research Center
Cleveland, Ohio 44135

Fatigue failure of metal-matrix composites (MMC's) is a complex process. Matrix cracking, fiber/matrix interfacial failure, and fiber fracture can be major elements of the failure process. All these processes can work together to result in fatigue failure. However, depending on the failure process of the composite system of interest, a dominant failure mode can be identified. Modeling of dominant failure modes can serve as the basis of a fatigue life prediction scheme for MMC's.

The material studied in this research, a tungsten-fiber-reinforced, copper-matrix composite, is a candidate material for rocket nozzle liner applications. Previous research (ref. 1) on the fatigue behavior of a 10-vol % tungsten/copper composite at high temperatures has shown that the composite fails primarily from copper-matrix degradation. Fatigue cracks initiate and propagate inside the copper matrix through a process of initiation, growth, and coalescence of grain boundary cavities. The ductile tungsten fibers neck and rupture locally after the surrounding matrix fails. Complete failure of the composite then ensues.

This paper presents a simple fatigue life prediction model for the tungsten/copper composite system. The model is based on the failure mechanisms found through microscopic observations. Failure of the composite is assumed to occur when the matrix fails. The failure mechanisms of the fiber and its contribution to the overall composite fatigue life are neglected. It is assumed that no interfacial debonding or degradation occurs. The analysis in the present study is limited to isothermal fatigue of a unidirectional composite.

In the model the composite is assumed to fail when the average cavity in the matrix reaches a critical size. The cavity nucleation process in the copper matrix is neglected by assuming the preexistence of cavities in the as-received composite. This assumption was confirmed through metallographic examinations. In addition, it has been reported by others that at high temperatures the cavity nucleation process is very fast relative to the cavity growth process (ref. 2). All cavities are assumed to begin to grow at the moment of load application, all at the same rate. The average cavity growth size as a function of time is calculated by using a cavity growth law developed for creep conditions (ref. 3). In this model it is assumed that cavities grow with a quasi-equilibrium shape controlled by coupled diffusion and plasticity. Instantaneous stresses and strain rates as measured during the fatigue experiments are used in the calculation of cavity size. The average matrix stress is used to calculate cavity size. The calculation of

^{*}National Research Council - NASA Research Associate.

the average matrix stress is based on the assumption of an isostrain condition between the fibers and the matrix.

The model-predicted fatigue lives were compared with the experimental results of a series of load-controlled, tension-tension fatigue tests conducted at 560 °C on 10-vol % tungsten/copper. The predicted lives were in good agreement with the experimental results. The variation of the numerically calculated cavity size as a function of cycle number was found to exhibit similar trends as the experimentally observed cyclic change of the composite maximum tensile strain. The model also predicted cavity shrinkage during the early stages of cavity growth, in agreement with the work of others (ref. 4).

References

1. Kim, Y.-S.; Verrilli, M.J.; and Gabb, T.P.: Characterization of Fatigue Failure Processes in Tungsten Copper Composites Under Fatigue Loading Conditions. NASA TM-102371, 1989.
2. Gittins, A.: The Mechanism of Cavity Growth in Copper During High Temperature Fatigue. *Met. Sci. J.*, vol. 2, 1968, pp. 51-58.
3. Martinez, L.; and Nix, W.D.: Effects of Capillarity on Intergranular Cavity Growth Controlled by Diffusion and Plasticity. *Scripta Met.*, vol. 15, 1981, pp. 757-761.
4. Tang, N.Y.; and Plumtree, A.: A Note on Grain Boundary Diffusion Controlled Cavity Growth During Elevated Temperature Fatigue. *Met. Trans. A*, vol. 16, 1985, pp. 300-302.

Objectives

- Present a fatigue life prediction methodology for an MMC
 - Model based on observed failure characteristics
- Compare predictions with experimental results

Figure 1

CD-91-52029

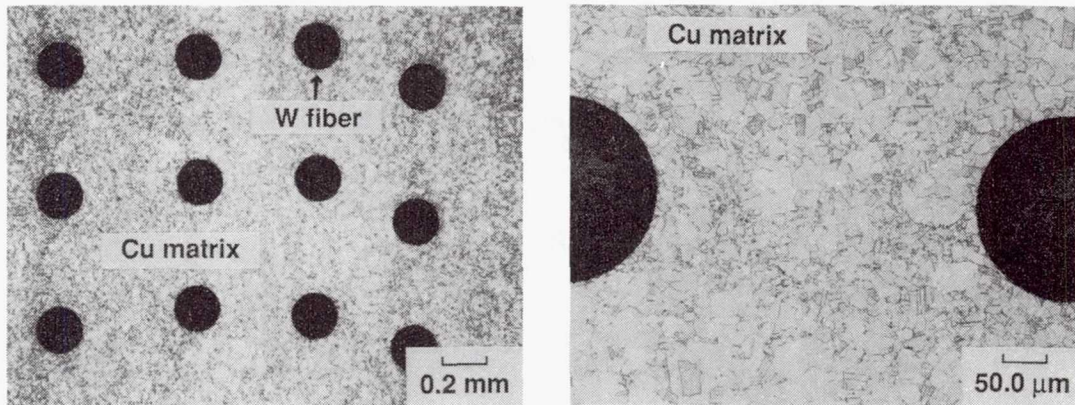
Tungsten-Fiber-Reinforced Copper

- Matrix, OFHC copper
- Fiber, GE 218 tungsten wire
- Fabrication, arc-spraying technique

Figure 2

CD-91-52030

As-Received Composite Microstructure



CD-91-52031

Test Conditions

- Temperature, 560 °C
- Control mode, load
- R-ratio, 0.05
- Waveform, triangular
- Cycle frequency, 3 cpm
- Environment, vacuum

Figure 4

CD-91-52032

Stress-Strain Curves for W/Cu Fatigued at 560 °C

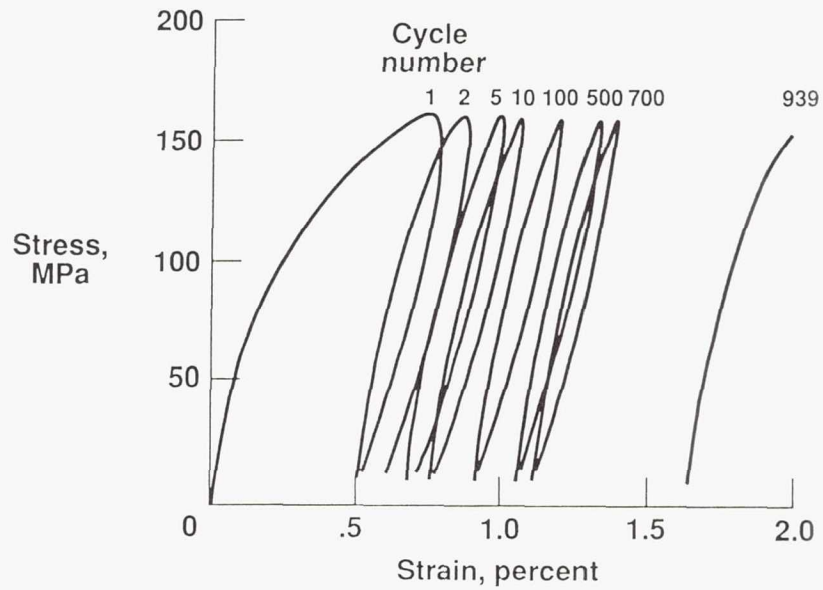
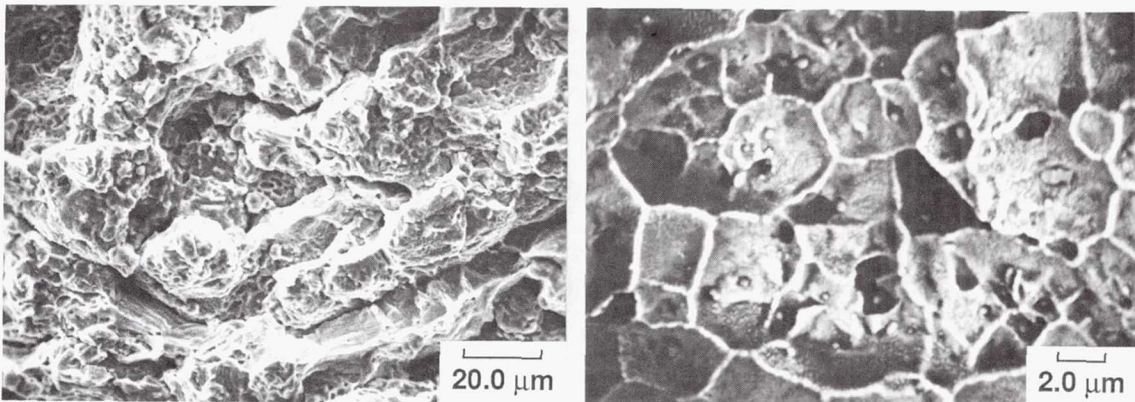


Figure 5

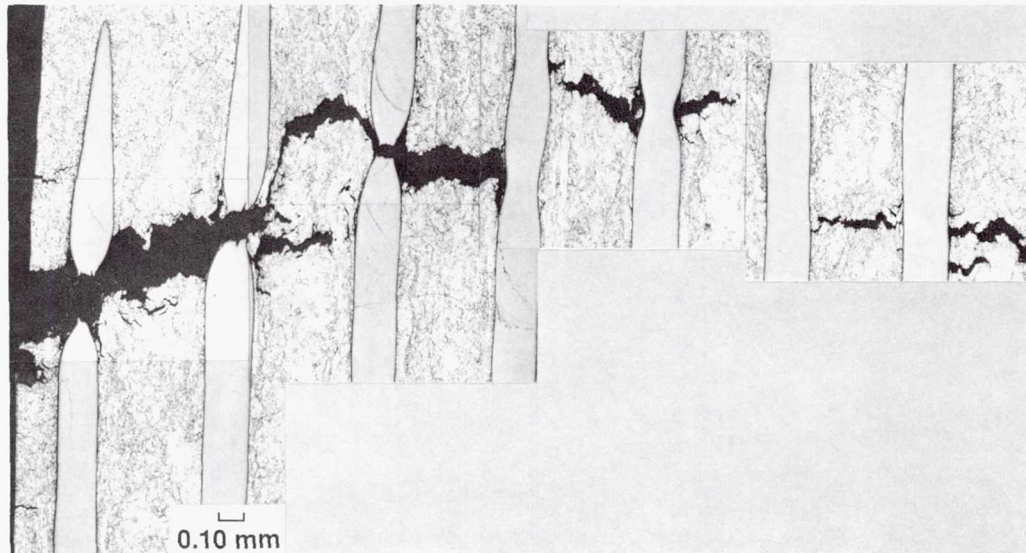
CD-91-52033

Fractographs of Specimens Fatigued at 560 °C



CD-91-52034

Overall Fatigue Crack Appearance in W/Cu Composite



CD-91-52035

Features of Numerical Model of Isothermal Fatigue Failure in W/Cu Composite

- Composite failure is assumed to occur when matrix fails (experimentally observed).
- Failure mechanism of composite is cavitation of matrix (experimentally observed).
- Creep cavity growth model can describe fatigue failure.
- Contribution of cavity nucleation to fatigue life is neglected (preexisting cavities experimentally observed).
- Failure characteristics of fibers are not considered.

Figure 8

CD-91-52036

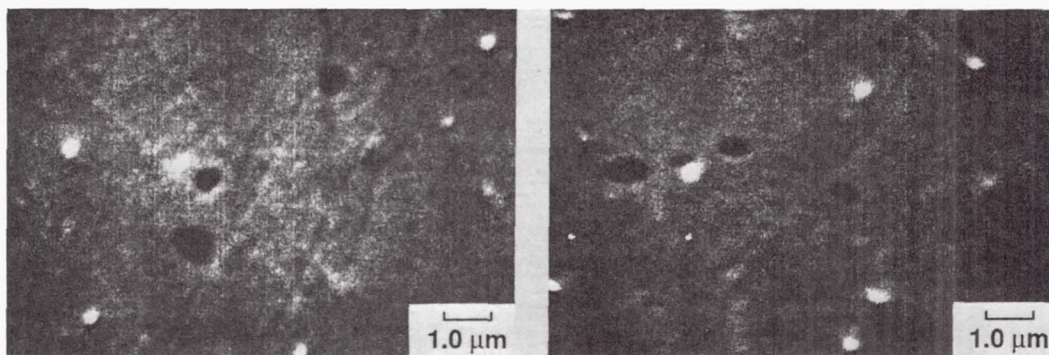
Features of Numerical Model of Isothermal Fatigue Failure in W/Cu Composite (Concluded)

- ϵ_{11} is the same (isostrain) in fibers and matrix.
- Interfacial debonding is not considered.
- Model applies only to isothermal cycling.
- Inelastic strain in matrix is described by simple power-law relations.
- Failure criterion: Area fraction of cavities = $a^2/c^2 = 0.8$
(based on observed fracture surfaces).

Figure 9

CD-91-52037

Preexisting Cavities in Cu Matrix



CD-91-52038

Cavity Growth Controlled by Coupled Diffusion and Plasticity

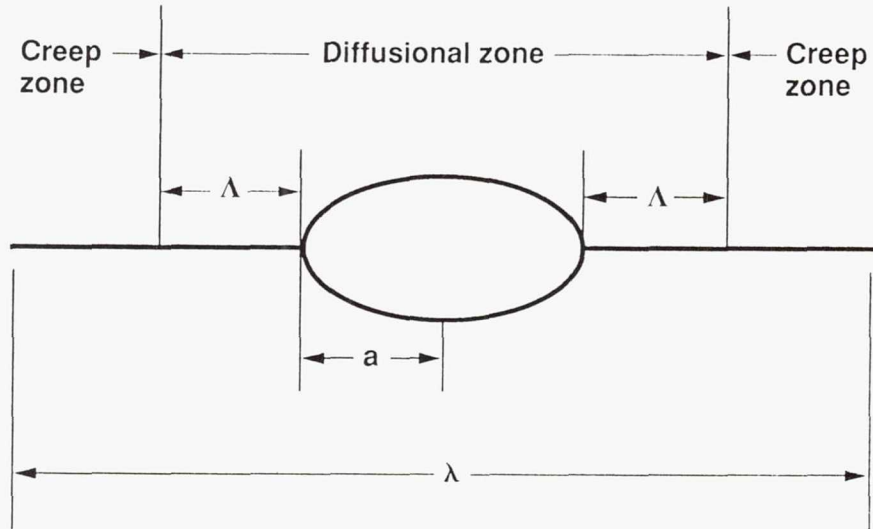


Figure 11

CD-91-52039

Cavity Growth Mechanism

Cavity Growth by Coupling of Diffusion and Power-Law Creep

- Characteristic diffusion length

$$\Lambda = \left(\frac{D_B \delta_B \Omega \sigma}{KT \dot{\epsilon}} \right)^{1/3}$$

- Cavity growth rate

$$\frac{da}{dt} = \frac{a \dot{\epsilon}}{2h(\Psi)} \left(\frac{\Lambda}{a} \right)^3 Q \left(\frac{a}{a + \Lambda} \right) \times \left\{ 1 - \frac{2a}{(a + \Lambda)^2} \frac{\gamma_s}{\sigma} - 2 \sin(\Psi) \frac{\gamma_s}{\sigma a} \left[1 - \left(\frac{a}{a + \Lambda} \right)^2 \right] \right\}$$

Figure 12

CD-91-52040

Deformation Mode of Cu Matrix During Fatigue

$$\epsilon = \epsilon_{\text{elastic}} + \epsilon_{\text{plastic}} + \epsilon_{\text{creep}}$$

$$\epsilon_{\text{elastic}} = \frac{\sigma}{E}$$

$$\epsilon_{\text{plastic}} = K \sigma^{\frac{1}{N}}$$

$$\dot{\epsilon}_{\text{creep}} = B \sigma^n$$

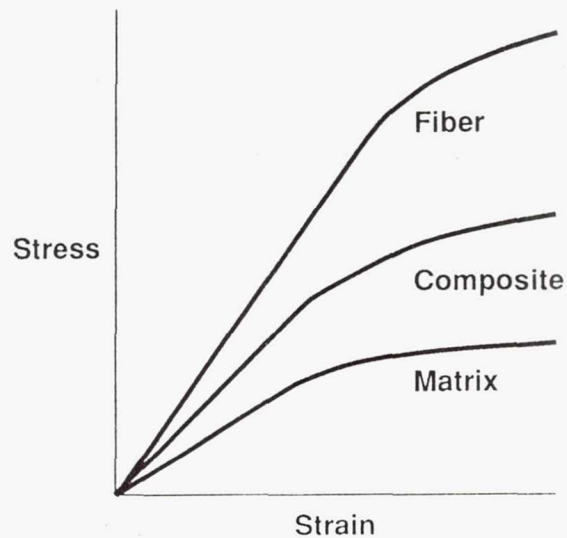
$$\dot{\epsilon} = \left(\frac{1}{E} + K \frac{1}{N} \sigma^{\frac{1}{N}-1} \right) \dot{\sigma} + B \sigma^n$$

$$\dot{\epsilon}_{\text{inelastic}} = K \frac{1}{N} \sigma^{\frac{1}{N}-1} \dot{\sigma} + B \sigma^n$$

Figure 13

CD-91-52041

Determination of Stress in Cu Matrix



- Isostrain condition
- Stress-strain curve of pure Cu at 833 K

Figure 14

CD-91-52042

Cavity Size Calculation

$$a = a_0 + \int_{t_1}^{t_2} \dot{a} dt$$

$$a_0 = \frac{2\lambda_s}{\sigma}$$

Figure 15

CD-91-52043

Calculated Cavity Size in Cu Matrix as Function of Time

Model-Predicted Cavity Growth; W/Cu Composite;
Temperature, 560 °C; Specimen Number, 0-15;
Initial Cavity Radius, 0.4 μm

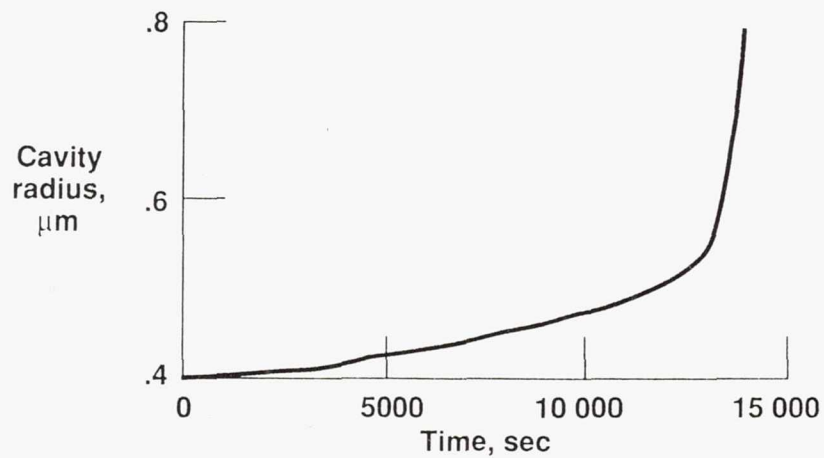


Figure 16

CD-91-52045

Maximum Cyclic Strain Versus Cycle Number for Fatigue of W/Cu at 560 °C

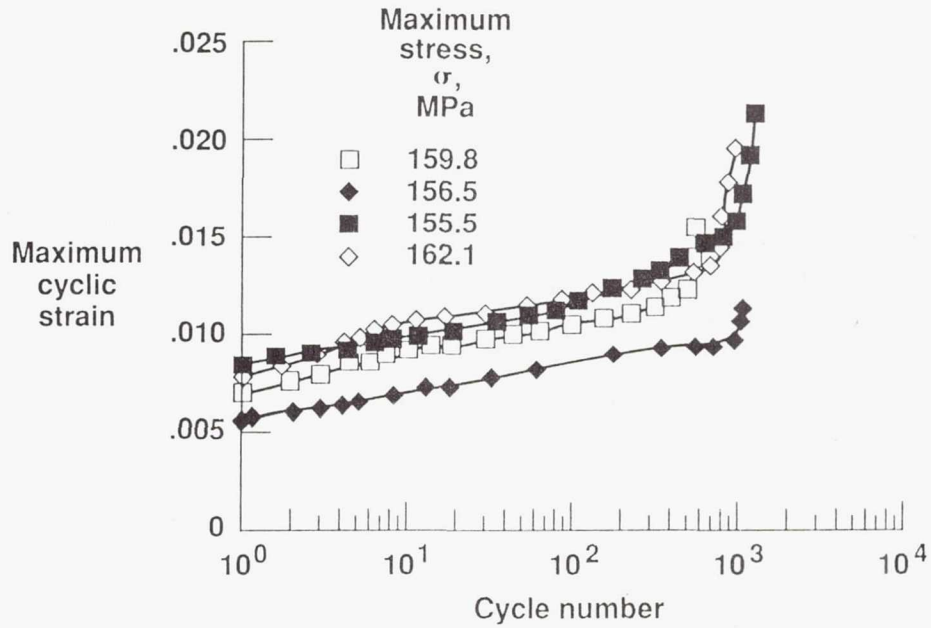


Figure 17

CD-91-52044

Comparison of Model-Predicted Results With Experimental Results

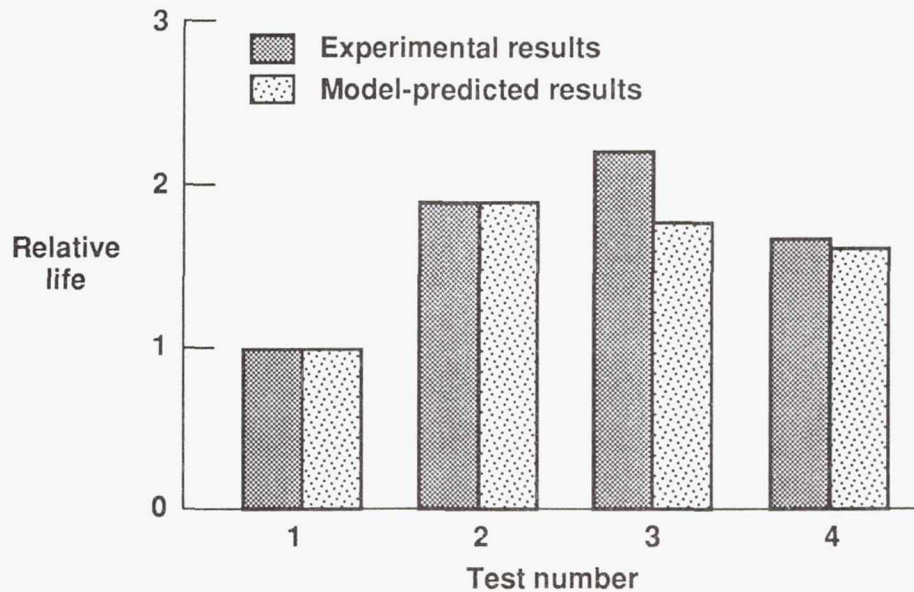


Figure 18

CD-91-52046

Conclusions

- A fatigue life prediction model was developed based on the failure characteristics found through microscopic observations.
- The model uses a quasi-equilibrium cavity growth mechanism controlled by coupled diffusion and plasticity. Instantaneous values of stress and strain rate during a fatigue cycle were used for the calculation.
- The predicted fatigue lives are in good agreement with the experimental results.
- The model can be more generalized by incorporating other mechanisms, such as grain boundary sliding and strain hardening of the Cu matrix, that can influence the fatigue life of the composite.

Figure 19

CD-91-52047

EXAMINATION OF THE EFFECT OF PROPULSION SYSTEM PERFORMANCE VARIABLES ON THE LIFE PREDICTION FOR THE SSME LOX POST

D. A. Russell, K. R. Rajagopal, G. Orient, and J. Keremes
Rocketdyne Division
Rockwell International
Canoga Park, California 91303

The objective of this task is to calculate damage evolution at the critical location of selected components of reusable space propulsion systems as a function of their operating environment(s) and to relate the evolution of damage at the critical locations to the performance variables of the propulsion system using advanced constitutive and damage models. The models so developed will be oriented toward use in an advanced diagnostic/prognostic health monitoring system for reusable propulsion systems. Further, the models developed must be amenable to a probabilistic interpretation in the future. The intent is to build on the state of the art of previous work in these fields whenever possible rather than to develop new models. The components to be modelled include, a Lox Post (injector element), a thrust chamber, and a turbine blade. The study conducted on the Lox Post is reported here.

The loads that contribute to the main injector lox post damage evolution are temperature, static and dynamic pressure loads, and vibration loads. The temperature load on the post is controlled by engine system variables such as preburner mixture ratio, hot gas temperature and flow rate, Lox temperature and flow rate, local hot gas and coolant film coefficients, and any other local geometric and material property parameters. The pressure loads are a function of fluid drag and turbulence and static pressure differential. In this particular application damage at a row 12 Lox post thread root location is computed and related to system variables. It is apparent that generation of a link between performance variables and damage will span several disciplines such as engine performance, fluid mechanics, heat-transfer, structural analysis, and material science.

In general, for any component only a subset of the system variables that influence damage are directly measured in an actual flight. Thus it becomes necessary to rely on a numerical engine model that will compute the system variables that influence damage directly from a set of measured more primitive (independent) and/or local system variables that control engine health, thrust and performance. The most frequently used form of the model is the influence coefficient model which derives its origin from the more computationally intensive engine balance model and test measurements. Typically, the influence coefficient model is generated such that it accurately portrays engine performance in the plus or minus 3 sigma range of engine

performance. One such influence coefficient model is used as part of this task.

The development of the system variable to structural response link require a large number of one time heat transfer and structural analysis runs covering the entire start transient, steady state, and cut off transient. Several parametric heat transfer analyses were run to set up influence coefficient models for different regions of the Lox Post that help to quickly compute the entire temperature field in the Lox Post over the full duty cycle given the local system variables. Using heat transfer influence coefficient models several parametric nonlinear structural analyses over two duty cycles were run to establish the link between system variables to temperature, stress levels, strain levels and, multiaxial factors at the critical locations of the hysteresis loop. A very refined axisymmetric model was used for this purpose. Since the temperature was low enough for this component, the standard rate independent plasticity model was considered adequate for this application.

The dynamic response due to random pressure and mechanical vibration was computed using a detailed beam finite element model. The pressure P.S.D. shape and power, correlation length and their relation to local mass flow rate and fluid density were obtained from fluid dynamics unit. These system variables are linked to other system variables through engine system models. The r.m.s. stresses due to mechanical vibration (harmonics and random) were obtained using a multibase excitation analysis. Thus the r.m.s. high frequency stress response due to dynamic excitation is linked to system variables.

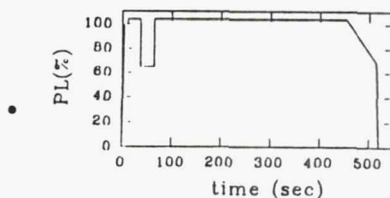
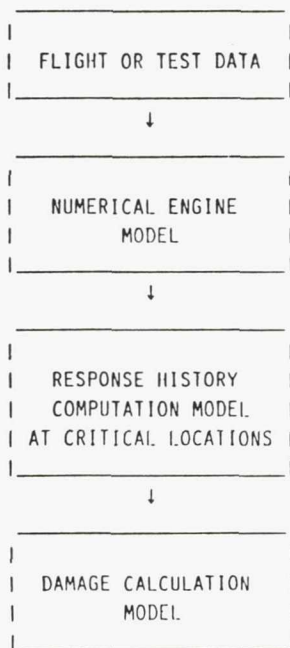
Thus at the end of above steps, the link between system variables to response variables that control damage evolution has been established. The damage computation module has been written with enough modularity to compute damage due to linear as well as nonlinear accumulation algorithms using the damage curve approach. Given the system variables, power level, and their duration the module computes the damage accumulated and if necessary computes the remaining flight life assuming that the last flight profile will be repeated in future flights. Several further options are available for the user to experiment with different stress amplitude distributions, order effect, hydrogen embrittlement and mutiaxiality factors, etc.

Future efforts involve the examination of system variables on life prediction of Main Combustion Chamber Liner and Turbine Blades. The main combustion chamber liner effort involves the implementation of thermal ratcheting and crack growth prediction models and turbine blade effort involves implementation of life prediction methodologies for anisotropic superalloys.

LIFE PREDICTION TASK OBJECTIVES

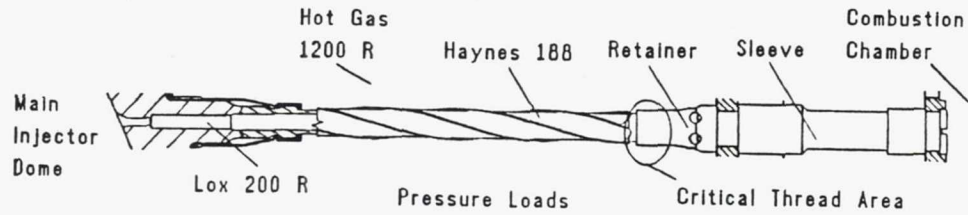
- DEVELOP LINK FROM PERFORMANCE VARIABLES TO DAMAGE
- USE ADVANCED CONSTITUTIVE AND DAMAGE MODELS
- MODELS USED MUST BE AMENABLE FOR EXTENSION TO PROBABILISTIC DOMAIN
- DEMONSTRATE METHODOLOGY FOR LOX POST, MAIN COMBUSTION CHAMBER LINER, TURBINE BLADE

LIFE PREDICTION LINK TO HEALTH MONITORING SYSTEMS



- APPROXIMATION MODEL DERIVED FROM FULL FLEDGED ENGINE BALANCE MODEL
- APPROXIMATION MODEL DERIVED FROM FULL FLEDGED FINITE ELEMENT AND ADVANCED CONSTITUTIVE MODELS
- DAMAGE CALCULATION USING ADVANCED MODELS

LOADS ON MAIN INJECTOR ELEMENT
ROW 12



- DOMINANT LOADS
 - TEMPERATURE DIFFERENTIAL
 - FLUID LOADS (DRAG AND DYNAMIC PRESSURE FLUCTUATION)
- LESS DOMINANT LOADS
 - MECHANICAL VIBRATION
- CRITICAL AREA LOOKED AT IS THE THREAD LOCATION

AN APPROXIMATE ENGINE PERFORMANCE MODEL
INFLUENCE COEFFICIENT MODEL

- EXTRACTED FROM NONLINEAR BALANCE MODEL
- POLYNOMIAL REGRESSION FIT
- STRONGLY CORRELATED WITH POWER LEVEL

INFLUENCE COEFFICIENT → $IC_{ij}(PL) = C_0 + C_1 PL + C_2 PL^2 + C_3 PL^3$

DEPENDENT VARIABLE MEAN VALUE → $y_i(PL) = a_0 + a_1 PL + a_2 PL^2 + a_3 PL^3$

- MAGNITUDE EVALUATION OF DEPENDENT VARIABLES

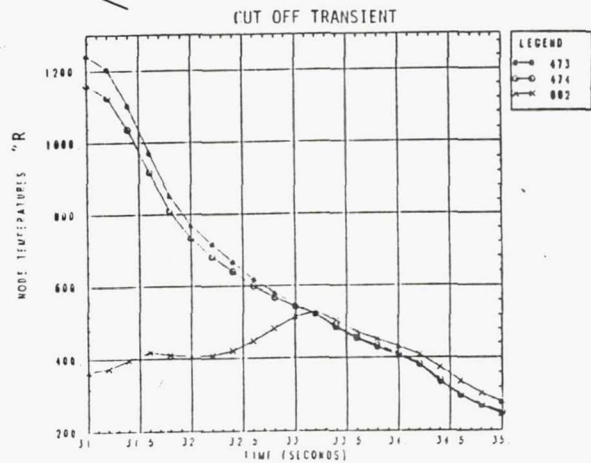
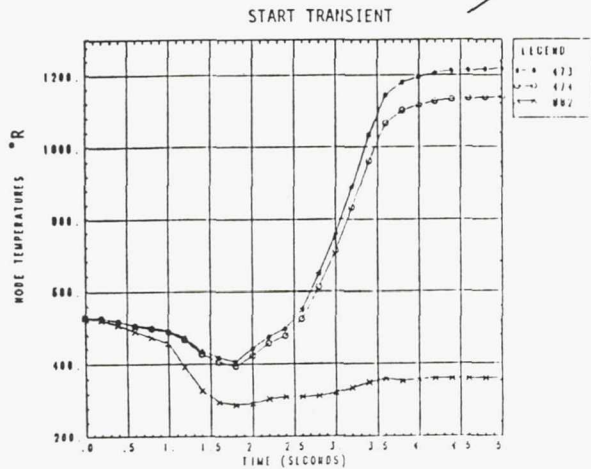
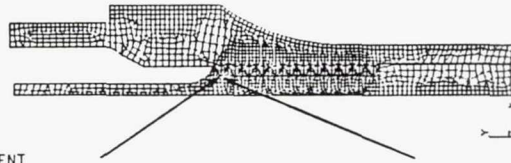
$$\frac{\Delta y_i}{y_i} = \sum_j IC_{ij} \frac{\Delta x_j}{x_j}$$

AN EXAMPLE OF INDEPENDENT AND DEPENDENT VARIABLE SET

| INDEPENDENT VALUES | | DEPENDENT VALUES | |
|-----------------------------|----------|-----------------------------|-------------|
| 1. FACILITY MIXTURE RATIO | 6.0260 | 1. HPOTP SPEED (RPM) | 28335.8600 |
| 2. FUEL INL TOTAL PR (PSIA) | 30.0000 | 2. HPFTP SPEED (RPM) | 35660.2700 |
| 3. OXID INL TOTAL PR (PSIA) | 100.0000 | 3. HPOTP PUMP DIS PR (PSIA) | 4321.3460 |
| 4. FUEL INL TEMP (DEG R) | 37.0000 | 4. HPFTP PUMP DIS PR (PSIA) | 6521.7120 |
| 5. OXID INL TEMP (DEG R) | 164.0000 | 5. OPB CHAMBER PR (PSIA) | 5308.2630 |
| 6. HPFTP TURB NOZZ AREA | 10.8000 | 6. FPB CHAMBER PR (PSIA) | 5213.4570 |
| 7. HPOTP TURB EFF MULT | 1.0310 | 7. ENGINE OXID FLOWRATE | 930.5878 |
| 8. HPOTP TURB NOZZ AREA | 2.8960 | 8. ENGINE FUEL FLOWRATE | 154.2625 |
| 9. THRUST CHAMB C* MULT | 1.0053 | 9. ENGINE THRUST | 490784.4000 |
| 10. HPFTP TURB EFF MULT | .9240 | 10. OXID PRESSURANT F/R | 1.6580 |
| 11. POWER LEVEL | 1.0400 | 11. FUEL PRESSURANT F/R | .7280 |
| 12. ETC. ... | | 12. OPOV POSITION | .6706 |
| | | 13. FPOV POSITION | .8001 |
| | | 14. MCC INJECTOR END PR | 3126.2170 |
| | | 15. HPPOP INLET PR (PSIA) | 386.2080 |
| | | 16. HPFP INLET PR (PSIA) | 206.8424 |
| | | 17. PBP DISCH PR (PSIA) | 7389.5130 |
| | | 18. HPPOP INLET TEMP | 169.7184 |
| | | 19. HPPOP DISCH TEMP | 192.0415 |
| | | 20. HPFP DISCH TEMP | 98.1692 |
| | | 21. PBP DISCH TEMP | 205.3588 |
| | | 22. HPFP INLET TEMP | 42.3058 |
| | | 23. LPOTP SPEED | 5166.0650 |
| | | 24. LPFTP SPEED | 15130.7500 |
| | | 25. HPOT DISCH TEMP A | 1285.8410 |
| | | 26. HPOT DISCH TEMP B | 1285.8410 |
| | | 27. HPFT DISCH TEMP A | 1735.9330 |
| | | 28. ETC. ... | |

THERMAL TRANSIENT ANALYSIS USING A REFINED THERMAL MODEL.

- ANSYS MODELING/SINDA THERMAL ANALYSIS
- FOUR DISTINCT ZONES



AN APPROXIMATE THERMAL ANALYZER MODEL
QUICK COMPUTATIONS ON TEMPERATURE FIELD

- INDEPENDENT VARIABLES
 - HOT GAS TEMPERATURE AND FLOW RATE
 - HOT GAS AND LOX h FACTOR
 - LOX TEMPERATURE AND FLOW RATE
 - HAYNES 188 K FACTOR
 - LOX PRESSURE
- INFLUENCE COEFFICIENT MODEL
- COEFFICIENTS OBTAINED FROM LARGE NUMBER OF PARAMETRIC RUNS

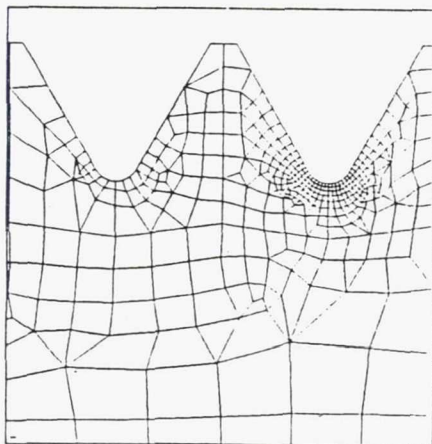
$$\frac{Max.Twg - Ref.Max.Twg}{Ref.Max.Twg} = k_1 \left[\frac{V - Ref.V}{Ref.V} \right] + k_2 \left[\frac{V - Ref.V}{Ref.V} \right]^2$$

$$\frac{Min.Twg - Ref.Min.Twg}{Ref.Min.Twg} = k_1 \left[\frac{V - Ref.V}{Ref.V} \right] + k_2 \left[\frac{V - Ref.V}{Ref.V} \right]^2$$

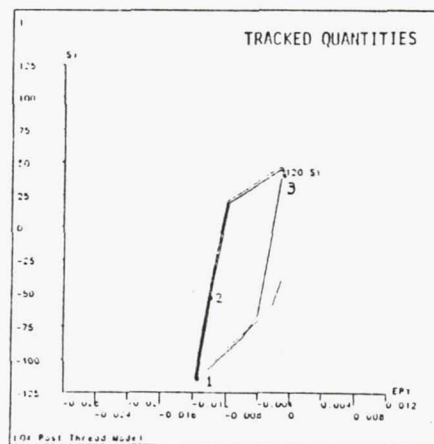
- DIFFERENT INFLUENCE COEFFICIENTS FOR FOUR ZONES

STATIC NONLINEAR ANALYSIS FOR TWO DUTY CYCLES USING A REFINED MODEL.

- ANSYS COMPUTER CODE USED
- SEVERAL PARAMETRIC ANALYSES CORRESPONDING TO PERTURBATIONS OF SYSTEM VARIABLES
- TWO DUTY CYCLE TEMPERATURE CYCLING



A REFINED MODEL.



A TYPICAL AXIAL $\sigma - \epsilon$ RESPONSE

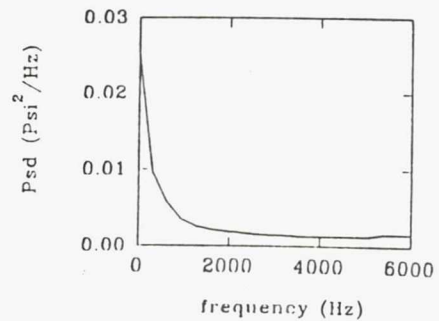
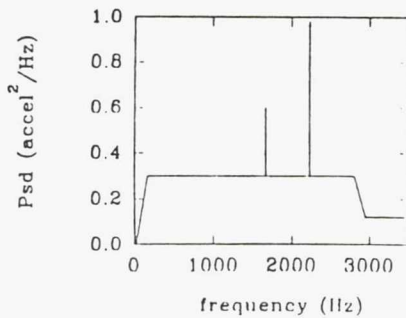
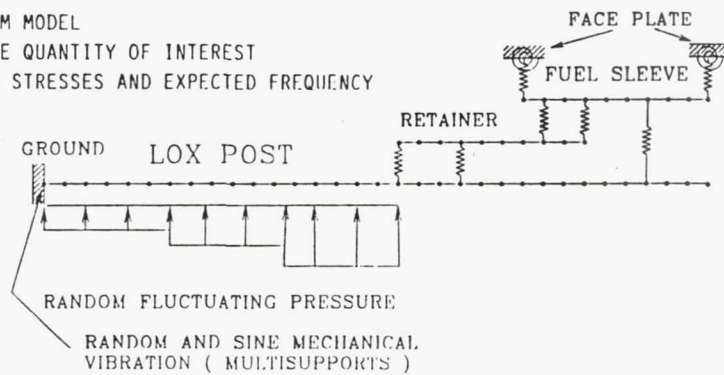
APPROXIMATE STATIC ANALYSIS MODEL LINKING RESPONSE TO SYSTEM VARIABLES
LCF DAMAGE DRIVERS

- RESPONSE VARIABLES
 - EFFECTIVE STRESS
 - TOTAL EFFECTIVE STRAIN
 - PLASTIC STRAIN
 - TEMPERATURE
 - MULTIAXIALITY FACTOR
- TRACKED AT THREE POINTS OF HYSTERESIS LOOP TO CALCULATE LCF DAMAGE
- A TYPICAL INFLUENCE MODEL

$$\epsilon_j^{tot} = b_0 + \sum_{i=1,9} b_i var_i^{indep} \quad \text{at the } j^{th} \text{ point of the loop}$$

DYNAMIC ANALYSIS OF LOX POST
LCF DAMAGE DRIVERS

- FEM BEAM MODEL
- RESPONSE QUANTITY OF INTEREST
 - RMS STRESSES AND EXPECTED FREQUENCY



LINKING RMS RESPONSE TO SYSTEM VARIABLES

- SCALING RELATION

$$\sigma_{RMS}^p(\dot{m}, \rho) = \sigma_{RMS,Ref} \sqrt{\frac{\rho_{Ref}}{\rho} \left(\frac{\dot{m}}{\dot{m}_{Ref}}\right)^3}$$

- TOTAL

$$\sigma_{RMS} = \sqrt{(\sigma_{RMS}^p)^2 + (\sigma_{RMS}^{Mech})^2}$$

- SINCE DYNAMIC RESPONSE IS DOMINATED BY FIRST BENDING MODE OF THE POST (1800HZ), EXPECTED FREQUENCY HAS NO SENSITIVITY TO SYSTEM VARIABLES

DAMAGE ACCUMULATION

- LOW AND HIGH CYCLE DAMAGE ACCUMULATION; LINEAR OR NONLINEAR (DAMAGE CURVE)
- LCF STRESS-STRAIN STATE DEPENDENT ON SPECIFIC MISSION INPUTS
- HCF DYNAMIC STRESS DEPENDENT ON TIME AT DIFFERENT POWER LEVELS DURING MISSION
- TEMPERATURE DEPENDENT FATIGUE CURVE
- ADJUSTMENT OPTIONS TO INCREASE LCF STRAIN RANGE DUE TO HCF "MAX" AMPLITUDE
- ADJUSTMENTS TO FATIGUE CURVE FOR MULTIAXIALITY AND HYDROGEN EFFECTS

HCF ACCUMULATION

- DYNAMIC STRESS AMPLITUDE DISTRIBUTION COULD BE RAYLEIGH OR USER DEFINED
- RANDOMIZED AMPLITUDE SELECTION OR BIN INTEGRATION METHOD FOR CALCULATING DAMAGE
- SHAKE DOWN OF MEAN DUE TO PEAK STRESS EXCEEDING YIELD
- NONLINEAR MEAN STRESS CORRECTION FOR POSITIVE MEAN STRESS

ADDITIONAL ELEMENTS OF THE DAMAGE MODEL

- DETERMINATION OF CONSISTENT CONSTITUTIVE AND FATIGUE CURVE
ASSUMPTIONS: RAMBERG-OSGOOD FORM OF CYCLIC STRESS-STRAIN CURVE, MANSON-COFFIN TYPE OF FATIGUE CURVE

$$\sum_{LCF} [\Delta\epsilon_i - (BN_i^b + CN_i^c)]^2 + \sum_{HCF} \left[\frac{2 \Delta\sigma_j}{E} + C \left(\frac{2}{BE} \right)^{c/b} \left(\frac{\Delta\sigma_j}{2} \right)^{c/b} - (BN_j^b + CN_j^c) \right]^2 \rightarrow \min$$

- EFFECT OF MAXIMUM RANDOM HCF LOAD ON LCF STRAIN RANGE THROUGH NOTCH PLASTICITY
ASSUMPTIONS: NEUBER'S RULE APPLIES AT POINT 2 OF THE HYSTERESIS LOOP

$$\sigma^{adj}(\epsilon^{adj} - \epsilon_2^{plast}) = \frac{(\sigma_2 + 3\sigma^{random})^2}{E}$$

- EFFECT OF THE MULTIAXIALITY FACTOR (MF) ON LIFE
MODIFIED FATIGUE CURVE CONSTANTS:

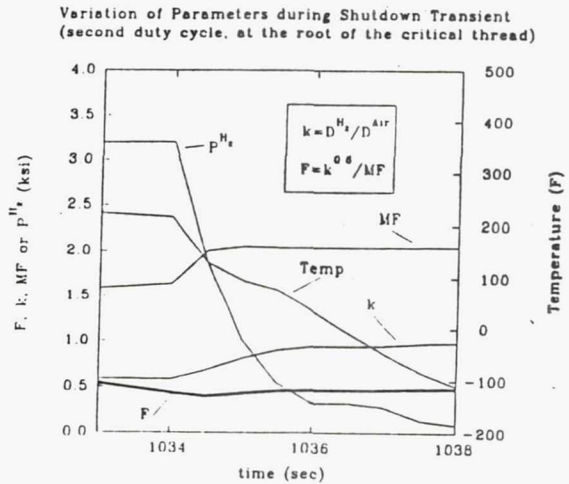
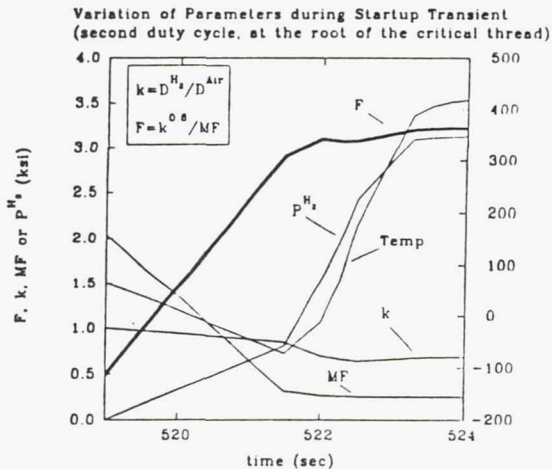
$$C' = \frac{C}{MF} \quad B' = \left(\frac{B}{MF} \right)^{b/c}$$

- EFFECT OF H₂ ENVIRONMENT THROUGH DUCTILITY LOSS
MODIFIED FATIGUE CURVE CONSTANT ACCORDING TO UNIVERSAL SLOPES EQUATION:

$$C' = \left(\frac{D^H}{D^{air}} \right)^{0.6} C$$

ADDITIONAL ELEMENTS OF THE DAMAGE MODEL (CONTINUED)

- CUMULATIVE MULTIAXIAL AND H₂ EFFECT IS DOMINATED BY MULTIAXIALITY NEAR THE END OF THE DUTY CYCLE



Page intentionally left blank

LIFE EXTENDING CONTROL— AN INTERDISCIPLINARY ENGINEERING THRUST

Carl F. Lorenzo and Walter C. Merrill
NASA Lewis Research Center
Cleveland, Ohio 44135

Systems with high performance requirements often have a small number of critical components that operate close to mechanical design margins and that define the effective lifetime of the system. The concept of life extending control¹ (LEC) proposes an active approach to simultaneously managing the damage accumulation of these components while maintaining dynamic performance to increase system effectiveness.

The concept depends on the prediction of fatigue life of the critical components. Currently, fatigue life prediction is based on local cyclic strain behavior such as:

$$\delta \epsilon = \left(\frac{\sigma_f - \sigma_{ave}}{E} \right) \left(\frac{2}{D_i} \right)^b + \epsilon_f \left(\frac{2}{D_i} \right)^c \quad (1)$$

Where D_i is the damage due to cycle i , and σ_f , E , b , ϵ , and c are material constants and σ_{ave} is an average tensile strength. Using the Palmgren-Minor approach the total damage is estimated as

$$D = \sum_i D_i$$

The life usage predicted by this equation is directly related to strain magnitude (figure 1). Other more accurate and complex approaches are also possible. With these approaches, damage can only be estimated upon the completion of a stress-strain cycle. With current cyclic forms of damage modelling only indirect or implicit forms of LEC are possible.

IMPLICIT LEC

The implicit approach to Life Extending Control recognizes that current fracture/fatigue science can not predict the differential damage on less than a full cycle of strain. The implicit approach (see figure 2) selects a sequence of typical command transients (and disturbances) that are representative of those the system would experience in service. Two performance measures are defined: J_p , an objective function that maximizes dynamic performance (possibly by minimizing quadratic state and control excursions) and J_D a damage measure which uses the best (current) fatigue/fracture theory available to calculate the damage accumulated over the sequence of command transients. An overall performance measure is defined where a represents the relative importance between

$$J = J_p + aJ_D \quad (3)$$

performance and life extension. The implicit approach then selects a "best" control algorithm which is applied for the full sequence of command transients.

The dynamic performance and damage accumulation over the sequence are optimized (relative to the selected measures) against the control algorithm parameters. The expectation is to find an algorithm such that the loss in dynamic performance is small (i.e. $J_{p,z,min} - J_{p,o,min}$ in figure 3), for a significant reduction in accumulated damage over the sequence of transients (i.e., $J_{D,o,min} - J_{D,z,min}$ is large and life is extended). Here the subscript o refers to optimizing for dynamic performance only. An actual operating gain set (point q in figure 3) is then chosen which satisfies the desired weighting between performance and damage (i.e. J). During the design process, two types of feedback variables are considered: 1) the performance variables normally used to manage dynamic performance and 2) nonlinear functions of the performance variable representative of the damage variables (stresses, strains, temperature and various rates). Various control algorithms are then examined within this feedback structure. That is, the sequence of selected performance and disturbance transients are applied to a simulated system with a trial control and performance J (or J_p and J_D separately) is calculated. Superior LEC algorithms can then be identified as those that minimize J (or J_p and J_D separately).

Algorithms for Implicit LEC may be formulated intuitively, i.e., minimizing the mean tensile stress, mean strain, and temperature levels and minimizing the cyclic amplitude of stress, strain, and temperature should minimize damage. Also, minimizing the number of cycles of stress and strain should contribute to extending critical component life.

LIFE MANAGEMENT LEC

A second indirect approach is called Life Management LEC and is shown in figure 4. Here the LEC would have a hierarchical structure similar to that found in other proposed intelligent control systems (ICS). At the coordination level, the task planner uses performance requirements and balances these against life usage and appropriate control commands or strategies are selected. This is accomplished by simulation of the system for a few pre-selected trajectories. From the results of this simulation and for a given performance definition, a commanded trajectory is selected that optimizes system performance and minimizes component damage over a sub-interval of the task. Within the task planner, information from a cyclic damage prediction model ranks various candidate trajectories of the successive interval in the planning and selection process. Outside of the task planner another cyclic prediction model assesses the actual damage accumulated during a sub-interval. The execution level implements the selected strategy in the interval by translating the commanded trajectory into control commands and applying these commands to the system.

CONTINUOUS LIFE PREDICTION APPROACH

The Implicit LEC approaches taken above do not directly control the damage rates of critical components. Direct control will require continuous forms of the damage laws instead of the current cyclic forms.

To achieve a continuous formulation of the life prediction process, an interdisciplinary approach is required. Here the knowledge of material properties and life prediction of fracture and fatigue scientists must be combined with the control engineers' knowledge of dynamics and modeling to develop these continuous forms. The objective is to functionally relate measurable performance information with a differential form of the damage laws. This would allow the direct use of the differential estimate of damage in the life extending control

law and, when integrated over complete cycles, would give equivalent or superior damage predictions to those associated with the cyclic theory. Two approaches are possible here: 1) derive such forms from basic theory (the current research thrust of the field) or 2) empirically select likely forms with a significant number of unspecified parameters and use optimization theory to best "fit" the parameters using available data sets. Adopting the second approach, several elementary forms, given in Table I, are proposed. These forms are determined either by intuition or by observing the important relationships embodied in the current theory of life prediction. Various weighted, linear and nonlinear combinations of these elementary forms would be linearly regressed against the available fatigue life data to obtain a continuous formulation.

MEASURED DAMAGE VARIABLES LEC

In this approach (figure 5) both the plant performance and the damage related variables (measured stresses, strains, temperatures, forces, etc.) associated with critical components are measured and used as feedback information for the control. Here the control attempts to directly regulate life as a resource. It is presumed that a "real-time" predictive damage model (described above) exists that would allow the prediction of the incremental damage as a continuous function of selected incremental control action. That is, the influence of changes in the performance variables (presumed to be controllable) on the behavior of the critical life variable is known. This is in the form of the local damage rates $DV_1, DV_2 \dots$ in figure 5. Thus, in figure 6, at a time A, the damage associated with damage variable DV1 can be predicted for any incremental control action (here actions u_1, u_2, u_3 are considered and result in damages D_1, D_2, D_3 respectively). (Note damage while shown as a continuous function of time will likely be modelled as a continuous function of local stresses, strains, etc.). The control problem then is to minimize damage of the critical life components while maximizing (dynamic) performance of the plant. The performance objective approach of equation (2) can be used to achieve this optimization.

One implementation of a measured damage variables LEC would achieve control performance by adaptively modifying the control feedback structure to permit damage to accumulate at a "setpoint" rate, a linear rate over time for example. The measured damage variables could be used directly in a feedback law or to modify the gains or even the structure of the existing control. The emphasis here is on obtaining desired system operation by an active, feedback control approach.

ESTIMATED DAMAGE VARIABLES LEC

Unlike the Measured Damage Variables LEC approach, this concept, shown in figure 7 uses a real time model to estimate the damage rates (and damage accumulation) of critical components. The models can be driven by performance variables or performance variables augmented by available damage measures. Conceptually the models can vary from simple, precomputed, linear, influence coefficients to detailed, non-linear, real time structural models which may require considerable computation. These models would be a direct consequence of the continuous life model described above and would result in a damage estimator that estimates real time damage rates. The controller design would follow in much the same manner as for the measured damage variables approach.

EXAMPLE SYSTEM

The example system of figure 8 is used to illustrate LEC. In figure 9 pulse sequence trajectory number 1 was applied to the system. Also shown in figure 9 are the system position and scaled force trajectory resulting from pulse trajectory 1. The performance endpoints were selected as $X1=-X2=1$. In this case, $N=11$ and $T=4.9$ sec. and $D=0.0213$ units of damage based upon a total component life of 1 unit were predicted.

A modified commanded pulse sequence trajectory, called trajectory number 2, was applied to the same system. The commanded trajectory, the system position, and the scaled force for case 2 is shown in figure 10. In case 2, $N=9$ and $T=4.6$ sec. and $D=0.0121$. Because the commanded pulse trajectory has been slowed slightly, the resultant force trajectory has smaller peak magnitudes. Consequently, the stress-strain cycles have smaller magnitudes and the damage will be less. The example results are summarized in Table II.

CONCLUSIONS

The concept of Life Extending Control was introduced. Possible extensions to the cyclic damage prediction approach were presented based on the identification of a model from elementary forms. Several candidate elementary forms were presented. These extensions would result in a continuous or differential form of the damage prediction model.

Two possible approaches to Life Extending Control based on the existing cyclic damage prediction method, called implicit LEC and life management LEC approach were proposed. Two possible approaches to Life Extending Control based on the proposed continuous damage prediction method, called measured variables LEC and estimated variables LEC approach were defined. Here damage measurements or estimates would be used directly in the LEC. A simple hydraulic actuator driven, position control system example is used to illustrate the main ideas behind Life Extending Control. Results from a simple hydraulic actuator example demonstrate that overall system performance, that is, dynamic plus life, can be maximized by accounting for critical component damage in the control design.

REFERENCE

1. Carl F. Lorenzo and Walter C. Merrill: Life Extending Control - A Concept Paper, to be published American Control Conference, June 26-28, 1991, Boston, MA.

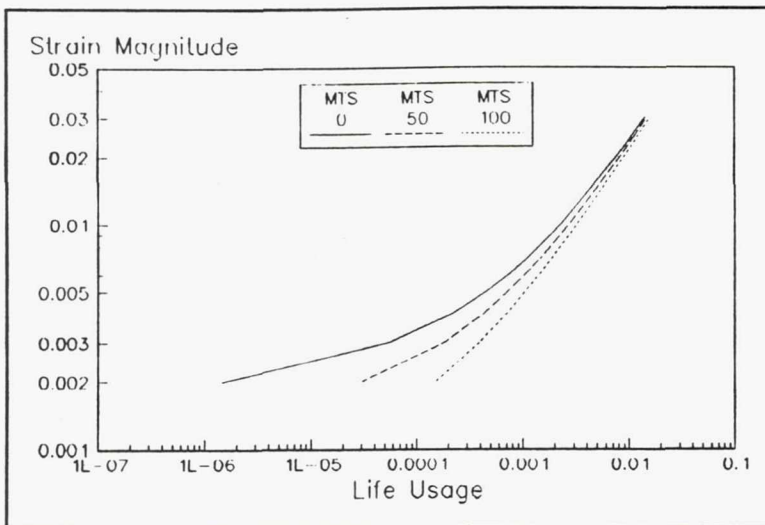


Figure 1. Life usage versus component strain parameterized by mean tensile stress.

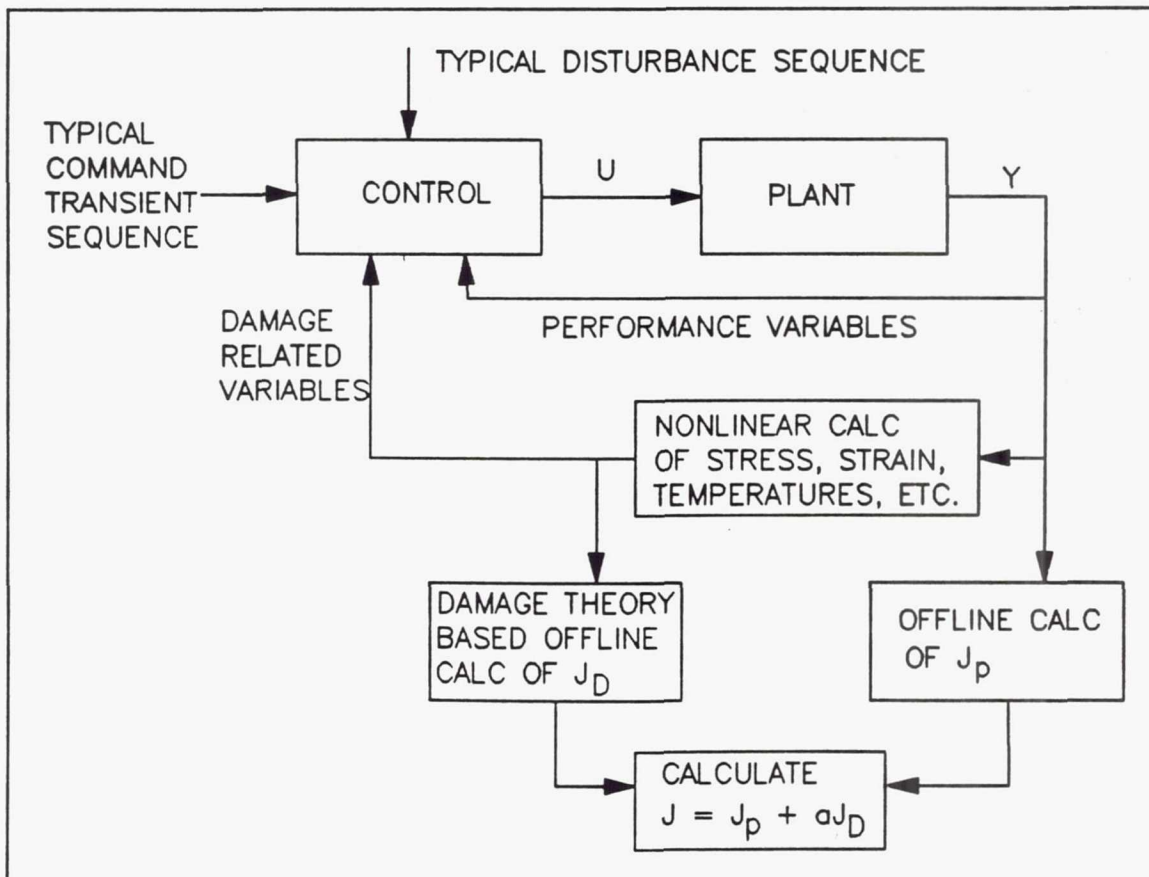


Figure 2. Implicit life extending control approach

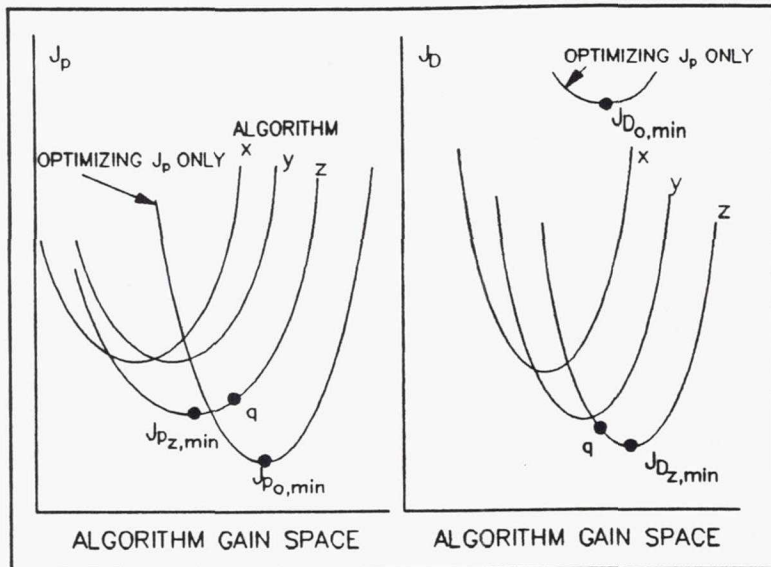


Figure 3. Effect of various life extending control algorithms on performance (J_p) and damage (J_d).

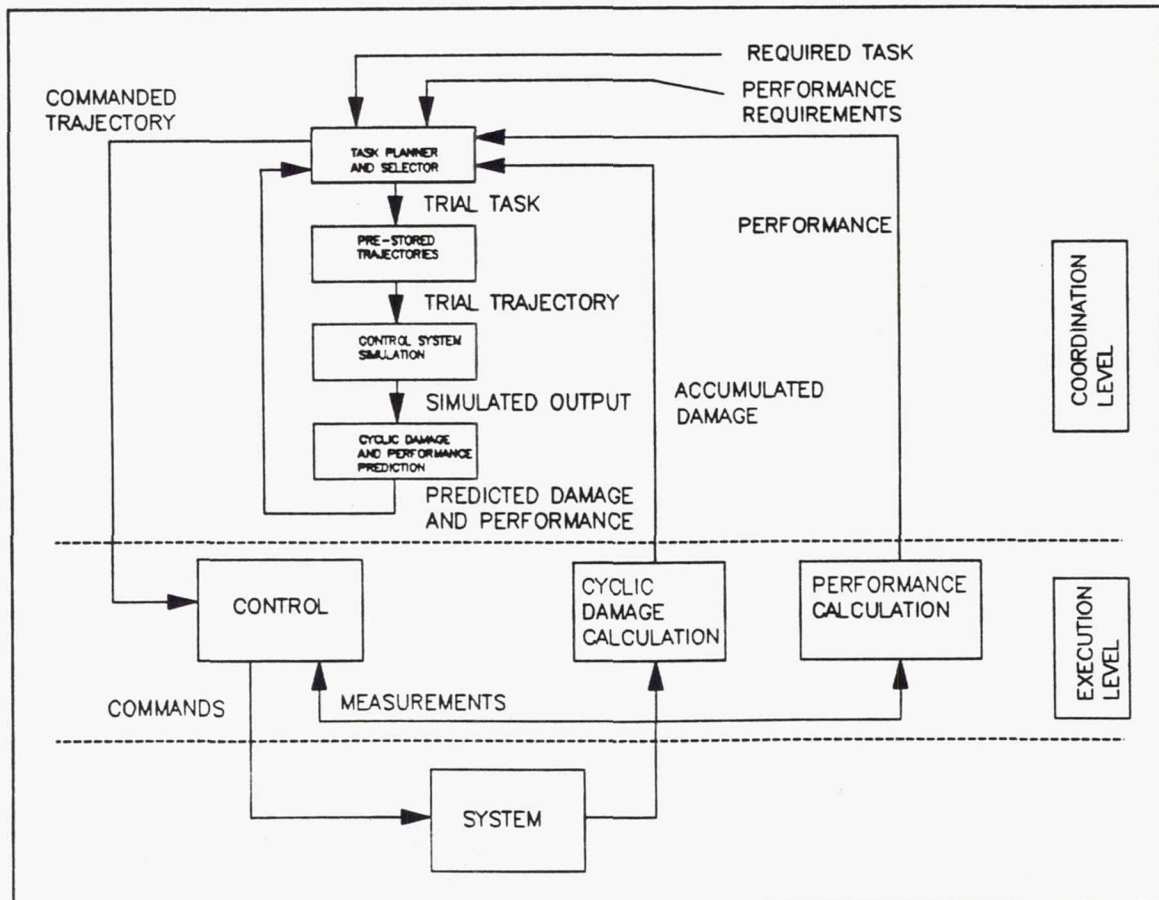


Figure 4. Life management life extending control approach.

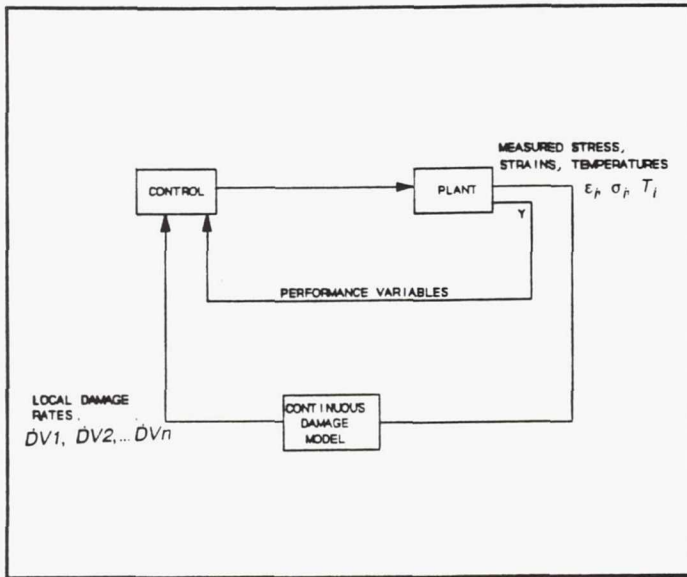


Figure 5 Measured damage variables life extending control approach.

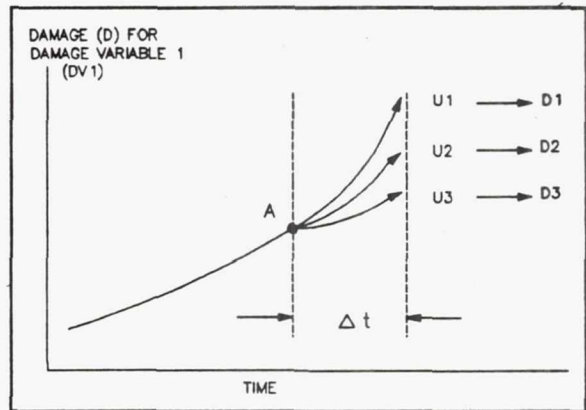


Figure 6. Incremental damage relationship

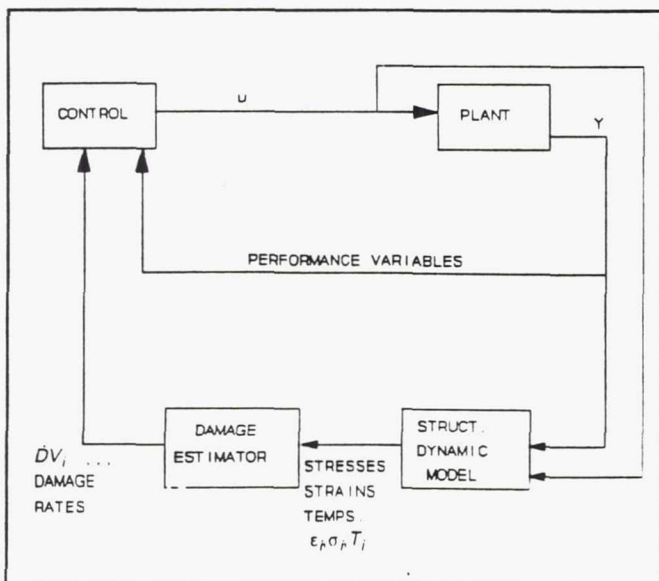


Figure 7 Estimated Damage Variables Life Extending Control Approach.

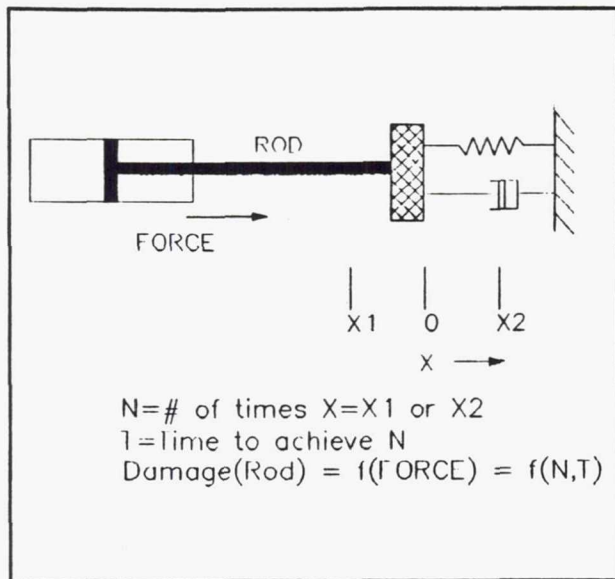


Figure 8 A hydraulic actuator position system.

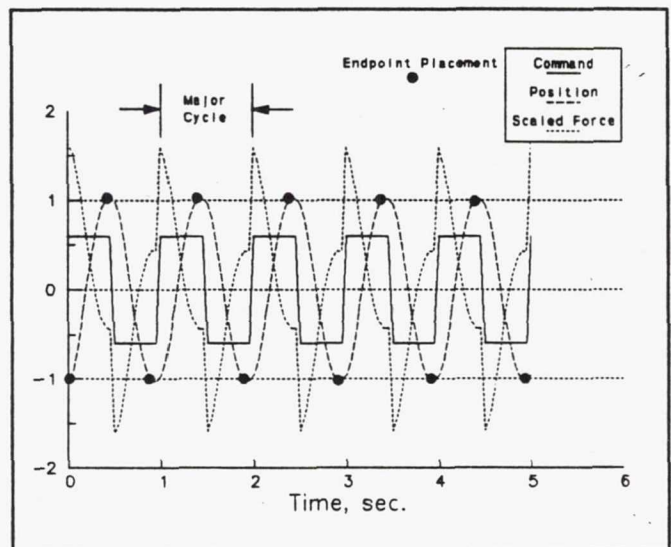


Figure 9 Example results for Case 1 trajectory command.

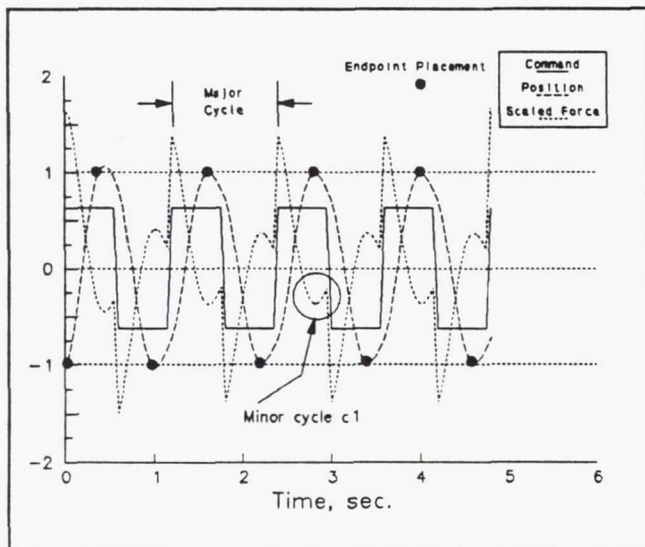


Figure 10 Example results for Case 2 trajectory command.

$$\begin{aligned}
|\text{Mean Stress Level}| &= \left| \frac{1}{T} \int_0^T \sigma(t) dt \right| \\
|\text{Mean Strain Level}| &= \left| \frac{1}{T} \int_0^T \epsilon(t) dt \right| \\
|\text{Cyclic Stress}| &= \int_0^T (\sigma^2 - [\frac{1}{T} \int_0^T \sigma(t) dt]^2) dt \\
|\text{Cyclic Strain}| &= \int_0^T (\epsilon^2 - [\frac{1}{T} \int_0^T \epsilon(t) dt]^2) dt \\
|\sigma T|; |\epsilon T|; |\sigma \epsilon T|; \\
\int_C \sigma d\epsilon; \int_C \sigma T d\epsilon \\
(a \sigma + b) \int_C \sigma d\epsilon \\
&\text{etc.}
\end{aligned}$$

Table I. Elementary damage prediction forms

Table II EXAMPLE LIFE EXTENDING CONTROL RESULTS

| CASE | N | T, sec | N/T | F _{MAX} | CYCLES | D | T _f | N _{total} | PERFORMANCE |
|------|----|--------|--------|------------------|--------------------|--------|----------------|--------------------|-------------|
| 1 | 11 | 4.9 | 2.2448 | 1.6 | 5 MAJOR | 0.0213 | 230 | 516 | 802 |
| 2 | 9 | 4.6 | 1.9565 | 1.4 | 4 MAJOR 8 MINOR | 0.0121 | 380 | 743 | 1106 |

Page intentionally left blank

AXIAL AND TORSIONAL FATIGUE BEHAVIOR OF A COBALT-BASE ALLOY

Peter J. Bonacuse
U. S. Army Aviation Systems Command
NASA Lewis Research Center
Cleveland, Ohio 44135

and

Sreeramesh Kalluri
Sverdrup Technology, Inc.
NASA Lewis Research Center Group
Brook Park Ohio 44142

The wrought cobalt-base alloy, Haynes 188 is used in high temperature, high thermal stress aerospace components. Some applications include combustor liners for gas turbine engines and liquid oxygen carrying tubes within the Space Shuttle Main Engine. Typically, during the engine start up and shutdown transients, these components are subjected to multiaxial states of stress. Fatigue life estimation under multiaxial stress states is necessary for safe and reliable operation of these components. In order to develop elevated temperature multiaxial fatigue life prediction models, a multiaxial fatigue data base is required. To satisfy this need, an elevated temperature experimental program on Haynes 188 which consists of axial, torsional, inphase and out-of-phase axial-torsional fatigue experiments has been designed. As a part of this experimental program, elevated temperature axial and torsional fatigue experiments were conducted under strain-control on thin-wall tubular specimens of Haynes 188 in air.

The tensile ductility of Haynes 188 exhibits a minimum around 760 °C [1]. Since ductility governs low-cycle fatigue behavior, the axial and torsional fatigue experiments were conducted at 760 °C. The thin-wall tubular specimens were heated to the test temperature with induction heating. The thermal gradient in the gage section of the specimen was kept to within 1% of the test temperature. Axial and torsional strains were measured by a commercially available high temperature extensometer. A data acquisition and control program developed specifically for axial-torsional fatigue tests was used to conduct the axial and torsional tests on a servo-hydraulic testing machine [2]. Test data were acquired at logarithmic intervals by the computer. Failure of the specimen was defined as a 10% drop in the peak axial or torsional loads referenced to a previously recorded cycle.

The axial and torsional fatigue life data were used to determine the elastic, plastic and total life relationships for Haynes 188 at 760 °C. Cyclic axial and shear engineering stress-engineering strain curves were also determined from the data acquired by the computer. The fatigue lives obtained from the

torsional fatigue experiments were compared against the predictions of three multiaxial fatigue life parameters. The following parameters were evaluated for this material: 1) von Mises Equivalent Strainrange, 2) Multiaxiality factor of Manson-Halford [3], and 3) Modified Smith-Watson-Topper [4]. Constants for the three parameters were derived from the axial fatigue life data generated also with thin-wall tubular specimens. The Fatemi-Socie parameter [5] which represents both the axial and torsional fatigue data by a single life relation was also evaluated for its applicability to Haynes 188 at 760 °C. The predictive and correlative capabilities of all parameters are presented.

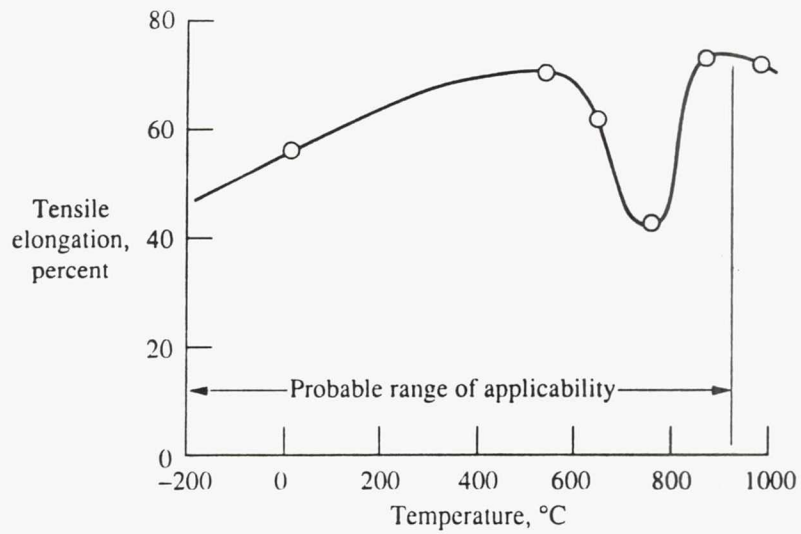
REFERENCES

- [1] Nickel Base Alloys. International Nickel Company, Inc., New York, 1977.
- [2] Kalluri, S. and Bonacuse, P. J., "A Data Acquisition and Control Program for Axial-Torsional Fatigue Testing," Applications of Automation Technology to Fatigue and Fracture Testing, ASTM STP 1092, A. A. Braun, N. E. Ashbaugh, and F. M. Smith, Eds., American Society for Testing and Materials, Philadelphia, 1990, pp. 269-287.
- [3] Manson, S. S. and Halford, G. R., Discussion to the paper "Multiaxial Low Cycle Fatigue of Type 304 Stainless Steel" by J. J. Blass and S. Y. Zamrik., Journal of Engineering Materials and Technology, Vol. 99, No. 3, July 1977, pp. 283-285.
- [4] Socie, D. F., "Multiaxial Fatigue Damage Models", Journal of Engineering Materials and Technology, Vol. 109, No. 4, 1987, pp. 293-298.
- [5] Fatemi, A., and Socie, D. F., "A Critical Plane Approach to Multiaxial Fatigue Damage Including Out-of-Phase Loading", Fatigue and Fracture of Engineering Materials and Structures, Vol. 11, No. 3, 1988, pp. 149-165.

(Extended abstract prepared for presentation at the Conference on Structural Integrity and Durability of Reusable Space Propulsion Systems to be held at NASA-Lewis Research Center, Cleveland, Ohio during May 14-15, 1991)

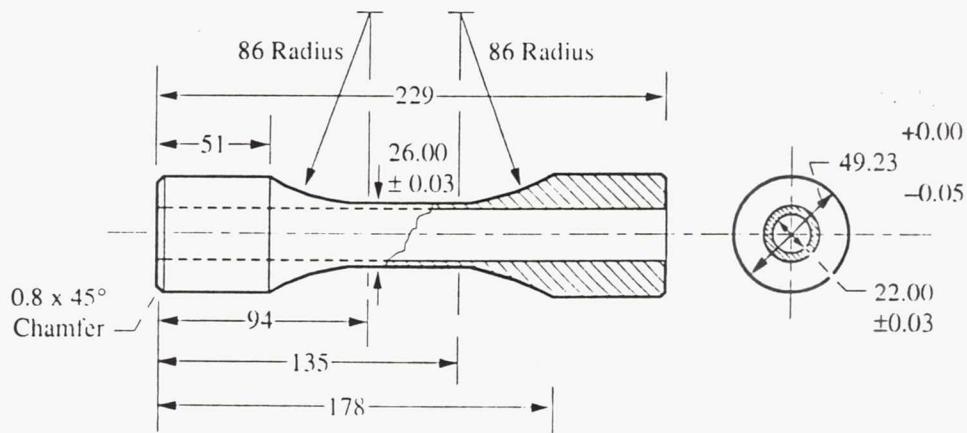
Tensile Elongation Versus Temperature

Haynes 188



CD 91 52277

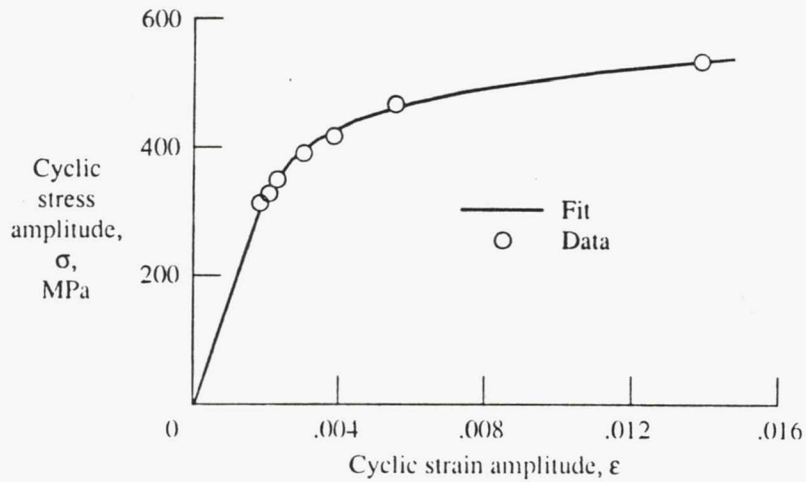
Axial-Torsional Fatigue Specimen



All dimensions in millimeters

CD 91 52278

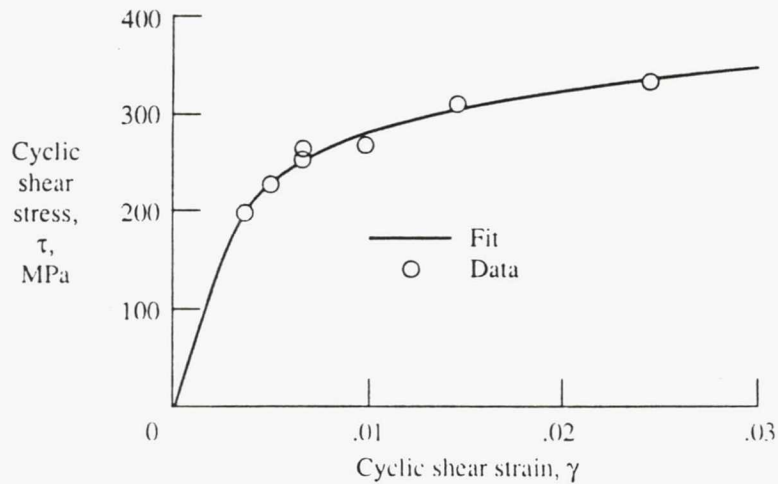
Cyclic Stress Amplitude Versus Cyclic Strain Amplitude for Haynes 188 at 760 °C



$$\epsilon = \frac{\sigma}{170\,200} + \left(\frac{\sigma}{860} \right)^{9.48}; \sigma \text{ in MPa}$$

CD-91-52279

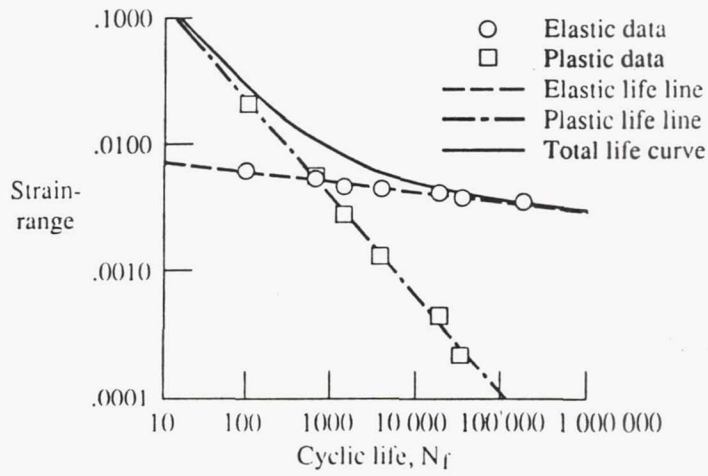
Cyclic Shear Stress Versus Cyclic Shear Strain for Haynes 188 at 760 °C



$$\gamma = \frac{\tau}{63\,490} + \left(\frac{\tau}{591} \right)^{6.99}; \tau \text{ in MPa}$$

CD-91-52280

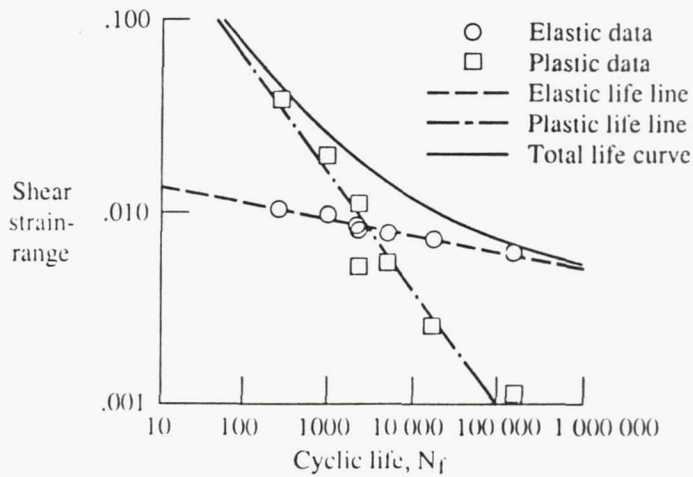
Axial Strainrange Versus Cycles to Failure for Axial Tests on Haynes 188 at 760 °C



$$\Delta\epsilon = \underbrace{0.00863 N_f^{-0.074}}_{\text{Elastic}} + \underbrace{0.689 N_f^{-0.754}}_{\text{Plastic}}$$

CD-91-82281

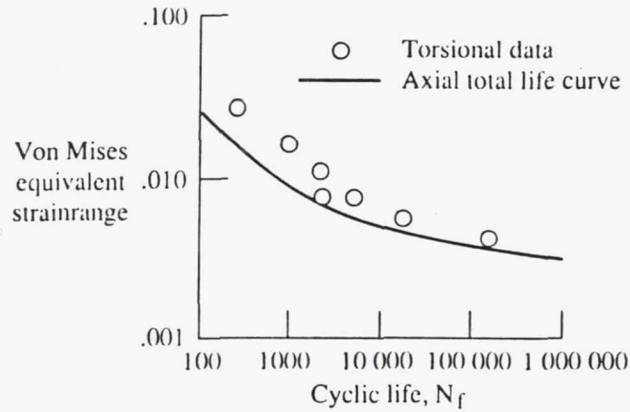
Shear Strainrange Versus Cycles to Failure for Haynes 188 at 760 °C



$$\Delta\gamma = \underbrace{0.0166 N_f^{-0.086}}_{\text{Elastic}} + \underbrace{1.002 N_f^{-0.601}}_{\text{Plastic}}$$

CD-91-82282

Von Mises Equivalent Strainrange Versus Cycles to Failure for Haynes 188 at 760 °C



$$\Delta\epsilon_{\text{cq}} = 0.00863 N_f^{-0.074} + 0.689 N_f^{-0.754}$$

For torsion:

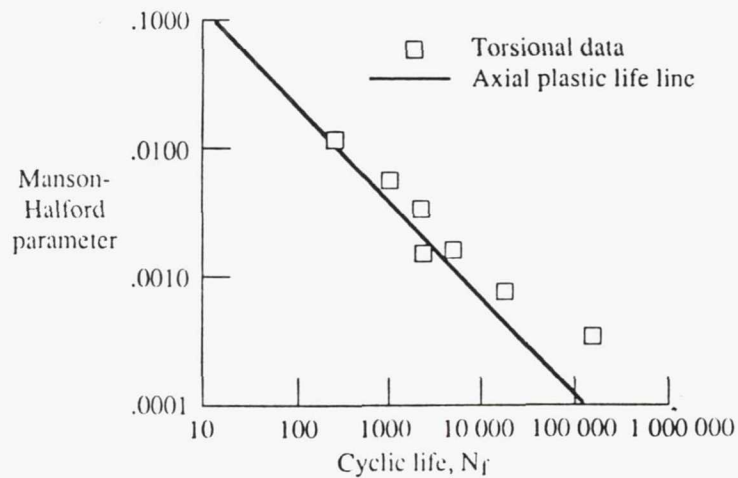
$$\Delta\epsilon_{\text{cq}} = \left[\frac{3}{4} \frac{\Delta\gamma^2}{(1 + \nu^*)^2} \right]^{1/2}$$

Where:

$$\nu^* = 0.5$$

CD 91-52283

Manson-Halford Parameter Versus Cycles to Failure for Haynes 188 at 760 °C



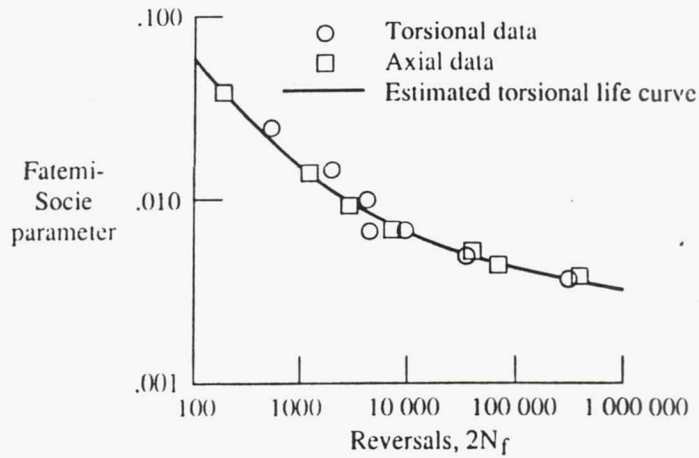
$$MF (\Delta\epsilon_{\text{in}})_{\text{cq}} = 0.689 N_f^{-0.754}$$

For torsion:

$$MF = \frac{1}{2}$$

CD 91-52284

Fatemi-Socie Parameter Versus Reversals to Failure for Haynes 188 at 760 °C

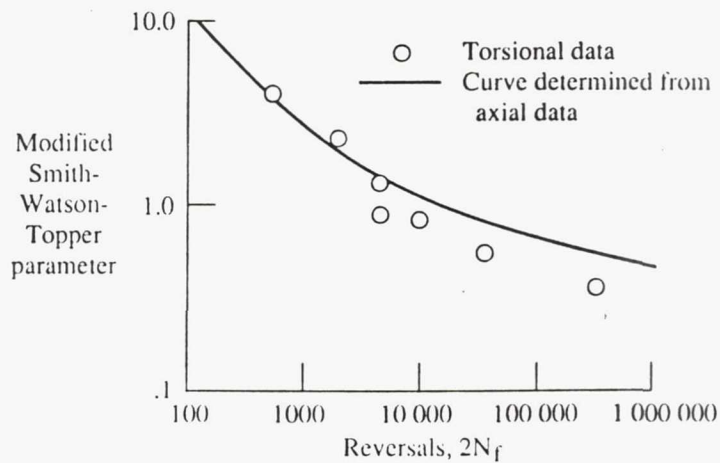


$$\frac{\Delta\gamma_{\max}}{2} (1 + 0.00335 \sigma_n^{\max}) = [0.006 (2N_f)^{-0.074} + 0.872 (2N_f)^{-0.754}] [1 + 1.296 (2N_f)^{-0.074}]$$

Value for k = 0.9

CD 91 52286

Modified Smith-Watson-Topper Parameter Versus Reversals to Failure for Haynes 188 at 760 °C

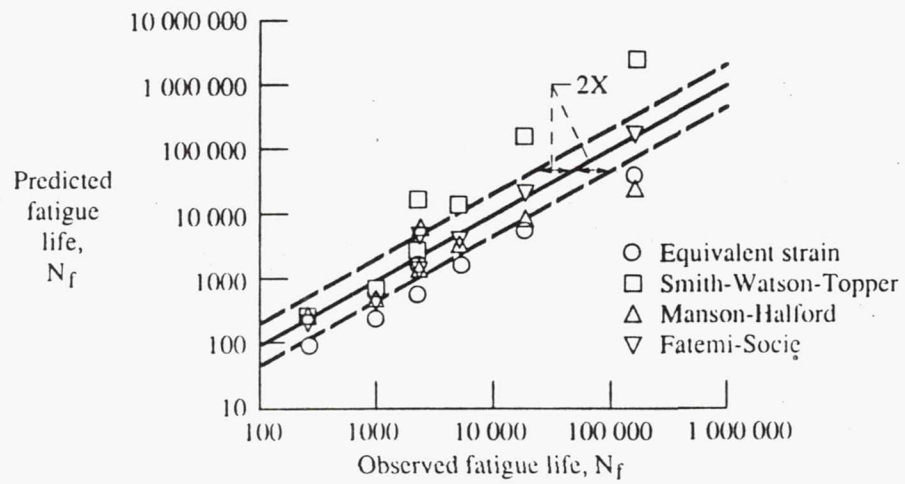


$$\sigma_1^{\max} \frac{\Delta\epsilon_1}{2} = 449 (2N_f)^{-0.828} + 3.51 (2N_f)^{-0.147}$$

CD 91 52285

Comparison of Fatigue Life Models

Torsional Fatigue Data of Haynes 188 at 760 °C



CD 91 52287

OVERVIEW OF AEROTHERMODYNAMIC LOADS DEFINITION STUDY

Raymond E. Gaugler
NASA Lewis Research Center
Cleveland, Ohio 44135

INTRODUCTION

For a number of years now, NASA has been conducting the Advanced Earth-to-Orbit (AETO) Propulsion Technology Program, now part of the Civil Space Technology Initiative (CSTI) Program. The program objective is to provide the knowledge, understanding, and design methodology that will allow the development of advanced earth-to-orbit propulsion systems with high performance, extended service life, automated operations, and diagnostics for in-flight health monitoring. This program supports both current and future engine and vehicle developments. The technology needs of the current Space Shuttle Main Engine (SSME) have thus far provided the main focus for the AETO efforts. Organizationally, the program has been divided into technology working groups made up of people from both the Marshall Space Flight Center and the Lewis Research Center. The focus of this report is the Lewis effort under the Fluid and Gas Dynamics working group, the Aerothermodynamic Loads Definition Study.

The objective of the Aerothermodynamic Loads Definition Study is to develop methods to more accurately predict the operating environment in advanced ETO propulsion systems, such as the Space Shuttle Main Engine (SSME) powerhead. Development of time averaged and time-dependent, three dimensional viscous computer codes as well as experimental verification and engine diagnostic testing are considered to be essential in achieving that objective. Time-averaged, nonsteady, and transient operating loads must all be well defined in order to accurately predict powerhead life.

The approach taken under this study consists of two parts: 1) to modify/apply/disseminate existing computational fluid dynamics (CFD) tools in response to current needs, and 2) to develop new technology that will enable more accurate computation of the time-averaged and unsteady aerothermodynamic loads in reusable space propulsion systems. The new technology development effort is further divided into three parts: 1) new computer code development, 2) experiments to provide data for physical models required by the codes, and 3) experiments to provide data for validating the codes. With the more accurate aerothermodynamic loads predictions providing boundary conditions to improve structural and fatigue life analyses, the goal of improved durability will be met.

The Aerothermodynamic Loads Definition Study was begun in October, 1983. The initial effort involved the use of existing CFD tools to analyze problems in the SSME fuel and oxidizer turbopump turbines, the fuel turbine turnaround duct, the fuel side preburner and the main injector LOX posts. Results of those efforts have been presented previously and will not be discussed here. What follows is a description of the currently active tasks and their status.

H4(a). UNSTEADY VISCOUS MULTI-BLADE-ROW TURBINE ANALYSIS

In this task, the objective is to develop a numerical simulation capability for unsteady viscous flow and heat transfer in interacting turbine blade rows.

The numerical simulation of unsteady viscous flows in turbines can provide much useful information on the factors effecting performance and life of these requires a means of reducing the three-dimensional, nonperiodic, multi-row problem remains intractable, a quasi-three dimensional treatment can be used to analyze much of the flow over the midspan portion of the turbine passage.

Existing turbulence models are being modified to incorporate known relevant unsteady flow effects. These models will be developed using unsteady boundary layer codes and then implemented in a highly efficient quasi 3D rotor-stator interaction code previously developed under this task. The resulting analysis will then be tested against data obtained from a low-speed turbine under task H4(e).

H4(b). Computation of 3D FLOW WITH HEAT TRANSFER

In this task, the objective is to develop an accurate, efficient numerical analysis of steady 3D viscous flow and heat transfer in turbine blade rows.

The approach being taken is to modify a 3D viscous turbomachinery code (RVC3D) to include an advanced turbulence model and increased resolution of near-wall gradients and to validate and upgrade the code by application to suitable 3D data sets. Figure 1 shows a preliminary comparison of experiment and computed results of endwall heat transfer using this code.

H4(e). 3D STATOR-ROTOR BLADE FLOW EXPERIMENTS

The objective of this task is to investigate the steady and unsteady 3D viscous flow field in an axial turbine stage, including stator-rotor interaction, mixing effects, blade and endwall boundary layers, and temperature gradient effects on secondary flow development. This work is being done in the Pennsylvania State University Axial Flow Turbine Research Facility.

A progress report will be presented later in this session.

H4(m). TURBULENCE MODELING FOR PROTEUS TURBOMACHINERY APPLICATION

The objective of this task is to develop the capability to predict turbulent flow losses and heat transfer in turbines typical of ETO propulsion systems using a 3D Navier-Stokes Code. Existing turbulence models are inadequate or require empirical tuning to generate reasonable results. Current effort is focused on the effect of turbulence on flow near the leading edge of turbine blades. Figure 2 shows computed effect of upstream vortices on surface temperature near the leading edge of a turbine blade.

H5(a). IMPROVED MODELING, PREBURNER FLOW

In this task, the objective is to obtain steady state reacting hydrogen data of mean and fluctuating velocities and concentrations and to compare benchmark data with predictions from computer models and evaluate turbulence-chemistry interactions.

Computations of the 3D flow in the advanced turbopump turbines requires knowledge of the condition of the gases exiting the burner. Current models for predicting those conditions are inadequate. Fluctuating concentration and velocity data can now be obtained with laser diagnostics. These measurements are necessary to determine the unmixedness of the reacting flow and the reaction rates. The measurements are also necessary for differentiating between the various computer models.

For this task, a team of computer modelers and experimentalist have defined the measurements required to verify turbulent-reacting flow models. Existing optical techniques will be used to make measurements within the shear layer-two component LDV, fluorescence for OH and temperature, and TiCl₄ for seeding and H₂O concentration.

The facility is now operational. Figure 3 is a photo of the rig, showing the laser beams being used to make measurements.

H5(f). HIGH REYNOLDS NUMBER AND UNSTEADY HEAT TRANSFER EXPERIMENT

In this task, the objective is to develop a fundamental understanding of the effects of high Reynolds number and Reynolds number variations, and also upstream unsteadiness, on heat transfer in turbulent boundary layers typical of turbine airfoils in the SSME turbopump turbines.

In order to be able to predict the surface pressure and temperature distributions within engine flow passages, and accurate turbulence and unsteadiness model is needed. Data in the proper range of Reynolds number and disturbance frequency are necessary for accurate modeling. A new in-house experimental rig, shown schematically in figure 4 has been built in which the major features of an SSME turbine airfoil are simulated, particularly the Reynolds number. A particular feature of the rig is the ability to span the Reynolds number range from conventional gas turbine levels up to SSME levels.

Figure 5 shows a comparison of preliminary measurements and computations of surface pressure and heat transfer coefficients. The facility is currently being modified, and tests will be continuing.

H5(g). UNSTEADY HEAT TRANSFER ANALYSIS

In this task, the objective is to formulate analytic models to aid in the prediction of the unsteady aero-thermal loads expected in the SSME turbopump turbines.

The ability to predict the aero-thermal loads in the turbine unsteady flow environment is an essential input to the ability to predict life and durability. There are two aspects to the unsteadiness which occurs on turbine blades. The first is due to free stream turbulence and wakes shed from upstream vanes and blades. The second is due to laminar/turbulent boundary layer transition which occurs some distance downstream from the blade leading edge. The transition effect on concave surface is being addressed in this research program.

For the boundary layer transition experiments, and experimental approach is being used to study the effects of concave curvature, which occurs on the pressure side of the SSME turbine airfoils, on the transition process.

LSVT23 IMPROVED AERO AND HEAT TRANSFER PREDICTION

In this task, the objective is to improve the calculation of the aerodynamic environment in low aspect ration turbines and experimentally obtain the unsteady surface heat transfer response to a temperature disturbance.

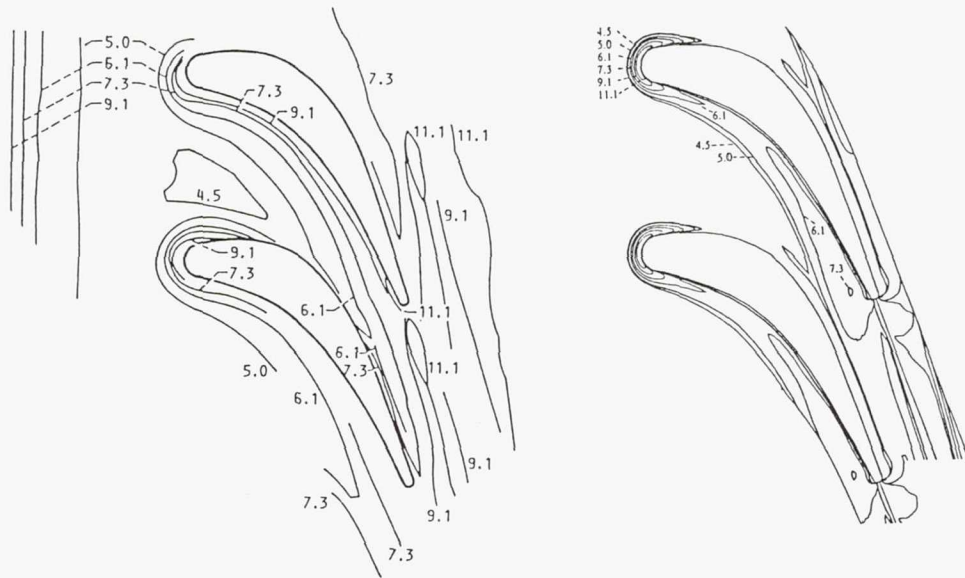
Knowledge of the local flow environment of turbine vanes and blades is essential for the accurate prediction of turbine temperature and heat transfer rates. In addition, the response of the turbine blade surfaces to rapid changes in stagnation temperature is unknown. Improved steady and unsteady heat transfer prediction is required for improved life and for turbine efficiency. An existing quasi-3D computer code will be activated at Calspan and used to compute pressure distributions over stator/rotor surfaces, substantially reducing the uncertainty in the aerodynamic environment and providing a reliable base for heat transfer predictions. The experimental phase will use actual SSME fuel turbine hardware, instrumented for time resolved heat transfer and pressure measurements.

A detailed description of the latest results under this task will be presented in another paper at this meeting.

SUMMARY

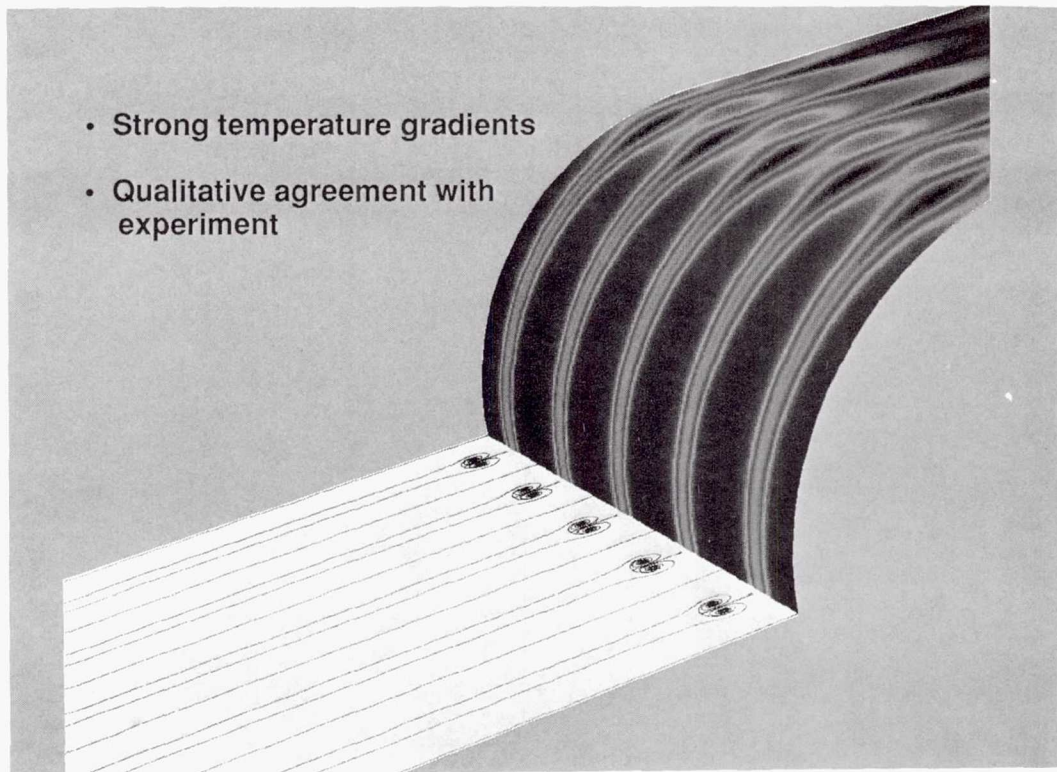
Significant progress is being made in the Aerothermodynamic Loads Definition Study, particularly in the turbomachinery area, where there is a distinct overlap between the ETO efforts and research in the aeronautical gas turbine field. The continuing work under this program will provide the knowledge, understanding and design methodology that will allow the development of advanced earth-to-orbit propulsion systems with high performance, extended service life, automated operations, and diagnostics for in-flight health monitoring.

Experimental and Computed Endwall Heat Transfer Contours of Stanton Number $\times 10^3$

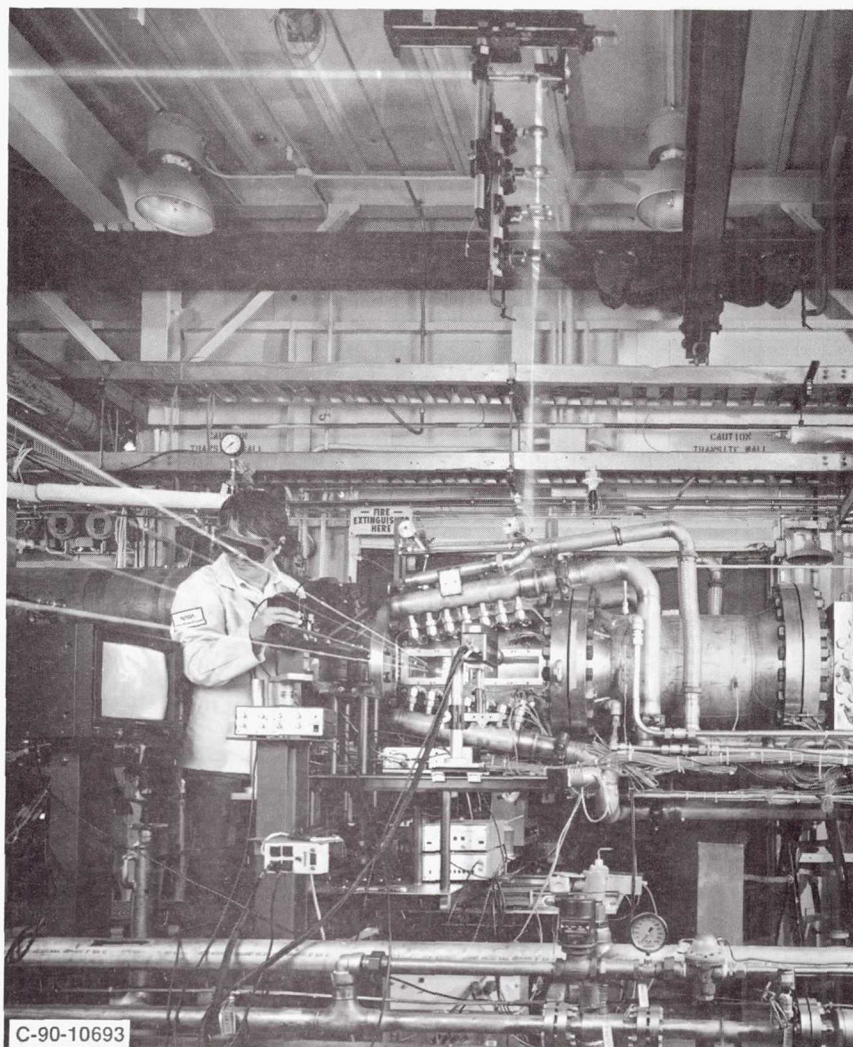


Experiment (data of Boyle and Russell) 3D Calculation (RVC3D)

Cylindrical Leading Edge Temperature Distribution Computed Effect of Free Stream Vortices



Reacting Shear Layer Facility

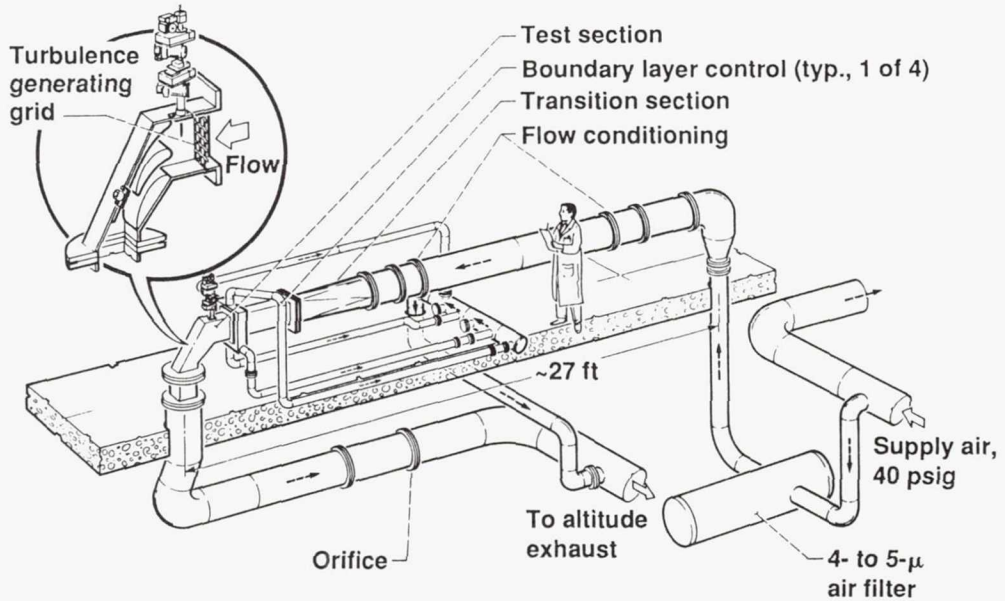


CD-91-52228

High Reynolds Number Heat Transfer Rig

Reynolds Number up to 7,500,000

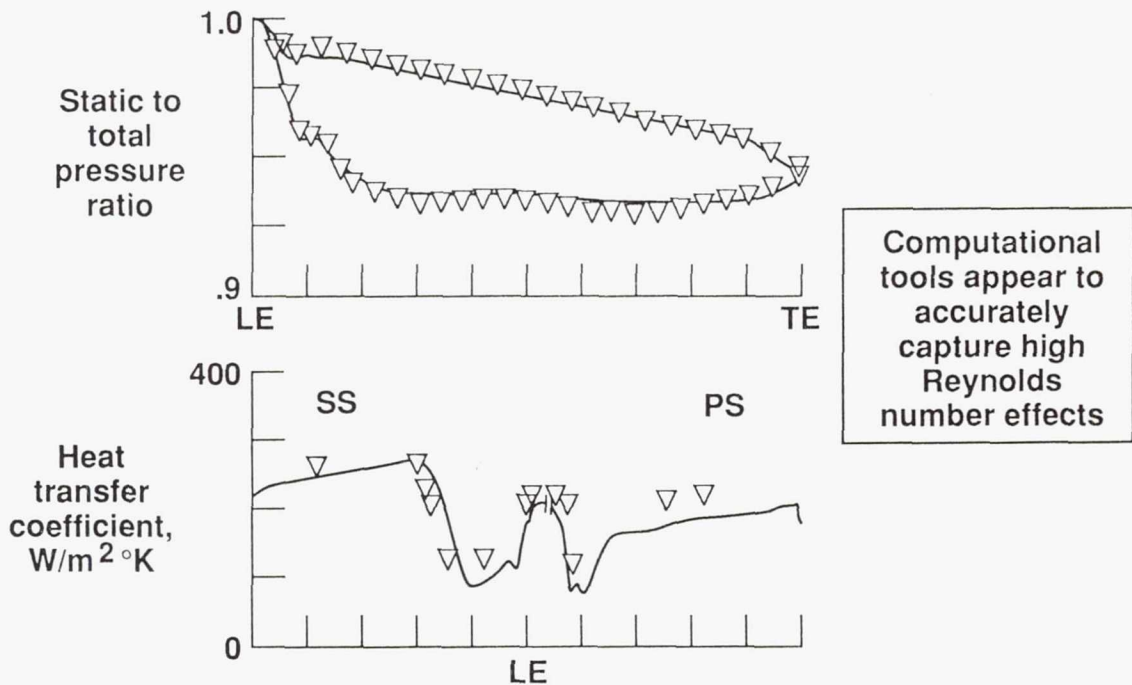
Test section cutaway



CD-91-52229

High Reynolds Number Heat Transfer

Comparison of Measured and Computed Blade Surface Relative Pressure and Heat Transfer Coefficient



CD-91-52230

THREE-DIMENSIONAL ANALYSIS OF THE PRATT & WHITNEY ALTERNATE DESIGN SSME FUEL TURBINE

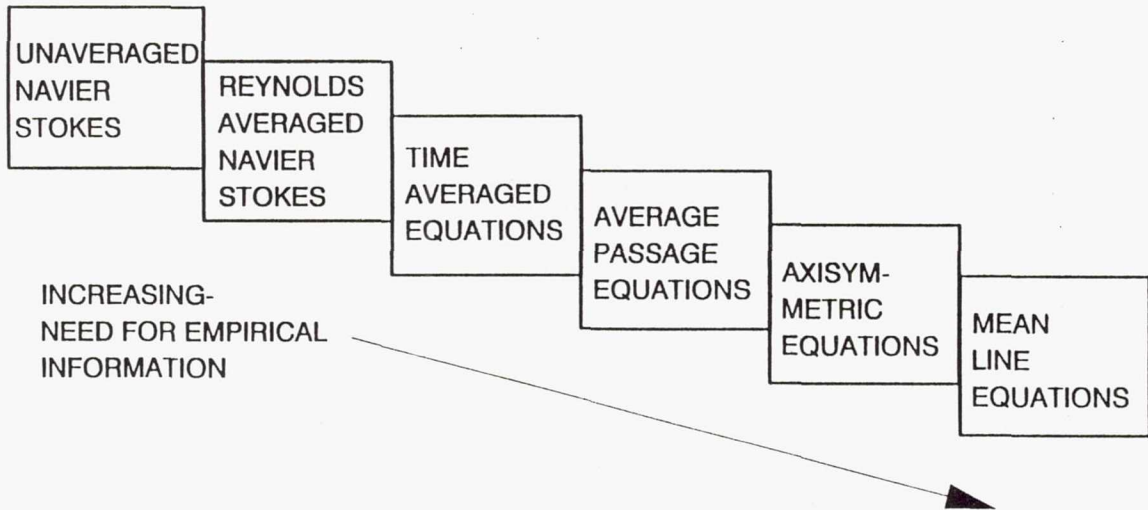
K. R. Kirtley and T. A. Beach
Sverdrup Technology, Inc.
Lewis Research Center Group
Brook Park, OH 44142

and

J. J. Adamczyk
NASA Lewis Research Center
Cleveland, OH 44135

The three-dimensional viscous time-mean flow in the Pratt & Whitney alternate design space shuttle main engine fuel turbine is simulated using the average passage Navier-Stokes equations. The migration of secondary flows generated by upstream blade rows and their effect on the performance of downstream blade rows is studied. The present simulation confirms that the flow in this low aspect ratio two stage turbine is highly three-dimensional and dominated by the tip leakage flow. The tip leakage vortex generated by the first blade persists through the second vane and influences the loading of the second blade and adversely affects its performance. The greatest mixing of the inlet total temperature distortion occurs in the second vane and is due to the large leakage vortex generated by the upstream rotor. It is asserted that the predominant spanwise mixing mechanism in this low aspect ratio turbine is the radial transport due to the deterministically unsteady vortical flow generated by upstream blade rows. A by-product of the analysis is accurate pressure and heat loads for all blade rows under the influence of neighboring blade rows. These aero loads are useful for advanced structural analysis of the vanes and blades.

EQUATIONS HIERARCHY



AVERAGE PASSAGE EQUATION SYSTEM

$$\int \frac{\delta}{\delta t} (\lambda \mathbf{q}) dV + L (\lambda \mathbf{q}) = \int \lambda \mathbf{S} dV + \int \lambda \mathbf{K} dV$$

$$\mathbf{q} = [\rho, \rho u_z, \rho u_r, \rho u_\theta, \rho e_o]^T$$

$$L = \int_{dA} [\lambda F dA_z + \lambda G dA_r + \lambda H dA_\theta]$$

λ = blockage factor < 1 over smeared blade rows

\mathbf{K} = source term due to r - θ - z coordinates

\mathbf{S} = source term which includes:

- body forces
- energy sources
- momenta/energy temporal correlations
- spatial mixing correlations

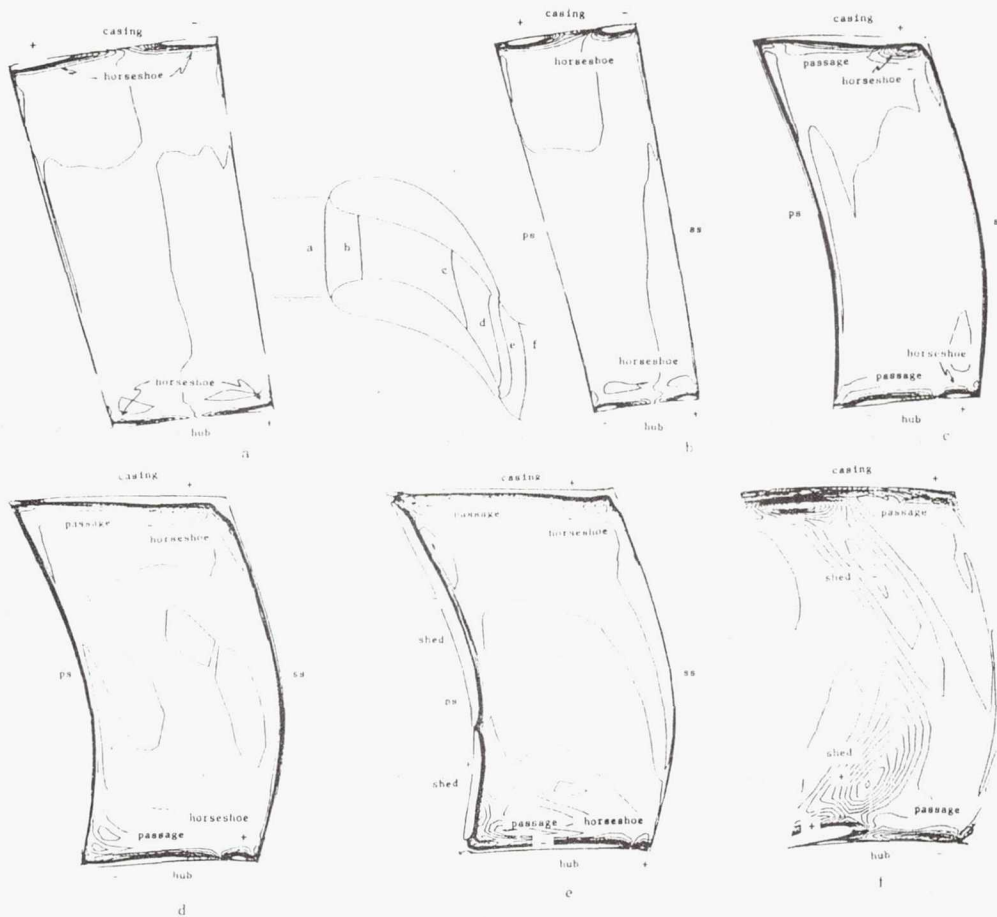
PRATT & WHITNEY SSME ALTERNATE TURBOPUMP TURBINE DESIGN

AVERAGE PASSAGE MODEL ANALYSIS

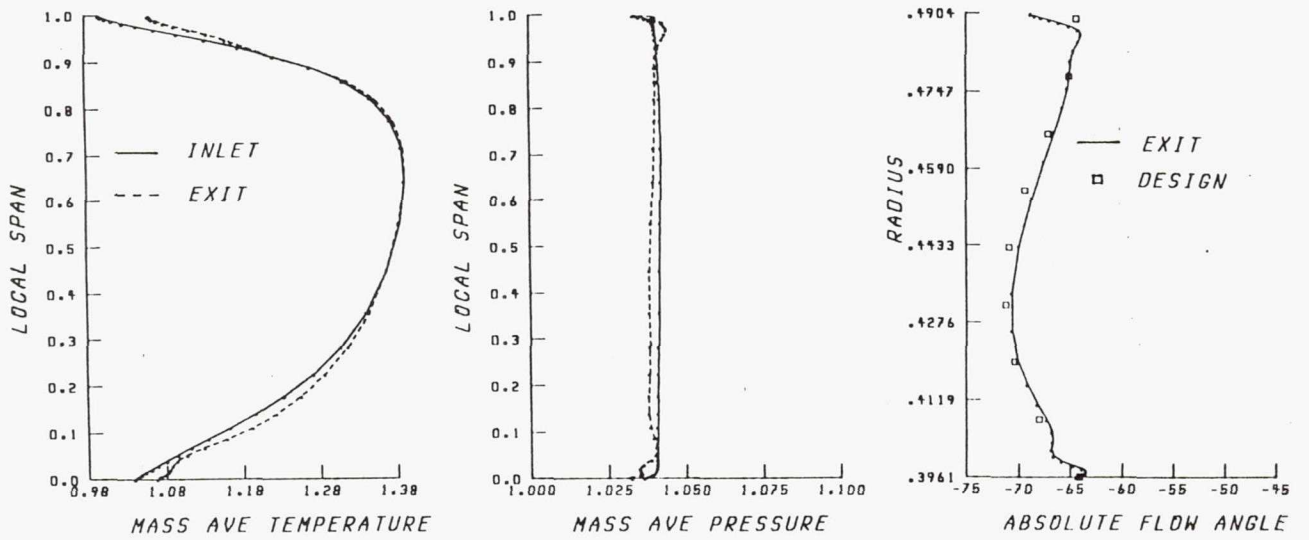


| | $\Delta T_0/T_{0,in}$ | | $P_{0,in}/P_{0,out}$ | |
|---------|-----------------------|-----------|----------------------|-----------|
| | MEANLINE | AVE. PASS | MEANLINE | AVE. PASS |
| VANE 1 | 0 | 0 | 1.0044 | 1.0032 |
| BLADE 1 | 0.0433 | 0.0429 | 1.2052 | 1.1870 |
| VANE 2 | 0 | 0 | 1.0202 | 1.0085 |
| BLADE 2 | 0.0335 | 0.0286 | 1.1360 | 1.1250 |
| TOTAL | 0.0753 | 0.0711 | 1.4030 | 1.3530 |

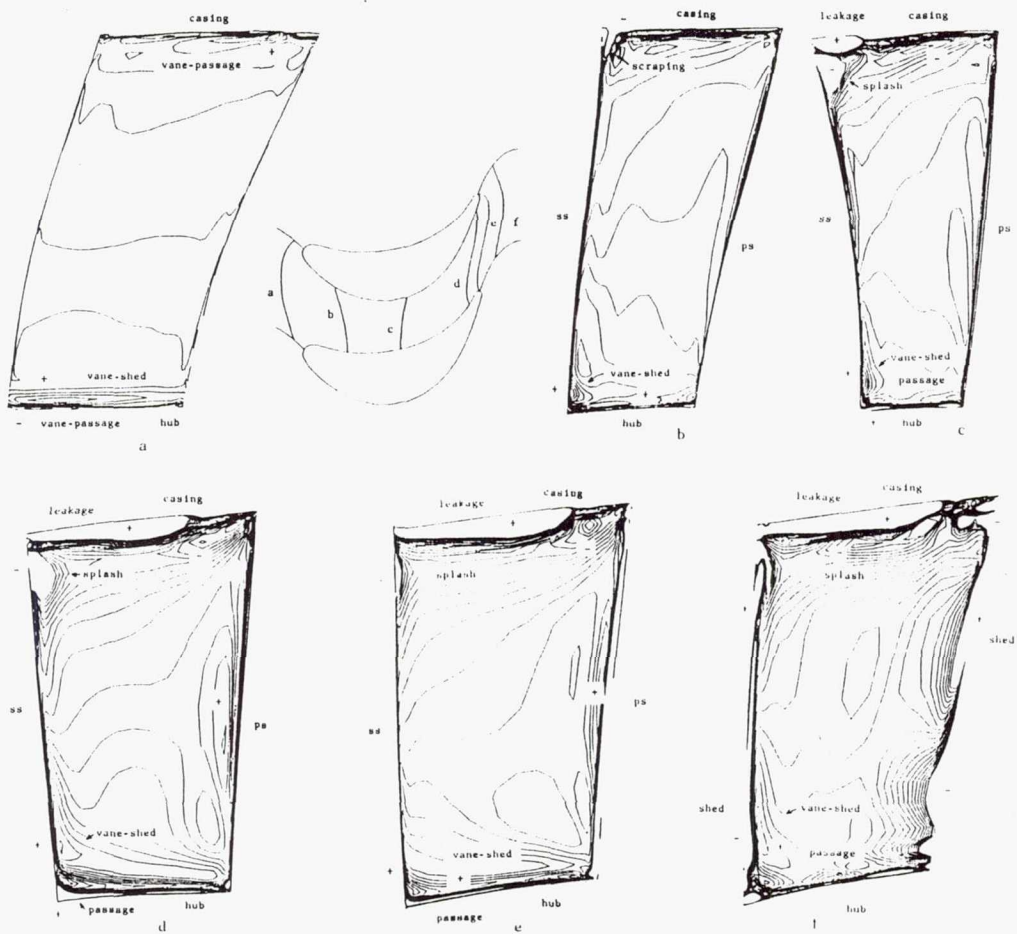
VANE 1 STREAMWISE VORTICITY



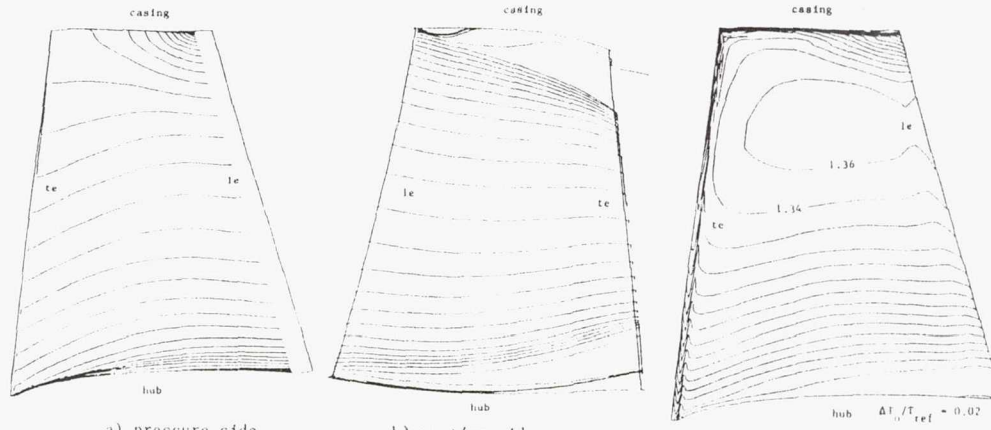
VANE 1 AXISYMMETRIC FLOW



BLADE 1 STREAMWISE VORTICITY

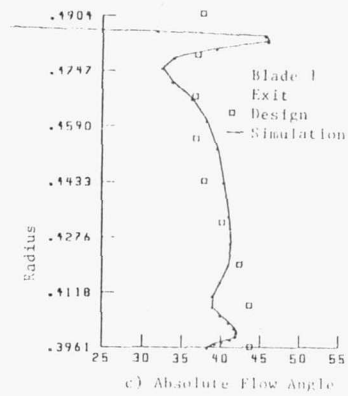
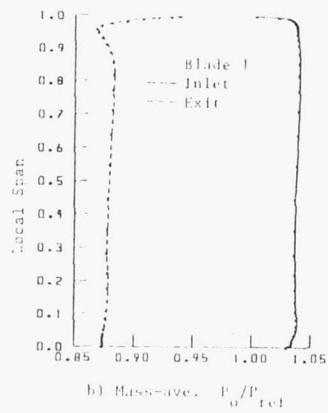
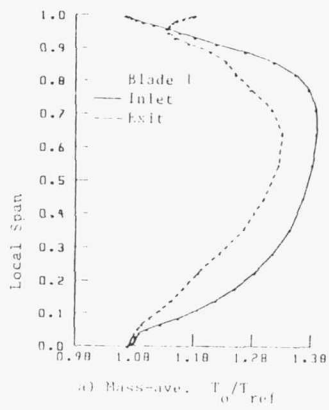


BLADE 1 SURFACE & AXISYMMETRIC FLOW



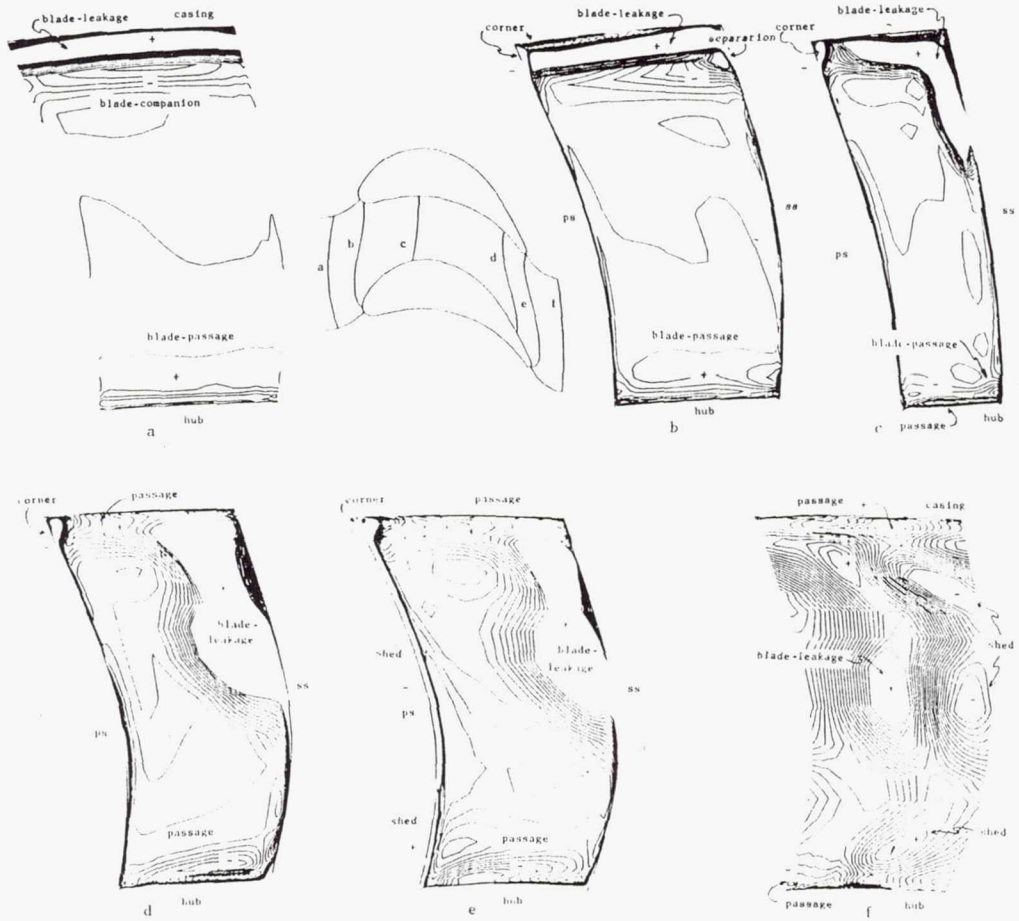
Streaklines on Blade 1

Pressure side T_0/T_{ref}

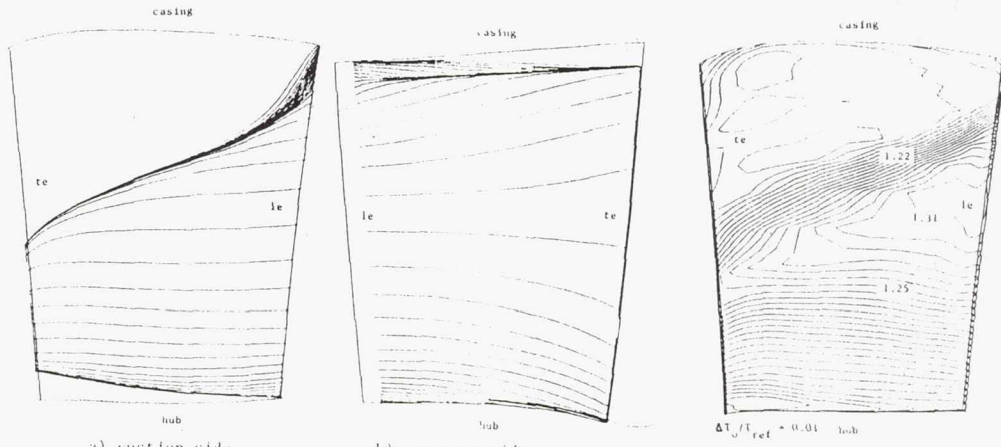


Blade 1 Axisymmetric Flow

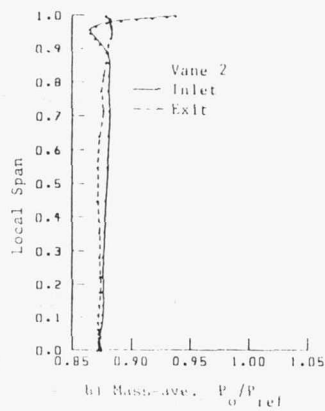
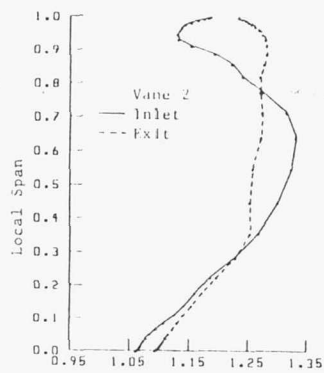
VANE 2 STREAMWISE VORTICITY



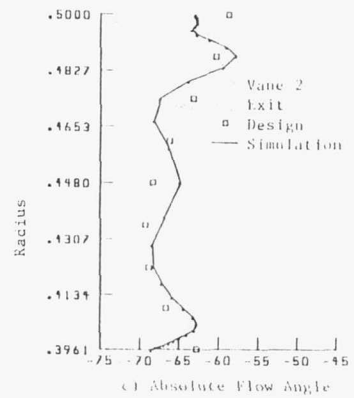
VANE 2 SURFACE & AXISYMMETRIC FLOW



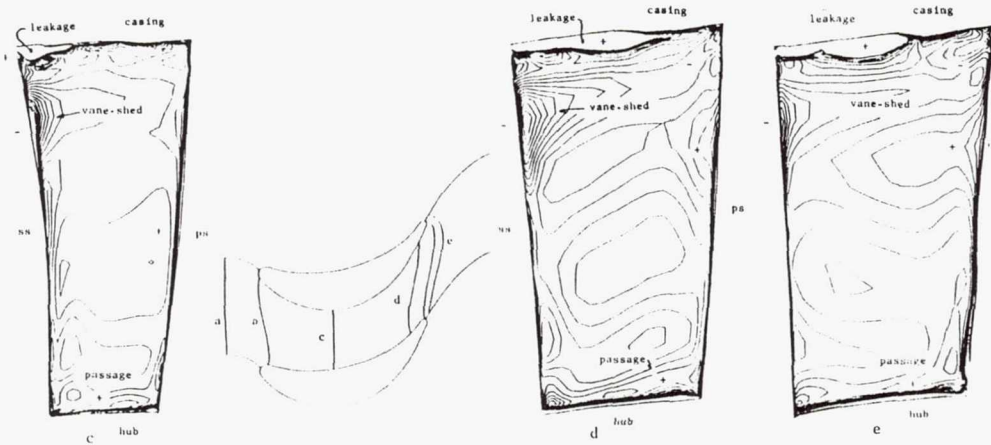
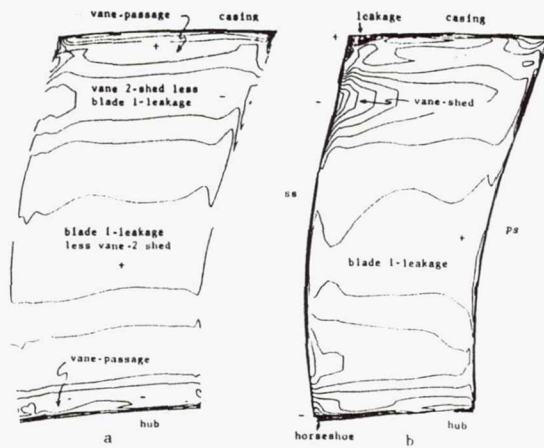
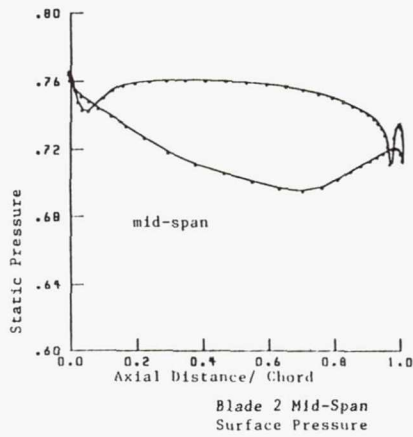
Streaklines on Vane 2



Suction side T_0/T_{ref}



BLADE 2 STREAMWISE VORTICITY



CONCLUSIONS



Flow in the Pratt & Whitney ATD SSME HPFTP is highly 3-D and dominated by the leakage flow.



The tip leakage vortex from the first rotor blade persists through the second vane and alters the second blade's loading.



The predominant spanwise mixing mechanism in this low aspect ratio turbine is convection due to deterministic unsteady vortical flows.

THREE-DIMENSIONAL FLOW CALCULATIONS INSIDE SSME GGGT FIRST STAGE BLADE ROWS

Chunill Hah
NASA Lewis Research Center
Cleveland, Ohio 44135

Steven Nash
Sverdrup Technology, Inc.
Lewis Research Center Group
Brook Park, Ohio 44142

and

Gregory Swartwout
NASA Lewis Research Center
Cleveland, Ohio 44135

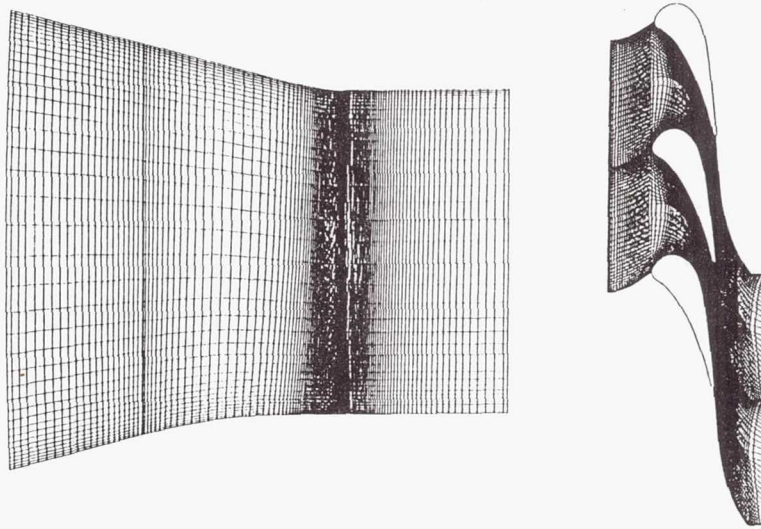
A numerical analysis of the first stage of the SSME GGGT was conducted using a 3-D Reynolds-averaged Navier-Stokes flow solver. This turbine stage was designed to improve both aerodynamic efficiency and durability. The blade has an unconventional shape; with a large blade thickness, and no experimental data is available to verify the computational results. The objective of the current study is to analyze this turbine blade stage with a well established Navier-Stokes computational method in order to determine if the turbine is operating in the subsonic flow regime and also if there are any significant separated flow regions. The stage was analyzed in a steady state flow condition. The inlet vane was analyzed with the flow conditions from the axisymmetric entire stage solution. The viscous flow solution of the first vane is used as the inlet flow condition for the rotor.

A structured I-grid included a tip grid inside the clearance region across the blade surface so as to accommodate the need for analysis in this important region of the flow. The relative velocity vectors for the guide vane shows no regions of separation, and the solution also showed that all of the flow is subsonic in the blade passage. The results for the first stage rotor reveals the stronger radial velocities at the hub and tip regions near the suction surface. Relative velocity vectors near the suction surface show that a vortex near the blade tip produces strong radial velocities a considerable distance in the

spanwise direction from the tip. On the pressure side, the tip vortex has an expectedly less anomalous effect on the overall flow, but is still fairly well resolved in the numerical solution.

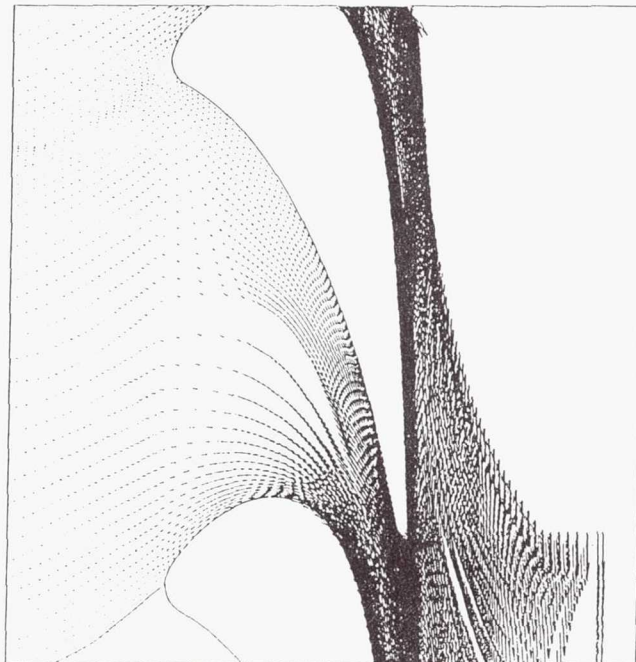
Overall analysis of the velocity vectors for the first stage rotor reveal no regions of separation. A spanwise comparison of the velocity vectors shows that indeed the tip region influences the flow measurably as far away as 10% span from the tip. Inside the tip clearance region, the solution resolved the tip vortex fairly well. Pressure contours in this region indicate the telltale signs of vortex effects. Further corroborating evidence that the tip region harbors the anomalous contributions to the flow is shown in the study of the total temperature distribution in the spanwise direction. There is no perceptible difference in total temperature until up to the 98% span distance.

Computational Grid for the Nozzle



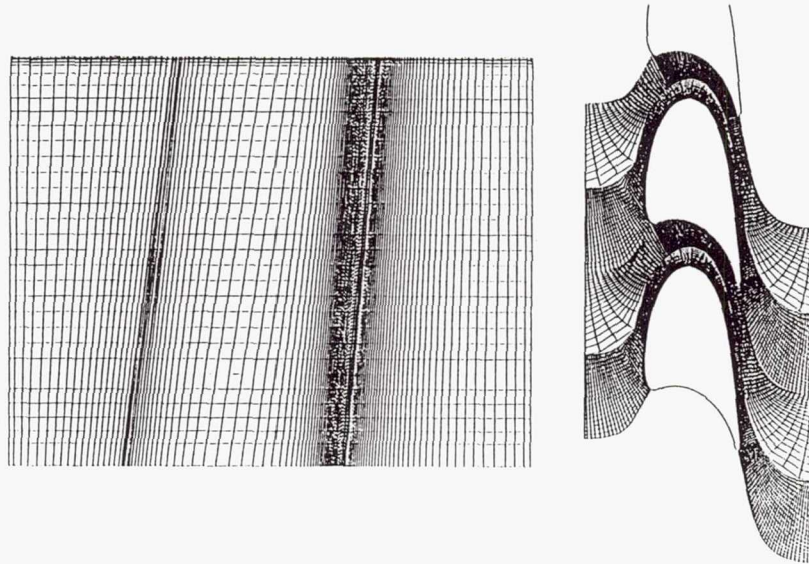
CD-91-52211

Calculated Velocity Vectors at Midspan



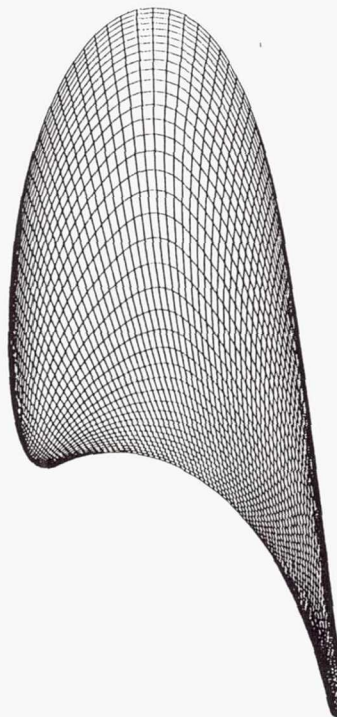
CD-91-52212

Computational Grid for the Rotor



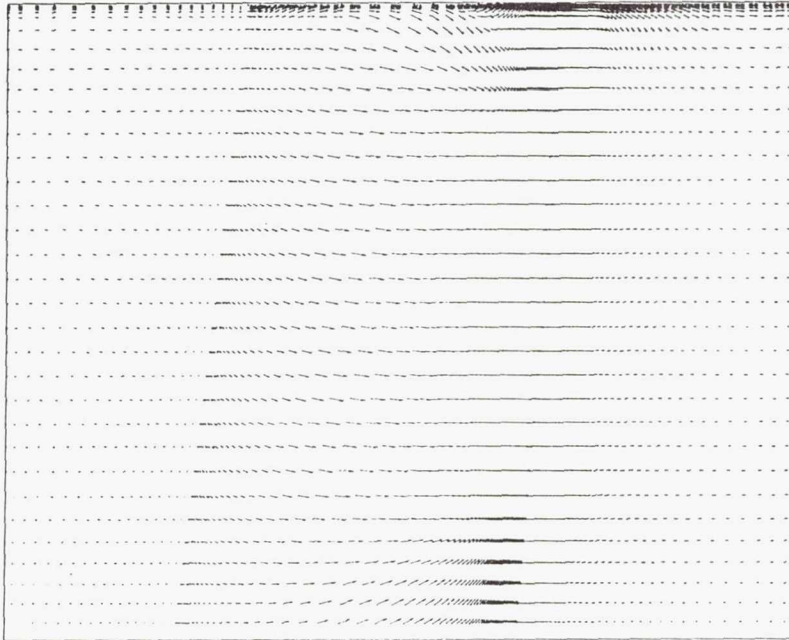
CD-91-52213

Tip Grid



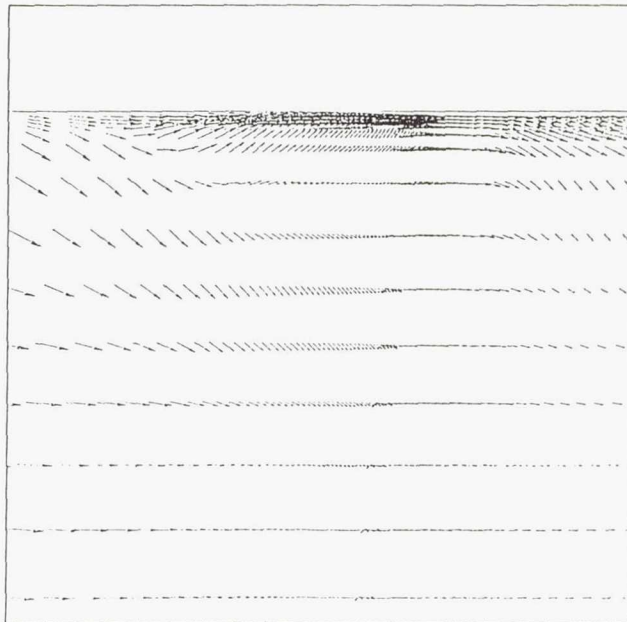
CD-91-52214

Relative Velocity Vectors Near Suction Surface



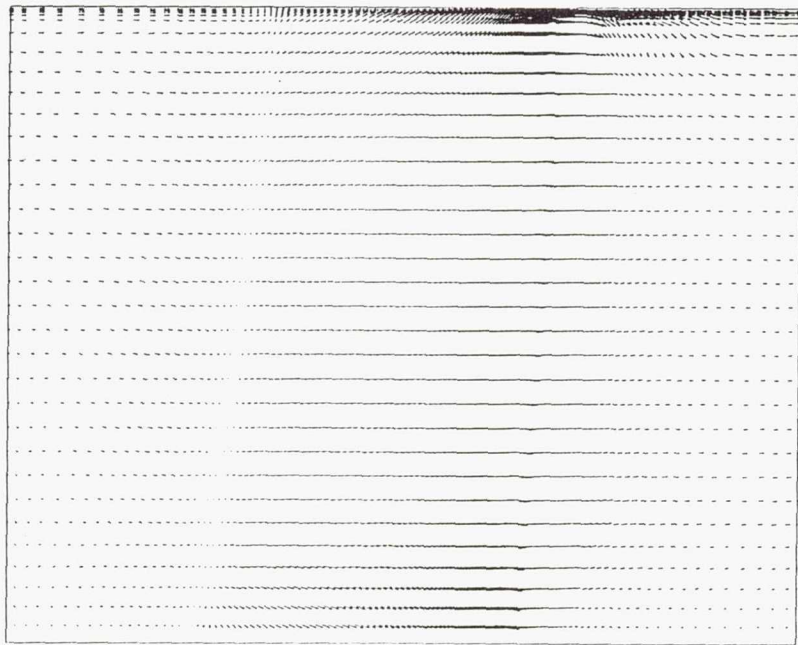
CD-91-52215

Velocity Vectors Near Tip (Suction Side)



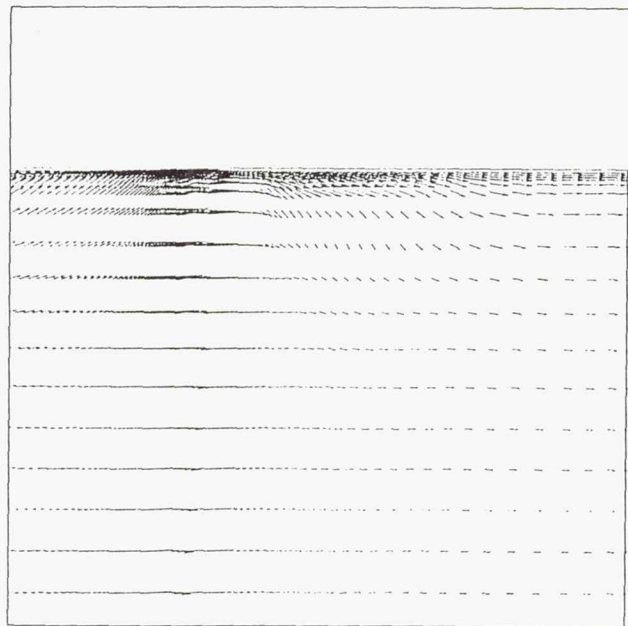
CD-91-52216

Relative Velocity Vectors Near Pressure Surface



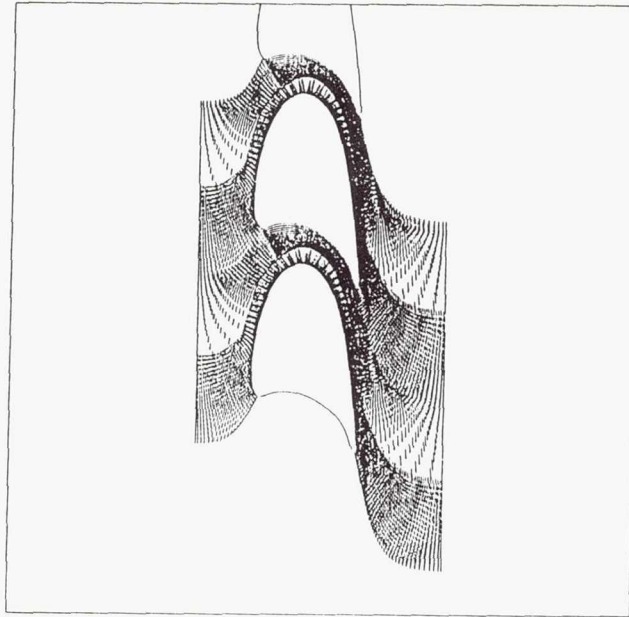
CD-91-52217

Velocity Vectors Near Tip (Pressure Side)



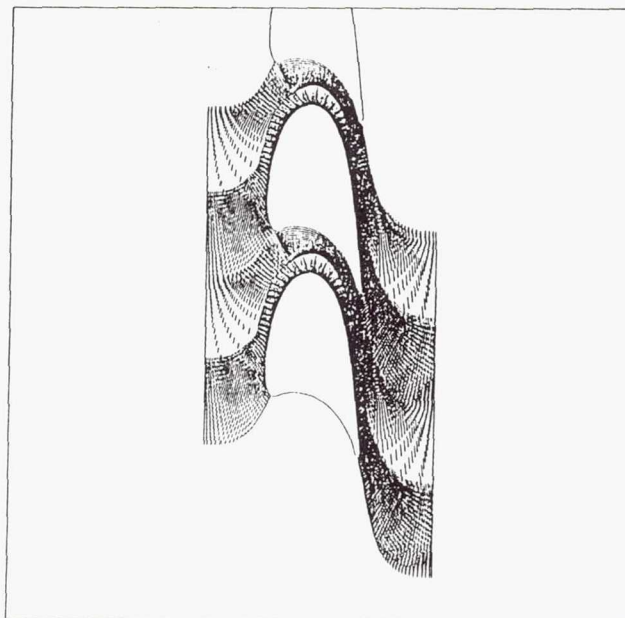
CD-91-52218

Relative Velocity Vectors Near the Hub



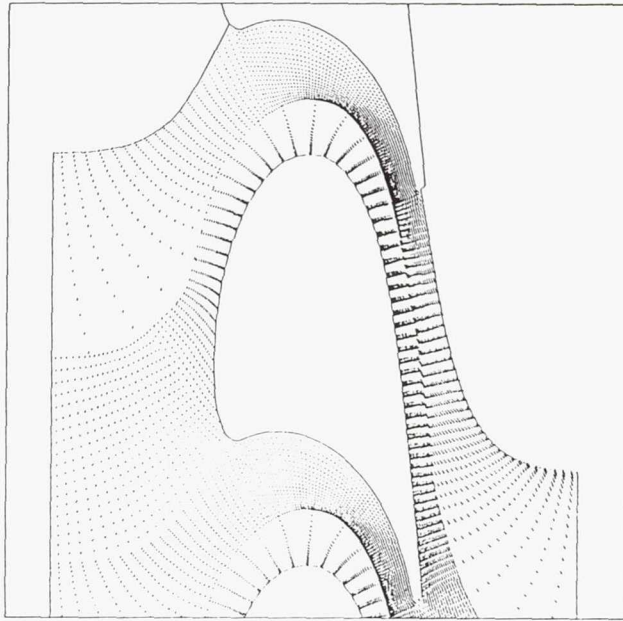
CD-91-52219

Relative Velocity Vectors Near Midspan



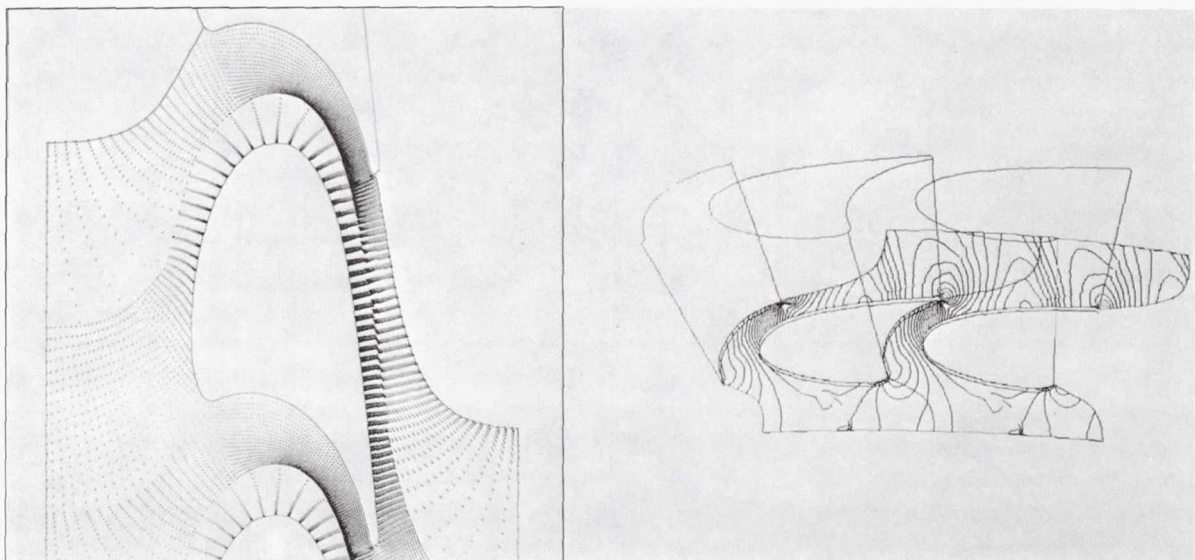
CD-91-52220

Relative Velocity Vectors Near the 90% Span



CD-91-52221

Calculated Velocity Vectors and Pressure



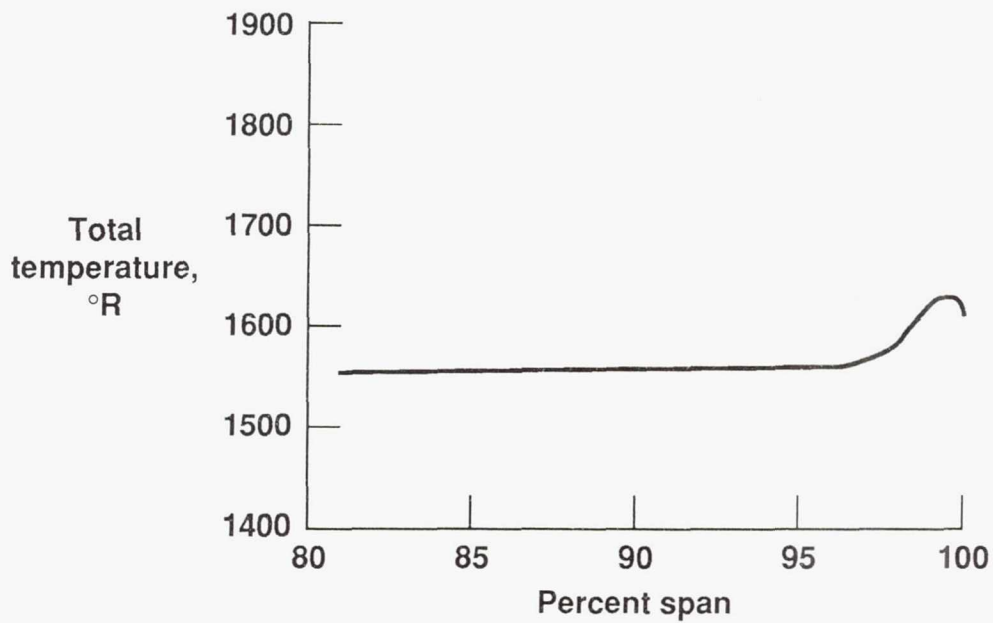
CD-91-52222

Pressure Contours Inside Blade Passage at 60% of Tip-Clearance Height



CD-91-52223

Total Temperature Distribution



CD-91-52224

Page intentionally left blank

LOCALIZATION OF AEROELASTIC MODES IN MISTUNED HIGH-ENERGY TURBINES

Todd E. Smith
Sverdrup Technology, Inc
Lewis Research Center Group
Brook Park, Ohio 44142

Christophe Pierre
The University of Michigan
Ann Arbor, Michigan 48109

and

Durbha V. Murthy^{*}
The University of Toledo
Toledo, Ohio 43606

Perfect periodicity, or cyclic symmetry, is a convenient, frequent assumption when analyzing the dynamics of bladed-disk assemblies. A primary reason for taking advantage of cyclic symmetry is that the blade response and excitation can always be expressed in terms of constant *interblade phase angle* modes that uncouple the equations of motion, thereby reducing the size of the problem to that of one blade. Unfortunately, such ideal periodicity is always disrupted by differences in the blade structural properties and modes of vibration, which are a result of manufacturing and material tolerances. This phenomenon, known as mistuning, not only increases tremendously the size and cost of the analysis of blade assemblies, but may also alter *qualitatively* their dynamics.

The present work investigates the effects of blade mistuning on the aeroelastic characteristics of a class of bladed-disk assemblies, namely high-energy turbines. The specific rotor we analyze is the first stage of turbine blades of the oxidizer turbopump (HPOTP) in the space shuttle main rocket engine (SSME). The common occurrence of fatigue cracks for these turbine blades indicates the

^{*}NASA Resident Research Associate at Lewis Research Center.

possibility of high dynamic loading. Since mistuning, under conditions of weak interblade coupling, has been shown to increase blade response amplitudes drastically for simple structural models of blade assemblies, it provides a plausible explanation for the occurrence of cracks. In this work, we are focusing on the effects of frequency mistuning on the aeroelastic stability of the assembly and on the aeroelastic mode shapes.

The rotor consists of 78 blades equally spaced on the disk. A three-dimensional finite element model is used to calculate the first four free vibration natural frequencies and mode shapes of individual blades in a vacuum. To account for blade root flexibility linear springs are included at the surfaces of the firtree lobes. However, we do not include in our model the structural coupling between blades through the disk. Thus we assume that coupling between blades arises solely from aerodynamic effects. The unsteady, motion-dependent aerodynamic forces are calculated from a two-dimensional, linearized, unsteady aerodynamic theory applied in axisymmetric strips along the airfoil span. This results in a matrix of aerodynamic influence coefficients. No structural energy dissipation is included in the present models, although linear structural damping could be added easily. The aeroelastic analysis for a rotor of blades having identical frequencies, known as a tuned rotor, has been developed in ref 1.

Applying component mode analysis to the finite element equations, we obtain a set of $78 \times M$ differential equations in the modal amplitudes of the blades, where M is the number of component modes for each blade (in our analysis, $M=4$). Assuming harmonic motion, we obtain the aeroelastic eigenvalue problem:

$$([K] + \lambda^2([M]+[A]))\{u\} = 0$$

where $\{u\}$ is the $78 \times M$ -dimensional complex eigenvector of blade modal amplitudes, $[M]$ is the diagonal mass matrix (which reduces to the identity matrix for

orthonormalized modes), $[K]$ is the diagonal stiffness matrix of the individual blades' natural frequencies squared. The matrix $[A]$ is the fully-populated aerodynamic influence matrix that provides interblade coupling ($[A]$ depends on the flutter frequency), and λ is the complex eigenvalue. The real part of λ represents the aerodynamic damping in the corresponding aeroelastic mode and thus determines stability and occurrence of flutter. The imaginary part of λ represents the damped natural frequency of oscillation, and should be equal to the assumed flutter frequency where $[A]$ was evaluated.

For a tuned system, all blades are identical and the stiffness matrix has only M distinct diagonal elements (for example, for a one mode per blade model, $[K]$ is proportional to the identity matrix). In the tuned case all matrices in the above equation are block-circulant. For a mistuned system, we assume that the individual blade frequencies are random and uniformly distributed about the frequency of the nominal blade with a small standard deviation. For a multi-mode per blade model, we take the patterns of frequency mistuning in the various component modes to be identical. For a mistuned assembly, the stiffness matrix $[K]$ is no longer circulant, but with the assumption of frequency mistuning, the mass and aerodynamic matrices remain circulant.

We have solved the aeroelastic eigenvalue problem for the tuned rotor and for various strengths of mistuning. We have used four modes of vibration in the component mode analysis to represent the motion of each blade. For the tuned system, we have found that most of the interblade phase angle modes in the second group (corresponding to blades vibrating primarily in their second normal mode) feature an unstable motion. This means that flutter occurs for an edgewise motion of the blades. No flutter was found in the other groups of modes. Therefore, we have focused our investigation of the effects of mistuning on the edgewise aeroelastic modes. It is important to note at this point that the current analysis assumes that there is no damping of the blade due to either structural or hysteretic means. The operational HPOTP contains blade-to-blade friction dampers

which provide sufficient damping to stabilize the rotor in terms of flutter (ref 1). Mechanical damping was neglected in order to investigate the effect of mistuning on rotors which were already unstable, although all results apply equally well to an initially stable rotor.

The primary finding of our study is that the dynamics of the first stage turbine stage of the SSME turbopump is severely sensitive to small blade mistuning. Both aeroelastic eigenvalues and eigenvectors undergo *qualitative* changes when perfect cyclicity is altered, due to frequency mistuning. First, the root locus of the aeroelastic eigenvalues (in the damping-frequency plane) loses the regular pattern that characterizes the tuned system to become apparently randomly scattered for small mistuning. Second, the constant interblade phase angle mode shapes of the tuned system become *strongly localized* to a few blades of the assembly when mistuning is present. The transition from extended to localized modes is very rapid in the turbopump's first turbine stage. In all cases, the standard deviations of mistuning we consider are smaller than 2%. The results from the present analysis are similar to those presented for a generic rotor in Reference 2, although the HPOTP results in considerably higher sensitivity and localization than the rotor of the prior work.

Figure 1 displays the variation of the real part of the most unstable aeroelastic eigenvalue versus the standard deviation of the frequency mistuning of the randomized blade frequencies. Note that the least stable eigenvalue becomes more stable when mistuning is present, indicating the well-known stabilizing effect of mistuning. Furthermore, observe the drastic alteration of the corresponding aeroelastic mode shape by mistuning. As expected, the mode shape in the tuned configuration features identical amplitudes for all blades. When mistuning increases, the whole assembly ceases to participate in the motion and the vibration is confined to a few of the blades, i.e., localization occurs. The extreme sensitivity of the assembly dynamics to mistuning is clearly illustrated in Figure 1: even for a very small mistuning of 0.03%, the blade amplitudes vary widely throughout the

rotor; for a mistuning of 1%, only a couple of blades participate in the motion! This indicates that the transition from extended to localized modes is very rapid. Also this transition is doubtlessly very complex, as shown by the rather irregular variation of the most unstable eigenvalue with mistuning in Figure 1a. An important focus of continued work is examining this transition region between a tuned rotor to a localized rotor in more detail.

Figure 2 displays the root locus of the 78 aeroelastic eigenvalues in the edgewise component mode for various mistuning values. Note the regular pattern of the root locus for very small mistuning (0.01%), which is characteristic of a tuned assembly. As mistuning increases, the regularity of the root locus is lost, and for small mistuning of 0.1% the locus consists of a constellation of eigenvalues with little discernible pattern. This is another illustration of the extreme sensitivity of the structure of the eigensolution to mistuning. Finally, note that mistuning results in a narrowing of the range of the real parts of the eigenvalues (damping) but in a stretching of the root locus along the imaginary direction (frequency).

The above results demonstrate that the aeroelastic characteristics of the first turbine stage of the SSME turbopump are highly sensitive to frequency mistuning. Strong mode localization and scattering of the root locus occur for values of mistuning that cannot be avoided in practice. This means that, for the turbopump model studied, most tuned aeroelastic calculations are probably invalid. We expect the forced response of the assembly to be affected by mistuning in a similar way, because the response can be expressed as a combination of motions in the free aeroelastic modes.

Continued research into this topic will focus on the following points; first, we will perform an in-depth examination of the transition region between constant interblade phase angle modes (tuned rotor) to localized modes for the mistuned system. Second, we will apply perturbation schemes to predict and understand

the onset of mode localization. These methods will also allow us to quantify the degree of localization of the modes. We are also hoping they will lead to the definition of a *sensitivity measure* that will enable us to predict the occurrence of localization and the sensitivity of the assembly in a simple way.

REFERENCES

1. T.E. Smith, "Aeroelastic Stability Analysis of a High-Energy Turbine Blade", AIAA Paper 90-2351, Presented at the AIAA/SAE/ASME/ASEE 26th Joint Propulsion Conference, Orlando, FL, July 16-18, 1991
2. C. Pierre, D.V. Murthy, "Aeroelastic Modal Characteristics of Mistuned Blade Assemblies: Mode Localization and Loss of Eigenstructure", AIAA 91-1218, To be presented at the AIAA/ASME/ASCE/AHS/ASC 32nd SDM Conference, Baltimore, MD, April 8-10, 1991

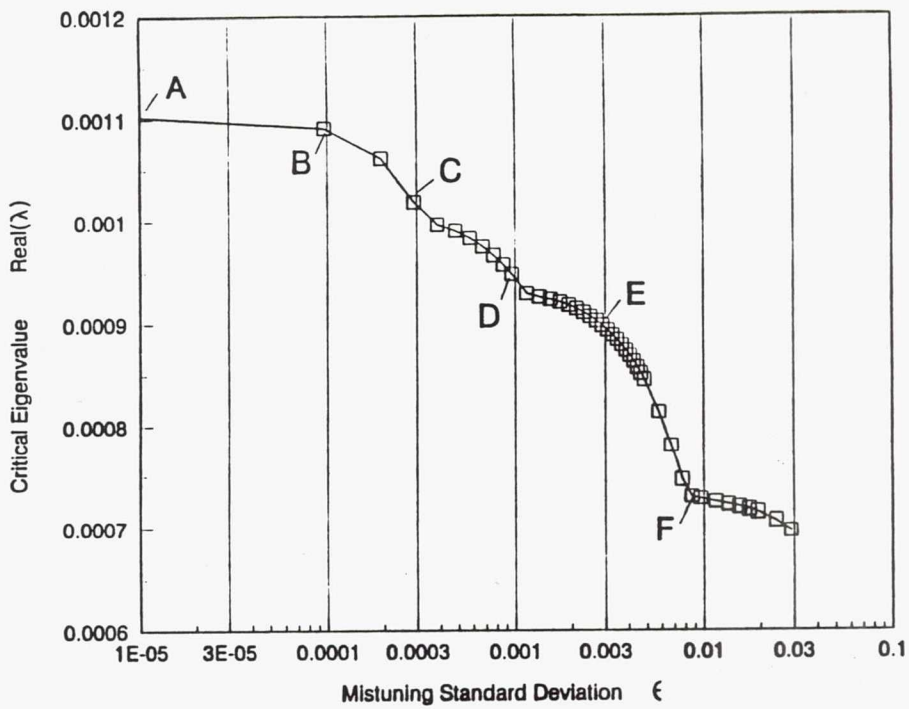


Figure 1.a Real part of the most unstable eigenvalue (damping) versus mistuning standard deviation, ϵ

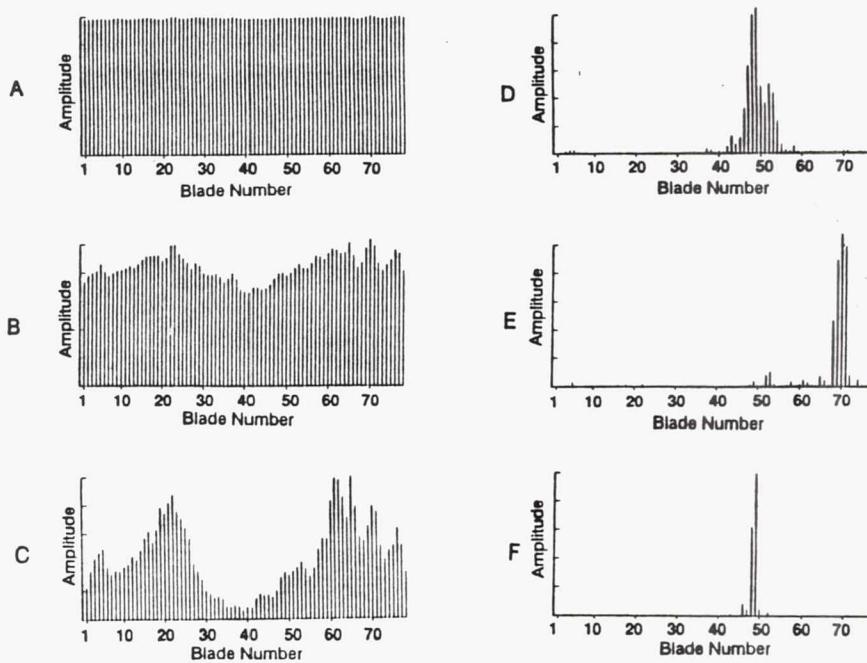


Figure 1.b Amplitude of the rotor aeroelastic mode shapes corresponding to most unstable eigenvalue for various values of mistuning

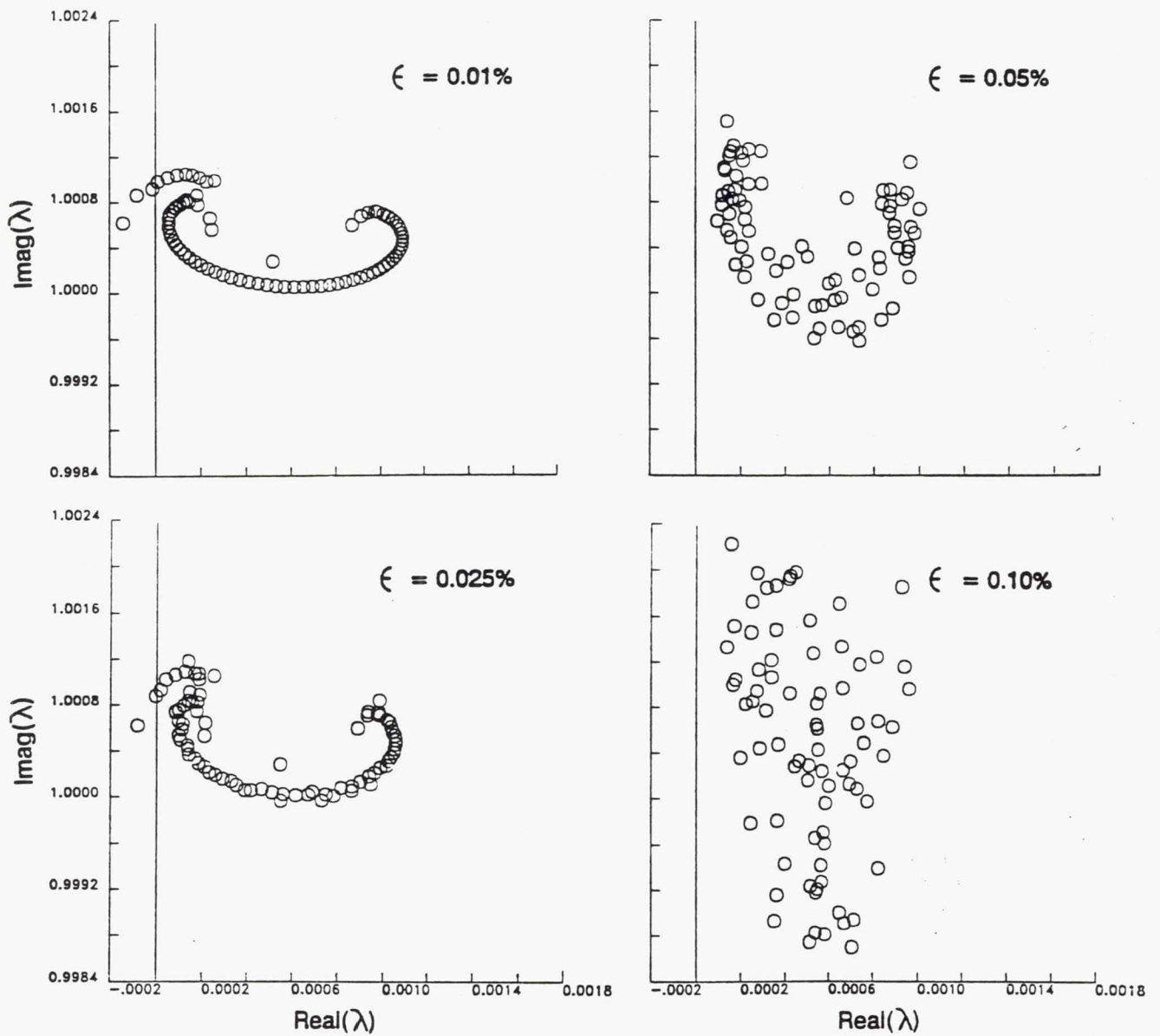


Figure 2 Root locus of the 78 aeroelastic eigenvalues (frequency vs damping) for various values of mistuning (Edgewise motion only)

HEAT TRANSFER AND PRESSURE MEASUREMENTS FOR THE SSME FUEL TURBINE

Michael G. Dunn and Jungho Kim
Calspan - UB Research Center
Buffalo, New York 14225

ABSTRACT

A measurement program is currently underway at the Calspan-UB Research Center (CUBRC) using the Rocketdyne two-stage Space Shuttle Main Engine (SSME) fuel turbine. The measurements utilize a very large shock tunnel to produce a short-duration source of heated and pressurized gas which is subsequently passed through the turbine. Within this environment, the turbine is operated at the design values of flow function, stage pressure ratio, stage temperature ratio, and corrected speed. The first-stage vane row and the first-stage blade row are instrumented in both the spanwise and the chordwise directions with pressure transducers and heat-flux gages. The second-stage vane row is instrumented at midspan with heat-flux gages. There are no pressure transducers on the second vane row. The second-stage blade row contains neither pressure nor heat-flux gages at the present time. The specific measurements to be taken include time-averaged surface-pressure and heat-flux distributions on the vane and blade, flow passage static pressure, flow passage total pressure and total temperature distributions, and phase resolved surface pressure and heat flux on the blade.

This paper will provide a current status of the measurement program. Examples of results obtained to date will be presented. Reference ¹

* Paper Submitted for Presentation at the SSME Durability Conference to be Held at NASA Lewis Research Center, May 14-15, 1991

¹ Dunn, M.G., "Heat Transfer and Pressure Measurements for the SSME Fuel-Side Turbopump," paper presented at the 1990 Earth-to-Orbit Conference, Marshall Space Flight Center, May 15-17, 1990.

presented a description of the hardware, the instrumentation, and the measurements being performed on the turbine components and along the flowpath. Table 1 presents a description of flow conditions for which measurements are being obtained.

Table 1

Test Conditions for SSME Fuel Turbine Measurements

| T_O , °R | P_O , psia | Flow Function | Re_{chord} | Total to Total Press. Ratio | Rotor Speed rpm |
|------------|--------------|---------------|-------------------|-----------------------------|-----------------|
| 1000 | 260 | 2.27 | 9.9×10^5 | 1.47 | 9292 |
| 1000 | 150 | 2.27 | 5.7×10^5 | 1.47 | 9292 |
| 1000 | 100 | 2.27 | 3.8×10^5 | 1.47 | 9292 |
| 1000 | 50 | 2.27 | 1.9×10^5 | 1.47 | 9292 |
| 1000 | 600 | 2.27 | 2.3×10^6 | 1.47 | 9292 |

The data point at 100 psia inlet pressure corresponds to the run condition recently completed at the NASA Marshall Space Flight Center for a companion SSME fuel turbine. The Marshall measurement program produced turbine efficiency results for a number of operating points, time averaged surface pressure distributions as a function of chord and span for the first vane row, and time averaged surface pressure distributions along midspan for the second vane row. The first vane pressure results obtained at MSFC will be directly comparable to the CUBRC pressure results. Pressure measurements were not performed on the rotor for the MSFC experiments. No heat-flux measurements were performed for the Marshall configuration.

PENN STATE AXIAL FLOW TURBINE FACILITY: PERFORMANCE AND NOZZLE FLOW FIELD

B. Lakshminarayana and M. Zaccaria
The Pennsylvania State University
University Park, PA 16802

and

S. Itoh
National Defense Academy
Yokosuka, Japan

The objective of the research presented in this paper is to gain a thorough understanding of the flow field in a turbine stage including three-dimensional inviscid and viscous effects, unsteady flow field, rotor-stator interaction effects; including unsteady blade pressures, shear stress and velocity field in rotor passages. A brief progress report on the research carried out towards this goal is presented in this paper. The performance of the turbine facility at the design condition is measured and compared with the design distribution. The data on the nozzle vane static pressure and wake characteristics are presented and interpreted. The wakes are found to be highly three-dimensional, with substantial radial inward velocity at most spanwise locations.

Notations

| | |
|----------------------|--|
| C | Chord length |
| C_p | Static pressure coefficient $(P_{atm} - p)/0.5\rho U_t^2$ |
| C_{ps} | Blade static pressure $(p - P_{atm})/0.5\rho V_{x1}^2$ |
| C_{pt} | Stagnation pressure coefficient $(P_{atm} - p)/0.5\rho U_t^2$ |
| C_{pw} | Wake static pressure $(p - P_{atm})/P_{atm}$ |
| p | Static pressure |
| P | Stagnation pressure |
| P.S. | Pressure side of wake |
| R | Radius normalized by blade tip radius |
| S | Streamwise distance |
| S.S. | Suction side of wake |
| U_t | Blade tip speed |
| V_θ, V_r, V_x | Absolute tangential, radial and axial velocity components |
| V | Absolute velocity |
| X | Axial distance normalized by axial blade chord (=0 at LE, =1 at TE) |
| Y | Tangential distance normalized by blade spacing (=0 at wake center, +ve on pressure side, -ve on suction side) |
| α | Flow outlet angle measured from axial direction |

Subscripts

| | |
|----------------|---|
| r, θ, x | Radial, tangential and axial components |
| h | Hub |
| t | Tip |
| 1,2,3 | Inlet, exit of nozzle, exit of rotor |

INTRODUCTION

The present knowledge of turbine flow field, especially the rotor flow field is not adequate. The flow field is three-dimensional and unsteady, with the presence of laminar, transitional and turbulent regions near the blade surface. Some of the three dimensional effects present are compressibility, radial density (or temperature) gradient, radially varying thickness, annulus wall area changes and flaring, radially varying enthalpy, radial component of blade force, radially varying blade heat transfer, non-uniform entry flow and temperature field, and leakage and secondary flows. The three dimensional viscous flows and turbulence effects are mainly caused by the three dimensional boundary layers on blades and wakes, annulus wall and hub wall boundary layers, shock boundary layer interaction, and secondary flows in annulus wall and hub wall boundary layers. The presence of horseshoe vortex near the blade leading edge, combined with thick blades and rapidly varying passages and flow turning, makes the flow field truly complex.

There are many other basic problems related to turbines that remains unresolved. These are the vane-blade interaction and its effect on the unsteady pressure, reliability, unsteady heat transfer and vibration. These interactions are both inviscid and viscous in nature and can considerably affect the aerothermodynamic performance of a stage. A major objective of this research is to develop and validate quantitative understanding of the unsteady interactions in a turbine. Large scale, low speed rig testing will permit extensive use of sophisticated instrumentation that will facilitate a better understanding of the vane-blade interaction process. The experimental results directly feed and support the analytical and computational tool development. The large scale, low speed rig available at Penn State will facilitate these experiments because it permits extensive use of high frequency response instrumentation on the stationary vanes and, more importantly, on the rotating blades. Furthermore, it facilitates detailed nozzle wake, rotor wake and boundary layer surveys. The large size of the rig also has the advantage of operating at Reynolds numbers representative of the engine environment. This allows duplication of Reynolds-number-sensitive fluid flow characteristics, such as wakes and boundary layers. The time dependent static pressure distributions will directly validate the computational results from the unsteady, time marching flow solution under development at Penn State and elsewhere.

FACILITY DESCRIPTION

The Axial Flow Turbine Research Facility of The Pennsylvania State University is an open circuit facility 91.4 cm in diameter and a hub to tip radius ratio of 0.73, with advanced axial turbine blading configurations. The facility consists of a large bellmouth inlet, a turbulence generating grid section, followed by a test section with a nozzle vane row and a rotor. There are 23 nozzle guide vanes and 29 rotor blades followed by outlet guide vanes. Provisions exist for changing the vane-blade axial spacing from 20 to 50 percent of chord. The bellmouth inlet is housed in an enclosure covered with wire mesh and a thin layer of rubber foam to filter the air prior to entry to the inlet. A complete description of the facility is given in Reference 1 and a brief description is given in Reference 2.

A variable through flow is provided by two auxiliary, adjustable pitch, axial flow fans and an aerodynamically designed throttle. This system allows accurate control of the mass flow through the experimental stage up to a maximum of 22,000 cfm. The two fans in the series produce a pressure rise of 74.7 mm Hg (40" of water) with a mass flow of 10.4 m^3 per second under nominal operating conditions. The power generated by the experimental turbine rotor assembly is absorbed by an eddy-current brake which is capable of absorbing up to 90 Hp. The speed of the rotor can be varied between 175 and 1695 RPM with the "dynamic-adjustor speed" control system and can be held

constant to ± 1 RPM, with normal fluctuations in line voltage. The eddy current brake is cooled by a closed loop chilled water cooling system.

The rotor and nozzle vane passages are instrumented with high frequency instrumentation to measure steady (time averaged) and unsteady pressures, shear stresses. The details of the instrumentation used on the nozzle vane, rotor blade, nozzle casing, rotor hub, and nozzle hub is described in References 1 and 2. Provision has been made for a laser window for LDV measurement of the flow field upstream of the nozzle, nozzle passage, spacing between the rotor and the nozzle, rotor passage, and downstream of the rotor passage. The facility is equipped with two traversing mechanisms. One of the probe traverse units is mounted directly behind the rotor disk and has provisions for the radial and circumferential traverses in the rotating frame. It is controlled by a stepping motor driven by a computer indexer at tangential increments of 0.019 degrees/step to allow accurate measurement of the rotor wakes.

The rotating to stationary interface data transmission system, attached to the rotor shaft ahead of the nose cone, is an integral part of the facility. It consists of a 150 ring mechanical (brush/coin type) slip ring unit, and a specialized ten-channel low noise/signal ratio mercury slip ring unit. A 32 channel electronic pressure scanner unit is located in the rotating drum downstream of the turbine rotor. The electrical signals carrying the pressure information is carried to the stationary frame through the slip ring assembly. The rotor frequency will be accurately determined by using an infrared emitter/receiver sensor located on the casing of the turbine rotor. This device senses the reflected infrared emissions from the tip of a selected rotor blade and directly provides the rotor frequency (once per revolution pulse-OPR).

A completely automated data processing system is built around a micro-computer with a clock rate of 27 MHz. The system consists of a 32 bit computer with 8 Mb random access memory, a disk operating system, 150 Mb hard disk storage space, printer and plotter. All of the data from both stationary and rotating instrumentation can be processed on-line. One of the long range goals of the turbine research is to acquire unsteady heat transfer and aerodynamics data simultaneously.

The aerodynamic design, while not representing any specific current future GE product, does embody modern turbine design philosophy. Stage loading flow coefficient, reaction, aspect ratios, and blade turning angles are all within the ranges of current design practice. State-of-the-art quasi-3D design methods were used to design the airfoil shapes. It is felt that the design is fully capable of meeting the intended research applications. At the inception of the design the objective was that, where possible, the blading should be representative, both geometrically and aerodynamically, of a state-of-the-art HP turbine. Detailed design characteristics, philosophy, and design performance parameters were presented in Reference 1 and 2.

PERFORMANCE MEASUREMENTS AT DESIGN CONDITION

The probes and instrumentation used for the performance measurements includes a 5-hole probe, a pitot probe, a single sensor hot-wire probe and the wall static pressure taps.

In order to determine the axisymmetry and turbulence upstream of the nozzle, a single sensor hot wire probe is used to measure the radial distribution of axial turbulence intensity and mean velocities at three tangential locations (120 degrees apart) at the inlet. The flow was axisymmetric and the axial turbulence intensity was nearly constant at around 1 to 1.5 percent, except near the hub and casing. The freestream velocity was 89.2 ft/s with a Reynolds number of 3.30×10^5 based on nozzle vane chord at midspan. The wall boundary layers were turbulent, with a thickness of 10% blade

span at the hub (0.48 inches) and 20% blade span at the tip (0.96 inches). These radial and tangential velocities were almost negligible upstream of the nozzle.

The radial distribution of total and static pressures, total, axial, radial and tangential velocities, and rotor exit flow angle at design conditions were measured two chords downstream of the rotor blade row using a five hole probe. Figures 1 through 3 show the experimental data compared with the design values. The stagnation and static pressure drop coefficients, shown in Figure 1, are about 8 percent less than the design values and this is consistent with the design and estimated efficiencies. The total absolute velocity at the exit (Figure 2) is close to the design values, with higher than design values near the mid-span and lower than the design values near hub and annulus walls. Likewise, the axial velocity distribution shown in Figure 3 indicates the axial velocities are higher in the mid-third of the blade height (due to blockage effect) with low values in the secondary and horseshoe vortex regions. Similar trend can be observed in the tangential velocity distribution shown in Figure 3. The radial velocities are negligibly small (Figure 2). Since the measuring station is located about two chords downstream, this is as expected. Evidence of substantial secondary flow region near the hub is clear from the tangential velocity distribution shown in Figure 3. No attempt is made to draw any conclusions regarding the magnitude of secondary flows, as this data represents average values of rotor flow sensed by a stationary five-hole probe.

NOZZLE FLOW FIELD DATA

Nozzle Vane Pressure Distribution

The nozzle vane has one fully instrumented passage with 154 static pressure taps at several chordwise and radial locations on the suction and the pressure surfaces. The static pressure holes are more closely spaced near the hub and the tip, since the vane surface static pressure distribution changes more rapidly in this region due to the complexity of the endwall flow. Figure 4 shows the static pressure distribution at $R=0.87$ and 0.74 at 1300 rpm at design conditions. The experimental blade pressure distribution is compared to that obtained by the panel code and the design distribution. On the pressure surface an initial rapid acceleration is followed by a very slow acceleration which occurs up to midchord. From midchord to the trailing edge, the flow accelerates rapidly. On the suction surface there is a steady acceleration of flow until close to the trailing edge, after which the flow decelerates until the outlet pressure is reached at the trailing edge. The agreement between the computational and the measured pressure distribution is good on the pressure surface, but on the suction surface the measured flow accelerates less rapidly than the design values. This could be attributed to the boundary layer growth on the suction side.

Nozzle Wake Data

Measurements of the pitch and yaw angle and pressures were taken in the wake region of the nozzle vane at one axial and three radial locations ($X=1.08$, $R=0.74$, 0.79 and 0.87). A five-hole probe connected to a scanivalve and a pressure transducer is used to measure the velocity, static and stagnation pressures.

A plot of the total and axial velocity profile across the wake at three radii at 8% of the axial chord downstream of the trailing edge ($X=1.08$) is shown in Figure 5. The streamwise distance is approximately 15% of the total chord at this location. The wake decay is much faster than those measured in cascades and compressor rotors (Ref. 3). One of the causes of this faster decay is the radial velocity that exists in this wake. The wake is appreciably thick (about 20 to 30 percent of blade spacing) at all three radial locations and the wake width is maximum near the tip of the blade. The

axial velocity profile is similar to the total velocity and in all cases, the wake is asymmetric, and the wake defect is nearly constant for various radii. Similar wake measurements have been reported by Dring, et al. (Ref. 4) and Goldman and Seasholtz (Ref. 5). The tangential velocity profile across the wake at $R=0.92, 0.87, 0.79$ are shown plotted in Figure 6. The tangential velocity profiles are similar to axial and total velocity profiles presented earlier. The data presented later indicate that the outer angle variation is ± 2 degrees across the entire wake. One of the most interesting features is the radial velocity distribution shown in Figure 6. Radial velocities are inward at all locations and the maximum values occur near the tip of the blade. The static pressure gradient is nearly constant in the wake, but the centrifugal force in the radial direction caused by the tangential velocity, decreases as the wake center line is approached. This induces radial inward velocity which is consistent with the data shown in Figure 6. The hub has the least radial inward velocity and the tip has the maximum inward velocity. These inward velocities represent approximately 10 degrees in the pitch angle. Thus, the wakes emanating from the nozzle vanes are three-dimensional and with a substantial variation in tangential, axial and the radial component across the wake. The wakes are fairly thick and this should have a substantial influence on the unsteady pressure and velocity distribution, in the subsequent rotor passage. Attempts will be made to measure the wake at other axial locations including one near the rotor blade leading edge using laser doppler velocimeter.

The outlet angles variation across the wake is shown in Figure 7. This indicates that the outlet angle variation is not substantial. The maximum deviation being ± 2 degrees with overturning on one side of the blade, underturning on the other side as expected. The static pressure distribution across the wake is also shown in Figure 7 and this indicates that the static pressure is nearly constant across the wake at this axial location.

Acknowledgments

This work was sponsored by NASA through the Grant NAG3-555, with C. Civinskas and J. Schwab as technical monitors. Grateful acknowledgment is made to C. Camci and I. Halliwell for their participation in the facility, blading and instrumentation development.

REFERENCES

1. Lakshminarayana, B., Camci, C., Halliwell, I. and Zaccaria, M., "Penn State Axial Flow Turbine Facility: Design Fabrication and Performance," Penn State University, PSU Turbo 9101, 1991.
2. Lakshminarayana, B., Camci, C. and Halliwell, I., "A New Facility to Study Three-Dimensional Viscous Flow and Rotor-Stator Interaction in Turbines," Proc. Conf. Structural Integrity and Durability of Space Propulsion Systems, NASA CP 10030, 1989.
3. Raj, R. and Lakshminarayana, B., "Characteristics of the Wake Behind a Cascade of Airfoils," J. Fluid Mechanics, Vol. 61, pp. 707-730, 1973.
4. Dring, R. P., Joslyn, H. D. and Blair, M. F., "The Effects of Inlet Turbulence and Rotor/Stator Interaction on the Aerodynamics and Heat Transfer of a Large Scale Rotating Rig," NASA CR 179469, 1987.
5. Goldman, L. J. and Seasholtz, R. G., "Laser Anemometer Measurements in an Annular Cascae of Core Turbine Vanes and Comparison with Theory," NASA Tech. Paper 2018, 1982.

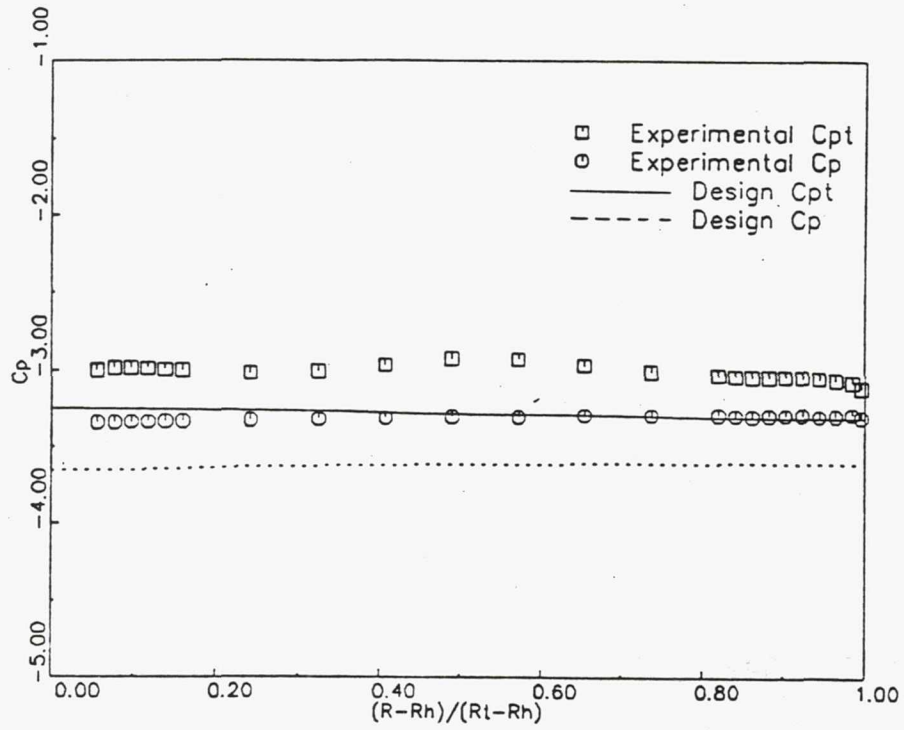


Figure 1 Total & Static Press. Coeffs. 2 Chords Downstream of Rotor

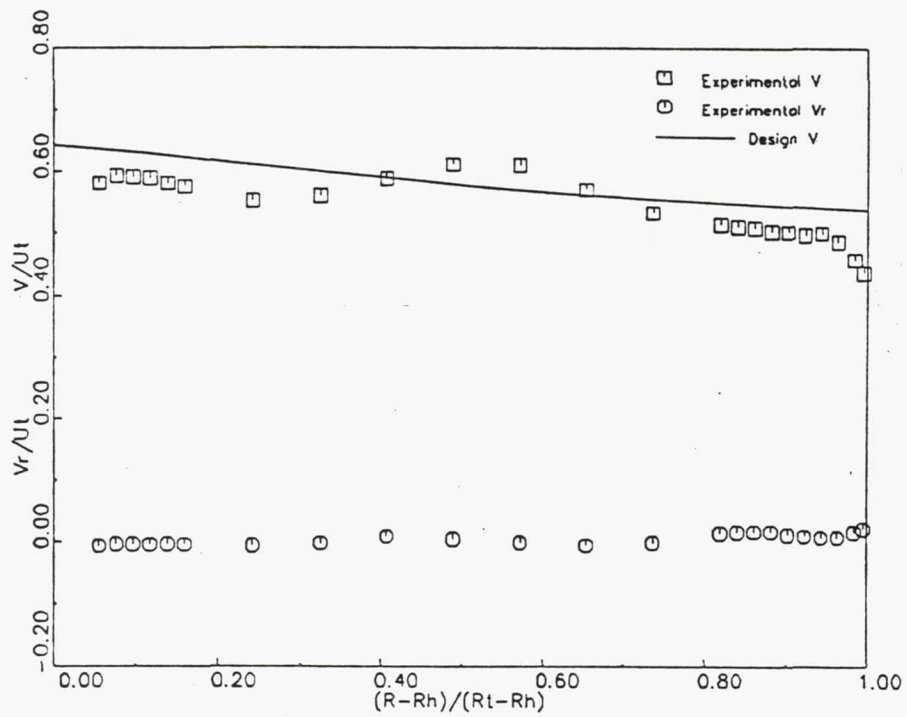


Figure 2 Velocity Profiles 2 Chords Downstream of Rotor

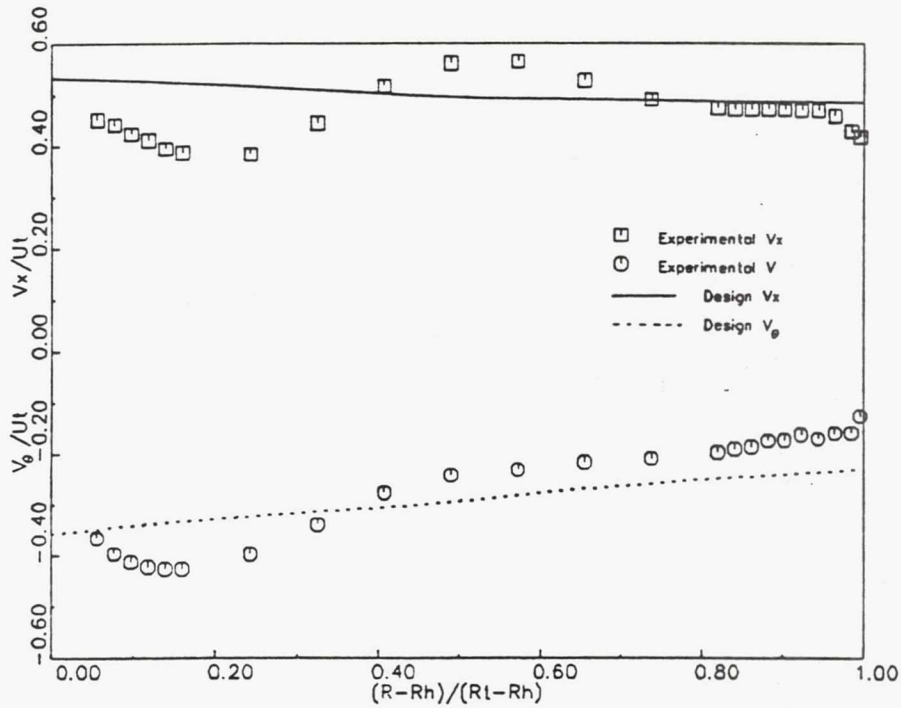


Figure 3 Velocity Profiles 2 Chords Downstream of Rotor

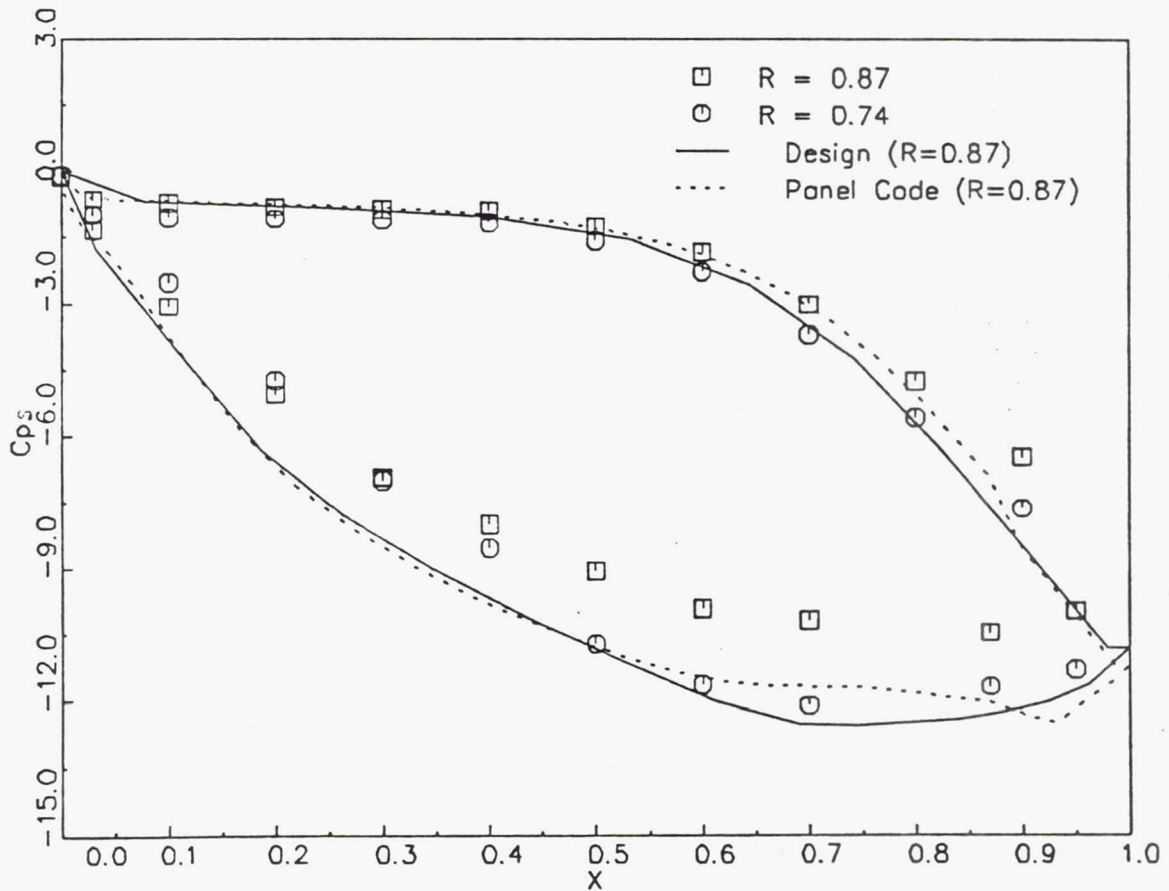


Figure 4 AFTRF NOZZLE SURFACE STATIC PRESSURE DISTRIBUTION

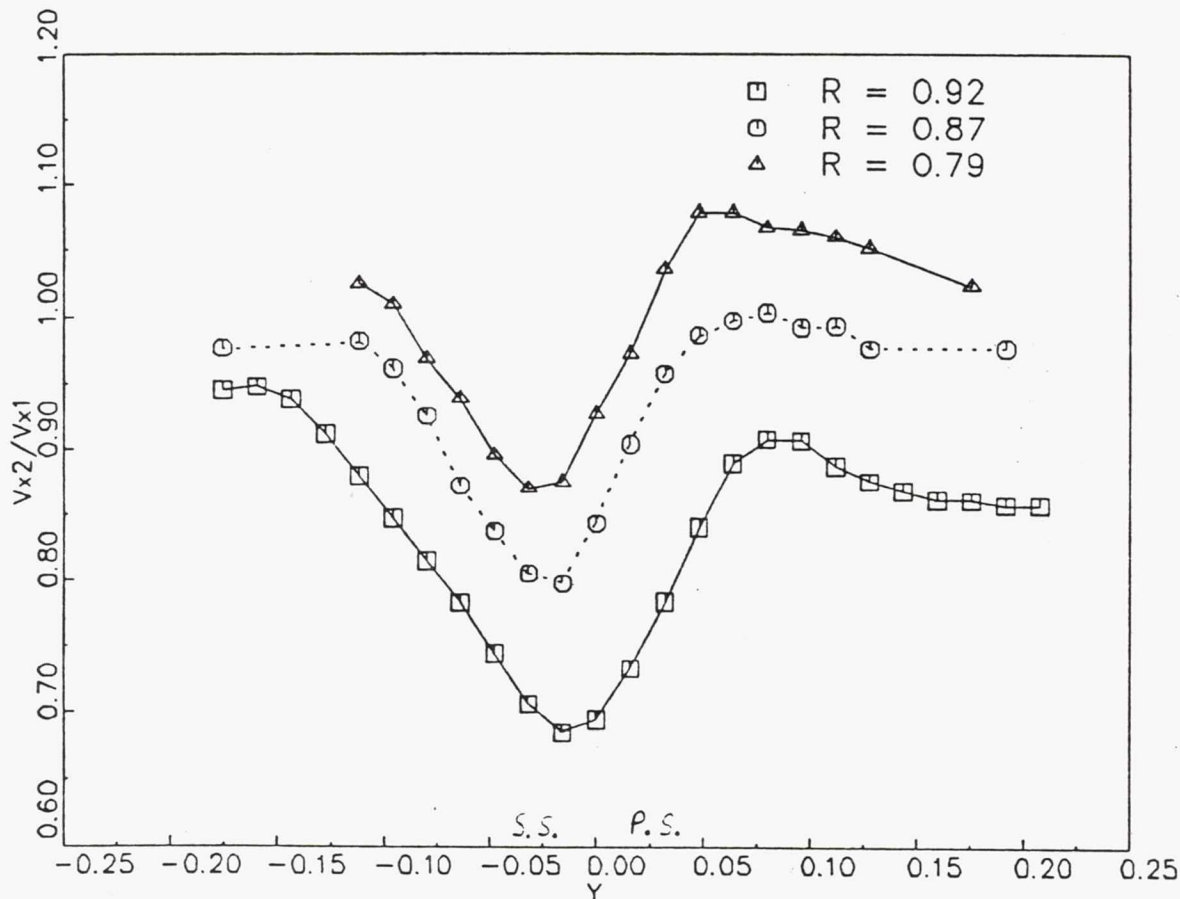
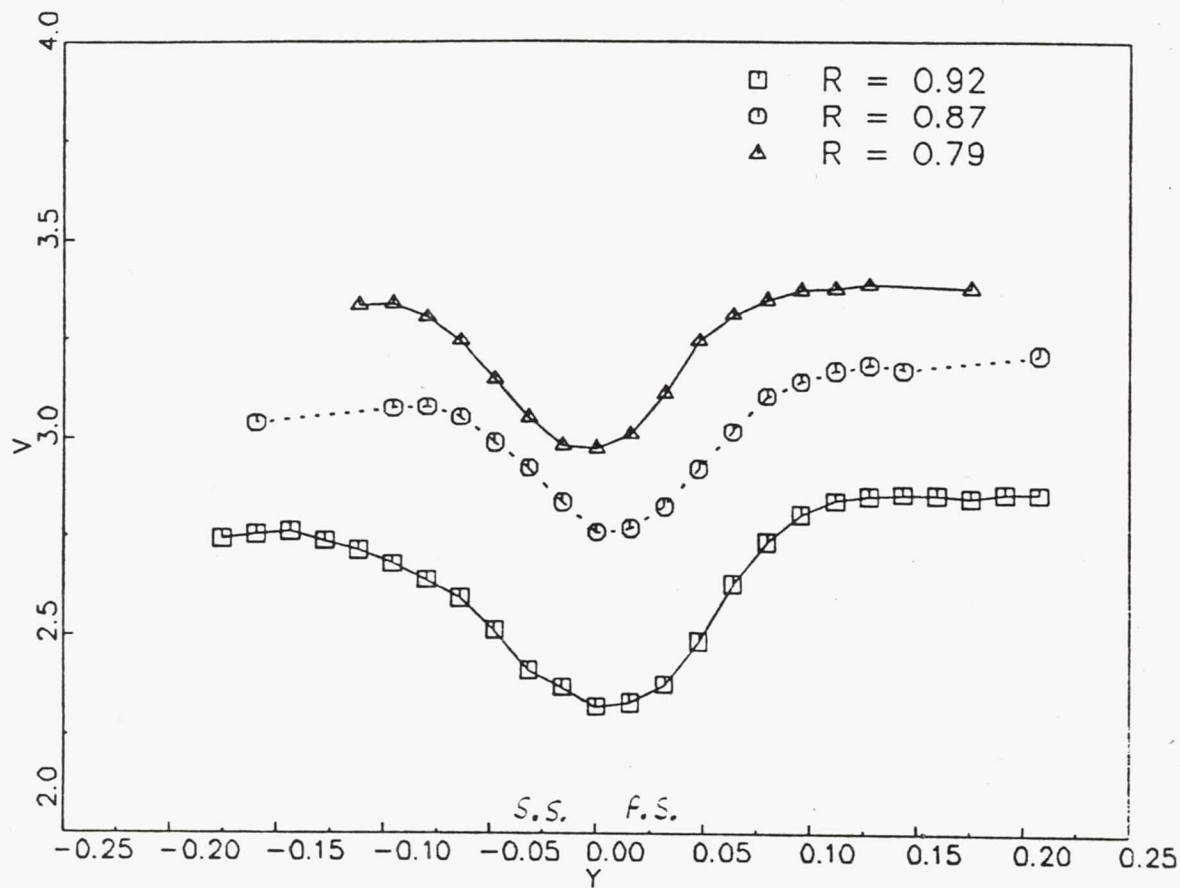


Figure 5. Total and axial velocity variation across the nozzle wake ($x=1.00$)

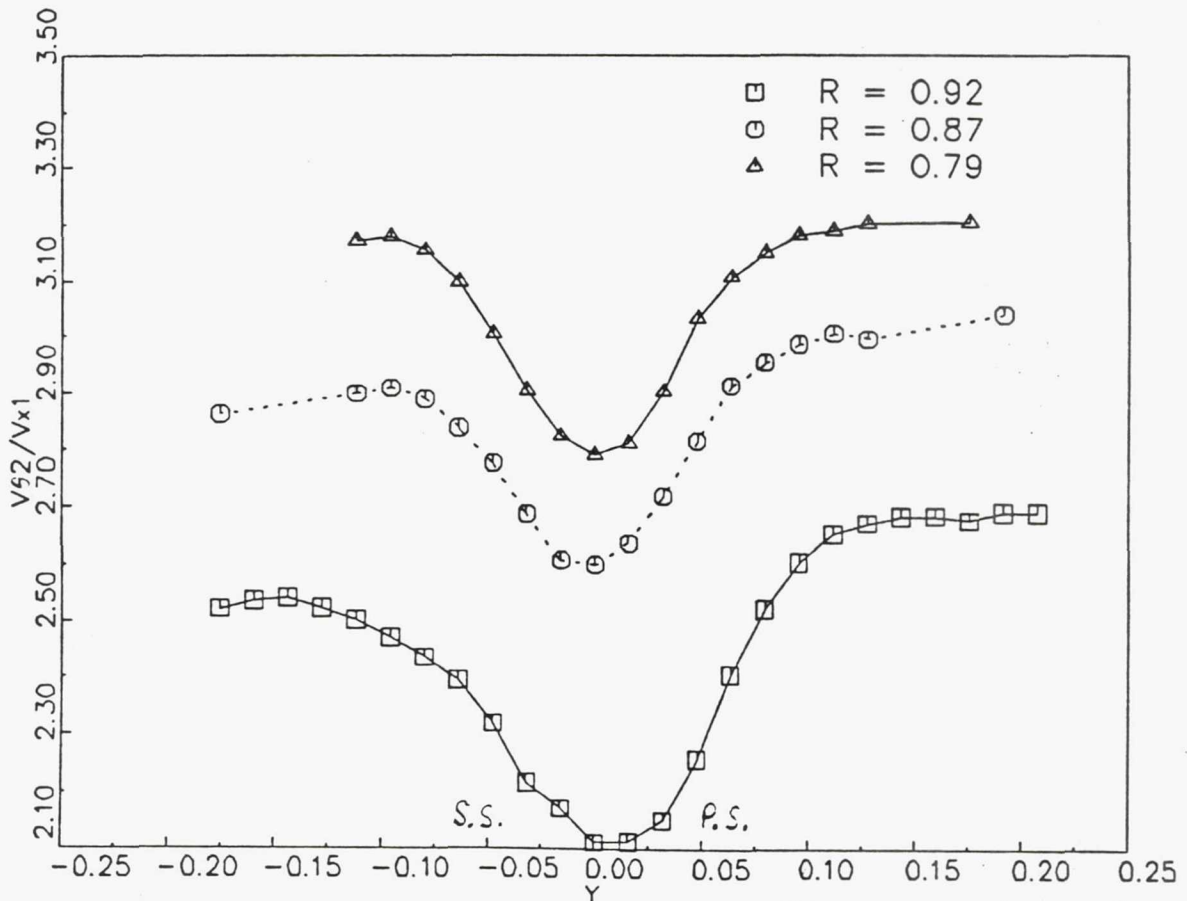
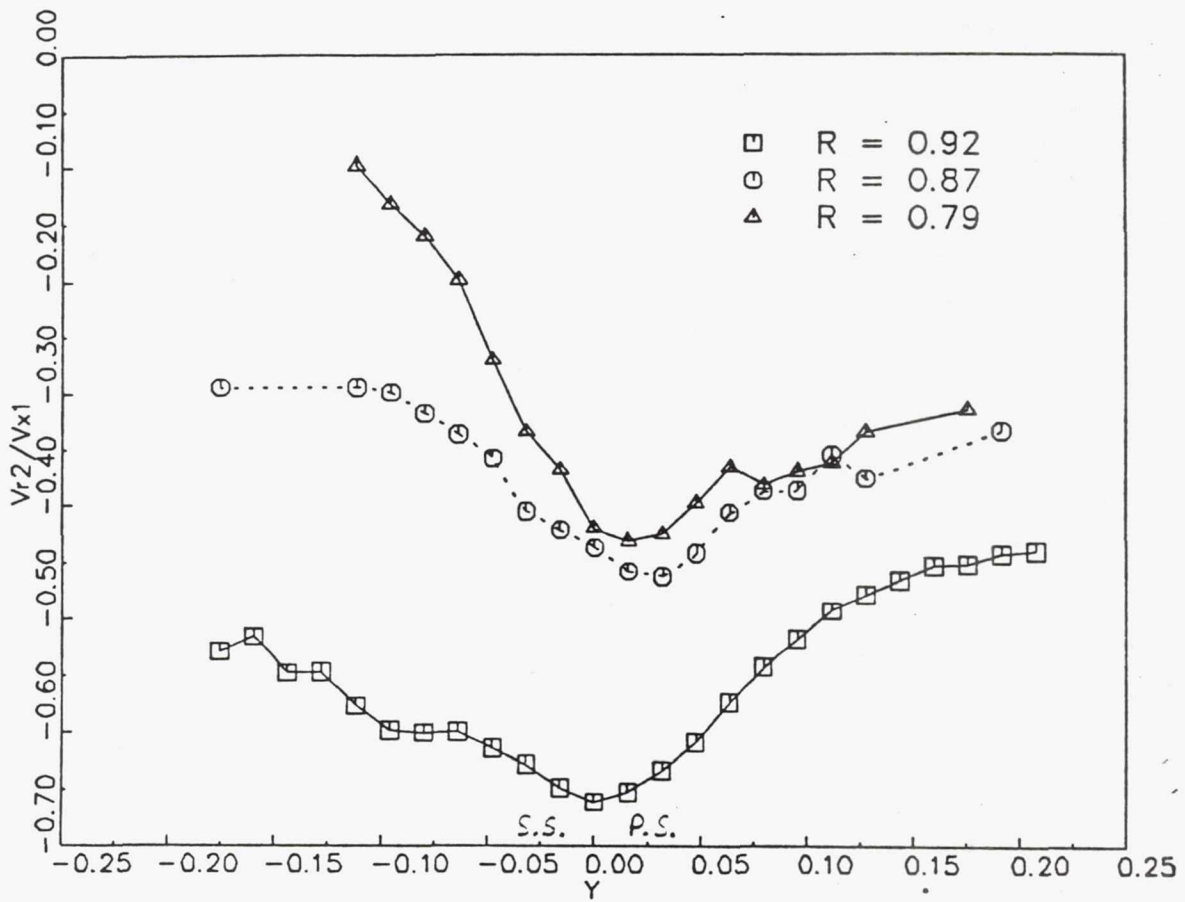


Figure 6. Tangential and radial velocity profiles across the nozzle wake ($X=1.08$)

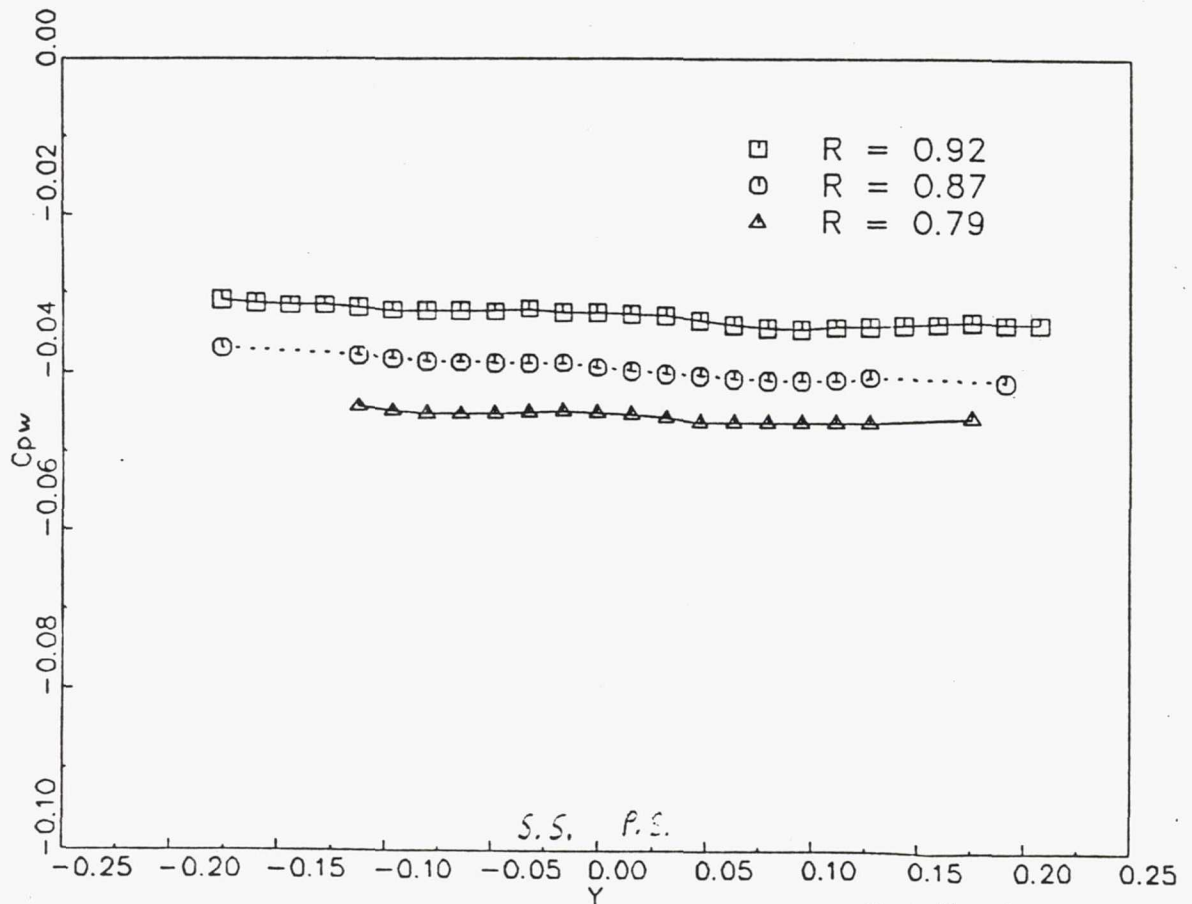
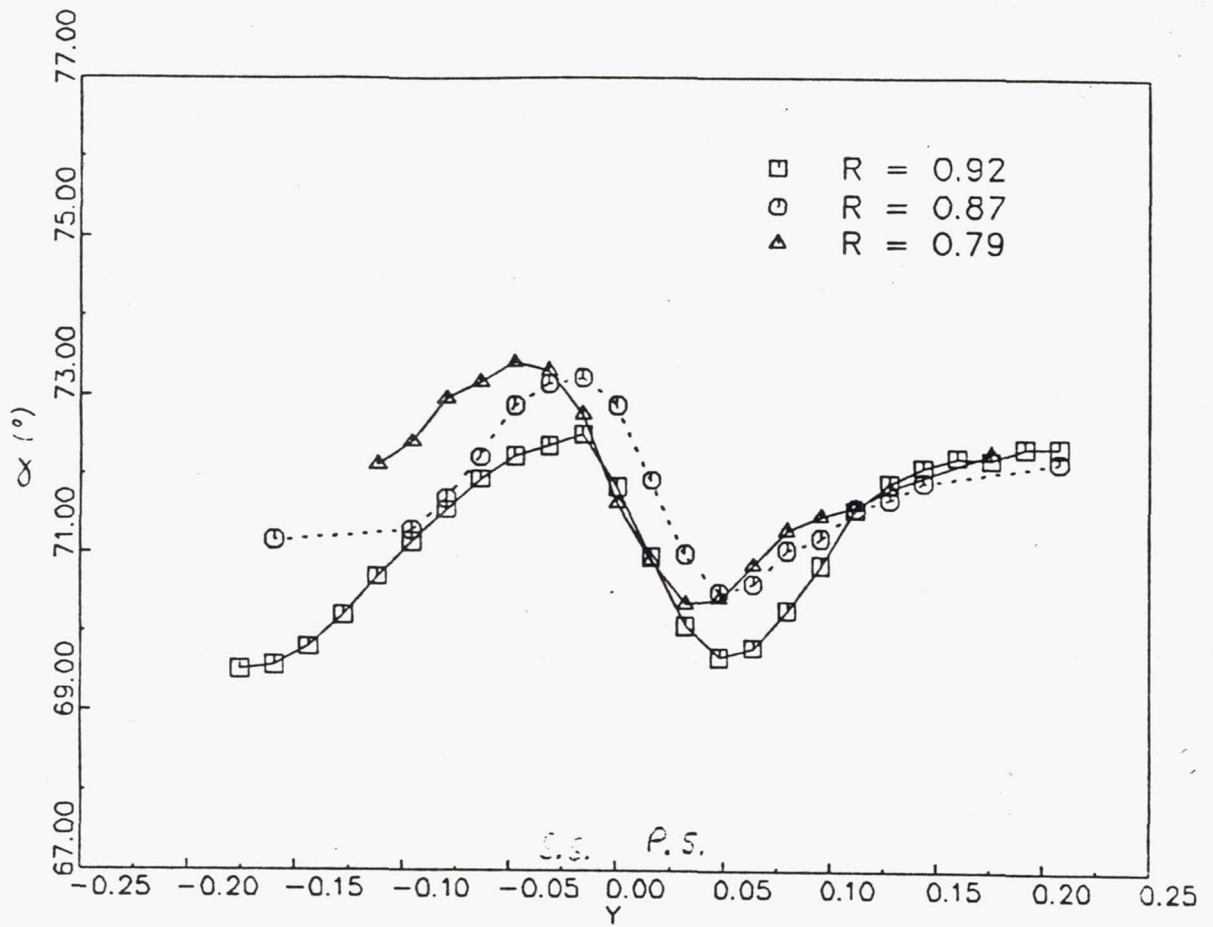


Figure 7. Flow outlet angle and static pressure distribution across the nozzle wake ($X=1.08$)

| | | | | | |
|---|--|--|---|---|-------------------|
| 1. Report No. NASA CP-10064 | | 2. Government Accession No. | | 3. Recipient's Catalog No. | |
| 4. Title and Subtitle Structural Integrity and Durability of Reusable Space Propulsion Systems | | | | 5. Report Date May 1991 | |
| | | | | 6. Performing Organization Code | |
| 7. Author(s) | | | | 8. Performing Organization Report No. E -6068 | |
| | | | | 10. Work Unit No. 553-13-00 | |
| 9. Performing Organization Name and Address National Aeronautics and Space Administration Lewis Research Center Cleveland, Ohio 44135 - 3191 | | | | 11. Contract or Grant No. Conference Publication | |
| | | | | 13. Type of Report and Period Covered | |
| 12. Sponsoring Agency Name and Address National Aeronautics and Space Administration Washington, D.C. 20546 - 0001 | | | | 14. Sponsoring Agency Code | |
| | | | | | |
| 15. Supplementary Notes | | | | | |
| 16. Abstract A two-day conference on the structural integrity and durability of reusable space propulsion systems was held on May 14 and 15, 1991, at the NASA Lewis Research Center. Presentations were made by industry, university, and government researchers organized into four sessions: aerothermodynamic loads; instrumentation; fatigue, fracture, and constitutive modeling; and structural dynamics. The principal objectives of the conference were to disseminate research results and future plans in each of four areas. This publication contains extended abstracts and the visual material presented during the conference. | | | | | |
| 17. Key Words (Suggested by Author(s)) Earth-to-orbit propulsion; Reusable rocket systems; Aerothermodynamic loads; Fatigue; Life; Structural dynamics; Instrumentation | | | 18. Distribution Statement LIMITED DISTRIBUTION DOCUMENT Because of its significant technological potential, this information which has been developed under a U.S. Government program is being given a limited distribution whereby advanced access is provided for use by domestic interests. This legend shall be marked on any reproduction of this information in whole or in part. Date for general release <u>May 1993</u> Subject Category 20 | | |
| 19. Security Classif. (of the report) Unclassified | | 20. Security Classif. (of this page) Unclassified | | 21. No. of pages 296 | 22. Price* A13 |